NASA-CR-205181

STRUCTURE IDENTIFICATION WITHIN A TRANSITIONING SWEPT-WING BOUNDARY LAYER

by

Keith Chapman and Mark Glauser

Department of Mechanical and Aeronautical Engineering
Clarkson University
Potsdam, NY 13699-5725

Report No. MAE- 319
December 1996

The undersigned have examined the dissertation entitled:

Structure Identification within a Transitioning Swept-Wing Boundary Layer

presented by Keith Lance Chapman,
a candidate for the degree of Doctor of Philosophy,
and hereby certify that it is worthy of acceptance.

_____   _____
Date   Dr. M. Glauser, Advisor

_____
Dr. G. Ahmadi

_____
Dr. C. Jahnke

_____
Dr. S. P. Lin

_____
Dr. H. Shen

_____
Dr. D. Valentine

Abstract

Extensive measurements are made in a transitioning swept-wing boundary layer using hot-film, hot-wire and cross-wire anemometry. The crossflow-dominated flow contains stationary vortices that breakdown near mid-chord. The most amplified vortex wavelength is forced by the use of artificial roughness elements near the leading edge. Two-component velocity and spanwise surface shear-stress correlation measurements are made at two constant chord locations, before and after transition. Streamwise surface shear stresses are also measured through the entire transition region.

Correlation techniques are used to identify stationary structures in the laminar regime and coherent structures in the turbulent regime. Basic techniques include observation of the spatial correlations and the spatially distributed auto-spectra. The primary and secondary instability mechanisms are identified in the spectra in all measured fields. The primary mechanism is seen to grow, cause transition and produce large-scale turbulence. The secondary mechanism grows through the entire transition region and produces the small-scale turbulence.

Advanced techniques use linear stochastic estimation (LSE) and proper orthogonal decomposition (POD) to identify the spatio-temporal evolutions of structures in the boundary layer. LSE is used to estimate the instantaneous velocity fields using temporal data from just two spatial locations and the spatial correlations. Reference locations are selected using maximum RMS values to provide the best available estimates. POD is used to objectively determine modes characteristic of the measured flow based on energy. The stationary vortices are identified in the first laminar modes of each velocity component and shear component. Experimental evidence suggests that neighboring vortices interact and produce large coherent structures with spanwise periodicity at

double the stationary vortex wavelength. An *objective* transition region detection method is developed using streamwise spatial POD solutions which isolate the growth of the primary and secondary instability mechanisms in the first and second modes, respectively. Temporal evolutions of dominant POD modes in all measured fields are calculated. These scalar POD coefficients contain the integrated characteristics of the entire field, greatly reducing the amount of data to characterize the instantaneous field. These modes may then be used to train future flow control algorithms based on neural networks.

Dedicated to my parents:

Jacqueline B. Chapman and Samuel J. Chapman III

and

In loving memory of my grandmother:

Bertha Chapman

"Don't let what you cannot do interfere with what you can do."

John Wooden

Acknowledgments

The author is greatly indebted to Dr. Mark Glauser, for his guidance, technical expertise and friendship. I am particularly grateful for his philosophy on learning and the many opportunities he has presented before me to visit other research facilities such as the NASA Dryden Flight Research Center and Arizona State University. One certainly learns more with greater exposure. The author would also like to thank Dr. William Saric for his invaluable insights, friendship and the opportunity to work at the Arizona State University Unsteady Wind Tunnel Facility (ASU UWT). His contributions have greatly affected the direction of this research effort and will continue to do so in future projects.

The author wishes to thank the many co-workers at Arizona State University. The help of Dr. Mark Reibert was and continues to be a significant contribution to this research effort. He has participated in many technical discussions, assisted with the experiments and supplied several figures in this dissertation. The author would also like to thank Dan Clevenger, the ASU UWT technician, for his invaluable support and abilities. The assistance of Tonja Krutckoff and Ruben Carrillo are greatly appreciated, as are the many technical discussions and mountain biking adventures with Dr. Tim Haynes.

NASA has played a major role in this study by providing direction and financial support. This research was mostly supported by the NASA Dryden Flight Research Center under grant NAG-2-724. Supplemental funds have been contributed by the NASA/Clarkson University Space Grant. The author is indebted to Edmund Hamlin, Paul Harney, Rod Bogue and William McCain for the many internships at NASA Dryden and continued support throughout the years. I would like to thank Michael Bowman for his assistance with all things electronic. The author also recog-

Table of Contents

Page

List of Figures

List of Tables

CHAPTER 1

Introduction

1.1 History and Motivation

For over a century, scientific investigations of flows over solid surfaces have been at the heart of fluid mechanics research. It is this study of the boundary layer that has given birth to countless developments in technology, including advances in aviation and aerodynamics, turbomachinery, heat-transfer systems, marine and ground transportation and even atmospheric and environmental studies. Several historic fundamental studies have led to practical engineering applications which have literally changed society, such as the birth of aviation, perhaps one of the most influential. Ever since the first aircraft, researchers have tried to enhance and improve flight conditions. Eventually, aircraft were commonly being used for both civil transportation and military operations. As the need for even faster and more efficient aircraft came about just before the second world war, the issue of reducing drag came to the forefront of aircraft design and control of boundary-layer flows became a primary focus in fluid mechanics. Even still, some fifty years later, many researchers are developing ways to control boundary-layer flows. This investigation hopes to contribute to the building of a solid foundation upon which dynamic flow control strategies can be developed.

Of course, developing effective flow control strategies requires understanding the flow physics as much as possible. It also requires powerful analysis techniques to translate the flow's current state into useful data on which a control decision can be made to produce a desired effect. It is in this light, that the current investigation of a three-dimensional, swept-wing boundary layer is presented. The current experimental work is designed to further our knowledge on boundary-layer

transition mechanisms and origins of coherent structures in turbulent boundary layers and to, therefore, develop a method of extracting the data needed to make effective control decisions. Thus, using our knowledge of boundary-layer evolution over a swept wing, from its origin at the leading edge to transitional breakdown to turbulence, we can produce effective techniques which may lead to future flow control strategies. With the results presented here, future flow control strategies may be developed with the hopes of delaying transition, thereby achieving reduced drag (i.e., better fuel-efficiency), better maneuverability and safer flight in general.

1.2 Swept-Wing Flows

1.2.1 Historical Origins

In 1935, during the worldwide quest for a faster aircraft, Busemann formally presented the concept of sweeping back the wings of an aircraft to reduce drag at transonic and supersonic speeds. Busemann's basic principle suggested that the component of the freestream velocity parallel to the leading edge would not be perturbed by the wing thus preserving laminar flow. The critical conditions would only be reached when the freestream velocity component normal to the leading edge was locally accelerated at some point on the wing to the local sonic speed. Although this theory could only be true on an ideal infinite-span wing of constant section, it did set the foundation for swept-wing research. In 1939, the continuing theoretical work of Betz suggested that swept wings delayed the formation of shocks on the wing surface. This was confirmed experimentally by Ludweig in same year. Since that time, swept-wing flow has become a fundamental aspect of modern aerodynamics. The reader is referred to Schlichting (1960) and von Kármán (1963) for a more detailed historical perspective on the development of the swept wing and the work of Busemann, Betz and Ludweig.

Further investigations by Gray (1952) demonstrated that high-speed swept wings have only minimal laminar flow compared to the same wings without sweep. Researchers then discovered the presence of basic instabilities in swept-wing flow and other three-dimensional boundary layers which caused the abrupt transition from a laminar boundary layer to a turbulent one (Owen and Randall 1952; Gregory et al. 1955; Brown 1959). The discovery of these instabilities and the problems they cause stimulated the beginnings of research on laminar flow control. Pfenninger

2
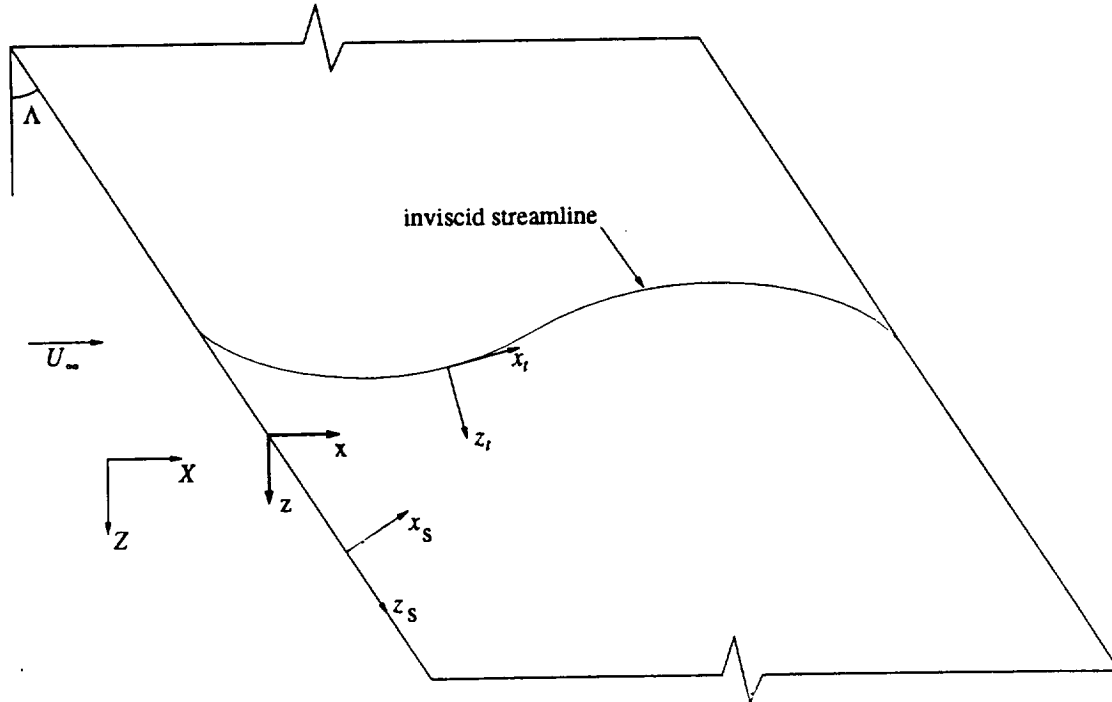
Figure 1.1: Schematic plan view of a swept wing showing four coordinate systems and an inviscid streamline. Figure adapted from Reibert (1996a).

(1957) led these early research efforts by examining the effects of suction applied to the swept-wing boundary layer which influenced a series of laminar flow control experiments referenced in Pfenninger (1977). Pfenninger's group was able to achieve full-chord laminar flow at a chord-based Reynolds number of 29 million through the use of suction, providing a promising future for laminar flow control strategies.

1.2.2 Coordinate Systems

Discussing the flow over a swept wing requires familiarization with the typical coordinate systems used in analytical and experimental work. Figure 1.1 shows four common coordinate systems used to describe a swept wing with a positive sweep angle, Λ. The flow is from left to right as indicated by the freestream velocity, U_∞. The universal coordinates (X, Y, Z) are aligned to $\Lambda = 0°$, i.e., to the leading edge and chord line if the wing were unswept. This reference frame is generally aligned to the test-section walls in experimental wind-tunnel testing and is sometimes used to describe the instrumentation traverse system's motions. This right-handed coordinate sys-

3

tem consists of the streamwise direction, X, which is in the flow direction, the Y coordinate which is normal to the test-section side wall and the Z coordinate which is the vertical direction.

A similar coordinate system which is referred to as the global coordinate system is represented by (x, y, z) in figure 1.1. This system is aligned similarly to the universal coordinate system but is attached to the leading edge of the wing. The x coordinate is aligned to the X direction. The y coordinate is normal to the chord line and the z coordinate is parallel to $\Lambda = 0°$ and to the Z direction. This system is primarily used to develop the analytical equations in chapter 2 and to describe some of the measurements. The corresponding total velocity components are denoted by $(\bar{u}, \bar{v}, \bar{w})$. Also within this system are the two-component surface shear stresses, expressed as $(\bar{\tau}_x, \bar{\tau}_z)$. The $\bar{\tau}_x \perp \bar{\tau}_z$ plane is perfectly aligned with the x and z axes.

The model-oriented, swept coordinate system (x_s, y_s, z_s) shown in figure 1.1 is referenced from the swept wing-chord plane and is simply the global coordinate system angled Λ degrees in the x-z plane. The x_s coordinate is normal to the leading edge of the wing. The y_s coordinate is normal to the chord line and the z_s coordinate is parallel to the leading edge in the swept, spanwise direction. The corresponding total velocity components in this system are $(\bar{u}_n, \bar{v}_n, \bar{w}_n)$. Also within this system, the two-component surface shear stresses are expressed as $(\bar{\tau}_{nx}, \bar{\tau}_{nz})$. The $\bar{\tau}_{nx} \perp \bar{\tau}_{nz}$ plane is perfectly aligned with the x_s and z_s axes.

Figure 1.1 also displays a fourth coordinate system (x_t, y_t, z_t) referenced to the boundary layer and aligned with the inviscid streamlines. The x_t direction is tangent to the inviscid streamline. The y_t direction is normal to the model surface and the z_t coordinate is orthogonal to the inviscid streamline. Likewise, the corresponding total velocity components in the boundary-layer system are $(\bar{u}_t, \bar{v}_t, \bar{w}_t)$. Similarly the two-component surface shear stresses are expressed as $(\bar{\tau}_{tx}, \bar{\tau}_{tz})$ whose plane is perfectly aligned with the x_t and z_t axes.

1.2.3 Boundary-Layer Transition

The flow over a swept wing and other three-dimensional boundary-layer flows have recently been

studied with the focus of understanding the fundamental instability mechanisms which cause transition from a laminar boundary layer to a turbulent one. This transition process can usually be described by three phases of boundary-layer evolution. The first of these is referred to as the receptivity mechanism. Receptivity is the mechanism by which freestream disturbances enter the boundary layer (Morkovin 1969). Although this mechanism is not yet well understood, it is known to provide the initial amplitude, frequency and phase of unstable waves within the boundary layer (Saric 1994b). These initial conditions originate from external disturbances, such as wing surface roughness or vibration or acoustic and vortical fluctuations in the freestream. These conditions, the geometry of the wing and flow conditions give birth to several possible instability modes within the boundary layer.

The second phase of transition is described as the initial growth of small disturbances in the boundary layer. The small fluctuations resulting from the initial receptivity mechanism are amplified and have been described by linear stability theory, a mathematical model of the flow using linear, unsteady disturbance equations derived from the nonlinear Navier-Stokes equations (Mack 1984; Reed et al. 1996). This theory applies rather well to two-dimensional flows (Saric 1992b) but does not fully describe the different instability mechanisms in three-dimensional boundary layers (Reed and Saric 1989).

The third phase of boundary-layer transition is the nonlinear interaction of multiple instability modes. Mathematically, this occurs when the disturbances gain enough energy and their amplitudes grow to make the nonlinear terms in the Navier-Stokes equation significant. Physically, the disturbance growth distorts the basic-state boundary layer which in turn produces rapid growth in the secondary instabilities thus leading to the onset of turbulence (Saric 1992b).

Once the flow has transitioned to turbulence, the boundary layer contains eddies or coherent structures, irregular and generally unpredictable fluctuations of high frequency superimposed on the main-stream boundary layer. At high Reynolds numbers, typical of swept-wing flows, the mean flow constantly supplies energy to large eddies in the boundary layer. Energy is also dissipated, predominantly by the small scales in the flow very close to the wall. Because of its complexity and effects that increased drag, a turbulent boundary layer over a wing surface is certainly not an optimal flow state. However, it is not the least desirable case either since it does remain attached in most cases due to pressure increases. A separated flow over a wing is far less desirable than an attached, turbulent boundary layer whose complexity makes flow control, flow modeling

and prediction extremely difficult. By understanding how these fluctuations or eddies originate, flow control strategies can focus on turbulence prevention. Also, by observing how these coherent structures develop, propagate and evolve, other flow control strategies might be designed to break down the large eddies into smaller eddies thus transferring energy from the generation mechanisms to the dissipating mechanisms. Ideally, however, one would generally prefer an attached, laminar boundary layer across the entire wing, drastically reducing drag and maintaining safe flight conditions. Hence, the current experiment focuses on transition and the origins of turbulence in the swept-wing boundary layer.

1.2.4 Instabilities

In general, there are four specific fundamental modes of instability which cause transition on swept wings. These are attachment-line, centrifugal, streamwise and crossflow instabilities. The attachment-line instability is associated with the basic instability of the attachment-line boundary layer and its contamination by, for example, turbulent disturbances propagating along the leading edge. The end result is effectively a premature "tripping" of the boundary layer. Wings with large leading-edge radii are particularly prone to these instabilities (Poll 1979, 1985; Hall et al.1984; Hall and Malik 1986). The centrifugal instability mechanism is a result of the shear flow over concave surfaces generally producing Görtler vortices (Floryan 1991; Benmalek and Saric 1994; Saric 1994a). The streamwise instability mechanism is associated with the pressure gradient and chordwise velocity component. It is comparable to Tollmein-Schlichting waves in two-dimensional flows. This instability appears in regions along the wing with zero or weakly positive pressure gradients (Gray 1952; Saric 1992b). The crossflow instability is an inviscid mechanism caused by the combined effect of wing sweep and pressure gradient (see Section 1.2.5). These instabilities may exist individually or in any combination in a swept-wing flow field depending on various conditions involving Reynolds number, surface roughness and curvature, sweep angle and pressure gradients.

1.2.5 Crossflow Instability

Perhaps the most common instability in swept-wing flows is the crossflow instability, a physical mechanism resulting from the combined effects of wing sweep and a favorable pressure gradient. As the potential flow reaches the leading edge of the wing, the streamlines begin to immediately

bend outboard (in the positive z direction) due primarily to the sweep and declining pressure. Just aft of the attachment line on most airfoils, the streamlines then curve inboard and start aligning with the chord-line until the chordwise pressure minimum is reached. Here the streamlines then bend in an outboard direction as the trailing edge is approached due to the pressure recovery.

Flow near the surface of the wing has much less streamwise momentum than in the freestream and therefore is actually deflected more by these pressure gradient and sweep effects than the inviscid streamlines. Therefore the boundary-layer flow is not completely in the direction of the inviscid streamlines. Figure 1.2 shows a sketch of the general velocity-component profiles in the laminar boundary layer of a swept-wing. The figure demonstrates the tangential velocity component following the streamline and the crossflow velocity component perpendicular to the streamline. For positively swept wings ($\Lambda > 0$) as shown in figure 1.1, the crossflow velocity component is positive and propagates in the z_t direction as defined in figure 1.1. The resulting total velocity profile (shaded in figure 1.2) follows the streamline near the edge of the boundary layer and twists outboard in the z_t direction closer to the surface. The crossflow profile obeys the no-slip condition at the surface and asymptotically disappears at the boundary-layer edge, thus producing an inflection point which directly corresponds to an inherent inviscid instability. Thus, the crossflow instability manifests itself as co-rotating vortices within the boundary layer whose axes are just barely offset from the potential-flow direction. Transition to a turbulent boundary layer begins when these vortices gain enough energy and momentum to "spill" upon themselves, becoming unstable and eventually breaking down into turbulent eddies and smaller scales.

The crossflow instability also exhibits two fundamental disturbances that may be amplified, stationary crossflow waves and travelling crossflow waves. Both may cause transition but the dominant mechanism is usually identified through analysis of the boundary-layer receptivity. Studies by Bippes et al. (1991), Deyhle et al. (1993) and Deyhle and Bippes (1996) have shown that travelling waves tend to dominate in flows with significant unsteady freestream disturbances. However, stationary crossflow waves tend to dominate transition when in low-disturbance environments. And since the flight environment is generally better represented by low-disturbance surroundings, the stationary crossflow instability mechanism is expected to dominate and hence is the case under study for the current experiment.

The stationary crossflow waves are typically weak in the spanwise and wall-normal direc-
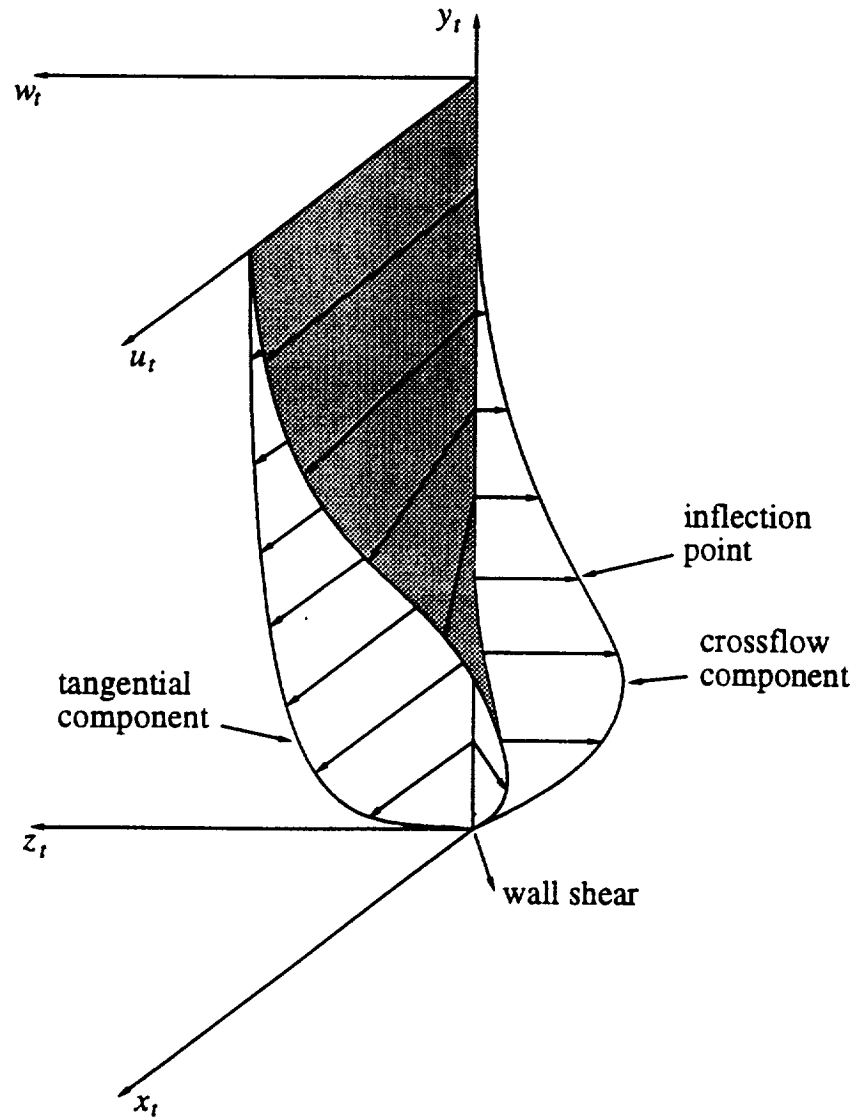
Figure 1.2: Schematic of the swept-wing boundary-layer profile showing the tangential, crossflow and total velocity profiles. Figure courtesy of Reibert (1996a).

tions and therefore are assumed by most to be linear in nature. However, recent experiments have shown that these waves demonstrate highly nonlinear effects (Dagenhart et al. 1990; Bippes et al. 1991; Radeztsky et al. 1994; Reibert et al. 1996). The source of this nonlinearity is found in the fact that the wave fronts are indeed immobile with respect to the wing surface and that they are nearly aligned to the inviscid streamlines. Because of this, the waves have a cumulative effect by interacting with the same fluid (propagating along the potential flow streamlines) creating large

streamwise distortions in the velocity profile. The weak waves create these distortions by convecting low-speed fluid away from the surface and high-speed fluid towards the surface. This results in spanwise spatial variation of the mean streamwise velocity profile. As the distortions grow further downstream, an alternating pattern of accelerated, deccelerated and doubly-inflected velocity profiles emerges in span. These doubly-inflected profiles are inherently unstable and are subject to a high-frequency secondary instability which is highly amplified and rapidly breakdowns locally (Kohama et al. 1991). This local breakdown causes a nonuniform saw-tooth pattern of turbulent wedges to appear in span making way for the onset of turbulence.

1.3 Literature Review

Over the course of the past century, there have been numerous landmark research projects that have laid the foundation for studying two- and three-dimensional flows. Significant contributions have been made in experimental observations, flow modeling and deriving theories on transition yet much remains to be explored. The reader is referred to the following comprehensive reviews of past research efforts.

The fundamental flow over a rotating disk displays the same crossflow instability mechanisms that are found in the swept-wing boundary layer, yet are easier to study. The symmetric geometry, the fact that the flow is an exact solution of the Navier-Stokes equation and a boundary layer of constant thickness allow simpler applications of theory, computational techniques and experimental techniques. Hence, it is worthwhile to review the significant contributions from these fundamental studies as they may directly apply to more complex three-dimensional boundary-layer flows. In fact, this crossflow-dominated flow and its relative properties to swept-wing crossflow instability are further discussed in chapter 2. Fundamental properties of this flow and the stability of three-dimensional boundary layers in general are described in detail by Gregory et al (1955). Reed and Saric (1989) provide an excellent review of three-dimensional boundary layers and give extensive literature surveys of rotating disk flows, as well as swept-wing, rotating cone and rotating sphere flows. The reader is particularly referred to Aubry et al. (1994) who investigated transition to turbulence on a rotating disk using biorthogonal analysis techniques, similar to the proper orthogonal decomposition used in the current study, to quantify the growth of

9

complexity in the flow state as Reynolds number was increased.

For historical reviews of pioneering work in swept-wing development, the reader should consult von Kármán (1963) and Schlichting (1960). For more recent swept-wing and other three-dimensional boundary-layer research efforts regarding transition and instability studies, the reader is referred to Reed and Saric (1989). For the most recent review of swept-wing flows, specifically focusing on the crossflow instability, the reader is referred to Arnal (1992), Dagenhart (1992) and Radeztsky (1994). The fundamentals of transitioning flows is explained in Saric (1992b). Theoretical research efforts, including transition prediction methods and control possibilities, are summarized in Arnal (1984, 1986), Poll (1984), Arnal et al. (1990) and Reshotko (1994). Mack (1984) and Reed et al. (1996) give excellent reviews of linear stability theory, its use and limitations. With these references readily available, only material directly related to the current research effort will be cited here.

Experimental investigations on the crossflow instability have been performed since the early 1950's (Gray 1952; Owen and Randall 1952; Stuart 1953; Gregory et al. 1955). Gray (1952) is credited with first identifying the crossflow instability. He was able to visualize the crossflow-vortex pattern using sublimating chemicals applied to the surface of a swept wing. Gregory et al. (1955) established the complete disturbance equations for a three-dimensional boundary layer thus providing a general theory for these early research efforts. Soon thereafter, laminar flow control strategies involving boundary-layer suction were investigated by Pfenninger and his co-workers (Pfenninger 1957; Brown 1959; Gault 1960; Pfenninger and Bacon 1961). The early developments of laminar flow control are summarized in Pfenninger (1977).

More recently, Saric and Yeates (1985) studied crossflow mechanisms on a 25° swept flat plate. They used a wall bump to create the necessary pressure gradient and found the first experimental evidence of superharmonics of the fundamental mode which implies a degree of nonlinearity in modal interactions. Michel et al. (1985) investigated transition experimentally and theoretically on an approximate infinite-span, swept wing. Recent studies on initial conditions and nonlinear effects of the crossflow instability are found in Deyhle et al. (1993), Lerche and Bippes (1995) and Deyhle and Bippes (1996). These efforts show that the level of freestream turbulence determines whether travelling (high turbulence levels) or stationary (low turbulence levels) crossflow waves dominate transition. Kohama et al. (1991) found that the stationary crossflow instability causes transition through the rapid growth of high-frequency secondary instabilities. This

demonstrates the importance of stationary waves in low-disturbance environments, such as in flight, and thus is the subject of the current investigation.

Also of importance to the present investigation is the effect of surface roughness which has been studied in detail by Radeztsky et al. (1993a, 1994). These results show that local transition can be induced on a swept-wing by micron-sized, three-dimensional surface roughness elements placed just aft of the attachment line. Spacing these roughness elements appropriately can isolate specific modes in the crossflow instability and create uniform transition fronts (Reibert et al. 1996; Chapman et al. 1996; Reibert 1996a). This technique was used for the current experiment to simplify the modal content of the crossflow instability. Dagenhart et al. (1989, 1990), Dagenhart (1992) and Radeztsky et al. (1994) have investigated the effects of natural surface roughness on transition and have determined that this is a major cause for the uneven saw-tooth transition pattern frequently seen by flow-visualization techniques on swept-wings. The modal isolation method overrides this complexity.

1.4 Present Investigation

In most real-world applications, particularly in flight, full-chord laminar flow over swept wings as obtained by Pfenninger (1957) is very uncommon, even with boundary-layer suction applied. In most cases, all three flow regimes, laminar, transitional and turbulent, are found on swept wings and other aircraft surfaces. Therefore, an understanding of each flow regime and how they evolve is absolutely necessary for analyzing and designing effective swept-wing planforms and flow control systems. Determining the active modes resulting from known instability mechanisms in each regime will allow more appropriate modeling of swept-wing flow which could greatly influence future designs of aircraft surfaces. This is why the current study includes an analysis of all three flow regimes in the swept-wing boundary layer dominated by a single stationary crossflow instability mechanism, the most important on swept-wing aircraft.

This investigation consists of several multi-point measurements in a 45° swept-wing boundary layer, which is forced to the dominant crossflow-vortex wavelength by the placement of three-dimensional surface-roughness elements just aft of the attachment line. The crossflow-vortex wavelength is determined by mean-velocity boundary-layer profiles and surface flow visualization

techniques. Hot-wire, cross-wire and hot-film anemometry is used to make multi-point correlation measurements. Calculating various spatio-temporal correlations and related spectra for simultaneous velocity and surface shear-stress measurements allows the use of two multi-point correlation analysis techniques, linear stochastic estimation (LSE) and proper orthogonal decomposition (POD). These powerful and objective techniques provide valuable insight into the various structural modes of the flow in each regime which capture the evolution of the boundary layer. A greater understanding of what the structures in the flow are doing and where they come from is essential to developing effective flow control strategies. The combined use of LSE and POD identifies these significant flow structures and how they evolve. Therefore by making appropriate measurements, the evolution of the boundary layer can indeed be better understood.

There is often a large gap between fundamental scientific exploration and real-world application. It is the author's hope and long-term goal that the techniques presented here be translated to real-world applications, particularly to those related to actual flight and active flow control. Thus the immediate goals of the current investigation are:

(1) to determine active spatial and temporal modes and structures in the crossflow-dominated swept-wing boundary layer just before transition and just after, in the turbulent regime, through extensive correlation measurements and application of correlation analysis techniques,

(2) to compare two-component velocity measurements in the boundary layer to surface shear-stress measurements on the surface at corresponding span and chord locations,

(3) to suggest techniques that will allow the estimate of internal velocity information from calibrated surface measurements only and

(4) to develop and suggest methods of extracting necessary information about a flow field for use in active and passive flow control.

1.5 Outline

The details of the experiment and analysis techniques are explained in the remaining chapters. Chapter 2 presents some theoretical considerations including the derivation of the governing equations. Chapter 3 describes the Arizona State University Unsteady Wind Tunnel facility, where the experiment is performed, and the various data acquisition equipment used. Chapter 4 dis-

cusses the various instrumentation used in the experiment. It also describes the calibration schemes used for each type of sensor, including a new technique in calibrating hot-film sensors. Chapter 5 discusses the various experiments that are performed including flow visualizations, mean-velocity boundary-layer scans, two-component, two-point velocity correlation measurements and several multi-point surface-shear-stress correlation measurements. The multi-point correlation analysis techniques are presented in Chapter 6 which include the basic theory of linear stochastic estimation (LSE) and proper orthogonal decomposition (POD), a brief review of significant literature on each technique, and the various calculations made. Chapter 7 includes the various correlation and spectra calculations and results. The one-dimensional POD results and the results from the complimentary technique (a method which harnesses the advantages of both the LSE and the POD) are presented in Chapter 8. Chapter 9 then includes a discussion of significant conclusions, proposed methods on how to apply these techniques to flight and suggestions for future work.

CHAPTER 2
Theoretical Considerations

2.1 Governing Equations

Governing equations are generally derived to describe a flow field such that certain conditions or events may be studied analytically. In fundamental flows of simple geometries, the equations act as a check and balance system for experiments and provide the engine for computer simulations, transition prediction methods and other flow models.

The swept-wing boundary layer, however, is far from simple and requires a great deal of theory consisting of complex nonlinear equations involving such principles as wing surface curvature, sweep, viscous flow, and three-dimensionality. It is well beyond the scope of this investigation to account for a complete analytical derivation of these types of equations. Efforts such as that by Haynes (1996) go into great theoretical detail in describing the nonlinear equations for a crossflow-dominated swept-wing boundary layer in support of complex computer simulations of the flow. His work is based on the current experimental configuration and provides a valid and detailed analysis of the disturbance equations.

The current work only requires a simplified approach, one that will focus on the fundamental physics of the boundary layer. Physically important effects such as the wing surface curvature are neglected here. However, through the derived simplified equations we see the very basic and fundamental laws of fluid particles within the boundary layer and can perhaps infer general flow behaviors. Actually tracking the origins of instability and their growth requires more intensive analysis and cannot be accomplished with these simplified equations. The reader is referred to Mack (1984), Michel et al. (1985), Arnal et al. (1990), and Haynes (1996) for detailed summaries of more involved analytical approaches.

2.1.1 Reynolds Decomposition

Since this experimental investigation is primarily concerned with the evolution of the spatial disturbances in the laminar boundary layer and of the large scale structures within the turbulent regime, it is convenient to treat the mean and fluctuating parts of velocities, surface shear stresses and pressures separately. In studying scales in turbulent flows, one is generally more interested with the fluctuations and their evolution. Hence, Reynolds decomposition, a method of separating these quantities outlined in Tennekes and Lumley (1972), is used in all flow regimes. By using this separation technique in each of the boundary-layer states, we can observe the role of terms associated with the fluctuating quantities that eventually develop through transition into eddies or coherent structures in the turbulent state.

Application of Reynolds decomposition allows the total velocity components, $(\tilde{u}, \tilde{v}, \tilde{w})$, to be separated into a mean flow, $(\overline{U}, \overline{V}, \overline{W})$, and fluctuations, (u, v, w) such that for a single spatial position

$$\tilde{u} = \overline{U} + u$$
$$\tilde{v} = \overline{V} + v \tag{2.1}$$
$$\tilde{w} = \overline{W} + w.$$

Each mean variable denoted by the overbar ($\overline{}$) is interpreted as a time-averaged quantity of the total variable denoted by the tilda ($\tilde{}$). Therefore, by definition, the mean value of any individual fluctuating quantity at one point in space is zero. However, the product of two fluctuating quantities at one point in space is not zero when time averaged. These properties of the Reynolds decomposition only hold true if the mean flow is steady, i.e., the time derivative of each mean quantity must be zero. The same principles apply to pressure and to the two surface shear-stress components as expressed below.

$$\tilde{p} = \overline{P} + p$$
$$\tilde{\tau}_x = \overline{T} + \tau_x \tag{2.2}$$
$$\tilde{\tau}_z = \overline{T} + \tau_z$$

When analyzing a flow field that contains all three flow regimes, one has to merge the nota-

tions used in transition studies with those typically used in turbulence studies. In particular to the present investigation is the consideration of the disturbances in the laminar regime. These quantities are functions of space and time and are therefore not necessarily equal to zero when time averaged. The spatial dependence remains since the (u, v, w) velocities have spatio-temporal dependence. However, in the laminar regime of the swept-wing boundary layer, the time dependence is produced solely by the travelling crossflow waves. Thus, when the total velocity is time averaged in the swept-wing laminar regime, the mean velocities $(\bar{U}, \bar{V}, \bar{W})$ remain, but the travelling waves are averaged out of (u, v, w) and only the spatial dependence remains, i.e., only the stationary crossflow waves remain. Therefore, the time-averaged total velocity has two components in the laminar regime, the mean flow velocity and the spatial disturbances describing the stationary crossflow waves. To avoid confusion, the spatial disturbances are mathematically represented by a new set of variables, (u', v', w'). They are defined as

$$
\begin{aligned}
u'(x, y, z) &= \overline{u(x, y, z, t)} \\
v'(x, y, z) &= \overline{v(x, y, z, t)} \\
w'(x, y, z) &= \overline{w(x, y, z, t)}
\end{aligned}
\tag{2.3}
$$

and represent the stationary disturbances only. The pressure and surface shear stresses may also be represented accordingly for the variables p', τ'_x and τ'_z. Now, employing a linear stability approach by assuming a parallel basic state (i.e., $\bar{U} = \bar{U}(y)$, $\bar{V} = 0$ and $\bar{W} = \bar{W}(y)$), the time-averaged total velocities are then defined as

$$
\begin{aligned}
\overline{u(x, y, z, t)} &= \bar{U} + u'(x, y, z) \\
\overline{v(x, y, z, t)} &= v'(x, y, z) \\
\overline{w(x, y, z, t)} &= \bar{W} + w'(x, y, z) \ .
\end{aligned}
\tag{2.4}
$$

Note that effect of the travelling waves is essentially neglected in this definition. This is because the stationary crossflow waves dominate in the current experiment due to the extreme low levels of freestream turbulence (as explained in section 1.2.5). This notation is used in section 5.3 where the travelling waves are averaged out from measurements to show the streamwise velocity and the

stationary crossflow vortices in the y_s-z_s plane. Therefore, throughout the remainder of this document, (u', v', w') are referred to as disturbances (mostly for transition studies) and (u, v, w) are referred to as fluctuations (mostly for turbulence studies).

2.1.2 Mass Conservation

The mass conservation or continuity equation for an incompressible, three-dimensional flow field in Cartesian coordinates, i.e., in the global coordinate frame, (x, y, z), is given as

$$\frac{\partial \tilde{u}}{\partial x} + \frac{\partial \tilde{v}}{\partial y} + \frac{\partial \tilde{w}}{\partial z} = 0. \tag{2.5}$$

Applying Reynolds decomposition as expressed in equation 2.1 to equation 2.5 then results in the following expression.

$$\frac{\partial \bar{U}}{\partial x} + \frac{\partial u}{\partial x} + \frac{\partial \bar{V}}{\partial y} + \frac{\partial v}{\partial y} + \frac{\partial \bar{W}}{\partial z} + \frac{\partial w}{\partial z} = 0 \tag{2.6}$$

By time averaging equation 2.6, the fluctuating quantities become zero and a mass conservation equation for the mean flow remains.

$$\frac{\partial \bar{U}}{\partial x} + \frac{\partial \bar{V}}{\partial y} + \frac{\partial \bar{W}}{\partial z} = 0 \tag{2.7}$$

Subtracting the mean continuity equation 2.7 from the total continuity equation 2.5 then produces the continuity equation for the fluctuating velocities.

$$\frac{\partial u}{\partial x} + \frac{\partial v}{\partial y} + \frac{\partial w}{\partial z} = 0 \tag{2.8}$$

Using the same procedure, a similar equation may be obtained for the disturbances.

$$\frac{\partial u'}{\partial x} + \frac{\partial v'}{\partial y} + \frac{\partial w'}{\partial z} = 0 \tag{2.9}$$

When multiplied by a fluctuating velocity, say u, equation 2.8 becomes a balance of accelerations of a fluid particle which becomes a useful tool in simplifying the momentum equations.

2.1.3 Momentum Equations

The acceleration of a fluid particle in the swept-wing boundary layer is governed by the three-dimensional Navier-Stokes equations. These momentum equations, expressed for each component of velocity, are given below for an incompressible fluid (ρ = constant) with no body forces. Also, generally speaking, the temperature variations are small and therefore, the viscosity (ν) is considered to be a constant. The $\tilde{u}$-component momentum equation in global coordinates is

$$\frac{\partial \tilde{u}}{\partial t} + \tilde{u}\frac{\partial \tilde{u}}{\partial x} + \tilde{v}\frac{\partial \tilde{u}}{\partial y} + \tilde{w}\frac{\partial \tilde{u}}{\partial z} = -\frac{1}{\rho}\frac{\partial \tilde{p}}{\partial x} + \nu\left(\frac{\partial^2 \tilde{u}}{\partial x^2} + \frac{\partial^2 \tilde{u}}{\partial y^2} + \frac{\partial^2 \tilde{u}}{\partial z^2}\right). \tag{2.10}$$

The $\tilde{v}$-component momentum equation is

$$\frac{\partial \tilde{v}}{\partial t} + \tilde{u}\frac{\partial \tilde{v}}{\partial x} + \tilde{v}\frac{\partial \tilde{v}}{\partial y} + \tilde{w}\frac{\partial \tilde{v}}{\partial z} = -\frac{1}{\rho}\frac{\partial \tilde{p}}{\partial y} + \nu\left(\frac{\partial^2 \tilde{v}}{\partial x^2} + \frac{\partial^2 \tilde{v}}{\partial y^2} + \frac{\partial^2 \tilde{v}}{\partial z^2}\right). \tag{2.11}$$

The $\tilde{w}$-component momentum equation is

$$\frac{\partial \tilde{w}}{\partial t} + \tilde{u}\frac{\partial \tilde{w}}{\partial x} + \tilde{v}\frac{\partial \tilde{w}}{\partial y} + \tilde{w}\frac{\partial \tilde{w}}{\partial z} = -\frac{1}{\rho}\frac{\partial \tilde{p}}{\partial z} + \nu\left(\frac{\partial^2 \tilde{w}}{\partial x^2} + \frac{\partial^2 \tilde{w}}{\partial y^2} + \frac{\partial^2 \tilde{w}}{\partial z^2}\right). \tag{2.12}$$

Since the current investigation is primarily concerned with the fluctuating components of the flow field, Reynolds decomposition is applied to these equations to isolate the fluctuation momentum equations. After this substitution for the total velocities using equation 2.1, the full momentum equations are then time averaged, thus removing the terms dependent on only one fluctuating quantity. These resulting mean-based momentum equations are shown in equations 2.13, 2.14 and 2.15 for the $\overline{U}$, $\overline{V}$ and $\overline{W}$ components respectively.

$$\overline{U}\frac{\partial \overline{U}}{\partial x} + \overline{u\frac{\partial u}{\partial x}} + \overline{V}\frac{\partial \overline{U}}{\partial y} + \overline{v\frac{\partial u}{\partial y}} + \overline{W}\frac{\partial \overline{U}}{\partial z} + \overline{w\frac{\partial u}{\partial z}} = -\frac{1}{\rho}\frac{\partial \overline{P}}{\partial x} + \nu\left(\frac{\partial^2 \overline{U}}{\partial x^2} + \frac{\partial^2 \overline{U}}{\partial y^2} + \frac{\partial^2 \overline{U}}{\partial z^2}\right) \tag{2.13}$$

18

$$\overline{U}\frac{\partial\overline{V}}{\partial x} + \overline{u\frac{\partial v}{\partial x}} + \overline{V}\frac{\partial\overline{V}}{\partial y} + \overline{v\frac{\partial v}{\partial y}} + \overline{W}\frac{\partial\overline{V}}{\partial z} + \overline{w\frac{\partial v}{\partial z}} = -\frac{1}{\rho}\frac{\partial\overline{P}}{\partial y} + \nu\left(\frac{\partial^2\overline{V}}{\partial x^2} + \frac{\partial^2\overline{V}}{\partial y^2} + \frac{\partial^2\overline{V}}{\partial z^2}\right) \quad (2.14)$$

$$\overline{U}\frac{\partial\overline{W}}{\partial x} + \overline{u\frac{\partial w}{\partial x}} + \overline{V}\frac{\partial\overline{W}}{\partial y} + \overline{v\frac{\partial w}{\partial y}} + \overline{W}\frac{\partial\overline{W}}{\partial z} + \overline{w\frac{\partial w}{\partial z}} = -\frac{1}{\rho}\frac{\partial\overline{P}}{\partial z} + \nu\left(\frac{\partial^2\overline{W}}{\partial x^2} + \frac{\partial^2\overline{W}}{\partial y^2} + \frac{\partial^2\overline{W}}{\partial z^2}\right) \quad (2.15)$$

Note that terms containing only one fluctuating expression are lost in the time averaging. However, those terms that are a product of two fluctuating expressions are preserved.

Now by multiplying the continuity equation for the fluctuating quantities (equation 2.8) by u, time averaging the result and adding it into the left side of the $\overline{U}$-component mean momentum equation, we can simplify equation 2.13 by combining terms through the multiplication rule of differentiation demonstrated below.

$$\frac{\partial\overline{uv}}{\partial x} = \overline{u\frac{\partial v}{\partial x}} + \overline{v\frac{\partial u}{\partial x}} \quad (2.16)$$

Doing this for each component (using the appropriate component in the continuity multiplication) results in the following simplified mean momentum equations.

$$\overline{U}\frac{\partial\overline{U}}{\partial x} + \overline{V}\frac{\partial\overline{U}}{\partial y} + \overline{W}\frac{\partial\overline{U}}{\partial z} = -\frac{1}{\rho}\frac{\partial\overline{P}}{\partial x} + \nu\left(\frac{\partial^2\overline{U}}{\partial x^2} + \frac{\partial^2\overline{U}}{\partial y^2} + \frac{\partial^2\overline{U}}{\partial z^2}\right) - \frac{\partial\overline{u^2}}{\partial x} - \frac{\partial\overline{uv}}{\partial y} - \frac{\partial\overline{uw}}{\partial z} \quad (2.17)$$

$$\overline{U}\frac{\partial\overline{V}}{\partial x} + \overline{V}\frac{\partial\overline{V}}{\partial y} + \overline{W}\frac{\partial\overline{V}}{\partial z} = -\frac{1}{\rho}\frac{\partial\overline{P}}{\partial y} + \nu\left(\frac{\partial^2\overline{V}}{\partial x^2} + \frac{\partial^2\overline{V}}{\partial y^2} + \frac{\partial^2\overline{V}}{\partial z^2}\right) - \frac{\partial\overline{uv}}{\partial x} - \frac{\partial\overline{v^2}}{\partial y} - \frac{\partial\overline{vw}}{\partial z} \quad (2.18)$$

$$\overline{U}\frac{\partial\overline{W}}{\partial x} + \overline{V}\frac{\partial\overline{W}}{\partial y} + \overline{W}\frac{\partial\overline{W}}{\partial z} = -\frac{1}{\rho}\frac{\partial\overline{P}}{\partial z} + \nu\left(\frac{\partial^2\overline{W}}{\partial x^2} + \frac{\partial^2\overline{W}}{\partial y^2} + \frac{\partial^2\overline{W}}{\partial z^2}\right) - \frac{\partial\overline{uw}}{\partial x} - \frac{\partial\overline{vw}}{\partial y} - \frac{\partial\overline{w^2}}{\partial z} \quad (2.19)$$

The new terms resulting from the simplification are brought to the right side of each equation because they are considered to be in the form of stresses resulting from fluctuations, referred to as

Reynolds stresses. The cross-correlated velocity terms such as $\partial \overline{uv}/\partial y$ represent time-averaged shearing stresses upon fluid particles and the auto-correlated velocity terms such as $\partial \overline{u^2}/\partial x$ represent time-averaged normal stresses. These Reynolds stresses play an important role predominantly in the turbulent boundary layer. They are generally neglected in the laminar regime, however, since they are relatively small compared to the other terms. This will be discussed in more detail as we derive the fluctuation momentum equations.

So, we may now use these simplified mean momentum equations to derive the fluctuation momentum equations. First, we multiply the fluctuation continuity equation (equation 2.8) by the u velocity component and add the result to the left side of the original momentum equation (equation 2.10) as previously done in deriving the mean momentum equation. Repeat this for each component using the appropriate component in the continuity multiplication and simplify using the rule demonstrated in equation 2.16. The mean momentum equations (equations 2.17, 2.18 and 2.19) are then subtracted from the results. The remaining equations form a system for the fluctuating quantities shown below each of the components.:

$$\frac{\partial u}{\partial t} + u\frac{\partial \overline{U}}{\partial x} + \overline{U}\frac{\partial u}{\partial x} + v\frac{\partial \overline{U}}{\partial y} + \overline{V}\frac{\partial u}{\partial y} + w\frac{\partial \overline{U}}{\partial z} + \overline{W}\frac{\partial u}{\partial z} =$$

$$-\frac{1}{\rho}\frac{\partial p}{\partial x} + \nu\left(\frac{\partial^2 u}{\partial x^2} + \frac{\partial^2 u}{\partial y^2} + \frac{\partial^2 u}{\partial z^2}\right) + \frac{\partial \overline{u^2}}{\partial x} - \frac{\partial u^2}{\partial x} + \frac{\partial \overline{uv}}{\partial y} - \frac{\partial uv}{\partial y} + \frac{\partial \overline{uw}}{\partial z} - \frac{\partial uw}{\partial z} \qquad (2.20)$$

$$\frac{\partial v}{\partial t} + u\frac{\partial \overline{V}}{\partial x} + \overline{U}\frac{\partial v}{\partial x} + v\frac{\partial \overline{V}}{\partial y} + \overline{V}\frac{\partial v}{\partial y} + w\frac{\partial \overline{V}}{\partial z} + \overline{W}\frac{\partial v}{\partial z} =$$

$$-\frac{1}{\rho}\frac{\partial p}{\partial y} + \nu\left(\frac{\partial^2 v}{\partial x^2} + \frac{\partial^2 v}{\partial y^2} + \frac{\partial^2 v}{\partial z^2}\right) + \frac{\partial \overline{uv}}{\partial x} - \frac{\partial uv}{\partial x} + \frac{\partial \overline{v^2}}{\partial y} - \frac{\partial v^2}{\partial y} + \frac{\partial \overline{vw}}{\partial z} - \frac{\partial vw}{\partial z} \qquad (2.21)$$

$$\frac{\partial w}{\partial t} + u\frac{\partial \overline{W}}{\partial x} + \overline{U}\frac{\partial w}{\partial x} + v\frac{\partial \overline{W}}{\partial y} + \overline{V}\frac{\partial w}{\partial y} + w\frac{\partial \overline{W}}{\partial z} + \overline{W}\frac{\partial w}{\partial z} =$$

$$-\frac{1}{\rho}\frac{\partial p}{\partial z} + \nu\left(\frac{\partial^2 w}{\partial x^2} + \frac{\partial^2 w}{\partial y^2} + \frac{\partial^2 w}{\partial z^2}\right) + \frac{\partial \overline{uw}}{\partial x} - \frac{\partial uw}{\partial x} + \frac{\partial \overline{vw}}{\partial y} - \frac{\partial vw}{\partial y} + \frac{\partial \overline{w^2}}{\partial z} - \frac{\partial w^2}{\partial z} \quad . \qquad (2.22)$$

Laminar Regime

Certain assumptions may now be employed to simplify these fluctuation momentum equations for the laminar boundary-layer state. Simplifying the governing equations isolates the driving physics behind a flow field and generally makes it easier to understand certain flow conditions and their effects on the spatio-temporal evolution of the boundary layer. Again, for flow modeling and prediction schemes, certain terms neglected here may prove to be significant for certain cases. However, the scope of this theoretical analysis is to simply visualize the fundamental mechanics of the flow field mathematically. Therefore, the assumptions used in this analysis may not be directly employable in flow modeling, simulations or transition prediction schemes, but it does promote understanding of the important fluid physics. It should also be noted that certain terms are treated as negligible in the laminar regime but may be significant in the turbulent state. Therefore, two sets of equations will be derived, one in the laminar state, the other in fully-developed turbulence. It should also be noted that all of the fluctuating quantities may be substituted with the disturbance quantities, such as the velocities expressed in equation 2.3. The only differences are that all time derivatives become zero, since by definition the disturbances defined in equation 2.3 are dependent on space only.

In this light, we still assume a parallel basic state for the laminar regime where there is generally no significant mean flow in the y direction, implying $\overline{V} \approx 0$. Also, the pressure change in the wall-normal direction within the boundary layer is very small, thus $\partial p / \partial y \approx 0$. It is also generally assumed that products of two fluctuating quantities are significantly smaller than a typical fluctuating quantity in the laminar regime (e.g. $(\partial \overline{u^2} / \partial x) \ll u$) and are therefore neglected. When analyzing or measuring the boundary layer locally as in this investigation, the mean velocities generally do not vary significantly in the plane parallel to the wing surface, i.e., the x-z plane. Therefore, mean velocities differentiated with respect to either the x or z direction are neglected. The resulting equations, after incorporating these assumptions, are presented below for the fluctuating u component in the laminar regime:

$$\frac{\partial u}{\partial t} + \overline{U}\frac{\partial u}{\partial x} + v\frac{\partial \overline{U}}{\partial y} + \overline{W}\frac{\partial u}{\partial z} = -\frac{1}{\rho}\frac{\partial p}{\partial x} + v\left(\frac{\partial^2 u}{\partial x^2} + \frac{\partial^2 u}{\partial y^2} + \frac{\partial^2 u}{\partial z^2}\right) \tag{2.23}$$

21

the fluctuating v component in the laminar regime:

$$\frac{\partial v}{\partial t} + \overline{U}\frac{\partial v}{\partial x} + \overline{W}\frac{\partial v}{\partial z} = \nu\left(\frac{\partial^2 v}{\partial x^2} + \frac{\partial^2 v}{\partial y^2} + \frac{\partial^2 v}{\partial z^2}\right) \tag{2.24}$$

and the fluctuating w component in the laminar regime:

$$\frac{\partial w}{\partial t} + \overline{U}\frac{\partial w}{\partial x} + v\frac{\partial \overline{W}}{\partial y} + \overline{W}\frac{\partial w}{\partial z} = -\frac{1}{\rho}\frac{\partial p}{\partial z} + \nu\left(\frac{\partial^2 w}{\partial x^2} + \frac{\partial^2 w}{\partial y^2} + \frac{\partial^2 w}{\partial z^2}\right). \tag{2.25}$$

For a steady flow or for the stationary disturbance equations, set all time derivatives equal to zero.

These assumptions mathematically reveal the underlying physics of the laminar swept-wing boundary layer which allows observation of certain conditions and their basic effects on stability. The accelerations due to stresses caused by the steady flow, i.e., by frictional forces, and the accelerations due to pressure gradients (if any) are located on the right sides of the equations, whereas the left sides of the equations represent the acceleration of the fluid particles in specific directions and in time. The pressure gradient terms do provide an important mechanism for certain instabilities particular to the current experimental study. The crossflow instability is found to dominate in negative pressure gradients. The streamwise instability tends to dominate in positive pressure gradients. Although this is not the only mechanism which promotes these instabilities, it is significant to note its presence in the simplified equations. This is discussed further with regards to the wing used in the current experiment in section 3.3.1.

Important physics are also revealed upon inspection of the spatial disturbance versions of equations 2.23, 2.24 and 2.25 (obtained by substitution of the fluctuating quantities with the spatial disturbance quantities). For a flow dominated by stationary waves, the time derivatives become zero and the effects of how each disturbance changes in space become very important to the stability of the boundary layer. The chordwise growth of the streamwise velocity disturbance is declared in the $\partial u'/\partial x$ term in equation 2.23. The spanwise distribution of the streamwise velocity also becomes tremendously important in the form of the $\partial u'/\partial z$ term of equation 2.23 which is shown to be directly related to the rollover structure of the stationary vortices in the laminar regime (seen experimentally in section 5.3). Also, the v' and w' disturbances are known to operate on the same streamwise fluid which appears in the x- and z-derivatives of equations 2.24

22

and 2.25. Section 5.3 discusses this mechanism and compares the v' and w' disturbance motion to the measurements of the time-averaged streamwise velocity $\bar{\bar{u}}$. Thus, all of the fundamental physics of the stationary crossflow-dominated swept-wing boundary layer emerge from the simplified disturbance equations.

Turbulent Regime

In a way similar to the laminar analysis, we shall now inspect the turbulent regime of the boundary layer where the fluctuating quantities are important. Here, the Reynolds stresses that result from the product of two fluctuating quantities cannot be readily neglected as in the laminar state. During transition, these additional stresses which are due to strong fluctuations grow and become significant in the turbulent boundary layer. Therefore, keeping all other assumptions of the laminar boundary layer, the fluctuation momentum equations for the turbulent boundary layer are, for the u component:

$$\frac{\partial u}{\partial t} + \overline{U}\frac{\partial u}{\partial x} + v\frac{\partial \overline{U}}{\partial y} + \overline{W}\frac{\partial u}{\partial z} =$$

$$-\frac{1}{\rho}\frac{\partial p}{\partial x} + v\left(\frac{\partial^2 u}{\partial x^2} + \frac{\partial^2 u}{\partial y^2} + \frac{\partial^2 u}{\partial z^2}\right) + \frac{\partial \overline{u^2}}{\partial x} - \frac{\partial u^2}{\partial x} + \frac{\partial \overline{uv}}{\partial y} - \frac{\partial uv}{\partial y} + \frac{\partial \overline{uw}}{\partial z} - \frac{\partial uw}{\partial z} \quad (2.26)$$

for the v component:

$$\frac{\partial v}{\partial t} + \overline{U}\frac{\partial v}{\partial x} + \overline{W}\frac{\partial v}{\partial z} =$$

$$v\left(\frac{\partial^2 v}{\partial x^2} + \frac{\partial^2 v}{\partial y^2} + \frac{\partial^2 v}{\partial z^2}\right) + \frac{\partial \overline{uv}}{\partial x} - \frac{\partial uv}{\partial x} + \frac{\partial \overline{v^2}}{\partial y} - \frac{\partial v^2}{\partial y} + \frac{\partial \overline{vw}}{\partial z} - \frac{\partial vw}{\partial z} \quad (2.27)$$

and for the w component:

$$\frac{\partial w}{\partial t} + \overline{U}\frac{\partial w}{\partial x} + v\frac{\partial \overline{W}}{\partial y} + \overline{W}\frac{\partial w}{\partial z} =$$

$$-\frac{1}{\rho}\frac{\partial p}{\partial z} + v\left(\frac{\partial^2 w}{\partial x^2} + \frac{\partial^2 w}{\partial y^2} + \frac{\partial^2 w}{\partial z^2}\right) + \frac{\partial \overline{uw}}{\partial x} - \frac{\partial uw}{\partial x} + \frac{\partial \overline{vw}}{\partial y} - \frac{\partial vw}{\partial y} + \frac{\partial \overline{w^2}}{\partial z} - \frac{\partial w^2}{\partial z} . \quad (2.28)$$

Again, for steady flow, set all time derivatives equal to zero. There are no "disturbances" typical of the laminar boundary layer in the turbulent regimes. Disturbances are considered those quantities that lead to an instability and cause transition through their growth. Since we are aft of the transition front, those quantities and their equations no longer apply.

2.1.4 Boundary Conditions

It is also important to consider boundary conditions for any analysis, particularly if models, flow predictions or simulations are to be made. The boundary conditions for this swept-wing experiment are presented here only for completeness and for inspection of the equation limits. They are the following:

$$y = 0 \ : \ \bar{u} = \bar{v} = \bar{w} = 0$$

$$y = \infty \ : \ \bar{u} = U_\infty \ ; \ \bar{v} = 0 \ ; \ \bar{w} = W_\infty \tag{2.29}$$

where U_∞ and W_∞ are the freestream velocities in the X and Z directions, respectively. It should also be noted that, for general purposes, the boundary-layer equations and appropriate assumptions of the previous sections are only valid within the range of x from 0 at the leading edge to approximately $c\cos\Lambda$ at the trailing edge (neglecting surface curvature), where c is the chord length and Λ is the wing sweep angle. Outside of this range, the boundary layer does not exist and other freestream or wake equations prevail. The limits of z are not important for this investigation, since the wing is assumed to have infinite span. Section 3.3.2 explains how this condition is approximated experimentally.

2.1.5 Surface Shear-Stress Equations

In two-dimensional boundary layers, there generally exists only one component of surface shear stress. However, in three-dimensional boundary layers, particularly in a laminar crossflow-dominated swept-wing boundary layer, there exists two significant components of surface shear stress. These exist in the x-z plane at $y = 0$ and are calculated from the slope of the u and w velocity profiles. In the global coordinate system explained in section 1.2.2, the two components of fluctu-

ating surface shear stress in the laminar regime are given by:

$$\tau_x = \mu\left(\frac{\partial u}{\partial y}\right)\Bigg|_{y=0} \tag{2.30}$$

and

$$\tau_z = \mu\left(\frac{\partial w}{\partial y}\right)\Bigg|_{y=0}. \tag{2.31}$$

Again, spatial disturbance equations may be obtained through the appropriate substitution for the laminar regime. Only equation 2.30 applies in two-dimensional flows which are used in chapter 4 to calibrate surface shear-stress sensors in a two-dimensional flat-plate boundary layer where the slope of the velocity profile is calculated from internal velocity measurements.

An important principle exists when considering shearing stresses in the turbulent boundary layer. A particle of fluid is exposed to Reynolds shear stresses as a result of the turbulent fluctuations. This refers to the cross-correlated terms such as $\partial uv/\partial y$ as discussed in section 2.1.3. These stresses create an additional term when computing shear stresses in the flow above the surface. Therefore, when analyzing shear stresses in the turbulent regime, one would suspect the contribution of these Reynolds shearing stresses upon fluid particles to be significant directly at the surface. However, this additional shear in fact does not create another term in the calculation of shear at the surface. This is primarily due to the no-slip condition which states that there are no turbulent fluctuations, i.e., no velocity at all, at the surface even in a turbulent boundary layer. The additional Reynolds stresses manifest themselves at the surface by altering the actual velocity profile thus effecting the $\partial u/\partial y$ and $\partial w/\partial y$ terms in equations 2.30 and 2.31, respectively. The profile of the turbulent boundary layer is more accelerated than that of the laminar boundary layer which in turn creates a stronger gradient in the y direction.

2.1.6 Equation Summary

Included below are two tables summarizing the equations derived in this section. Table 2.1 summarizes the general equations valid in every regime. Table 2.2 summarizes which equations are valid in laminar or turbulent swept-wing boundary layers. Disturbance equations are just substi-

tuted versions of the fluctuating equations (e.g., u is replaced by u' and time derivatives are 0) but are only valid in the laminar regime.

Table 2.1: General governing equations for total, mean and fluctuating velocities.

Equation	total	mean	fluctuating
continuity	2.5	2.7	2.8
u-momentum	2.10	2.17	2.20
v-momentum	2.11	2.18	2.21
w-momentum	2.12	2.19	2.22

Table 2.2: Fluctuation equations for laminar and turbulent regimes.

Equations	laminar	turbulent
u-momentum	2.23	2.26
v-momentum	2.24	2.27
w-momentum	2.25	2.28
x-surface shear stress	2.30	2.30
z-surface shear stress	2.31	2.31

2.2 Rotating Disk Flow

Due to the complexity of the swept-wing boundary layer, it is often helpful to look at simpler flow geometries which exhibit similar flow properties. Flow near a rotating disk, also a three-dimensional boundary layer, exhibits similar instability mechanisms to that of the crossflow-dominated swept-wing boundary layer. Refer to von Kármán (1946), Gregory et al. (1955) and Brown (1959) for reviews of early analytical and experimental work on rotating-disk flows. The distinct advantage to looking at this simpler flow is that the laminar rotating-disk flow is an exact solution to the

Navier-Stokes equations. This promotes a fundamental understanding of the crossflow instability and therefore, provides further insight to the crossflow-dominated swept-wing boundary layer.

The following text provides a brief discussion on the governing equations and the physics of the rotating-disk flow field. By so doing, one can create analogies to the more complex swept-wing flow and develop a conceptual understanding of the crossflow instability. Solutions to the rotating-disk flow may be obtained and used to infer flow behavior in the swept-wing boundary layer. For instance, if a particular term or terms in the governing equations of the rotating-disk flow exhibit strong growth, one can perhaps expect analogous terms in the swept-wing equations to perform similarly. It is for this reason that the governing equations are presented below. Although no numerical solutions are computed here, comparisons of the analytical equations are made to demonstrate the similarities.

2.2.1 Physical Description

The rotating-disk flow is best described in cylindrical coordinates where r is the radial direction, θ is the circumferential direction and z is the axial direction. The corresponding total velocity components in those directions are u, v and w, respectively and p is the pressure.

The flow, illustrated in figure 2.1, is produced by a flat disk which rotates about an axis perpendicular to its plane (the z axis in figure 2.1) with a uniform angular velocity, ω, in a fluid otherwise at rest. The layer of fluid near the disk surface is carried by the disk itself through frictional forces and is thrown outwards due to centrifugal forces inherent in the rotating motion. This fluid motion draws particles toward the disk axially which, in turn, are carried by the disk and ejected centrifugally as well, thus producing a fully three-dimensional flow.

2.2.2 Governing Equations

The governing equations are derived here for an infinite rotating plane in a laminar state, but may easily be extended to include a finite-radius disk by letting r range from 0 at the center of the disk to R at the edge of the disk on the condition that edge effects are neglected. Given the notation in the cylindrical coordinate system, the continuity equation for this flow may be expressed as

$$\frac{\partial u}{\partial r} + \frac{u}{r} + \frac{1}{r}\frac{\partial v}{\partial \theta} + \frac{\partial w}{\partial z} = 0 \qquad (2.32)$$

27
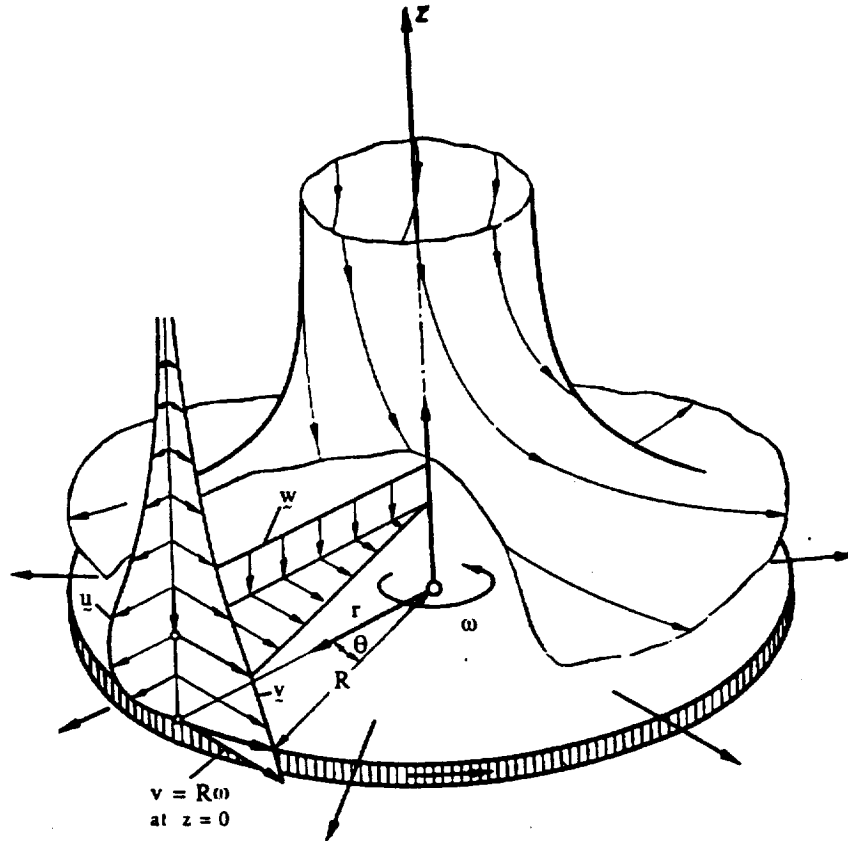
Figure 2.1: Flow in the neighborhood of a rotating disk.
Figure adapted from Schlichting (1987).

which may be simplified, using rotational symmetries, to

$$\frac{\partial u}{\partial r} + \frac{u}{r} + \frac{\partial w}{\partial z} = 0 \ . \tag{2.33}$$

Likewise, the three momentum equations, i.e., the Navier-Stokes equations, in cylindrical coordinates are expressed as follows for the u component:

$$\frac{\partial u}{\partial t} + u\frac{\partial u}{\partial r} + \frac{v}{r}\frac{\partial u}{\partial \theta} - \frac{v^2}{r} + w\frac{\partial u}{\partial z} = -\frac{1}{\rho}\frac{\partial p}{\partial r} + \nu\left(\frac{\partial^2 u}{\partial r^2} + \frac{1}{r}\frac{\partial u}{\partial r} - \frac{u}{r^2} + \frac{1}{r^2}\frac{\partial^2 u}{\partial \theta^2} - \frac{2}{r^2}\frac{\partial v}{\partial \theta} + \frac{\partial^2 u}{\partial z^2}\right) \tag{2.34}$$

for the v component:

$$\frac{\partial v}{\partial t} + u\frac{\partial v}{\partial r} + \frac{v}{r}\frac{\partial v}{\partial \theta} + \frac{uv}{r} + w\frac{\partial v}{\partial z} = -\frac{1}{\rho r}\frac{\partial p}{\partial \theta} + \nu\left(\frac{\partial^2 v}{\partial r^2} + \frac{1}{r}\frac{\partial v}{\partial r} - \frac{v}{r^2} + \frac{1}{r^2}\frac{\partial^2 v}{\partial \theta^2} - \frac{2}{r^2}\frac{\partial u}{\partial \theta} + \frac{\partial^2 v}{\partial z^2}\right) \quad (2.35)$$

and for the w component:

$$\frac{\partial w}{\partial t} + u\frac{\partial w}{\partial r} + \frac{v}{r}\frac{\partial w}{\partial \theta} + w\frac{\partial w}{\partial z} = -\frac{1}{\rho}\frac{\partial p}{\partial z} + \nu\left(\frac{\partial^2 w}{\partial r^2} + \frac{1}{r}\frac{\partial w}{\partial r} - \frac{1}{r^2} + \frac{1}{r^2}\frac{\partial^2 w}{\partial \theta^2} + \frac{\partial^2 w}{\partial z^2}\right) . \quad (2.36)$$

Using the rotational symmetries of the steady rotating-disk flow, these equations may be simplified, as expressed below.

$$u\frac{\partial u}{\partial r} - \frac{v^2}{r} + w\frac{\partial u}{\partial z} = -\frac{1}{\rho}\frac{\partial p}{\partial r} + \nu\left(\frac{\partial^2 u}{\partial r^2} + \frac{\partial}{\partial r}\left(\frac{u}{r}\right) + \frac{\partial^2 u}{\partial z^2}\right) \quad (2.37)$$

$$u\frac{\partial v}{\partial r} + \frac{uv}{r} + w\frac{\partial v}{\partial z} = \nu\left(\frac{\partial^2 v}{\partial r^2} + \frac{\partial}{\partial r}\left(\frac{v}{r}\right) + \frac{\partial^2 v}{\partial z^2}\right) \quad (2.38)$$

$$u\frac{\partial w}{\partial r} + w\frac{\partial w}{\partial z} = -\frac{1}{\rho}\frac{\partial p}{\partial z} + \nu\left(\frac{\partial^2 w}{\partial r^2} + \frac{1}{r}\frac{\partial w}{\partial r} + \frac{\partial^2 w}{\partial z^2}\right) \quad (2.39)$$

The appropriate boundary conditions for the rotating-disk flow is governed by the no-slip condition and are as follows.

$$z = 0 \;\; : \;\; u = w = 0 \;\; ; \;\; v = r\omega$$
$$z = \infty \;\; : \;\; u = v = 0 \quad\quad (2.40)$$

Also, if a finite-radius disk is to be analyzed, r will range from 0 to the disk radius, R.

The surface shear stress may be approximated using an estimate of the boundary layer thickness, δ, for the rotating-disk flow. An approximation of the laminar boundary-layer thickness,

$$\delta \sim \sqrt{\frac{\nu}{\omega}} , \quad\quad (2.41)$$

to estimate the total shear stress at the wall as

$$\tau_w \sim \frac{\rho v^2 \delta}{r} \sim \rho r \omega^2 \delta \sim \rho r \omega \sqrt{v \omega} \tag{2.42}$$

is generally used. For a turbulent rotating-disk flow, the boundary-layer thickness is usually approximated by

$$\delta \sim r^{3/5} \left(\frac{v}{\omega}\right)^{1/5} \tag{2.43}$$

as reported by Schlichting (1987).

2.2.3 Solution Methods

The system of laminar equations given in equations 2.33, 2.37, 2.38 and 2.39 may be solved through integration methods. It is convenient to introduce a dimensionless distance from the wall, $\zeta \sim z/\delta$, thus allowing $\zeta = z\sqrt{\omega/v}$. By defining functions of ζ for each unknown in the system of equations, i.e., for u, v, w and p, as F, G, H and P, respectively, we can then employ the following assumptions.

$$u = r\omega F(\zeta)$$

$$v = r\omega G(\zeta)$$

$$w = \sqrt{v\omega} H(\zeta) \tag{2.42}$$

$$p = p(z) = \rho v \omega P(\zeta) = \mu \omega P(\zeta)$$

These equations are then inserted into the system of equations governing the rotating-disk flow resulting in a system of four simultaneous ordinary differential equations based on the functions F, G, H and P. The velocity field is first evaluated from the equation of continuity and the momentum equations for the plane of motion parallel to the disk plane. The pressure distribution

is then found subsequently from the momentum equation perpendicular to the disk. These equations are:

$$2F + H' = 0$$

$$F^2 + F'H - G^2 - F'' = 0$$

$$2FG + HG' - G'' = 0 \qquad (2.45)$$

$$P' + HH' - H'' = 0$$

with the following boundary conditions calculated from equation 2.40:

$$\zeta = 0 \ : \ F = H = P = 0 \ ; \ G = 1$$

$$\zeta = \infty \ : \ F = G = 0 \ . \qquad (2.46)$$

These equations were solved using an approximate method of numerical integration by Sparrow and Gregg (1960) for the laminar regime. The theoretical equations agree quite well with experiments for Reynolds numbers up to about 3×10^5 (Schlichting 1987). At higher Reynolds numbers, the flow transitions to a turbulent boundary layer where different approximation methods prevail.

2.2.4 Flow Comparisons

The swept-wing equations demonstrated the importance of the spatial disturbances in the stability of the boundary layer. Likewise, in the rotating-disk flow, that spatial dependence arises in the spatial derivatives. The rotating-disk equations provide an advantage of solution in placing that spatial dependence all on one variable ζ. Therefore, by understanding the spatial evolution of the disturbances in the rotating-disk boundary layer, one can infer general behavior within the swept-wing boundary layer, particularly to the growth of the crossflow instability.

The physical similarities between the rotating-disk flow field and the crossflow-dominated swept-wing boundary layer revolve around the fact that they both contain an inflected velocity profile. The crossflow instability arises in the momentum equations because of this inflected velocity profile. The rotating-disk's inflected profile, the u component illustrated in figure 2.1, is

31

similar to the inflected w_t-component profile in the swept-wing boundary layer shown in figure 1.2. By analyzing the growth of these profiles either numerically or experimentally, one can infer analogous flow behaviors. Thus, solutions for F in equation 2.45 may physically represent the evolutionary development of the crossflow profile in the swept-wing boundary layer.

Performing stability analyses by numerically introducing disturbances to the rotating-disk basic-state equations may in turn reveal similar behavior to the receptivity mechanisms in the swept-wing boundary layer. Given the recent work of Haynes (1996), where the crossflow-dominated swept-wing boundary layer was studied by numerically perturbing a system of nonlinear parabolized stability equations, this numerical comparison may now actually be performed. Haynes and Reed (1996) have shown strong numerical agreement with the swept-wing experiments of Reibert (1996a). Thus, if any similarities arise from the comparisons between a numerical stability analysis of the rotating-disk and the swept-wing flows, they can then be related to both rotating-disk and swept-wing experiments.

Experimental Facility

3.1 Wind Tunnel

The data used in this investigation was acquired experimentally in the Unsteady Wind Tunnel at Arizona State University (ASU) while the author was in residence there. The closed-loop, low-speed wind tunnel was originally built in 1970 by Dr. Philip Klebanoff and calibrated by Dr. James McMichael for the National Bureau of Standards in Gaithersburg, Maryland. The tunnel was relocated in 1984 to ASU under the direction of Dr. William Saric. It was then modified to create a low-turbulence flow environment and became fully operational in 1987, ready for studies in the stability and transition of laminar boundary layers. Figure 3.1 shows a schematic of the wind-tunnel's current configuration which is described in greater detail in Saric (1992a) and Reibert (1996a).

Figure 3.1: Plan view of the ASU Unsteady Wind Tunnel. All dimensions in meters. Figure courtesy of Reibert (1996a).

The flow is produced by a 1.83 m diameter, axial fan which consists of nine adjustable-pitch blades and eleven stators. The single-stage fan, capable of a maximum 1350 rpm, is powered by a 150 hp, variable-speed DC motor. This results in a maximum speed of 35 m/s in the test section with the swept-wing model configuration of the present experiment. The speed of the fan is digitally controlled with a resolution of 0.02 rpm by the control-room computers and maintained to within 0.01% of the set point through a motor feedback system.

The low-turbulence environment is a result of carefully designed features. Wake turbulence from the motor assembly is decreased by a nacelle fitted over the end of the motor. Splitter plates are located just downstream of the motor nacelle to reduce the large vortices created by the fan. A sound-insulated wall running the length of the building separates the test section from the motor housing to reduce acoustic noise. The entire motor section and test section, each sitting on a concrete pad, are individually isolated from the rest of the facility foundation to reduce vibrations. Mechanical vibrations are also damped by the use of flexible couplings connecting the motor housing and the test section to the wind tunnel. Airfoil turning vanes (item 'a' in figure 3.1) are in each of the four corners of the closed loop to direct the flow. A honeycomb sheet (item 'b' in figure 3.1) and a series of screens (item 'c' in figure 3.1) are used to break up any large scale structures in the flow. These and other features described by Reibert (1996a) reduce the freestream turbulence levels in the test section to less than 0.02% at a freestream velocity of 20 m/s. Saric et al. (1988) and Mousseux (1988) provide more information on the calibration of the ASU Unsteady Wind Tunnel.

The facility is equipped with two interchangeable test sections, each with dimensions 1.4 m × 1.4 m × 4.9 m. One test section may be used in an experiment while the other is being prepared for a future experiment. A traverse system (see section 3.2.2) is mounted on the external window side of the test section in use and must be removed when test sections are changed. As mentioned above, the test section in use is isolated from vibrations by only a flexible coupling attachment and by being on its own concrete pad. By simply removing the couplings, the test section currently in use can easily be replaced by the other containing the next experiment, thus minimizing tunnel operations down time. Other test section features include an interchangeable window system. Either a flow-visualization window or a measurement-entry window may be placed on the control-room side of the test section (the bottom of figure 3.1). In order to take advantage of this configuration, the models are mounted vertically in the test section. One can then photograph the

model when using the flow-visualization window or take measurements within the test section by using the measurement-entry window and the traversing mechanism.

The ASU tunnel is also capable of generating unsteady flows in the test section. The unsteady configuration directs some of the flow through a secondary duct above the test section which has a rotating shutter system 90° out of phase with a shutter system in the primary duct. Velocity fluctuations up to 100% are possible at 25 Hz with still near-steady loading on the fan. Amplitude of the fluctuations is controlled by the number of engaged shutters. The present experiment is performed in the steady flow configuration; all shutters disengaged, the secondary duct closed and the shutters in the primary duct fixed open.

3.2 Data Acquisition

The ASU Unsteady Wind Tunnel facility is well equipped with several computer and automation systems to make the tasks easier for the experimentalist. With appropriate preparation, one can improve the reliability, consistency and efficiency of experiments with automation. The ASU Unsteady Wind Tunnel is constantly upgrading equipment and computer systems as needed. Therefore, the following account will not be the true current state of the ASU facility. Reibert (1996a) gives the most recent description of all upgrades and additions to the facility at the time of this writing. Below is a brief summary of the features of the ASU facility used at the time of the experiment presented here.

3.2.1 Computer Systems

The present experiment is automated by a primary computer system, an ACT486 PC running the Santa Cruz Operation's Open Desktop Server System version 2.0, a UNIX-based operating system (recently upgraded to a dual-processor Sun SPARC 20 612MP Workstation running the Solaris 2.4 UNIX-based operating system). The primary computer system is equipped with a National Instruments GPIB interface board which allows all instrumentation to be external to the computer system. Thus, all data acquisition equipment may be placed in close proximity to the actual experiment, minimizing signal noise inherent in the use of long cables. This also creates a

sense of modularity allowing for easy, independent equipment upgrades.

Also available at the ASU Unsteady Wind Tunnel are a DECstation 5000 running Ultrix version 4.41, another UNIX-based operating system, and a Macintosh Quadra 650 running the Macintosh OS version 7.5.3. These systems are available for general computing.

All automated control and data-acquisition programs are written internally at the ASU facility in the C language (C++ and LabVIEW languages are now also used). A standardized interface to all data acquisition and control instruments is maintained through the use of custom object-code libraries (Reibert 1996b), some based on the routines found in Press et al. (1992).

All programs for the multi-point correlation analysis of the present experimental data are written in the C language at Clarkson University on a Power Macintosh 6100/60AV. An Iomega Bernoulli 90 Mb removable hard drive system is used for data storage.

3.2.2 Traverse System

A three-dimensional instrument traverse, described in detail by Radeztsky (1994), is mounted outside of the window side of the test section and is controlled by the primary computer system to allow for accurate positioning of probes within the test section. The traverse mechanism is designed to allow only the instrument sting (probe holder) to enter the test section through a self-seaming gap in the plexiglass measurement-entry window. This and the design of the instrument sting minimizes flow disturbance, crucial for stability measurements.

The traverse carriage moves in the streamwise X direction on two stainless steel Thompson rails. A zipper attached to either side of the sting mount on the traverse assembly automatically slides as the traverse slides, thus keeping the flow leakage from the test section to a minimum. The wall-normal Y motion is obtained by two parallel, high-resolution lead screws mounted on the sting mount. This allows very fine steps normal to the test-section wall and is primarily used to finely progress through the boundary layer of a test model. The vertical Z motion is managed by to twin lead screws and rails which moves the sting mount up or down. Another set of twin lead screws and rails moves the plexiglass window in conjunction with the vertical motion of the sting mount.

The complete system is computer controlled via GPIB communications. All lead screws are driven by high-resolution microstepping motors and are monitored by optical encoders in a

Table 3.1: Traverse system capabilities.

Direction	X	Y	Z
Total Travel	1250 mm	100 mm	175 mm
Minimum Step	12 μm	0.7 μm	1.3 μm

motion feedback system. As a result, the traverse is capable of high resolution steps in any direction. The range and resolutions are listed in table 3.1.

3.2.3 Instrumentation Sting

The instrumentation sting used to place probes within the test section is shown in figure 3.2 and is described in detail by Radeztsky (1994). This is the same sting used in previous swept-wing experiments at the ASU Unsteady Wind Tunnel including Saric et al. (1990a), Kohama et al. (1991), Dagenhart (1992), Radeztsky (1994) and Reibert (1996a). The sting body is made of a carbon-composite material that is supported by an aluminum base plate machined for easy mounting to the traverse's sting platform. The sting's cantilever design is the result of a compromise between minimizing flow disturbance near the measurement site and minimizing vibrations. The sting had to be as non-intrusive as possible, yet strong enough to damp out significant oscillations
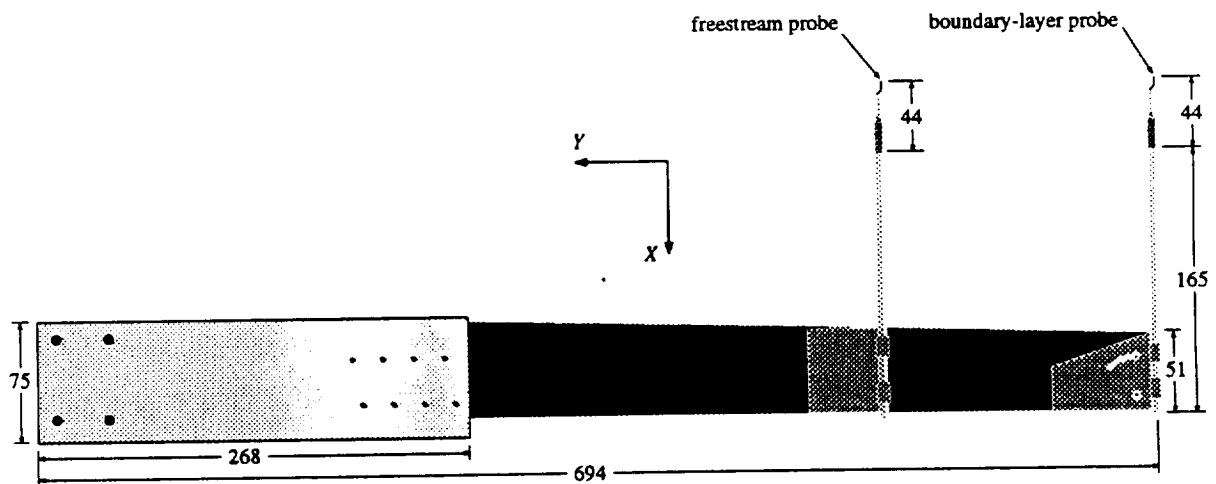
Figure 3.2: Plan view of instrumentation sting with single hot-wire probes. All dimensions in millimeters. Figure courtesy of Reibert (1996a).

due to fluid passing over the sting body.

In standard operations, two Dantec probe tubes are mounted to the composite body of the sting. The probe tubes house one single hot-wire probe each which are generally used to measure velocities in the freestream and in the boundary layer close to the model surface (see section 3.1.1). The freestream hot-wire probe is fixed within the tube mounted on the main body of the sting. The boundary-layer probe is placed in the tube mounted at the sting tip on a lockable swivel plate which allows rotation in the Z plane and about the probe body. This freedom of motion is necessary to appropriately align the probe to three-dimensional surfaces of models, such as that on the swept-wing.

3.2.4 Data Acquisition Instrumentation

The Unsteady Wind Tunnel is equipped with many instruments needed to determine flow conditions in the test section. Freestream temperature is measured at the furthest upstream plane of the test section with a thin-film resistance temperature detector (RTD). Static and dynamic pressure measurements are also taken in the freestream at this location by a Pitot-static tube. The dynamic pressure is measured by a MKS 398HD, 10 torr differential pressure transducer and the static pressure is measured by a MKS 390HA, 1000 torr absolute pressure transducer. Both pressure transducers are temperature compensated and are fed through 14-bit MKS 270B signal conditioners. The analog signals from both pressure transducers and from the thin-film RTD are then passed directly to the data-acquisition system.

Several forms of anemometry are used in this experiment to determine the state of the swept-wing boundary layer. They include single hot-wire, two-component cross-wire and multi-element hot-film sheet anemometry techniques. The specifications, designs and calibrations of each specific sensor type are discussed in detail in chapter 4. However, the actual anemometers that drive these sensors are discussed here.

The primary anemometer system at the ASU Unsteady Wind Tunnel is based on two Dantec 55M01 constant-temperature anemometers (CTAs), used predominantly for the single hot-wire sensors. These anemometers are equipped with Dantec 55M10 CTA standard bridges. A Stewart VBF44 filter/amplifier provides two channels of analog signal conditioning for AC measurements. The filter has two high-pass and two low-pass filter responses with cut-off frequencies ranging from 1 Hz to 255 kHz. The amplifier portion provides a maximum gain of 70 dB. All of these fea-

tures are programmable through a RS/232 serial interface. The amplified and filtered single hot-wire signals are then passed to the data-acquisition system.

The primary anemometer system generally used at Clarkson University was temporarily relocated to the ASU facility for this experiment. That system consists of 16 modular CTAs from A. A. Labs, model AN-1003, which are equipped with anti-aliasing low-pass filters capable of various cut-off frequencies ranging from 380 Hz to 14 kHz. These anemometers were used to drive the cross-wire and hot-film sensors. Their filtered signals are passed directly to the data-acquisition system.

All of these transducer and sensor signals, analog in nature, are digitized by three IOtech ADC488/8SA analog-to-digital (A/D) converters (two supplied by ASU, one supplied by Clarkson University). Each A/D converter is capable of simultaneous sample and hold on 8 channels at 16-bit resolution. When connected in a master/slave configuration, the A/D system can provide 24 channels of simultaneous conversion. Each channel is independently set to an appropriate input voltage range between ±1 and ±10 volts. The conglomerate sampling rate varies discretely from 0.02 Hz to 100 kHz. All communications from the primary computer system to the A/D converters are through a GPIB interface.

All of this instrumentation and hardware allows simultaneous sampling of a total of 18 channels of anemometry, 2 channels of freestream pressure measurements, and 1 channel of freestream temperature measurements. This still leaves 3 remaining channels for other possibilities.

3.3 Model Configuration

3.3.1 Swept-Wing Model

The model used in the current experiment is the same wing used in all previous three-dimensional boundary-layer experiments at the ASU Unsteady Wind Tunnel (Saric et al. 1990a, Kohama et al. 1991, Dagenhart 1992, Radeztsky 1994 and Reibert 1996a). It is a 45° swept wing with a constant-chord length of 1.83 m and a span of 1.97 m. The chord length allows for significant boundary-layer growth ($\delta \approx 4$ mm in the mid-chord region for moderate chord-based Reynolds
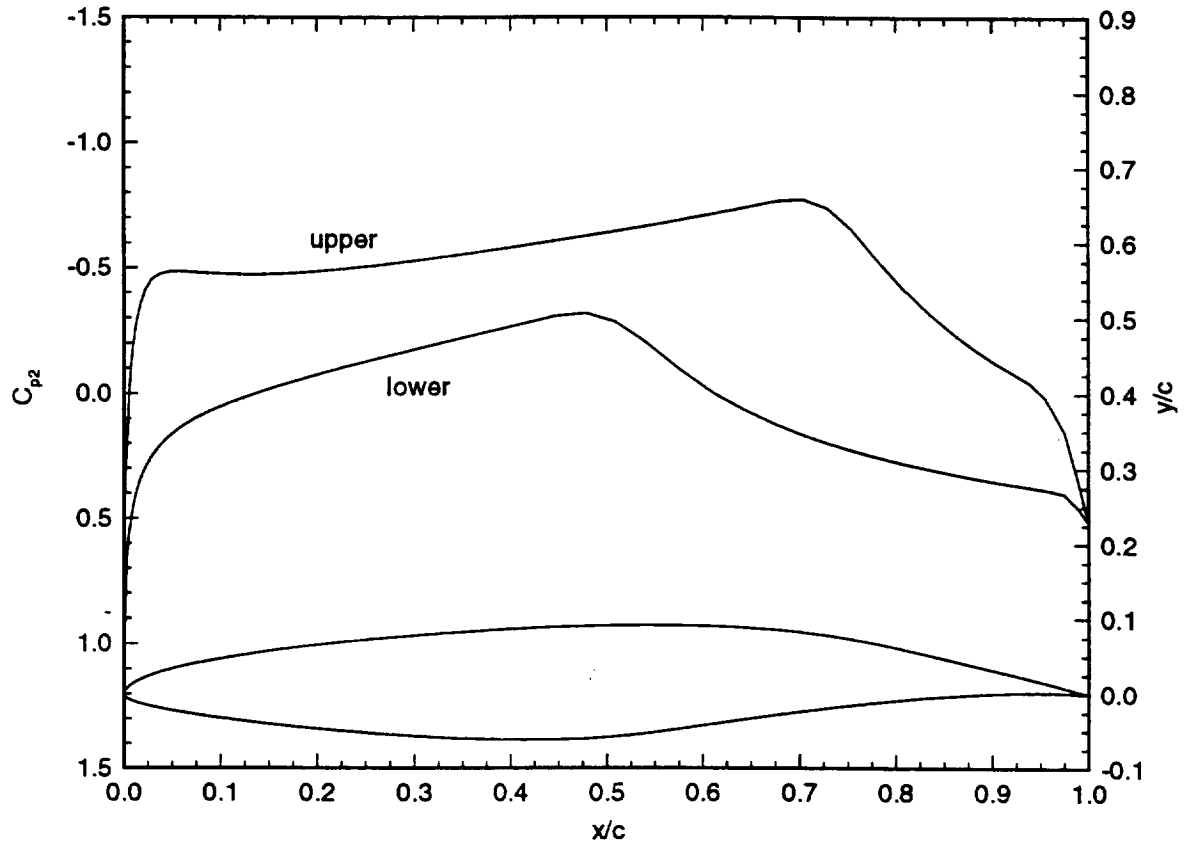
Figure 3.3: Unswept NLF(2)-0415 airfoil with free-air C_p for $\alpha = 0°$ and $\delta_F = 0°$.
Figure courtesy of Reibert (1996a).

numbers). The wing is constructed from the NLF(2)-0415 airfoil, shown in figure 3.3. It was originally designed by Somers and Horstmann (1985) as an unswept natural-laminar-flow airfoil for commuter aircraft.

Certain features of the airfoil design prevent specific instabilities from occurring. The leading-edge radius of the airfoil is small enough to eliminate any attachment-line instabilities at the range of chord-based Reynolds numbers used in the ASU experiments. Görtler instabilities are avoided by the lack of concave regions on the upper surface of the wing. The wing is also equipped with a 20% chord, trailing-edge flap capable of a maximum deflection angle (δ_F) of ±20°. Changing the flap's deflection angle allows additional contouring of the existing pressure distribution.

The airfoil is designed to maintain laminar flow on the upper surface by minimizing the
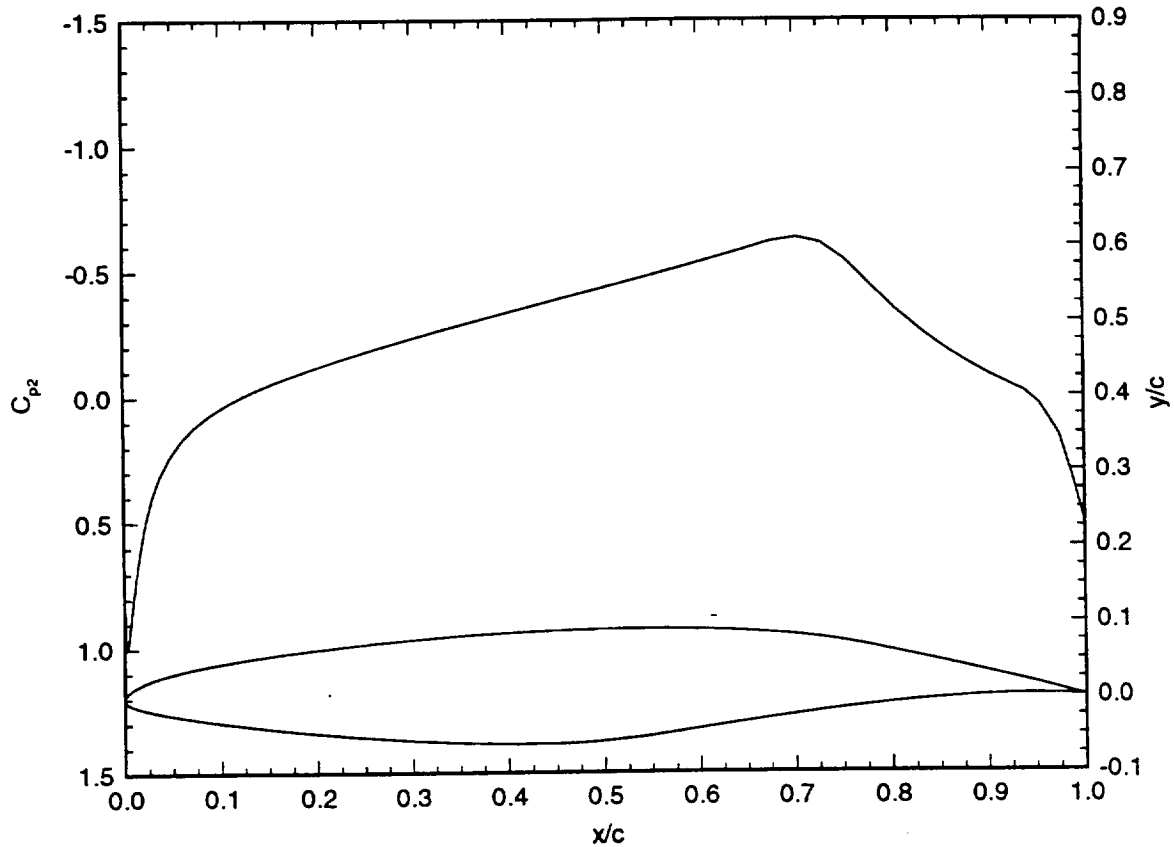
Figure 3.4: Unswept NLF(2)-0415 airfoil with upper-surface free-air C_p for $\alpha = -4°$ and $\delta_F = 0°$. Figure courtesy of Reibert (1996a).

Tollmein-Schlichting (T-S) instability. This is due to the favorable pressure gradient range (shown in figure 3.3) extending to the pressure minimum at $x/c = 0.71$. The crossflow and T-S instabilities remain weakly amplified at the design angle of attack (α) of $0°$. The favorable pressure gradient range for small negative angles of attack remains extended to $x/c = 0.71$ from the attachment line and strengthens the crossflow modes while stabilizing the T-S modes, thus isolating the crossflow instability. Dagenhart (1992) discovered that the crossflow modes were strongest at an angle of attack of $-4°$ with no flap deflection. Thus, the wing is a near perfect crossflow generator at these conditions. For these reasons, the current experiment is performed on the swept-wing in this configuration. Figure 3.4 shows the pressure distribution for the NLF(2)-0415 airfoil at these conditions.

At small positive angles of attack, the pressure minimum relocates to $x/c = 0.02$ giving

significant rise to the T-S modes. The crossflow modes remain but are significantly weaker than those produced at small negative angles of attack. Refer to Dagenhart (1992) for a detailed review of the predicted and actual operating ranges for the NLF(2)-0415 airfoil and the presence of instabilities for various conditions.

3.3.2 Test-Section Configuration

The swept-wing model is mounted vertically in one of the test sections such that the upper surface faces the front wall of the test section. This greatly simplifies instrumentation access through the measurement-entry window. The model attaches to the test section via a shaft and thrust bearing. The shaft is parallel to the leading edge of the wing and is located at $x/c = 0.25$ allowing for model rotation about the quarter-chord line within an angle-of-attack range of $\pm 4°$ in $1°$ increments.

One of the major concerns in wind-tunnel research is the effect of the tunnel walls on the flow under investigation. This is especially important with such a large model relative to the size of the test section (a wing of $c = 1.83$ m with a maximum thickness approximately 0.3 m, spanning from floor to ceiling in a test section 1.4 m × 1.4 m × 4.9 m). Aside from flow disturbance issues is also the prediction and proper modeling of the flow field through computer simulation. It is very difficult to model the flow over a swept wing that has wall effects. It is fairly straightforward to include the test-section side-wall effects (those opposite of the upper and lower surfaces), but very complicated to include the ceiling and floor effects. Essentially, the computational model would have to be a fully three-dimensional code to compute the basic state and stability of the boundary layer for a finite-span wing with end-wall effects. To account for both of these issues, the ASU Unsteady Wind Tunnel is equipped with contoured end liners on the floor and ceiling. These end liners, shown in figure 3.5 with the wing, are shaped to the inviscid streamlines of the wing, thus creating a simulated infinite-span swept-wing flow. This spanwise invariant flow is much easier to model computationally. It requires a two-dimensional code with periodic treatment of the spanwise velocity. The reader is referred to Haynes (1996) and Haynes and Reed (1996) for the computational efforts regarding these issues. Refer to Dagenhart (1992) for a discussion on the end-liner design procedure and to Radeztsky (1994) for a detailed explanation of the construction technique of the end liners.
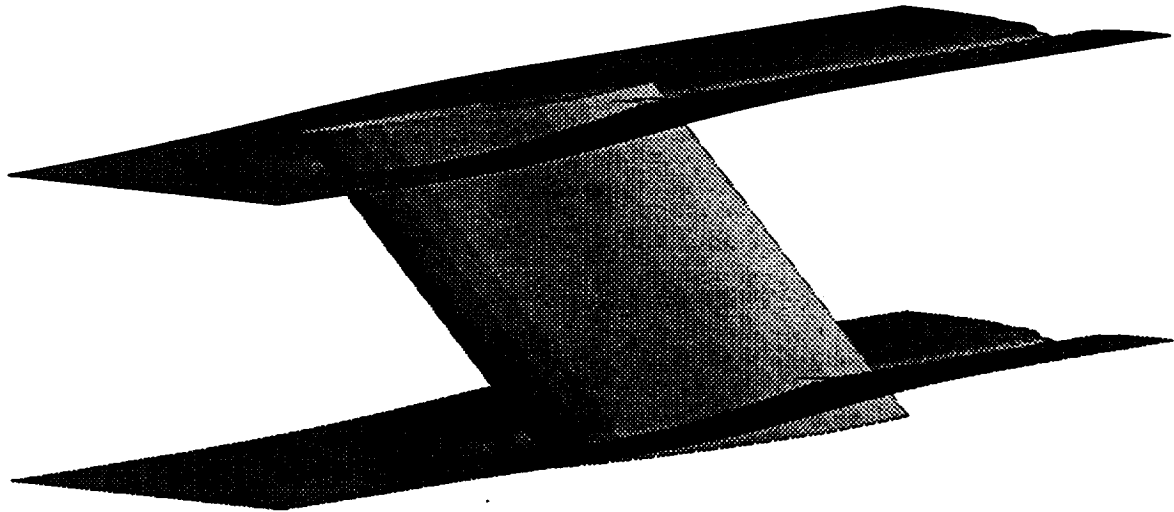
Figure 3.5: Test-section end liners and NLF(2)-0415 wing for $\alpha = -4°$.
Figure courtesy of Reibert (1996a).

3.3.3 Surface Roughness Elements

Although travelling crossflow disturbances are influenced primarily by freestream turbulence (Bippes et al. 1991; Deyhle et al. 1993; Deyhle and Bippes 1996), stationary crossflow disturbances are predominantly governed by surface roughness near the attachment line (Radeztsky et al. 1993a, 1994). Radeztsky et al. (1993a) have shown that micron-sized roughness elements placed just aft of the attachment line have a very significant effect on the transition pattern and where it occurs on the upper surface of the wing. The growth of stationary crossflow disturbances is strongly dependent on initial conditions. Therefore, it is vital to document and control the surface roughness near the attachment line.

For the ASU experiments, the aluminum surface of the wing has been finely polished to reduce the natural roughness near the attachment line. Profilometer measurements near the leading-edge region reveal a surface finish with 0.25 μm root-mean-square variations. Near the mid-chord region, similar measurements show a root-mean-square surface finish variation of 0.12 μm. This very smooth finish allows for a long natural growth region for the crossflow vortices before they breakdown near mid-chord at moderate Reynolds numbers (on the order of 2 million).

A primary objective of the present experiment is to determine the evolution of the spatial and temporal modes of the crossflow-dominated boundary layer through transition. The natural

surface roughness near the leading edge causes an uneven sawtooth pattern in the transition region as seen by flow visualization experiments (Dagenhart 1992; Reibert 1996a). This nonuniformity of the transition front implies that significant spanwise variations exist due to the roughness aberrations near the attachment line, thus making analytical interpretations very difficult. Therefore, to simplify the disparity problem, the dominant spatial mode, essentially the dominant crossflow vortex wavelength, is isolated and analyzed in the present work.

The dominant spatial mode is isolated by "overriding" the nonuniform surface roughness of $0.25 \, \mu m$ with larger, equally-spaced roughness elements placed just aft of the attachment line. The roughness elements used are Geotype #GS-104 circular, dry-transfer dots commonly used in the graphic arts industry. When rubbed onto the wing surface, these 3.7 mm-diameter dots produce a $6 \, \mu m$-thick roughness element. Although the surface of these dots is somewhat uneven, the edges are found to be quite clean and therefore provide a relatively organized and-even transition front near mid-chord. Radeztsky et al. (1993a, 1994) describe the ability of these and other types of artificial roughness elements to induce stationary crossflow waves in detail.

The Geotype dots are applied to the wing surface in full-span arrays along the z axis at $x/c = 0.023$, near the neutral point for the crossflow instability. Radeztsky et al. (1993a) have shown that this location maximizes the influence of the artificial roughness. The dominant spatial mode, i.e., the fundamental disturbance wavelength, is forced by the spanwise spacing of the elements. The current experiment is based on the findings of Reibert et al. (1996) and Reibert (1996a) who choose a spacing of 12 mm to amplify the dominant wavelength that appears in the natural transition process. This wavelength is determined from observation of the dominant wavelength present in the flow field without any artificial roughness and is predicted to be the most amplified wavelength from linear stability calculations (Reibert 1996a). The current experiment also includes measurements made with 36 mm spacing of the artificial roughness. This spacing allows for more modes to enter the flow field in the form of harmonics. The effects of the roughness elements are explained further in section 5.3.3. Reibert (1996a) also shows that the Geotype dots are small enough such that they do not trip the boundary layer or induce a local turbulent wedge in this configuration, yet are large enough to effect the transition front further downstream.

CHAPTER 4

Instrumentation

All quantitative velocity and surface shear-stress measurements within the swept-wing boundary layer in the current experiment involve anemometry techniques which use various combinations of three sensor types. These include single hot-wire probes, two-component cross-wire probes and three types of custom-designed hot-film sensor sheets containing multiple sensors. This chapter describes each sensor type and how they are calibrated.

4.1 Sensor Descriptions

4.1.1 Single Hot-Wire Probes

Single hot-wire anemometry is used in the current experiment to measure the streamwise component of velocity ($\bar{u}$ in the global coordinate system) within the boundary layer. The experiment uses two Dantec 55P15 boundary-layer probes illustrated in figure 4.1. They use 5 μm platinum-plated tungsten wires 1.25 mm in length between the probe tines which are 3 mm offset from the probe axis to allow measurements close to a model surface.

4.1.2 Cross-Wire Probes

Two-component cross-wire anemometry is also used in the current experiment to measure streamwise and crossflow velocities simultaneously within the boundary layer. The cross-wire probes, illustrated in figure 4.2, are custom designed by Auspex Corporation but are based on their standard AHWX-101 model. They use 5 μm tungsten wires, each 0.9 mm in length. The long ceramic

Top

Side

1.25 mm
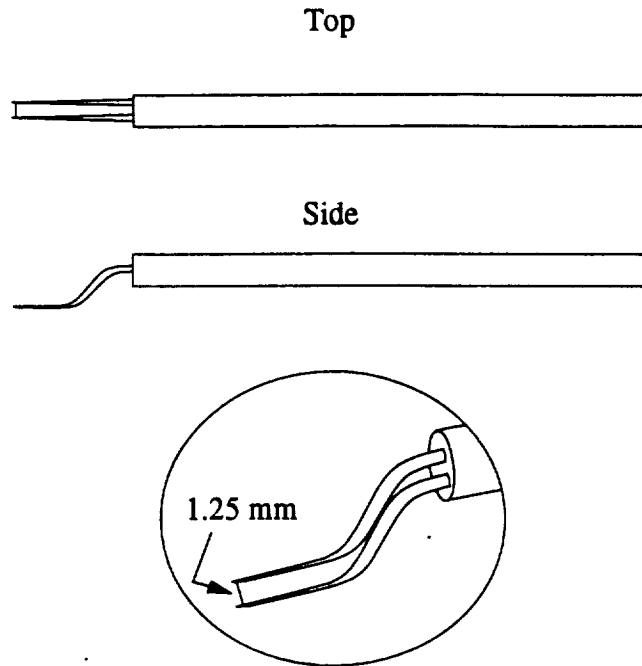
Figure 4.1: Schematic of single hot-wire boundary-layer probe. Not drawn to scale.

Probe Tines
Length: 15 mm

Probe Body
Length: 25 mm

Ceramic Tubing
Length: 38 mm

Leads

Wire Length
0.9 mm
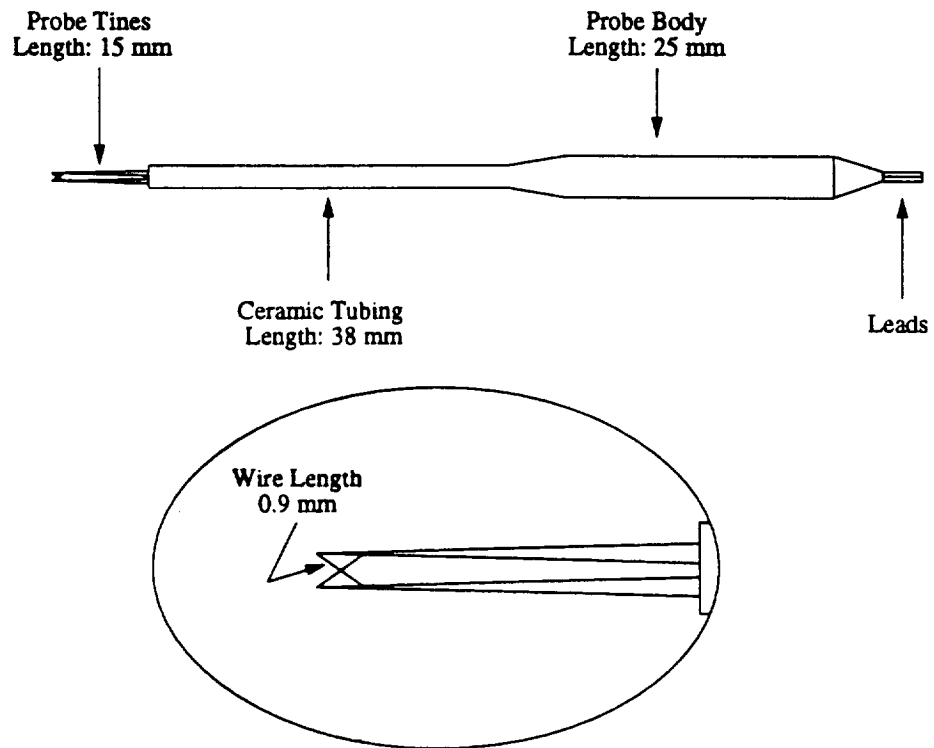
Figure 4.2: Schematic of cross-wire probe. Not drawn to scale.

tubing places the sensing area well upstream of the main probe body. This greatly reduces flow disturbance and therefore makes it well-suited for measurements in a turbulent flow. The cross wires are used for measurements in both laminar and turbulent regimes.

4.1.3 Hot-Film Sheets

The current experiment also uses hot-film anemometry techniques to measure shear stresses on the wing surface. This is accomplished by three types of custom-designed multi-element hot-film sheets. These include a sheet of finely-spaced array of hot-film sensors designed to specifically measure the surface shear stress in the crossflow direction (z_t in the boundary-layer streamline coordinate system), a sheet of sparse array of sensors designed to measure the streamwise propagation of the surface shear stress across the transition front (in the x_t direction in the boundary-layer streamline coordinate system) and a third sheet of sensors designed to locally measure two-components of surface shear stress in a very small area.

The hot-film sheets are fabricated at NASA Langley Research Center in Hampton, VA by vapor deposition of nickel and copper layers on a 50 μm thick Kapton sheet. They are similar to the multi-element hot-film sheets used in the experiments of Holmes et al. (1986), Dagenhart et al. (1989), Johnson and Carraway (1989), Mangalam et al. (1990) and Agarwal et al. (1991). By connecting the sheet leads to a connection terminal, one may use any combination of sensors simultaneously, provided enough anemometers are available. The sheets are mounted to the surface of the wing with a 50.8-μm-thick, uniform sheet of acrylic adhesive donated by MacTac Corporation. Thus, the total thickness of the hot-film sheet and adhesive is 100.8 μm and is indeed non-intrusive at the measurement locations chosen. This is determined by surface flow-visualization techniques as discussed in chapter 5.

The hot-film sheet shown in figure 4.3 is designed to simultaneously measure the spatio-temporal evolution of the crossflow vortices in the crossflow direction of the swept-wing boundary layer. The sheet consists of 31 parallel sensor elements spanning a range of 30 mm. The sensor spacing of 1 mm, fine enough to adequately resolve the structural form of at least two crossflow vortices, was determined from the analytical results of Chapman et al. (1994) for a similar experiment on the same wing by Dagenhart et al. (1989). The sensing elements are 0.127 mm wide and 1.5 mm in length. The length is designed to capture the larger scales in the flow, such as the cross-
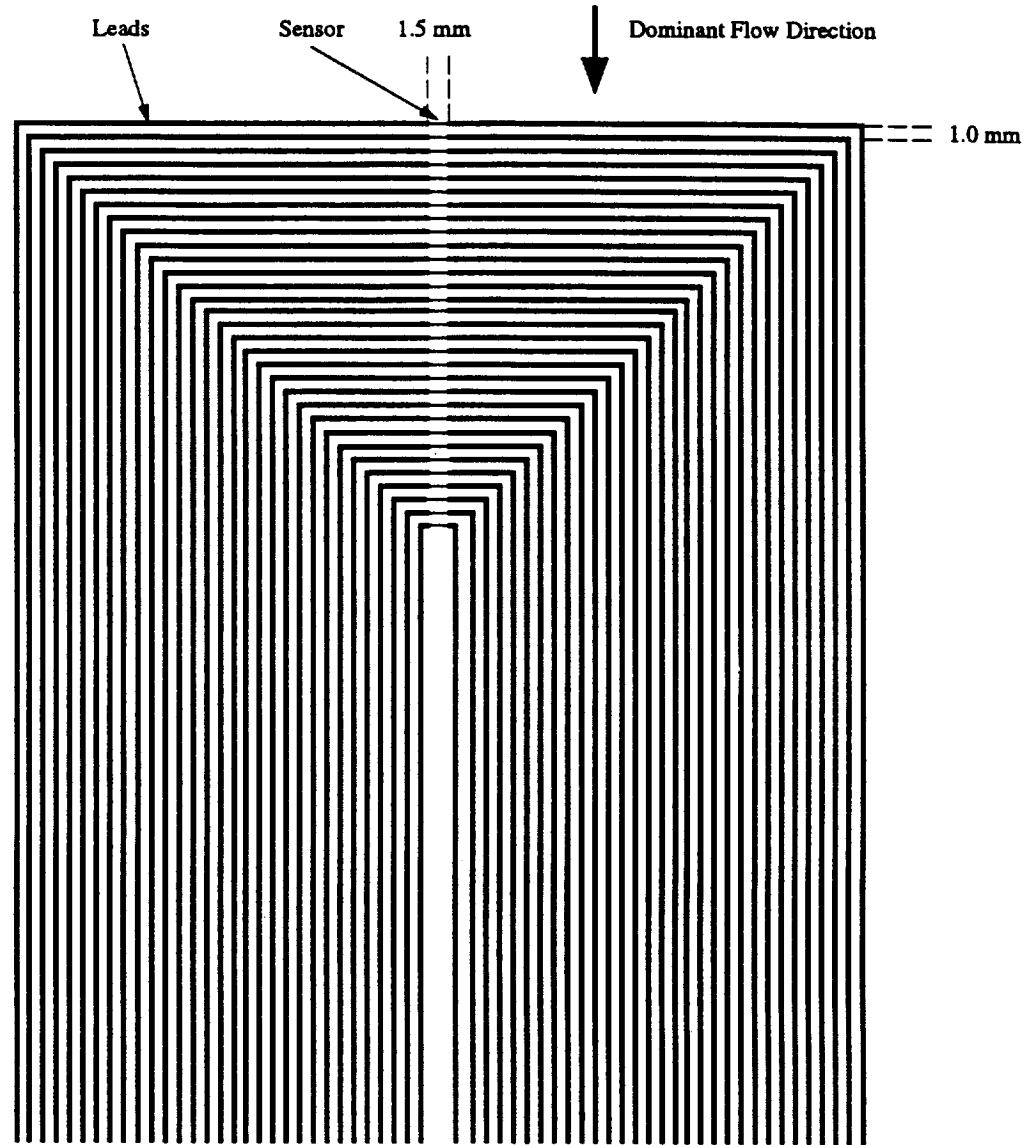
Figure 4.3: Layout of crossflow hot-film sensor sheet. Not drawn to scale.

flow vortices themselves, estimated to be no larger than 3.5 mm for a boundary-layer thickness of

approximately 4 mm at Reynolds numbers near 2×10^6. This estimate is based on the mean veloc-

ity profiles in the desired measurement locations acquired by Reibert (1996a).

Figure 4.4 shows a layout of a second hot-film sheet specifically designed to simultaneously

measure the surface shear stress across the transition front. The 16 parallel sensors are spaced 10

mm apart thus spanning a range of 150 mm. This is typically enough streamwise distance to cover

the entire transition front (i.e., with at least one sensor in the laminar regime and at least one
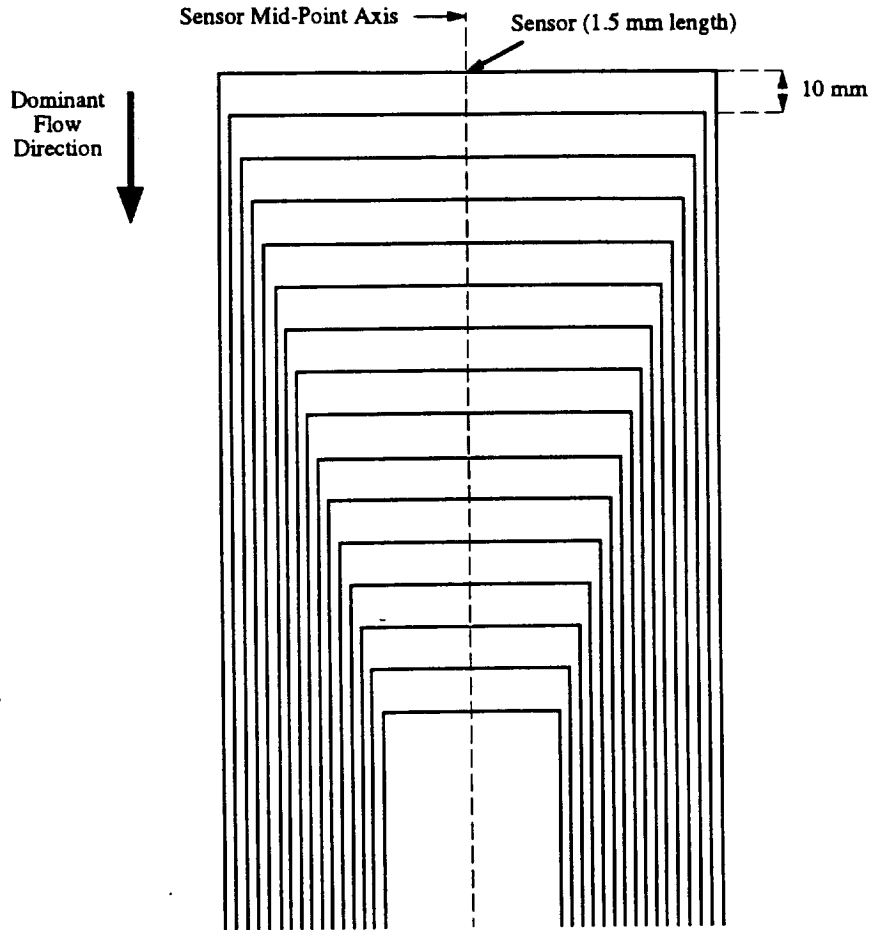
Figure 4.4: Layout of streamwise hot-film sensor sheet. Not drawn to scale.

within the fully turbulent regime) for chord-based Reynolds numbers on the order of 2×10^6 for the present wing configuration. The sensing elements have the same dimensions as the crossflow sheet for the same reasons.

A third hot-film sheet is illustrated in figure 4.5. This sheet is shown in actual size and with a 10 × enlarged sensing area. The sensor array, referred to as the "T-array", was designed to measure the two components of surface shear stress in a very small area. The design is intended to capture the small-scale surface shear and the dynamic interaction of the two components. Each of the 21 sensing elements are 0.051 mm wide and 0.572 mm in length, spaced 2.1 mm center-to-center in both directions in a 7 × 3 sensor array which covers a 12.60 mm × 4.77 mm measurement area.
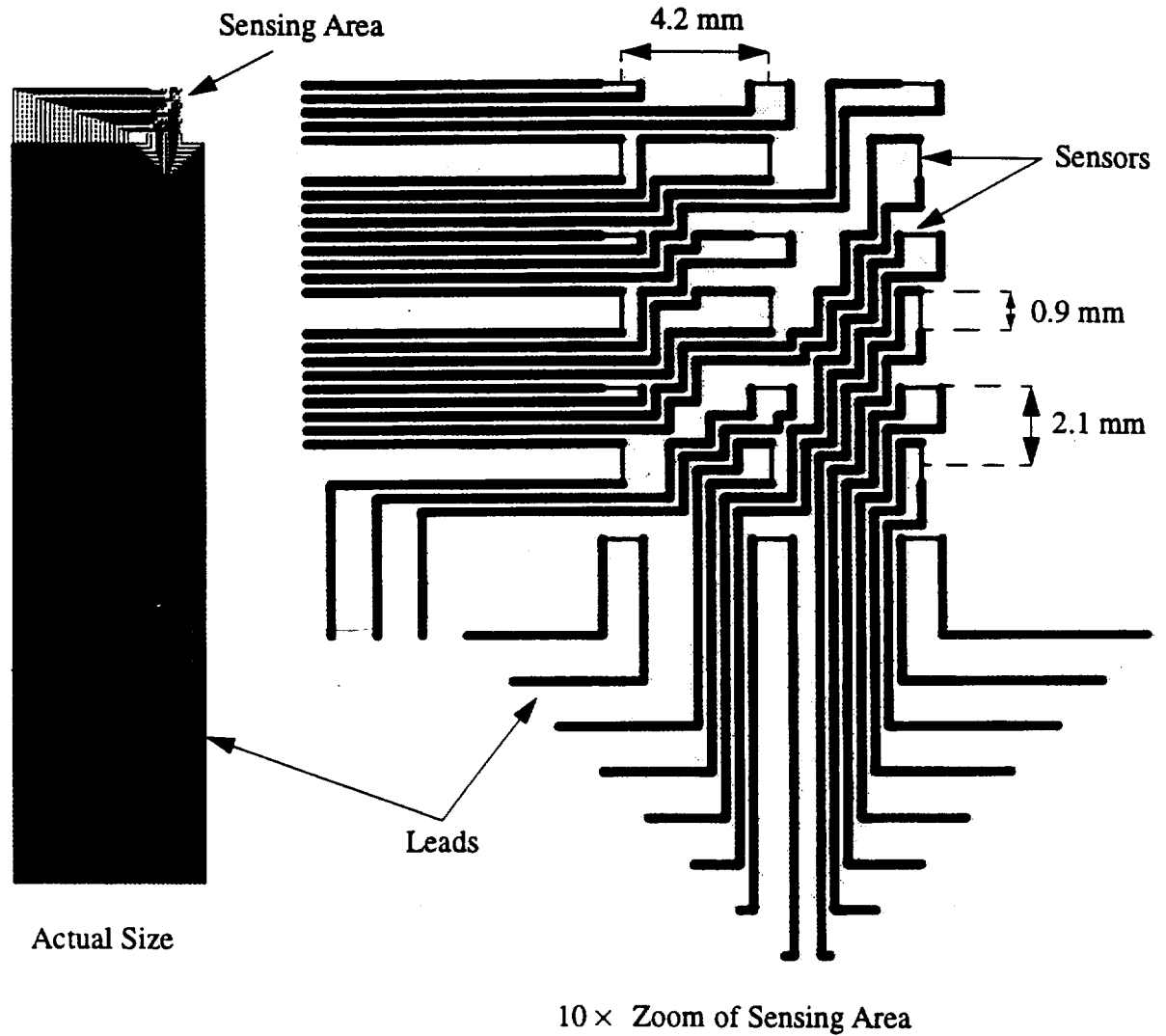
Figure 4.5: Actual size and enlarged view of two-component, local "T-array" hot-film sheet. Drawn to scale.

4.2 Wire Calibrations

Each of the three instrument types require specific calibration techniques. The hot-wire and cross-wire probes have standard procedures for properly calibrating the voltages from the constant temperature anemometers (CTA) to velocities, formulated over the years through various research

efforts. The calibration of the hot-film voltages to surface shear stresses, however, has not been well developed since obtaining a known shear stress on the surface is difficult. Thus, a new calibration procedure is presented separately in section 4.3. However, the wire calibration procedures are explained here.

4.2.1 Single Hot-Wire Calibration

Calibrating single hot wires at the ASU facility is a fully automated procedure which utilizes a customized temperature-compensation software package outlined in detail by Reibert (1996a, 1996b) and Radeztsky et al. (1993b). The procedure and relevant equations are summarized below.

The voltage output from a single hot-wire CTA system is directly related to the heat transfer from the heated-wire element to the fluid which is dominated by the fluid velocity and the temperature difference between the wire and fluid (Perry 1982). Assuming a fixed temperature difference, the effective velocity response of the anemometer may be modeled by a classic technique known as King's Law which is generally expressed for the velocity as

$$U_{eff} = (P + QE^2)^2 \qquad (4.1)$$

where E is the voltage from the anemometer and P and Q are coefficients incorporating the physical properties of the hot-wire element and the fluid (King 1915). The variable U_{eff} is the effective velocity "seen" by the hot-wire probe and may represent either total, mean or fluctuating velocities in equation 4.1 as long as the voltage corresponds to total, DC or AC voltages respectively. The approach used at the ASU facility generalizes this model by using a simple polynomial fit expressed as:

$$U_{eff} = \sum_{k=0}^{n} A_k E^k \qquad (4.2)$$

The coefficients A_k are determined such that equation 4.3 provides a best least-squares fit to a moderate amount of voltage-velocity data points. A fourth-order fit ($n = 4$) is used to match the

51
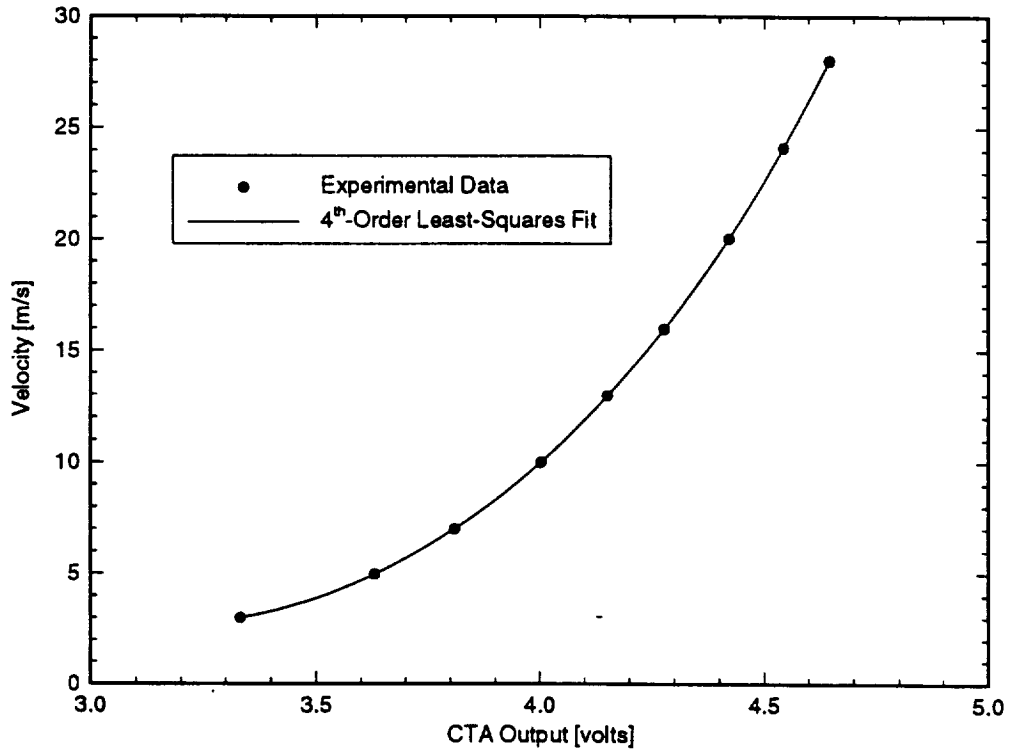
Figure 4.6: Typical velocity calibration curve for a single hot-wire probe.
Figure courtesy of Reibert (1996a).

order in equation 4.1. A fourth-order fit is commonly used since higher orders typically do not add any significant improvement (George et al. 1987). Figure 4.6 shows a typical hot-wire calibration curve.

The hot wires are dynamically calibrated in the freestream by acquiring the anemometer output voltages and the Pitot-static velocity as the tunnel is increased through a predetermined set of calibration speeds. The range of speeds must be chosen to encompass the operating speeds of the experiment to prevent extrapolation of a polynomial curve fit, a procedure which often tends to be unstable (Press et al. 1992). It is standard practice at the ASU facility to calibrate the single hot wires each morning to avoid DC voltage drift. Under full automation, the process takes less than five minutes to complete.

Before the hot-wire voltages are calibrated to velocities, they are appropriately compensated for temperature effects. As a closed-circuit wind tunnel in a desert environment, the ASU Unsteady Wind Tunnel experiences large temperature rises (as much as 20° C) within the test sec-

tion, particularly when running high-Reynolds-number experiments in the summer months. Thus, measurements from all temperature-dependent sensors are affected and must be appropriately compensated.

The temperature-compensation approach used at the ASU facility is based on the work of Bearman (1971) and Radeztsky et al. (1993b) and is explained in detail by Reibert (1996a). The model assumes a linear relationship between the square of the CTA voltage and fluid temperature such that

$$E_c^{\ 2} = E^2 + C_T(T_c - T) \qquad (4.3)$$

where E_c is the CTA equivalent voltage at the calibration temperature T_c. The compensation coefficient C_T is a function of velocity and is modeled with a second-order polynomial curve fit,

$$C_T = \sum_{j=0}^{2} B_j (U_{eff})^j \ , \qquad (4.4)$$

whose coefficients B_j are determined by the least-squares technique. Figure 4.7 shows a typical set of coefficient data points which is collected prior to the velocity calibration procedure outlined above. Therefore, the velocity calibration includes temperature effects and is truly a constant-temperature calibration. An implicit relationship for the temperature-compensated CTA voltage E_c is obtained mathematically by substituting equations 4.2 and 4.4 into equation 4.3:

$$E_c^{\ 2} = E^2 + \sum_{j=0}^{2} \left[B_j \left(\sum_{k=0}^{n} A_k E_c^{\ k} \right)^j \right] (T_c - T) \ . \qquad (4.5)$$

Therefore, given a temperature T and voltage E, this equation may be solved implicitly for E_c, the temperature-compensated CTA voltage. This temperature-compensated voltage is then converted to a velocity using equation 4.2. This temperature-compensated method reduces calibration errors from above 15% to less than 1% across the entire speed range (Reibert 1996a).
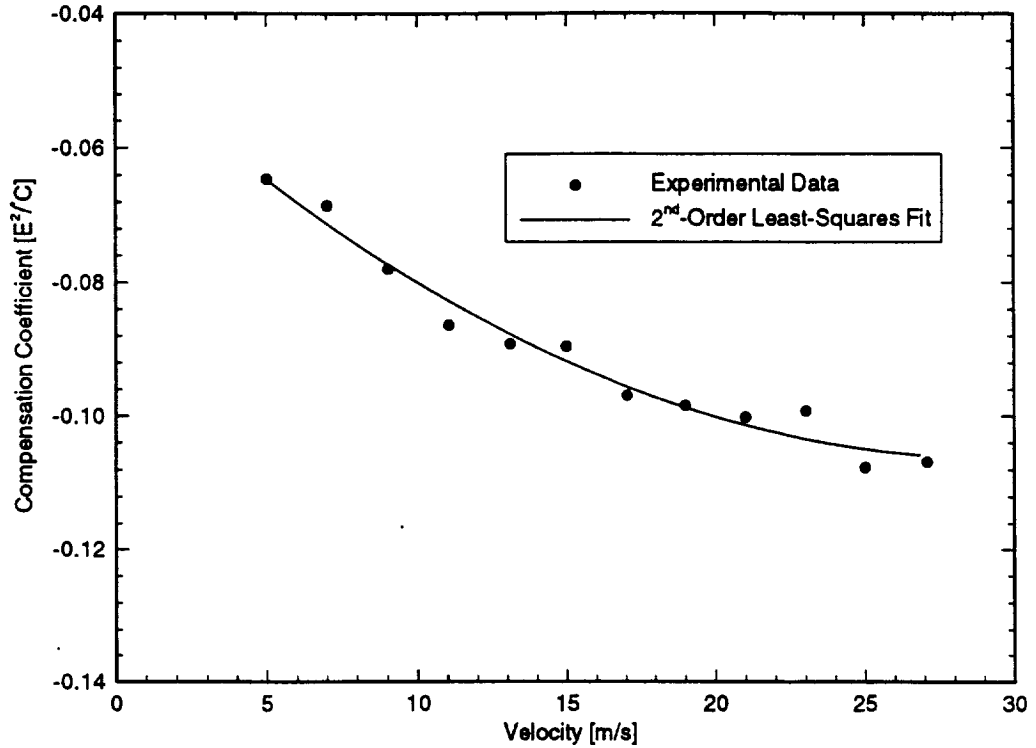
Figure 4.7: Typical temperature-compensation curve, compensation coefficient versus velocity. Figure courtesy of Reibert (1996a).

4.2.2 Cross-Wire Calibration

The calibration of the two-component cross-wire probes is similar to that of the single hot-wire calibration with the addition of an angle calibration to decipher the two components of velocity. To better explain the positioning and equations involved in this calibration, figure 4.8 illustrates the geometry of a cross-wire probe sensing area.

The cross-wire calibration procedure uses the temperature-compensation routines explained in section 4.2.1 and is performed in the freestream. The probes to be calibrated are mounted perpendicularly at the end of a circular tube which is inserted into the test section via the instrumentation window allowing rotation of the probe in the X-Z plane. The probes are mounted so this rotation, illustrated in figure 4.8, is in the plane of the cross-wire elements which allows each wire element to be placed perpendicular to the freestream velocity vector.

The first step in the calibration procedure is to align one of the cross-wire sensing elements (say wire #1 in figure 4.8) perpendicular to the flow, i.e., $\phi_1 = 0°$. This is accomplished by plac-

Probe Axis

Normal Line to Wire #2

Normal Line to Wire #1

Wire Element #2

90°   90°

Φ

ϕ_1

ϕ_2

Wire Element #1

β

Angle Calibration
Rotation

U_∞
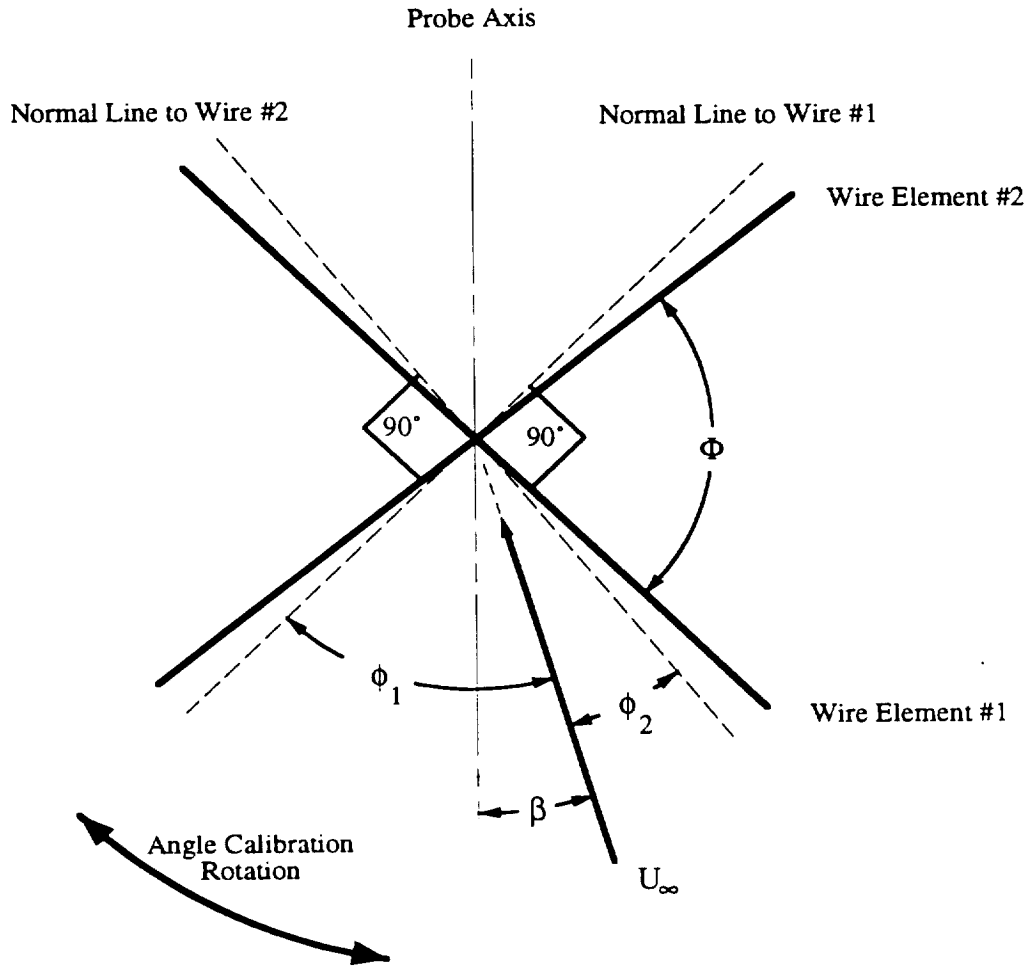
Figure 4.8: Geometry of cross-wire probe.

ing the probe near that position and rotating it until it reaches a maximum mean-voltage reading. A speed calibration is now performed on this wire as if it were a single hot-wire using the same procedure explained in section 4.2.1. A typical normal calibration curve obtained in this manner for each of the cross-wire elements is similar to that of the single hot wire shown in figure 4.6.

Next, an angle-speed calibration is obtained by acquiring the mean voltage from each wire as the angle between the probe axis and the X axis is varied. The range of speeds used in the normal calibration are run through for each angular position. The probe is rotated from wire #1 being perpendicular to the freestream velocity vector to wire #2 being perpendicular to the freestream velocity vector (i.e., where the mean voltage for wire #2 is a maximum) in increments of 5°. The mean voltages are sampled for each speed at each angular position. This results in an angle-speed
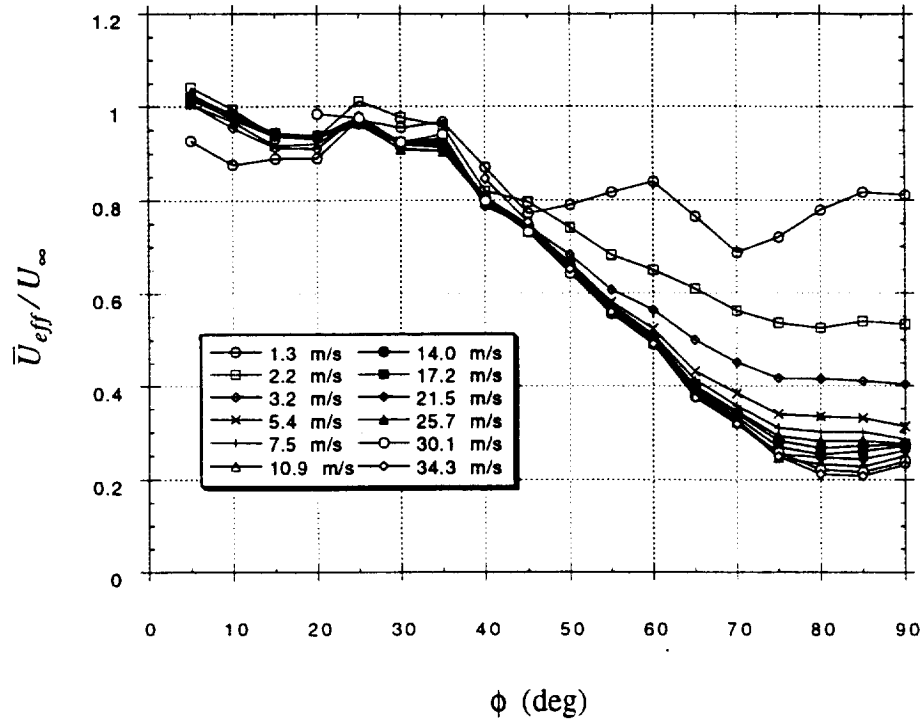
Figure 4.9: Typical angle-speed calibration for one cross-wire element.

calibration curve typical of that shown in figure 4.9, where the velocity ratio $\overline{U}_{eff}/U_\infty$ is simply a normalization of the effective mean velocity with the freestream velocity. The last set of angle-speed data obtained in this procedure will result in the normal calibration for the second wire element.

Now that all the data is acquired, it must be used to appropriately calibrate the voltages to actual velocity components. The efforts of Hinze (1959), Champagne et al. (1967a, 1967b) and Tutu and Chevray (1975) have produced a modified cosine law relating the freestream velocity to the effective velocity, i.e., the velocity "seen" by the cross-wire probe. This relationship is expressed as:

$$U_{eff}^2 = U_\infty(\cos^2\phi + k^2\sin^2\phi) \tag{4.6}$$

where ϕ is the angle between the line normal to a cross-wire element and the freestream velocity

vector and k is a heat-transfer coefficient of the wire's axial sensitivity, a function of velocity and the size of the wire element. Equations are then determined for each wire element by applying equation 4.6 to the geometry of the cross-wire probe in figure 4.8 to produce the modified cosine laws for each element.

$$U^2_{eff_1} = U_\infty(\cos^2\phi_1 + k_1^2\sin^2\phi_1)$$
$$U^2_{eff_2} = U_\infty(\cos^2\phi_2 + k_2^2\sin^2\phi_2)$$

(4.7)

Hinze (1959) indicates that k typically ranges between 0.1 and 0.3 depending on the magnitude of the velocity. Champagne et al. (1967a) found k to depend primarily on the size ratio of the wire, i.e., the length to diameter ratio (l/d). For platinum wires, they found $k \approx 0.2$ for $l/d = 200$ and decreasing with increasing size ratio, finally reaching zero at $l/d = 600$. Using the acquired angle-speed data in figure 4.9, equation 4.6 may now be iterated for k. For the current calibration, coefficients for each curve in figure 4.9 are determined through an iteration process until the relative error of the data model is less than 5%. Typical fits are presented in figure 4.10 with their corresponding k values. The k values decrease with increasing velocity. For the operating speeds of the current experiment (25 - 30 m/s), the heat-transfer coefficient is approximately 0.17 for both of the sensing elements on both Auspex cross-wires used in the current experiment. This value is in total agreement with $k \approx 0.2$ seen by Champagne et al. (1967a) for very similar conditions with a size ratio of $l/d = 180$. Therefore, a coefficient of $k = 0.17$ is used throughout the calibration for both k_1 and k_2 in equation 4.7. However, the governing calibration equations are presented in general terms.

The method of solution for the calibration, outlined by Glauser (1987), is achieved by computing the ratio of the two equations listed in equation 4.7 resulting in

$$\left(\frac{U_{eff_1}}{U_{eff_2}}\right)^2 = \frac{\cos^2\phi_1 + k_1^2\sin^2\phi_1}{\cos^2\phi_2 + k_2^2\sin^2\phi_2} .$$

(4.8)

Using the fact that $\phi_2 = \Phi - \phi_1$ from figure 4.8, some trigonometric substitutions and other

57
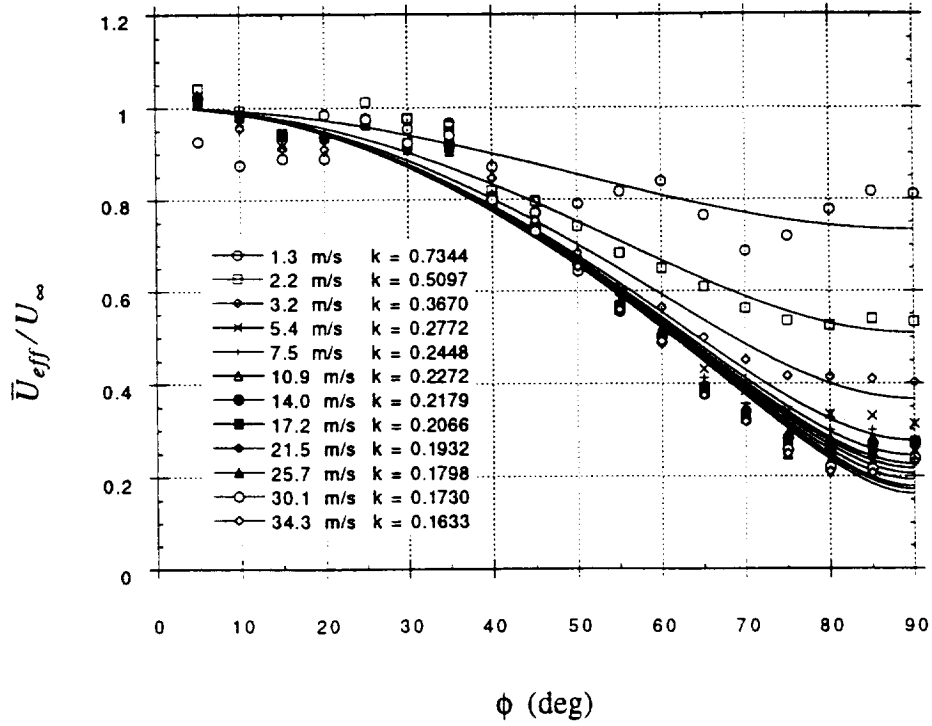
Figure 4.10: Typical curve fits of data in figure 4.9 using the modified cosine law of equation 4.6 with iterated values of k within 5% error.

mathematical manipulations, the following quadratic equation for $\tan\phi_1$ results:

$$C_2\tan^2\phi_1 + C_1\tan\phi_1 + C_0 = 0 \tag{4.9}$$

where the coefficients are defined as:

$$C_2 = Rk_2^2\cos^2\Phi + R\sin^2\Phi - k_1$$

$$C_1 = 2R(1 - k_2^2)\cos\Phi\sin\Phi$$

$$C_0 = R\cos^2\Phi + Rk_2^2\sin^2\Phi - 1 \tag{4.10}$$

$$R = \left(\frac{U_{eff_1}}{U_{eff_2}}\right)^2 .$$

58

The solution is governed by the physics of the probe, i.e., $\tan\phi_1 > 0$, and the quadratic formula resulting in

$$\tan\phi_1 = \frac{-C_1 + \sqrt{C_1^2 - 4C_2C_0}}{2C_2} \qquad (4.11)$$

under the constraint that the expression under the radical must be greater than or equal to zero. If the expression under the radical is negative, the solution cannot be determined. This phenomenon of not being able to convert voltage pairs to velocity components is referred to as "dropout" by Beuther et al. (1987) and usually only occurs when one of the wires experiences significantly higher turbulence intensity than the other, a condition that is never reached in the current experiment. These equations may be simplified for the current experiment as the sensing elements on each of the Auspex cross-wire probes were found to be perpendicular to one another, i.e., $\Phi = 90°$.

After ϕ_1 is solved from equation 4.11 using $k_1 = k_2 = 0.17$, the freestream velocity U_∞ may be calculated from rearranging the first equation listed in equation 4.7. The individual velocity components, $\tilde{u}$ and $\tilde{w}$ in the global coordinate system for the current experiment, may then be determined from:

$$\tilde{u} = U_\infty \cos\beta$$
$$\qquad (4.12)$$
$$\tilde{w} = U_\infty \sin\beta$$

where

$$\beta = \phi_1 - \frac{\Phi}{2} , \qquad (4.13)$$

the angle between the freestream velocity vector and the probe axis as shown in figure 4.8. The calibration procedure is now complete.

4.3 Film Calibrations

The calibration of hot-film sensors is not as straight-forward as that of the wire-based sensors. In fact, several techniques have been proposed either requiring measurement of local shear stresses on the surface near the hot-film sensor by other means or by relating the hot-film measurement to an analytical solution in a flow with a simple geometry. The early efforts of Ludwieg (1950), Liepmann and Skinner (1954), Myers et al. (1963) and Bellhouse and Schultz (1966) have determined that most hot-film sensors can be calibrated through the following relationship:

$$\tau_w^{1/3} = AE^2 + B \tag{4.14}$$

where τ_w is the total shear stress at the wall sensed by the hot film, A and B are constants descriptive of the film element and E is the CTA output voltage. Ramaprian and Tu (1983) suggest an improvement on this traditional calibration approach which corrects for calibration errors by applying a form of Reynolds decomposition and time averaging on equation 4.14. These approaches usually perform well but require either an independent measurement of the local surface shear stress or a theoretical approximation. The current problem is compounded by the three-dimensionality of the swept-wing flow and by the mounting technique of the hot-film sheets, a pseudo-permanent attachment. The sensor sheet is either destroyed or severely damaged once it is removed from the model surface due to the needed strength of the adhesive. Thus the same sheets used in the swept-wing experiment cannot readily be placed in a simpler flow geometry for direct calibration. Making an independent measurement of the surface shear stress on the swept-wing with other types of sensors is feasible. However, most of these techniques require a cavity in the model surface or other alterations to the model surface. Also, the swept-wing flow is too complex to use theoretical approximations realistically. Thus, due to all the complexities involved, only raw voltages were originally acquired from the hot-film sensors used in the current experiment.

However, in order to properly compare surface measurements to internal velocity measurements within the boundary layer, raw voltages do not suffice. Thus, a new calibration technique is developed which takes full advantage of the ASU Unsteady Wind Tunnel facility and the receptivity experiments performed there in an acoustically-excited flat-plate boundary layer. Although,

this calibration is performed on a different sensor sheet than that used in the actual swept-wing experiment, it does give an approximate calibration for the swept-wing data. The hot-film sheet fabrication process is well understood and monitored, resulting in sensors that are very similar (near exact in dimensions for each sheet type and every element for every sheet within a 17% variation range of resistance values). Therefore, the calibration presented here is not without error but is, in this author's opinion, far better than analyzing signals based on raw voltages. An improved method for future calibration of these types of hot-film sensors is suggested at the end of this section based on the observations from this first attempt presented below. The proposed technique allows for a direct calibration of the sensors in the swept-wing boundary layer itself.

4.3.1 Flat-Plate Receptivity Experiments

The calibration technique is based upon recent receptivity experiments performed in a flat-plate boundary layer at the ASU Unsteady Wind Tunnel. This research focuses on how Tollmein-Schlichting (T-S) waves are generated within the two-dimensional zero-pressure-gradient boundary layer under the influence of acoustic forcing with no other receptivity mechanisms other than the leading edge. This receptivity mechanism is what is used to calibrate the hot-film sensors as explained in section 4.3.2.

The flat-plate model used in the present calibration is the same as that used in the experiments of Mousseux (1988), Rasmussen (1993), Wei (1994), Saric et al. (1994) and Krutckoff (1996). The plate is 4000 mm (length) × 1370 mm (span) × 9.53 mm (thickness) with a 20:1 and 40:1 modified super ellipse (MSE) machined directly to each end. Either end may be used as the leading edge (Saric 1994c). Much care is taken in the design of the MSE (Lin et al. 1992), in assuring symmetric flow (Saric 1994c) and in eliminating curvature discontinuities (Saric et al. 1994a, 1994b).

The acoustic disturbances are introduced to the freestream by a set of nine 250-mm diameter, 300-watt woofers (by McCauley Sound Inc.) placed on the plenum wall upstream of the honeycomb section of the ASU Unsteady Wind Tunnel (refer to figure 3.1). Sound waves up to 130 dB are measured by a network of microphones placed in the walls at the leading-edge location to measure incidence angle and amplitudes.

Saric et al. (1994a, 1994b) and Krutckoff (1996) present detailed information on the flat-plate model, facility and results from the receptivity experiments. The ASU experiments and

many others, such as those by Tadjfar and Reda (1992) and Wlezien (1994), show that acoustic disturbances excite the growth of T-S waves in the flat-plate boundary layer at frequencies related to the disturbance. For instance, a sinusoidal waveform of a single frequency input to the speaker system will excite and amplify the T-S waves within the flat-plate boundary layer at that frequency. This property of the receptivity mechanism is used to dynamically calibrate the hot-film sensors. Further studies on the flat-plate receptivity mechanisms are summarized in Reshotko (1984), Heinrich et al. (1988), Saric (1994c) and Crouch (1994).

4.3.2 Calibration Concept and Procedure

The concept behind this dynamic hot-film calibration is as follows. Since the acoustic receptivity mechanism excites the amplitude of a T-S wave at the same frequency as that of a speaker-input sinusoid prior to flow transition, it is possible to acquire data from a hot-film sensor mounted to the surface of the flat plate for a specifically known flow condition, i.e., a laminar, acoustically-excited, periodic, streamwise flow at a locally constant frequency. Thus, by acquiring the hot-film raw voltage signal at several frequencies independently upstream from the transition front, one can construct a hot-film frequency response curve. However, this only relates the CTA output voltage to the input waveform and still leaves the problem of not knowing the surface shear stress at the calibration location. Thus, an independent measurement very close to the surface by a previously calibrated hot-wire probe at the same streamwise location as the hot-film sensor is sampled simultaneously with the film for each acoustic input frequency. The hot-wire voltage is calibrated to velocity (in m/s) and thus, the local shear stress at the surface may be estimated in proper stress units (in N/m^2) by equation 2.30, the surface shear-stress equation for two-dimensional flows. This approach is best suited for the near-linear section of the velocity profile close to the surface. This estimate derived from equation 2.30 may be expressed as

$$\tau_x = \mu\left(\frac{\partial u}{\partial y}\right)\bigg|_{y=0} \approx \mu\left(\frac{u_{hw}}{h}\right) \tag{4.15}$$

for the linear region of the velocity profile close to the wall where u_{hw} is the velocity from the hot wire and h is the height of the hot-wire sensing element from the surface of the plate. Thus a similar transfer function may be formulated for the surface shear stress estimate from the calibrated

hot wire. Now, since both the hot film and hot wire have frequency responses that are functions of the input acoustic frequency and are sampled simultaneously, a response may be derived which relates the calculated estimate of the surface shear stress and the hot-film voltage. This relationship is expressed as

$$H(f) = \frac{\hat{\tau}_x}{\hat{E}_{HF}}$$
(4.16)

where $\hat{\tau}_x$ and $\hat{E}_{HF}$ are the Fourier transforms of the surface shear stress and the hot-film voltage, respectively, and $H(f)$ is the transfer function. Thus, by estimating the surface shear stress from the hot-wire signal and Fourier transforming both quantities, a frequency response relationship between surface shear stress and hot-film voltage may be determined since they are acquired simultaneously with the same acoustic excitation. The raw voltage data from the similar hot-film sensors used in the actual swept-wing experiment may then be calibrated by solving equation 4.16 for $\hat{\tau}_x$. The swept-wing hot-film voltage data is Fourier transformed and then multiplied (using complex multiplication) by the transfer function derived in the calibration procedure. The complex product is then inverse Fourier transformed back to time resulting in a surface shear stress time history, i.e., a calibrated hot-film signal.

Eaton (1995) has shown that the frequency response of hot-film sensors similar to those used in the current experiment rolls off somewhere between 2000 Hz and 3000 Hz. Thus, a frequency range of 5 Hz to 3000 Hz is chosen for the calibration of the hot-film sensors. This range is later confirmed to be appropriate upon inspection of the computed hot-film frequency response. The resolution, i.e., the spacing between input acoustic frequencies for each calibration run, is finer for lower frequencies to better resolve the transfer function in an area for which some surface-mounted hot-film sensors experience a primary roll-off before a secondary roll-off near 2500 Hz (Eaton 1995). The spacing of the frequencies chosen for the current calibration are listed in table 4.1 for specific frequency ranges.

The lower frequencies from 5 Hz to 10 Hz are produced by modulating two higher frequency sine waves differing by the desired input acoustic frequency in order to avoid a low-end roll-off on the speaker frequency response of approximately 8 Hz and to prevent damage to the speaker. For example, to produce a 5 Hz wave, the sum of two sine waves of 500 Hz and 505 Hz

Table 4.1: Resolution of frequencies used in the hot-film calibration
for specific frequency ranges.

Frequency Range	Frequency Spacing
5 - 20 Hz	1 Hz
20 - 1000 Hz	10 Hz
1000 - 3000 Hz	50 Hz

are generated by the computer. The signals retrieved from the two sensors are band-pass filtered ±20% of 5 Hz and therefore only the modulation frequency of 5 Hz remains in the acquired signals.

Figure 4.11 illustrates the experimental set-up for the flat-plate calibration technique. The hot-wire probe is aligned outside of the boundary layer at the same streamwise location on the flat-plate as the hot-film sensor to be calibrated. Since the flat-plate is a two-dimensional, span-invariant flow the hot wire is actually offset in span by 2 mm to avoid any convective heating effects from the heated film element. The wind tunnel is then brought to the desired operation speed, one of three different speeds (8 m/s, 12 m/s and 18 m/s) for the current experiment. A specified sinusoid is then digitally generated and maintained throughout the calibration run (usually a period of 2 seconds) by the SUN SparcStation 20 computer and sent to a digital-to-analog converter which then translates the analog version of the sine wave to a set of amplifiers. The gained signal is then sent to the nine speakers at the tunnel wall upstream of the test section. The freestream acoustic disturbances enter the boundary layer through the receptivity mechanism and excite the T-S waves at the input frequency.

The hot-wire probe, mounted to the traversing system, is then marched towards the plate surface in increments of 50 μm, sampling data at each step. A ratio between the mean velocity for the current step and the boundary-layer edge velocity ($\overline{U}/\overline{U}_e$) is dynamically computed after data at each step is acquired. The probe is then stopped at $\overline{U}/\overline{U}_e = 0.15$, within the linear portion of the flat-plate boundary layer close to the surface. This final alignment of the hot-wire probe (still offset in span by 2 mm) is illustrated in figure 4.12. The location of the surface is obtained by extrapolating the profile to zero, thus providing the height h required in equation 4.15.
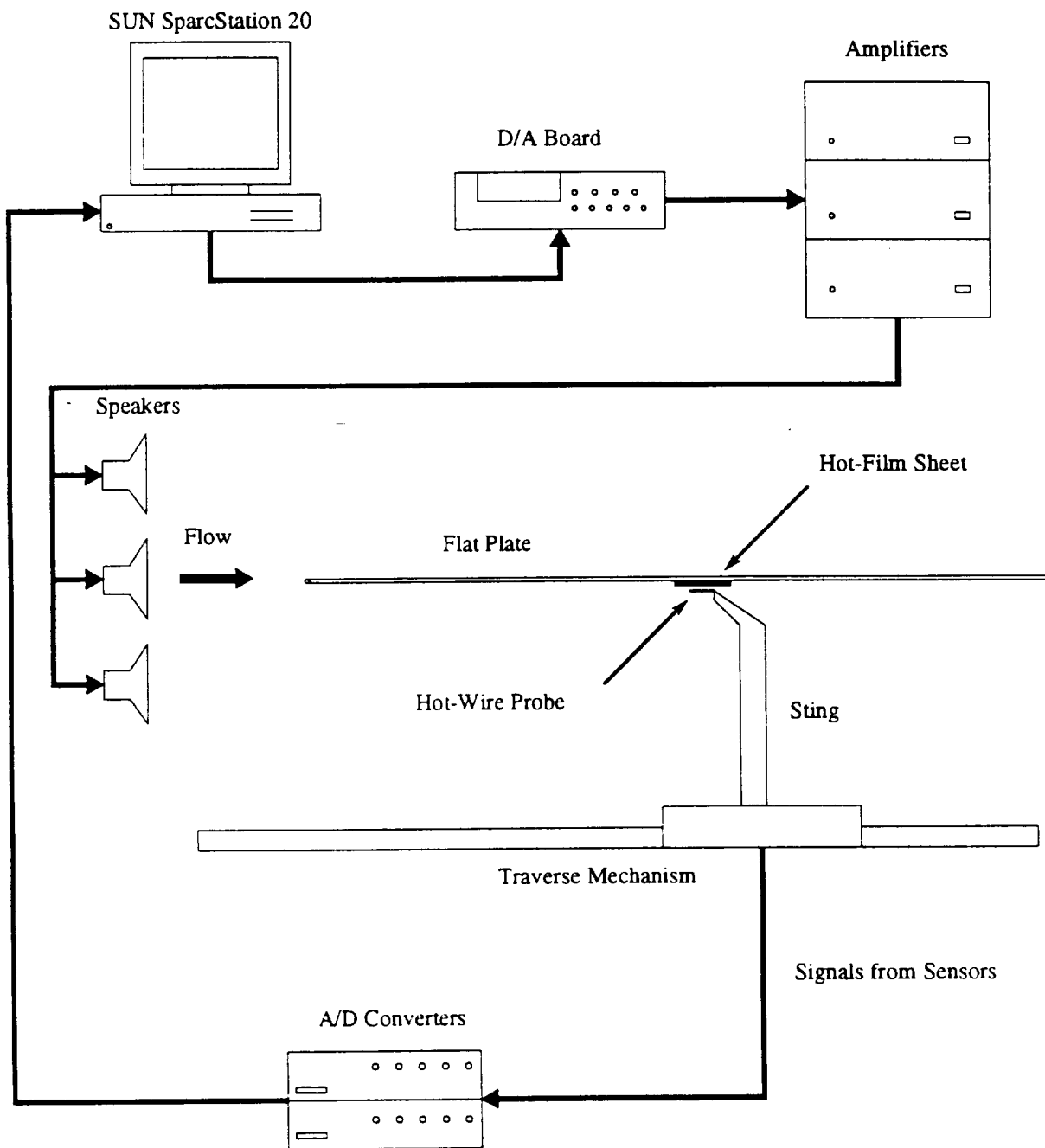
Figure 4.11: Schematic of experimental set-up for hot-film calibration on flat-plate model.
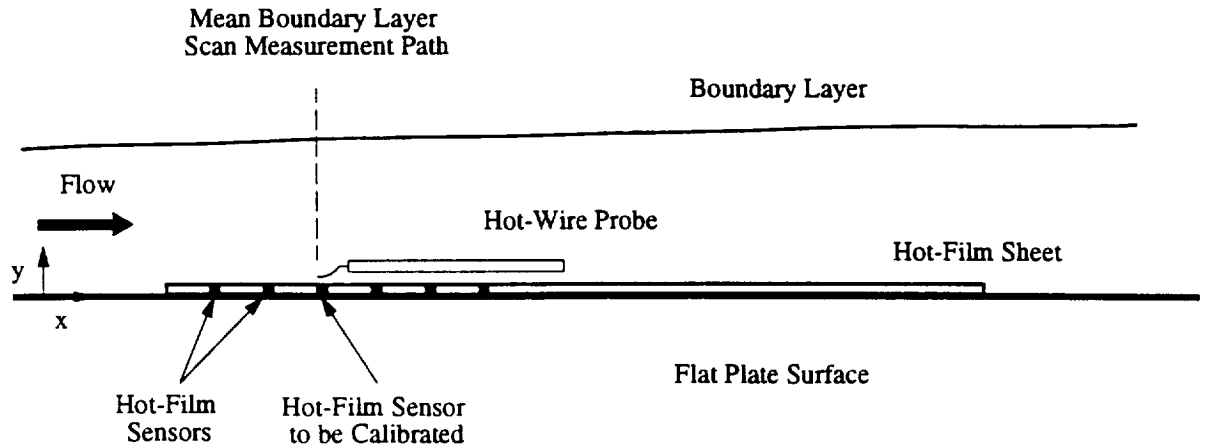
Figure 4.12: Schematic of sensor alignment in hot-film calibration.

Both of the raw voltage signals from the hot-film and hot-wire sensors are then simultaneously sampled for 2 seconds and band-pass filtered ±20% of the input acoustic frequency. The procedure is repeated for the next and remaining desired acoustic input frequencies until data for the complete desired frequency range is obtained. Thus one calibration run with one input acoustic frequency produces only one data point in the transfer function of equation 4.16. Therefore, by running several input frequencies, one may construct the frequency response of the hot-film sensor point by point.

4.3.3 Calibration Results

It has been found through developing this calibration technique that constructing the hot-film transfer function as outlined above requires averaging each acquired frequency data point over several completed runs. This was not done in the current calibration due to time constraints and as a result produced data with high oscillations. Thus, the transfer function is curve fitted and smoothed after using equations 4.15 and 4.16 for each input acoustic frequency. The raw transfer-function magnitude is shown in figure 4.13 for an operation speed of 18 m/s. The oscillations are certainly undesirable and are a direct result of not averaging over several runs. However, once curve fitted and smoothed (as shown in figure 4.14), the data displays the expected transfer-function trends as seen by Eaton (1995). In fact, the data starts to rolls off at about 1000 Hz thus validating the range of input acoustic frequencies chosen in section 4.3.2. Similar oscillations appear for the raw phase data shown in figure 4.15. Yet, as with the magnitude data, the curve-fitted and

66
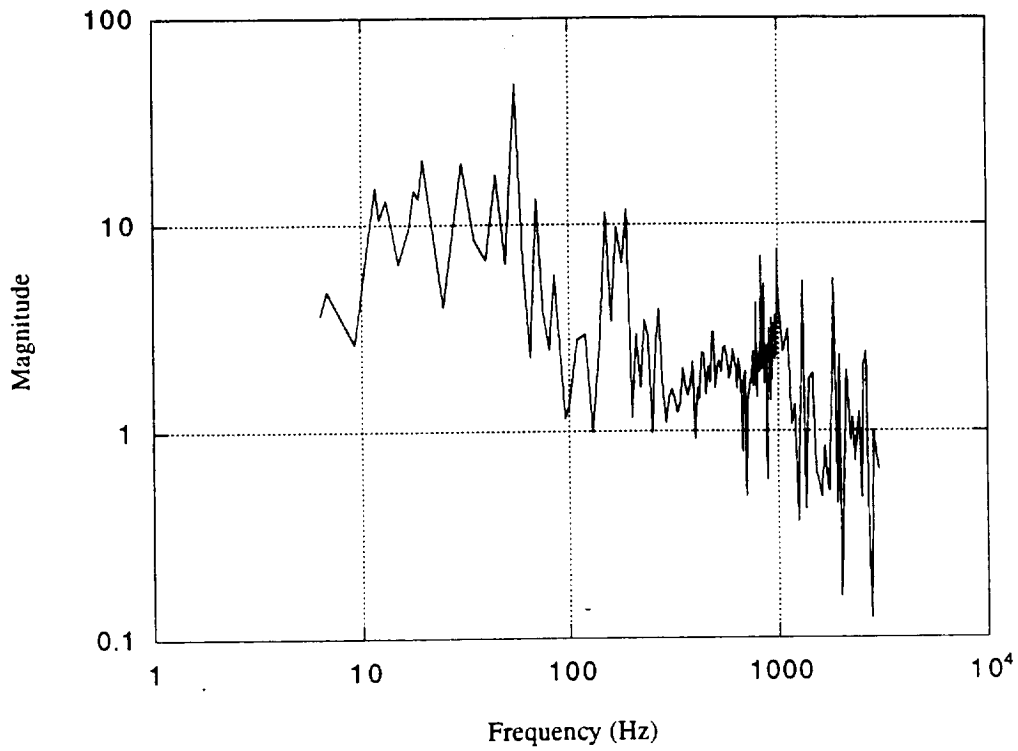
Figure 4.13: Raw magnitude of transfer function at 18 m/s.
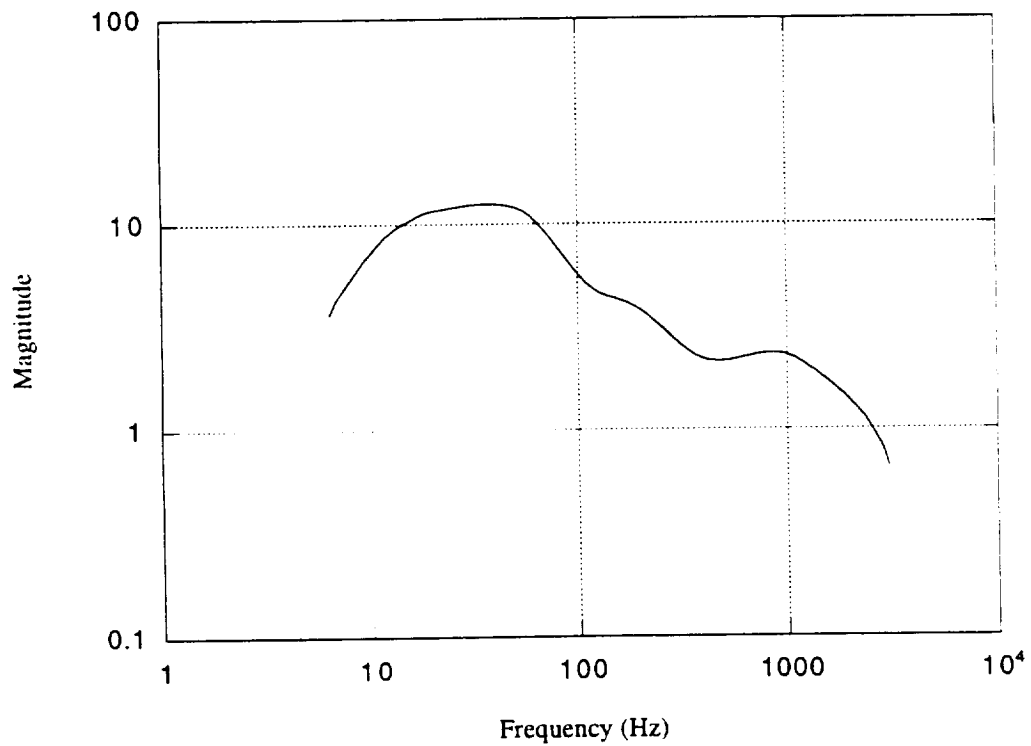
Figure 4.14: Curve fit and smoothing of transfer function magnitude at 18 m/s.

smoothed phase data in figure 4.16 behaves as expected. In fact, the curve-fitted phase data agrees quite well with the results of Eaton (1995). Therefore, although certainly not optimal, the lack of averaging does not completely hinder the physical response needed for calibration.

By comparing the curve-fitted and smoothed transfer functions for each of the three calibration speeds, one notices a slight dependence on velocity for the magnitude shown in figure 4.17 and very little for the phase data shown in figure 4.18. In calibrating the swept-wing data at speeds generally between 25 m/s and 30 m/s, the transfer function from the highest calibration speed of 18 m/s is used. A higher calibration speed would certainly be desired but is limited due to the increasing transition Reynolds number on the flat plate. Increasing the speed beyond 18 m/s would place the transition front on the flat plate well upstream of the area reachable by the traversing mechanism preventing precise alignment of the hot-wire measurements. Thus, a second problem arises in that the speed is not quite corresponding between experiments and calibrations. To approximate an appropriate solution, a linear scaling is used to match the transfer function at 18 m/s to higher speeds. For example, to calibrate hot-film sensors in a swept-wing flow with freestream velocities near 25 m/s, the amplitude of the transfer function is multiplied by the ratio $(25 \text{ m/s})/(18 \text{ m/s}) = 1.39$. Improvements to prevent these types of corrections in future calibrations are presented in section 4.3.4.

Now that the transfer function is best-matched to the conditions of the experimental data, it must be placed on a uniform grid matching the frequency resolution of the Fourier transformed raw voltage hot-film data from the swept-wing experiment. The frequency resolution of the raw hot-film voltage data is simply the sample rate divided by the total number of samples. This grid matching is performed by interpolating to a uniform grid within the frequency range obtained in the calibration (i.e., 5 Hz to 3000 Hz). The lower range from 0 Hz to 5 Hz is estimated with a second-order polynomial and the higher range above 3000 Hz is linearly extrapolated to zero, thus mathematically modeling the roll-off.

The swept-wing data is then Fourier transformed and multiplied by the transfer function on a uniform grid. The result is then inverse Fourier transformed, thus completing the calibration. Figure 4.19 shows a typical time-history segment of the raw hot-film voltage data. The calibrated data, a time-history segment of surface shear stress, is then shown in figure 4.20. The data appears to be filtered in figure 4.20. This is a result of two independent effects. The physical space between the hot-wire and hot-film measurement locations acts as a spatial low-pass filter, an issue
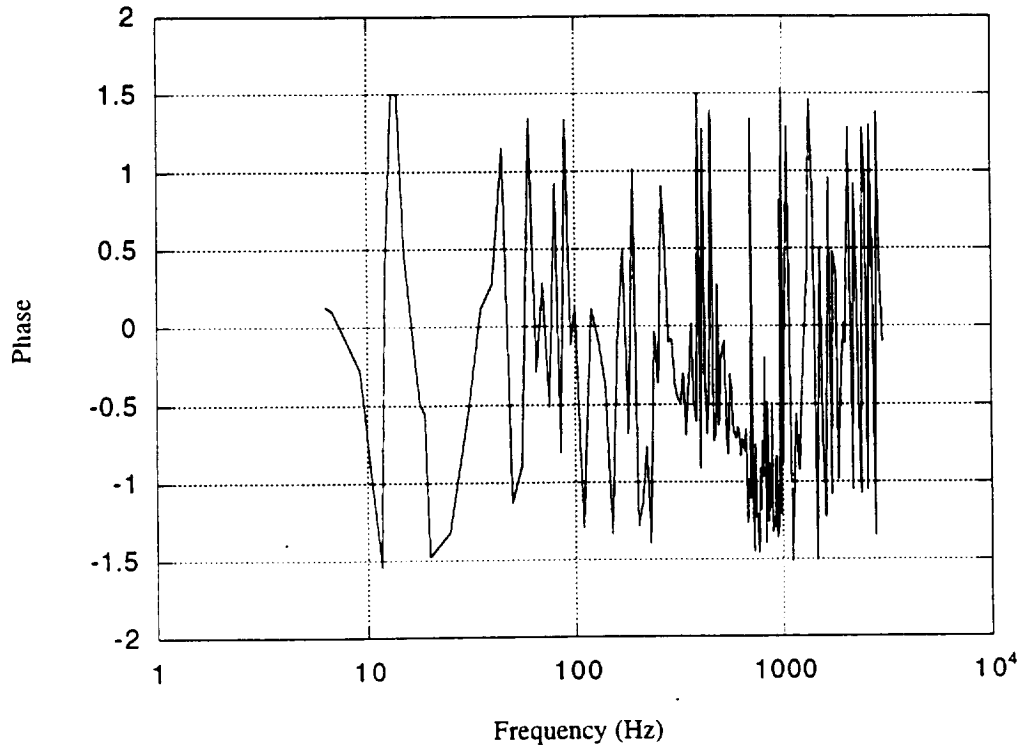
Figure 4.15: Raw phase data of transfer function at 18 m/s.
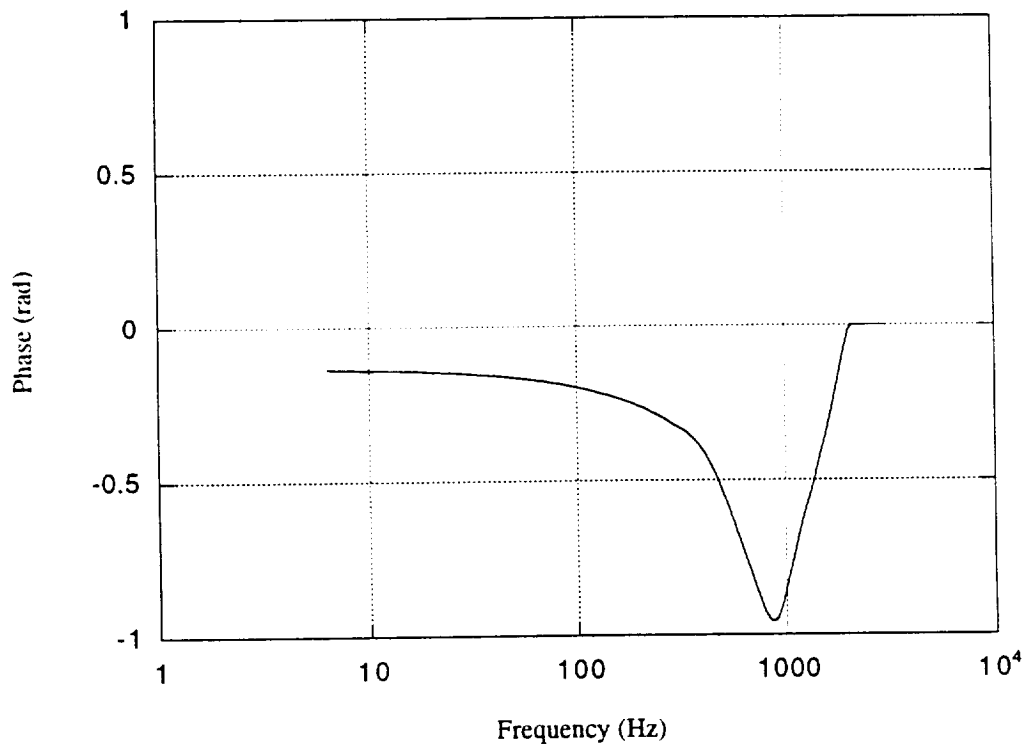
Figure 4.16: Curve fit and smoothing of transfer function phase data at 18 m/s.

69
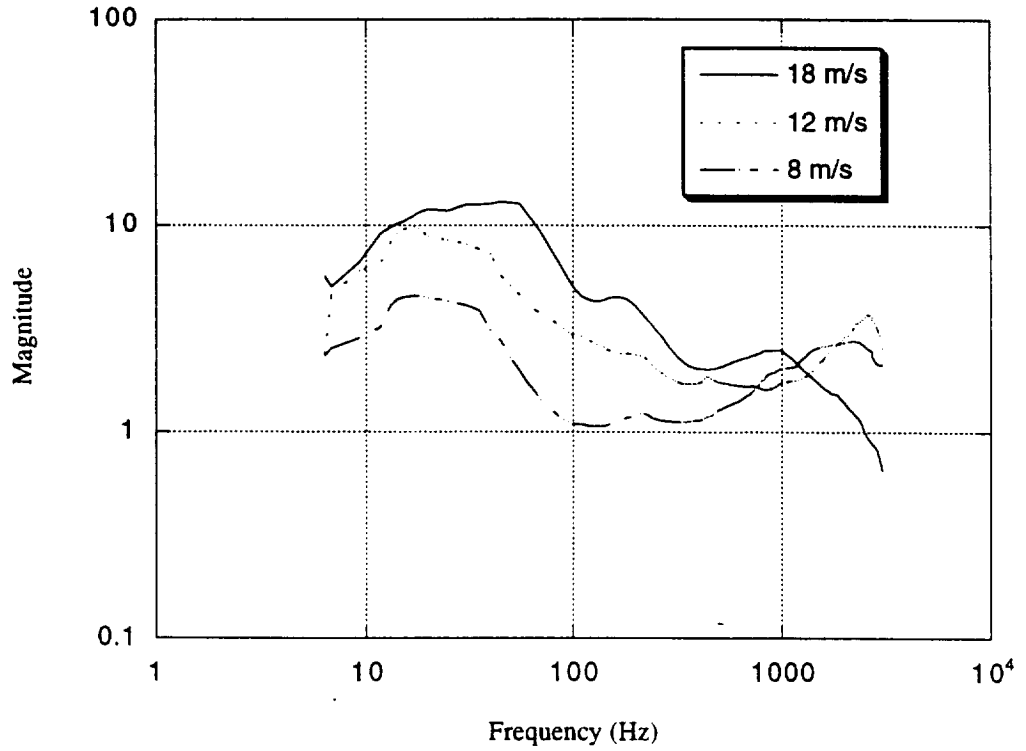
Figure 4.17: Transfer function magnitude comparison of three calibration velocities.
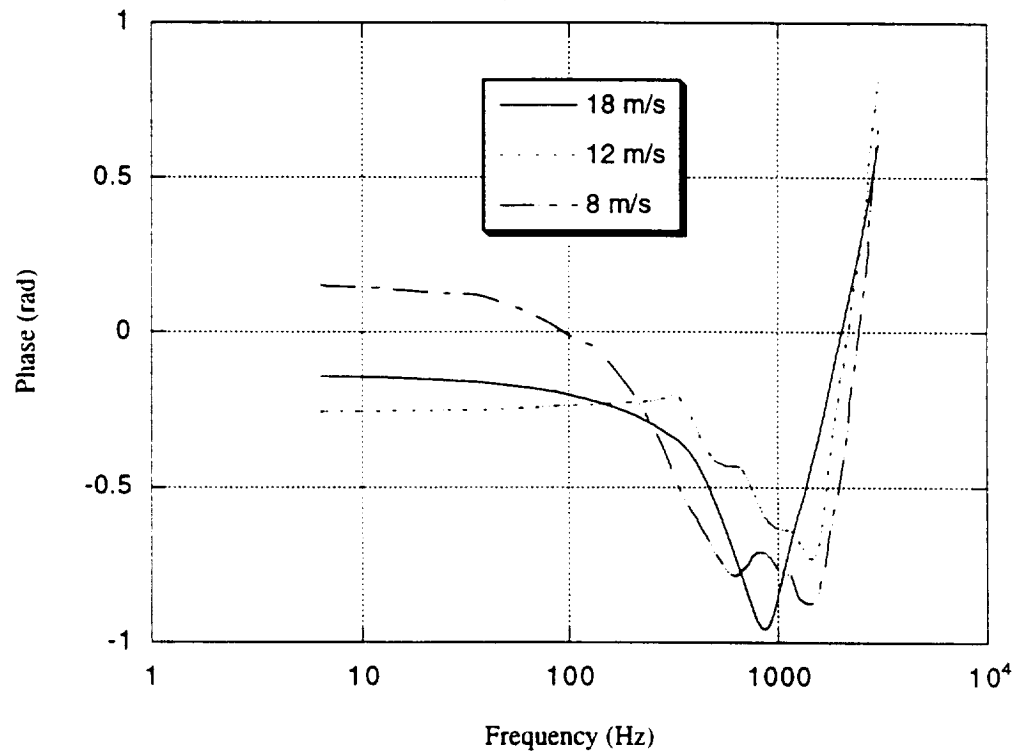
Figure 4.18: Transfer function phase comparison of three calibration velocities.
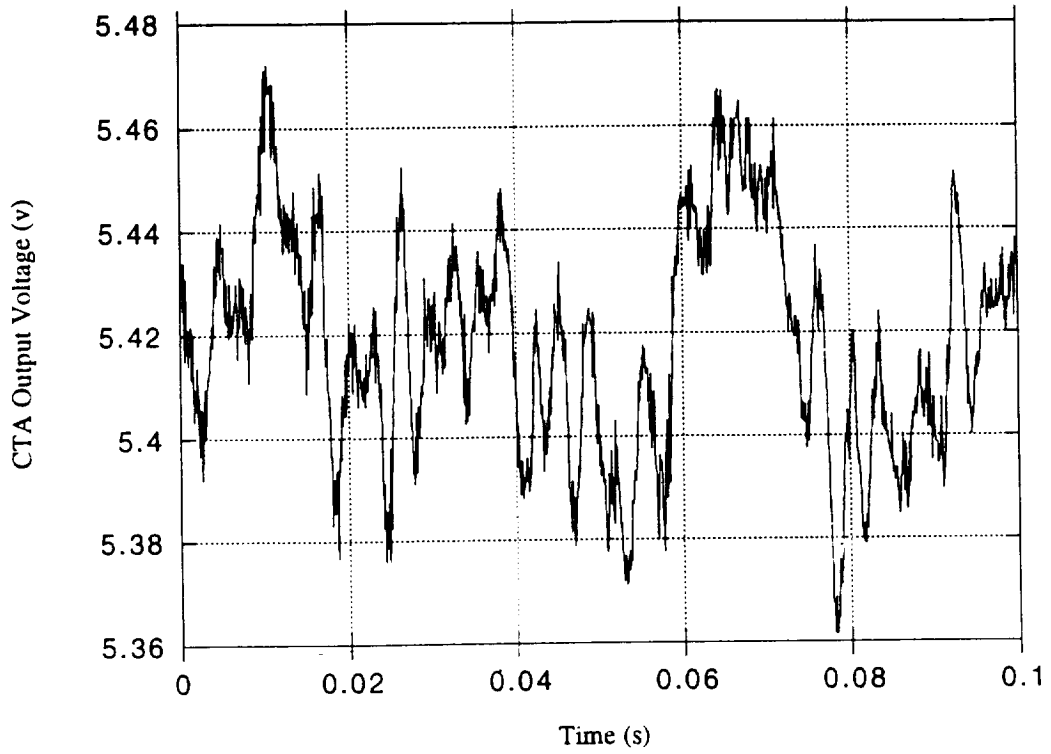
Figure 4.19: Typical raw hot-film voltage time history.
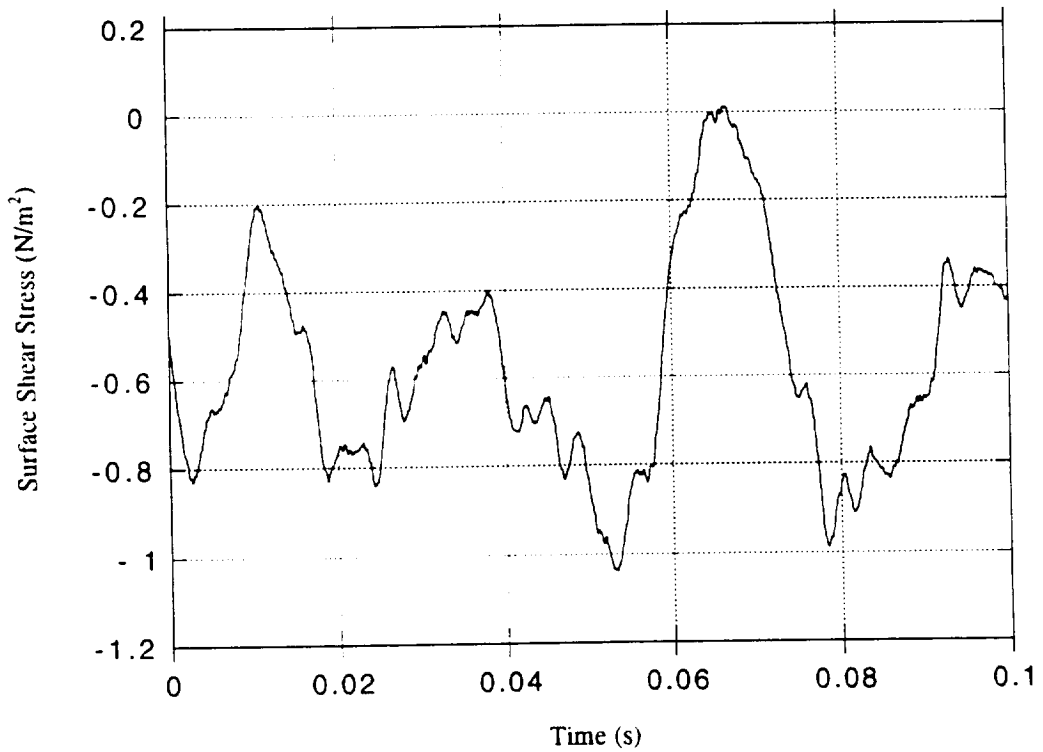
Figure 4.20: Calibrated hot-film surface shear-stress time history.

among spatial measurements (Glauser and George 1992). The effect arises from using a transfer function derived from one spatial location and applying it to data acquired at another spatial location. Also, higher frequency content above the linear extrapolation to zero from 3000 Hz is essentially filtered since their values are zero. These two effects do filter out some smaller events in the data but the calibration in general maintains a very descriptive signal of the raw voltage data.

4.3.4 Proposed Improvements

Thus, a few problems arise in this calibration technique, but given the circumstances at hand, it is a decent first approximation to a very difficult calibration problem. It has provided insightful evidence that with proper precautions and certain improvements, this technique may in fact provide a suitable calibration for surface-mounted hot-film sensors.

The results and observations throughout this first attempt at a dynamic calibration of hot-film sensors have allowed for an improved calibration technique to be developed. The following calibration technique is proposed to occur on the actual swept-wing model to be used in the experimental investigation. As stated in section 3.3.1, at small positive angles of attack, the swept-wing boundary layer is dominated by the streamwise instability in the form of T-S waves (Dagenhart 1992). The crossflow modes remain but are significantly weaker than those produced at small negative angles of attack. Therefore, by changing the angle of attack of the wing to create a T-S-dominated boundary layer, one may feasibly duplicate the calibration procedure explained above for the flat plate directly on the sensors to be used in the actual experiment.

Also, the full range of speeds needed is obtainable, but only for experiments in the laminar flow regime since the calibration technique cannot be performed aft of the transition front and the sensors cannot be moved once mounted. Appropriate Reynolds-number scaling techniques may be used for measurements in turbulent and transitional flow regimes. This would require a more detailed investigation into the speed dependence of the transfer function and hopefully result in an appropriate mathematical model to be used for scaling the calibration to higher speeds.

The other problem associated with the current calibration is the lack of averaging which is easily corrected for future calibrations on the swept-wing. The swept-wing flow at the ASU Unsteady Wind Tunnel is extremely repeatable thus allowing for several repeatable calibration runs. Averaging each frequency data point on the transfer function should resolve the data to a form similar to that in the curve-fitted data presented in section 4.3.3 and to that of Eaton (1995).

CHAPTER 5

Experiments

Several forms of measurement are used in the current experiment including flow visualization and anemometry techniques which employ the instrumentation discussed in chapter 4. This chapter discusses all of the measurements taken on the swept-wing for the current investigation. They include flow visualizations of the surface shear stress, single hot-wire mean-velocity boundary-layer scans, cross-wire correlation measurements of two velocity components and several surface shear-stress measurements via hot-film anemometry techniques. Some of the surface shear-stress data is acquired simultaneously with the cross-wire measurements for evolutionary comparisons. Not all of the measurements are used in the analysis portion of this work due to the large quantities of data acquired but are documented here for reference. These measurements are reserved for future continuing analyses.

5.1 Experimental Conditions

Each of the measurements discussed in detail below are acquired at the same environmental conditions for construction of the appropriate statistics needed for the correlation analysis techniques. This also allows for direct comparison of specific measurements by keeping the appropriate governing flow conditions as constant as possible. The ASU Unsteady Wind Tunnel has the ability to maintain a constant Reynolds number via the control systems discussed in chapter 3. This control feature is used to keep the chord-based, freestream Reynolds number within the test section set at 2.4×10^6 resulting in freestream velocities on the order of 25 m/s with the current wing's chord

length of 1.83 m. All of the experiments are performed with the wing at an angle of attack of -4° to produce a crossflow-dominated boundary layer (as discussed in section 3.3.1). Also, the tunnel is typically pre-heated during calibrations of the wire sensors each day, therefore reducing the effects of temperature differences. All of the experiments are performed with the 6 μm roughness dots placed at $x/c = 0.023$, spaced either 12 mm or 36 mm apart for reasons discussed in section 3.3.3. The sections which discuss the flow visualization technique and the mean-velocity boundary-layer scans articulate the effects of using the artificial roughness elements.

5.2 Surface Flow Visualizations

To properly design an experiment on the swept wing, one must be familiar with the general flow patterns. A clear way of obtaining this information is through flow visualization. A flow-visualization technique has been developed over the years at the ASU Unsteady Wind Tunnel that does not require flow seeding or mar the model surface. This surface flow-visualization technique uses naphthalene which sublimes at a rate proportional to shear stress at room temperature. Before applying the naphthalene to the wing surface it is dissolved in 1,1,1-trichloroethane. The saturated solution is then sprayed onto the model surface with a compressed-air sprayer. The solvent quickly evaporates and leaves a thin layer of naphthalene on the surface. In order to avoid leading-edge contamination, special care is taken to only spray the solvent aft of $x/c = 0.20$, well beyond the point where surface roughness affects the crossflow instability (Radeztsky et al. 1993a).

The tunnel is then brought to the desired operational speed. The naphthalene quickly sublimes in regions of high surface shear stress, but remains on the surface within regions of low shear. The resulting pattern for a Reynolds number of 2.4×10^6, the current experiments' operational speed, is shown in figure 5.1. A spanwise alternating pattern of streaks extends downstream until the boundary layer transitions where the shear becomes very high and sublimes the naphthalene in the entire turbulent regime. The technique is very useful for determining where the transition front is located for different Reynolds numbers, a required piece of information for determining sensor placement. The technique is also useful for visualizing the "foot-print" of the
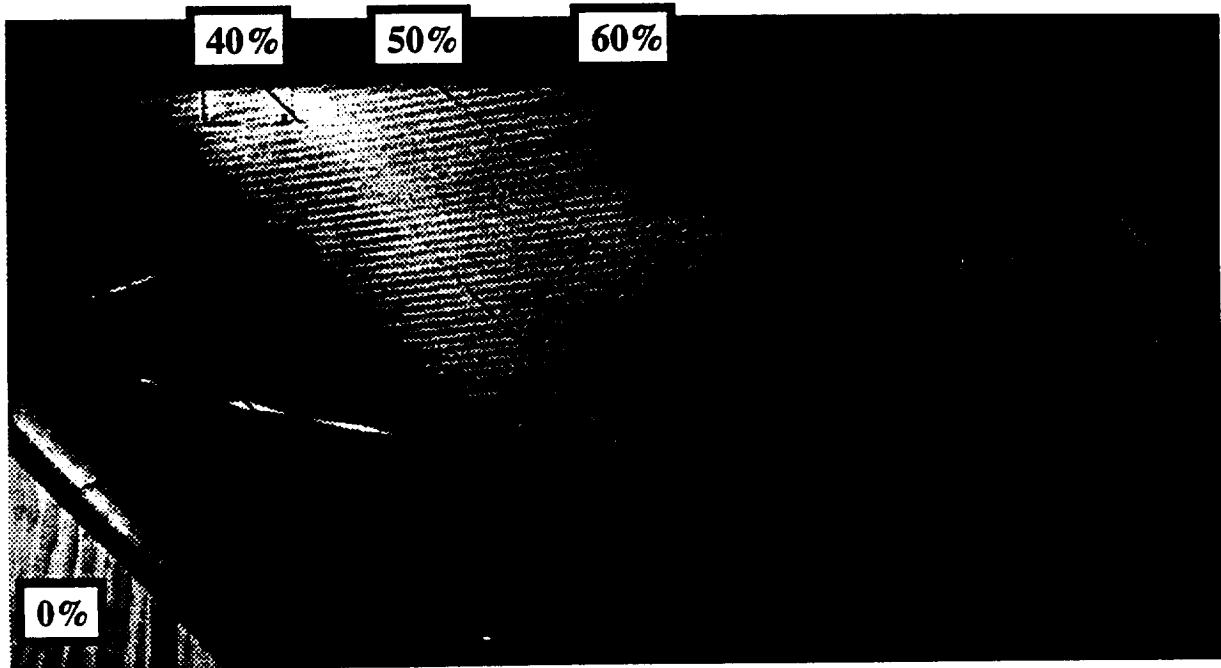
Figure 5.1: Naphthalene surface flow visualization of the swept-wing flow at $Re_c = 2.4 \times 10^6$ with 6 μm roughness elements spaced 12 mm in span at $x/c = 0.023$.

crossflow vortices in the laminar region of the boundary layer. A modulating surface shear-stress pattern, shown in figure 5.1, emerges due to the translation of low- and high-momentum fluid within the boundary layer.

Figure 5.1 shows the transition front starting near $x/c = 0.52$ for a Reynolds number of 2.4×10^6 and verifies the effect of the surface roughness elements in forcing the crossflow-vortex spanwise wavelength to approximately 12 mm. The technique may also be used to determine if surface-mounted sensors, such as hot-film sheets, disrupt the flow provided the sensors used will not be damaged by the spraying of the naphthalene solution. Any flow disturbance will alter the modulated surface shear-stress pattern and generally create high-shear regions immediately down-stream due to the turbulence created by the intrusiveness of the sensors. This test, shown in figure 5.2, is performed for the present experiment to verify that no flow disturbance is caused by the hot-film sheets in the regions to be measured. The crossflow pattern is unaffected by the presence of the hot-film sheets in these regions. All of the naphthalene sublimes just aft of the instrumenta-
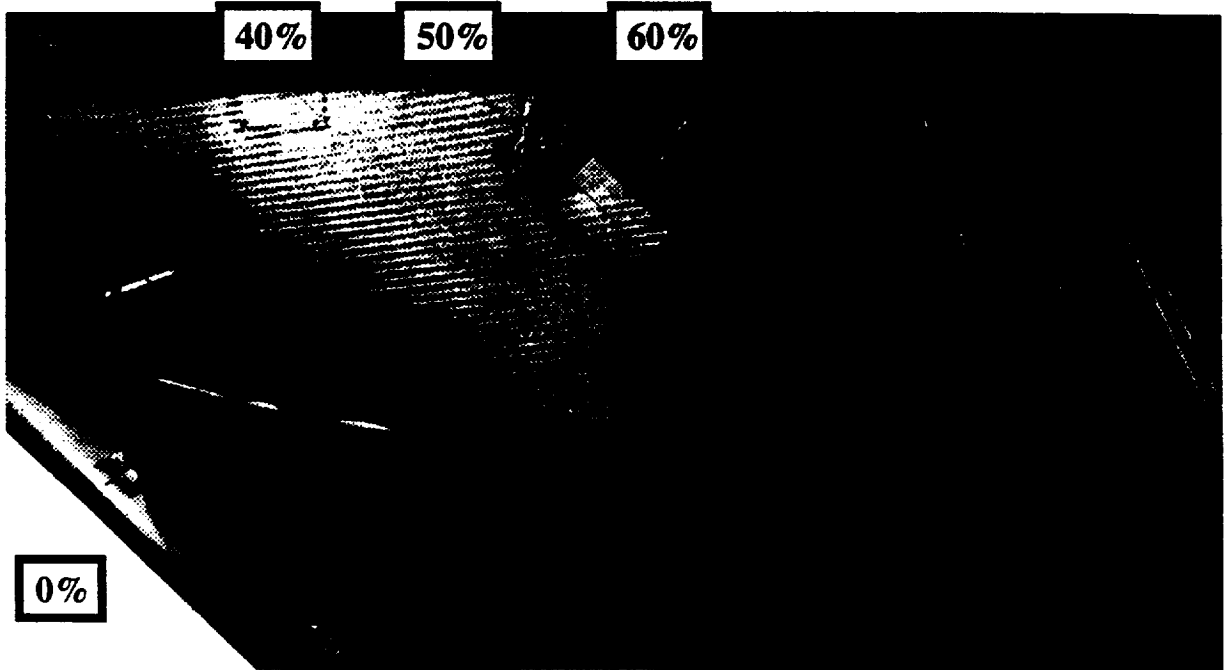
Figure 5.2: Naphthalene surface flow visualization checking hot-film sheet intrusiveness at $Re_c = 2.4 \times 10^6$ with 6 μm roughness elements spaced 12 mm in span at $x/c = 0.023$.

tion cables taped to the wing surface well above the measurement areas. However, the cables are placed far enough from the actual sensors that the crossflow vortices remain undisturbed near the measurement sites.

More detailed surface flow-visualization results for this wing at various flow conditions is documented in Dagenhart (1992). These studies show the transition front resulting from the natural surface roughness of the leading edge, i.e., the visualization is performed with no roughness elements placed on the wing. The natural transition front is significantly less uniform than that with the 12 mm spacing of roughness elements near the leading edge. In fact, the transition front varies so radically in span that it actually starts near $x/c = 0.48$ at one span location and starts at $x/c = 0.70$ at another span position for $Re_c = 2.4 \times 10^6$ (Dagenhart 1992). This drastic non-uniformity makes measurements and interpretation of results significantly more difficult and somewhat subjective. Thus, using the roughness elements to force the crossflow vortices into an "organized" pattern creating a distinct uniformity in span alleviates this complexity. The transition

front, best illustrated in figure 5.1, roughly ranges from $x/(c) = 0.52$ chord to $x/c = 0.57$ chord throughout the entire span when the roughness elements are used. This mean-flow uniformity becomes even more apparent through observation of the mean-velocity boundary-layer scans discussed in the next section.

5.3 Single Hot-Wire Boundary-Layer Scans

5.3.1 Hot-Wire Scanning Technique

A hot-wire anemometry technique is used extensively by Dagenhart (1992), Radeztsky (1994) and Reibert (1996a) to quantify the stationary crossflow disturbance amplitude by measuring spatial variations in the mean boundary-layer velocity. Wall-normal hot-wire scans progressing from just outside the boundary layer to very close to the surface which are taken at multiple span locations provide a detailed two-dimensional map of the spanwise evolution of the mean streamwise velocity, i.e., the spatial evolution of the time-averaged total velocity ($\bar{u} = \bar{U} + u'$) in the y_s-z_s plane of the swept coordinate system (refer to section 2.1.1 for the defined notation). Note the time averaging removes only the temporal dependence, effectively averaging out any effects from travelling waves. Spatial disturbances still remain.

A typical map, such as those in figures 5.3 and 5.4 (see section 5.3.3), includes 100 boundary-layer profiles taken at constant x/c with each scan separated by 1 mm in span. Each individual scan provides a single boundary-layer velocity profile with very fine resolution in the wall-normal direction.

Before the scans are acquired, the boundary-layer probe (positioned at the end of the instrumentation sting as shown in figure 3.2) is adjusted for local curvature effects and is properly aligned to measure the streamwise velocity. The probe is rotated such that both of the probe's tines are equidistant from the wing surface to prevent spatial averaging of the boundary-layer profile. The probe is then moved to just outside the edge of the boundary layer. This reference point is then acquired for 2 seconds at 1 kHz simultaneously with the freestream probe (also shown in figure 3.2) which resides in the external flow well above the boundary layer. The ratio of the mean boundary-layer edge velocity to the freestream velocity ($\bar{U}_e/U_\infty$) is then computed. The probes

are then stepped towards the model surface, acquiring the mean velocities from both wires at each wall-normal location. The mean boundary-layer velocity (effectively $\bar{\bar{u}}$) is normalized by the edge velocity $\bar{U}_e$ at each spatial position. The velocity $\bar{U}_e$ is computed at every spatial location by scaling the freestream hot-wire mean velocity by the ratio obtained at the reference point at the boundary-layer edge, i.e.,

$$\bar{U}_e = \bar{U}_{FS}\left(\frac{\bar{U}_e}{\bar{U}_\infty}\right)_{ref} \tag{5.1}$$

where the subscript FS denotes the freestream hot wire and the subscript ref denotes the data taken at the reference point. This normalization is necessary to account for any changes in the freestream velocity, usually due to tunnel heating effects. As the scan progresses in the wall-normal direction, the step size is scaled with $\bar{\bar{u}}/\bar{U}_e$ to provide finer resolution closer to the surface.

When the velocity ratio $\bar{\bar{u}}/\bar{U}_e$ reaches a predetermined threshold (usually near 0.15), the profile scan is terminated and the probes are relocated to the boundary-layer edge at the next span location. A new reference ratio is obtained and the procedure is repeated until all the desired profiles are obtained. After the entire scanning procedure is completed, the location of the surface is determined by extrapolating each profile to zero velocity. The slight pressure-induced curvature in the near-wall region of each velocity profile is ignored and fitted linearly to the zero velocity point from the last data point acquired in the experiment.

5.3.2 Usefulness of Measurements

The single hot-wire measurements presented here were taken by Reibert et al. (1996) and are documented in detail by Reibert (1996a). The data focuses on the spatial evolution of the crossflow instability in the spanwise and chordwise directions which provides a detailed map of the mean velocity distribution along the wing. Particular to the current experiment, these "flow maps" are used to identify the effects of using the 6-μm, 12-mm-spaced (denoted 6:12 throughout) artificial roughness elements and to determine the appropriate placement of the hot-film sensor sheets and the spanwise position grid for the cross-wire measurements. The mean velocity contours are later used to describe the location of the cross-wire measurements relative to significant events in the
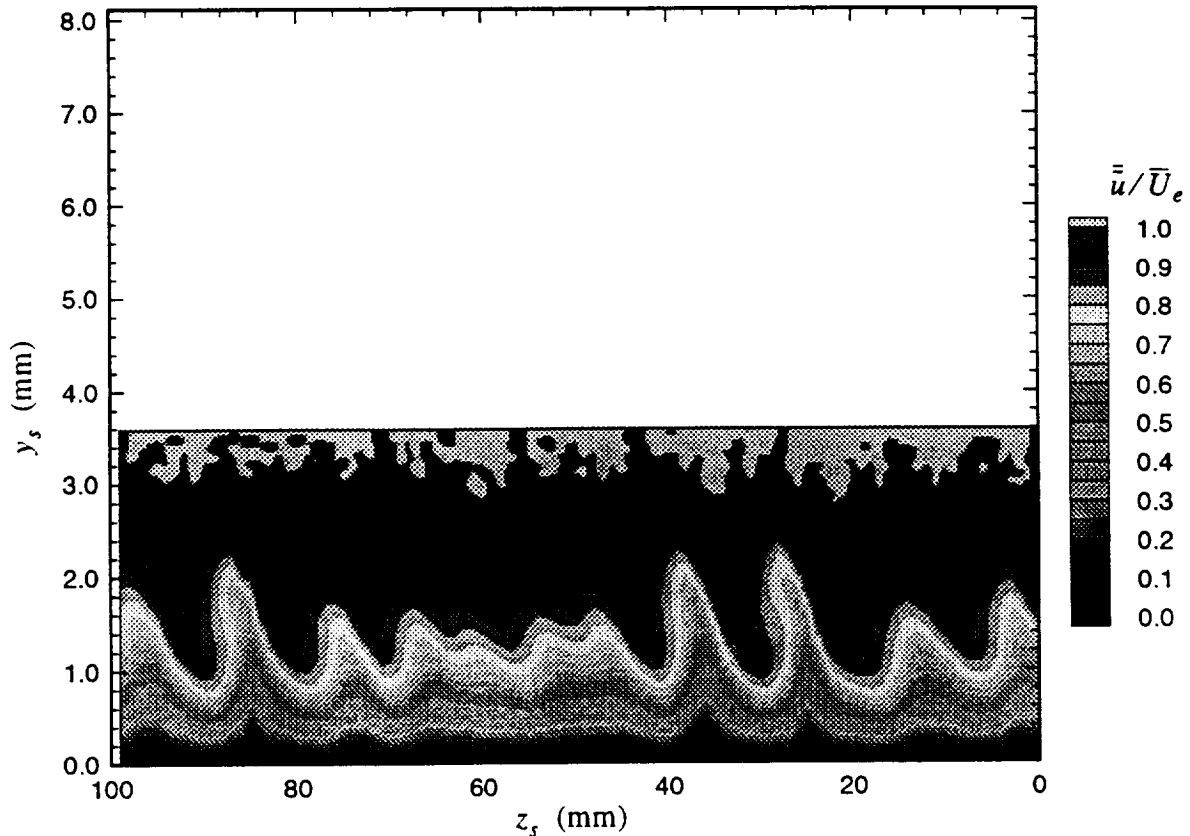
Figure 5.3: Streamwise velocity contours at $x/c = 0.45$, $Re_c = 3.0 \times 10^6$ with no artificial roughness. Figure adapted from Reibert (1996a).

laminar region of the boundary-layer flow. They also provide insight to the structure of the internal flow above the hot-film sensors. This is invaluable information in relating the surface shear-stress events to events in the internal flow.

5.3.3 Surface Roughness Effects

Figure 5.3 is a contour plot of the normalized mean boundary-layer velocity acquired at $x/c = 0.45$ for $Re_c = 3.0 \times 10^6$ with no artificial roughness applied to the surface of the wing. The plot shows the spatial evolution of the boundary layer in the y_s-z_s plane with the y_s axis magnified by a factor of 10 with respect to the z_s axis in order to provide adequate detail. The flow in figure 5.3 and all subsequent mean-velocity contours is such that the observer is looking

upstream into the oncoming internal flow which contains the right-handed rotation of the stationary vortices. An increasing span value corresponds to a spatial progression in the positive z_s direction where $z_s = 0$ mm denotes the start of the scan, not the test-section ceiling. The wave-like behavior of the contours represents the integrated effect of the weak stationary vortices on the streamwise velocity. The vortices are actually co-rotating disturbances weakly manifesting themselves in the v' and w' disturbances of the global coordinate system.

The nonuniformity of the wave-like structures is a direct result of the natural surface roughness of the wing. Given the wing's root-mean-square surface roughness of 0.12 μm (Reibert 1996a), this demonstrates the extreme sensitivity of the boundary layer to submicron surface anomalies near the leading edge. Clearly, highly nonlinear interaction of the various modes resulting from these roughness-induced initial conditions dominates the flow field. However, despite this nonuniformity of the vortices, a dominant stationary crossflow-vortex wavelength of approximately 12 mm still emerges which is predicted as the most amplified stationary wavelength according to linear theory (Reibert 1996a). Two of these dominant structures exist between $z_s = 20$ and $z_s = 40$ mm in figure 5.3.

Thus for the current experiment, the flow is forced to adhere to the dominant wavelength by placing the 6:12 artificial roughness elements near the attachment line at $x/c = 0.023$. The same contour of the time-averaged streamwise velocity shown in figure 5.3 without any artificial roughness is shown in figure 5.4 with artificial roughness elements spaced at the dominant crossflow wavelength of 12 mm. (The Reynolds number was lowered for the scan with artificial roughness to accommodate the increased strength of the disturbances.) The flow field remarkably becomes "organized" and very repeatable in span by overriding the natural roughness with a large enough artificial roughness. (The thickness of the artificial roughness must be large relative to the natural surface roughness but small enough to not trip the boundary layer resulting in premature transition.) This flow organization provides the experimentalist with the distinct advantage of measuring within a uniform, periodic distribution of the stationary vortices.

Surface shear-stress measurements are also taken with the 6-μm artificial roughness elements spaced 36 mm at the same x/c location near the attachment line. This allows other modes to enter the flow field which are actually harmonics of the dominant crossflow vortex wavelength

Figure 5.4: Streamwise velocity contours at $x/c = 0.45$, $Re_c = 2.4 \times 10^6$ with 6:12 artificial roughness. Figure adapted from Reibert (1996a).

(Reibert 199a). The mean streamwise velocity contour at $x/c = 0.45$ with 6:36 artificial roughness is shown in figure 5.5. The extra modes within the disturbances are clearly demonstrated by the periodic features of the mean flow. The repetition in span (every 36 mm) now contains four distinct events, a dominant rollover structure with a 12-mm wavelength (located between 20 mm and 32 mm in figure 5.5), a lower amplitude vortex with a 9-mm wavelength closely packed to the dominant structure (located between 31 mm and 40 mm), a very small structure with low amplitude with an approximate wavelength of 6 mm (located between 41 mm and 47 mm) and a slightly larger structure with a wavelength of 9 mm (located between 47 mm and 56 mm).

With the flow forced to specific modes, one avoids the ambiguity of selecting a single vortex to study and the difficulty in tracking that same vortex at different chord locations. Also, since the experiment potentially includes an infinite number of modes in the natural state, each excited by
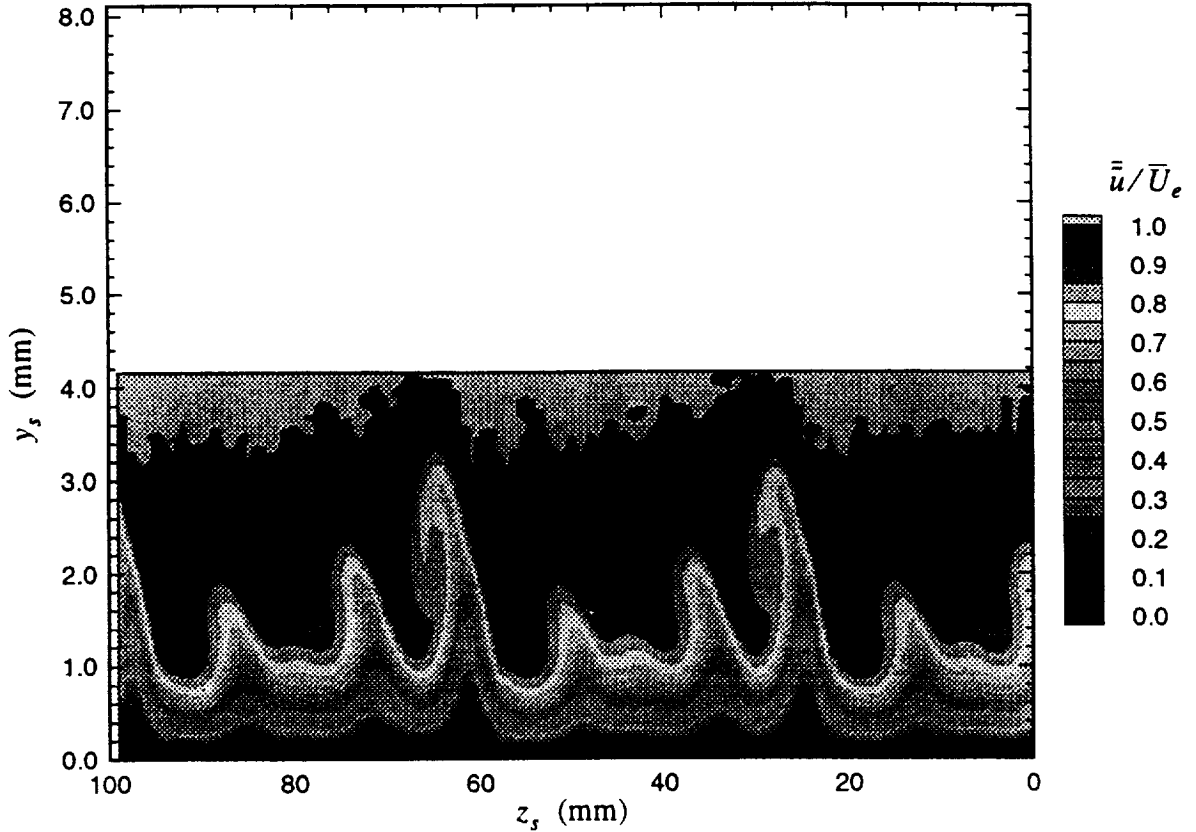
Figure 5.5: Streamwise velocity contours at $x/c = 0.45$, $Re_c = 2.4 \times 10^6$ with 6:36 artificial roughness. Figure adapted from Reibert (1996a).

the random natural surface roughness, comparison to theoretical and computation studies becomes extremely complex. Thus, by forcing the flow to the dominant mode, computations may model the experiment with a reasonable, finite number of modes. A comparison of the nonlinear growth of the crossflow instability which takes advantage of this forcing technique has already been performed for this airfoil by Reibert (1996a) (who provides the experimental data) and Haynes (1996) (who provides the computational data). The tremendous agreement of their results is only possible by eliminating the random effect of the natural surface roughness.

For the present experiment, the forced flow field creates a distinct advantage in the multi-point correlation analysis. In particular, the proper orthogonal decomposition (POD) results reveal the domination of the forced crossflow-vortex wavelength, even in the fluctuating-quantity solution. Without the uniformity of the vortices in the mean flow, the analyst has to deal with statisti-

cal data based on many ambiguities and may perhaps introduce subjectivity in the interpretation of the results. By isolating the dominant mode through the use of artificial roughness, the analyst now deals with a flow with fixed spectral content and recognizes dominant features in the flow field which may be sought in the analysis.

5.3.4 Vortex Structure and Evolution

Figure 5.6 shows an isolated stationary vortex on a 1:1 scale to demonstrate the rollover structure in the streamwise velocity previously discussed in chapter 2. The integrated effect of the v' and w' fluctuations cause this transport of low- and high-momentum fluid within the boundary layer. As the amplitude of the disturbances grows, the asymmetry of the co-rotating vortices distorts this momentum transfer and gives rise to the rollover structure. The very weak v' and w' disturbances
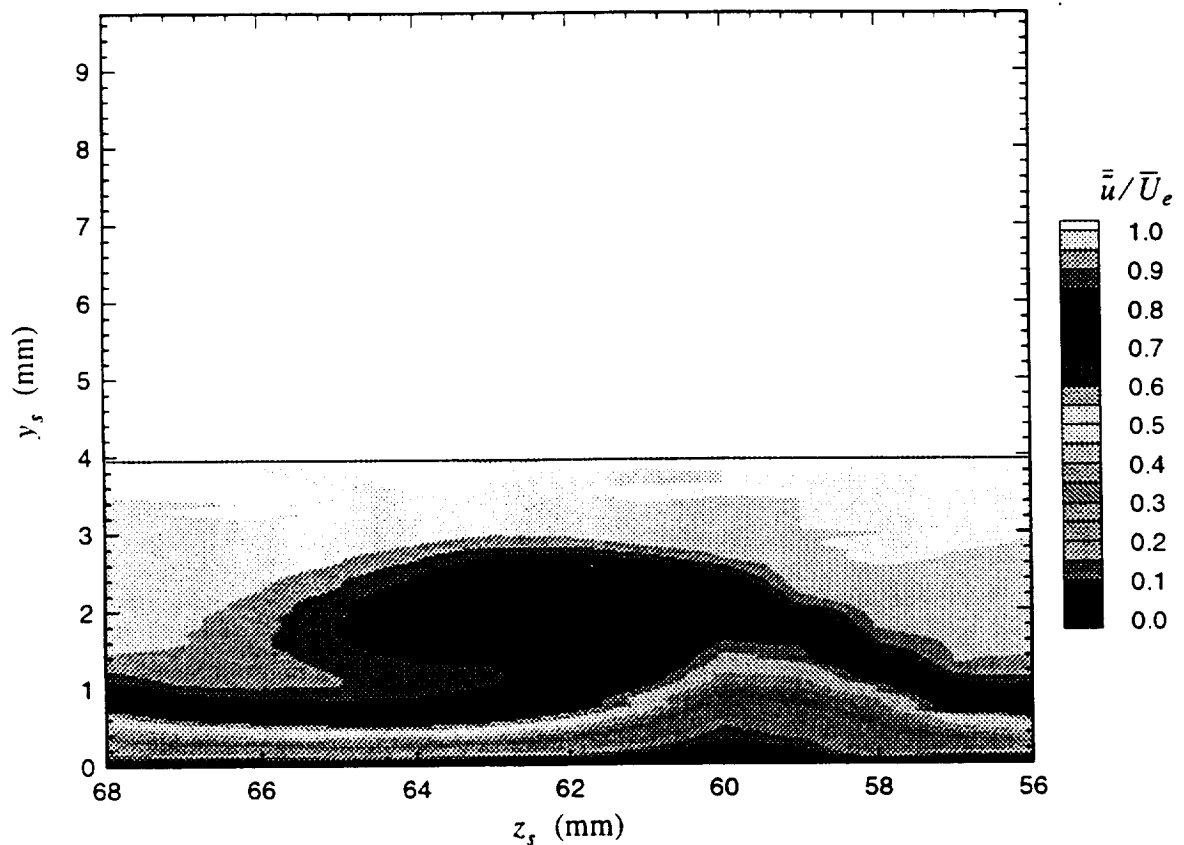
Figure 5.6: Single stationary crossflow vortex taken at $x/c = 0.50$, $Re_c = 3.0 \times 10^6$ with no artificial roughness, plotted on a 1:1 scale.

produce such a significant effect on the streamwise flow because the vortices are indeed stationary and closely aligned to the potential flow. A schematic of the weak v' and w' motion in the swept coordinate system is compared to the measured $\bar{u}/\bar{U}_e$ velocity contours in figures 5.7, 5.8 and 5.9 for two stationary vortices at $x/c = 0.20$, $x/c = 0.30$ and $x/c = 0.45$, respectively. The distortion of the u' disturbance develops so drastically further downstream because of the continuous presence of the vortices. The weak v' and w' disturbances operate on essentially the same streamwise fluid as the flow progresses downstream thus creating a significant physical effect. This continues until the integrated effect becomes critical and causes the flow to transition through the breakdown of these vortical structures (just aft of $x/c = 0.50$ for $Re_c = 2.4 \times 10^6$ with artificial roughness elements applied near the leading edge). Refer to Dagenhart (1992) and Reibert (1996a) for more discussion on the spatial evolution and growth rates of the mean velocities in the boundary layer of this swept wing at -4° angle of attack. Radeztsky (1994) investigates similar evolutions for the same wing at 0° angle of attack.
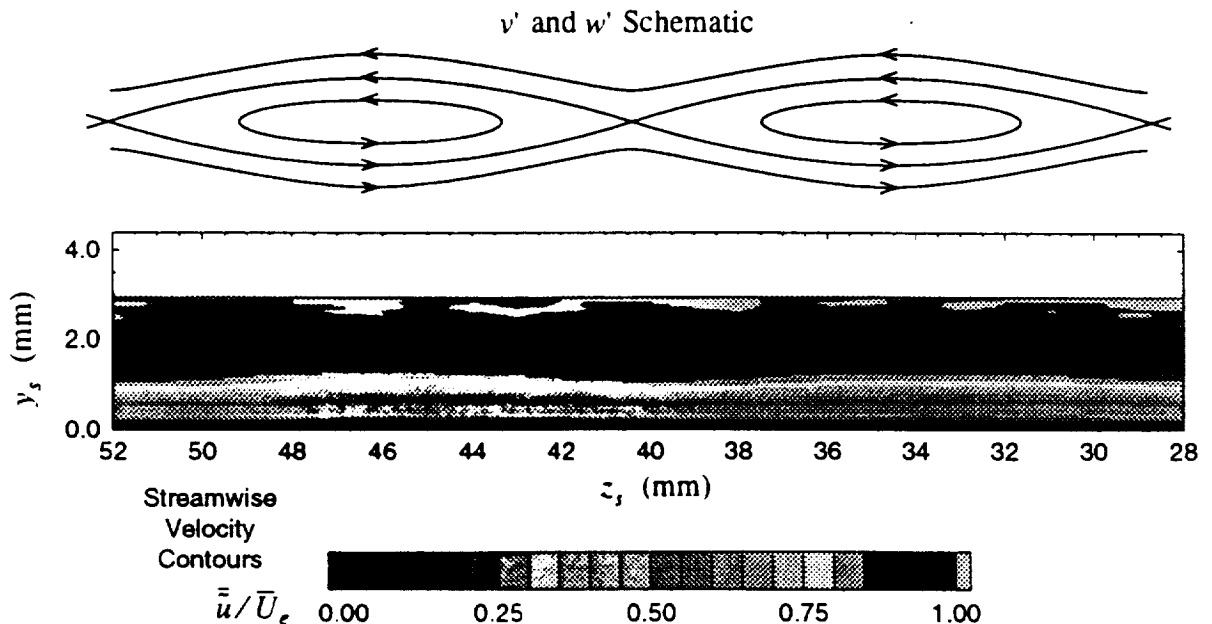
Figure 5.7: Effect of combined v' and w' disturbance motion on $\bar{u}/\bar{U}_e$ at $x/c = 0.20$, $Re_c = 2.4 \times 10^6$ with 6:12 artificial roughness. Figure adapted from Reibert (1996a).
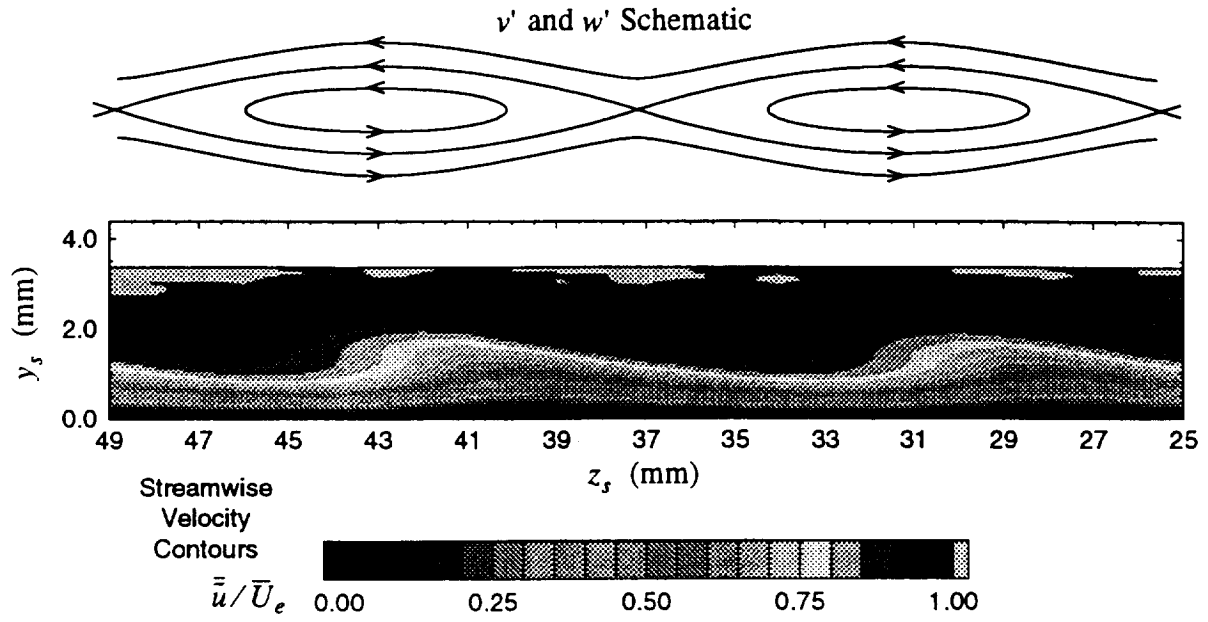
Figure 5.8: Effect of combined v' and w' disturbance motion on $\bar{\bar{u}}/\overline{U}_e$ at $x/c = 0.30$, $Re_c = 2.4 \times 10^6$ with 6:12 artificial roughness. Figure adapted from Reibert (1996a).
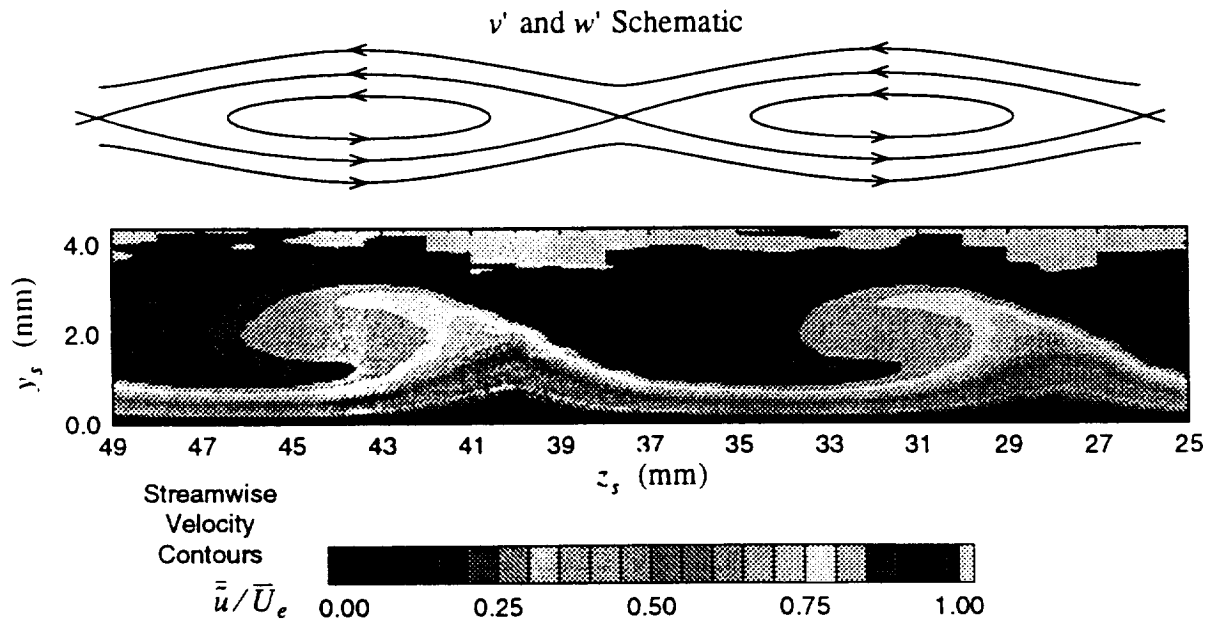
Figure 5.9: Effect of combined v' and w' disturbance motion on $\bar{\bar{u}}/\overline{U}_e$ at $x/c = 0.45$, $Re_c = 2.4 \times 10^6$ with 6:12 artificial roughness. Figure adapted from Reibert (1996a).

5.4 Surface Shear-Stress Measurements

Several surface shear-stress measurements are made in the present experiment using the various hot-film sheets described in section 4.1.3 which are calibrated through the method detailed in section 4.3. All data sets are acquired at a sample rate of 10 kHz for several blocks (usually 20) of various record lengths (usually 3 seconds). All hot-film sensors are wired to multiple-pin connectors for ease in switching between particular sensors from any of the hot-film sheets. All hot-film sensors are driven by the A. A. Labs anemometer system described in section 3.2.4. Figure 5.10 is a schematic illustrating the placement of all hot-film sheets used in the present experiment, three of which are pictured in the flow visualization of figure 5.3.

It should be noted that the streamwise sheet is mounted first. All data needed from this sheet alone is then acquired. The two crossflow sheets are then mounted to their respective locations
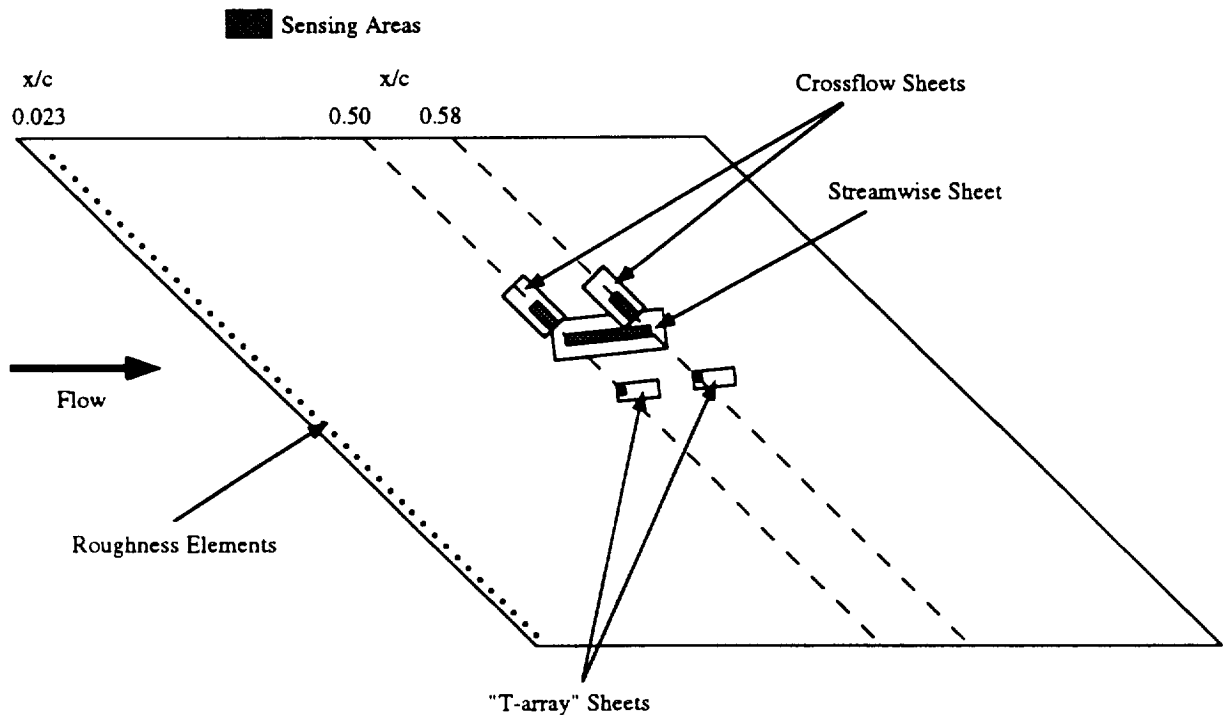
Figure 5.10: Schematic of hot-film sheet placement with artificial surface roughness elements.

and data is acquired from each crossflow sheet individually. Measurements are also collected from several sensors on all three sheets simultaneously. Then, finally, the "T-array" sheets are mounted to the wing and used to acquire the local two-component surface shear-stress data. This procedure is used to minimize flow disturbance from cable leads. Surface shear-stress measurements are also taken simultaneously with the cross-wire correlation measurements.

5.4.1 Streamwise Surface Shear-Stress Measurements

The streamwise sheet (illustrated in figure 4.4) is used over a range from $x/c = 0.49$ to approximately $x/c = 0.58$ (see figure 5.10) to measure the streamwise evolution of the surface shear stress through the transition front. The sheet is closely aligned parallel to the center line of the crossflow vortices visualized near $x/c = 0.50$ and therefore is specifically mounted to measure the spatio-temporal evolution of the surface shear stress predominantly progressing in the x_t direction. This alignment results in the hot-film sheet being angled approximately $-6°$ from the x direction.

As mentioned in section 5.3.3, tracking an individual vortex is often difficult, particularly for hot- or cross-wire probes. However, using a fixed hot-film sheet aligned in the predominant flow direction almost always guarantees a spatio-temporal measurement which captures a single vortex over at least a few chord locations provided the spacing and length of the sensors is appropriate for the flow field. It is certainly possible that a slight misalignment will result in tracking more than one vortex within the sensor range, but that traversing of the vortices will be recorded in the spatial data. Also, since 6:12 artificial roughness is used in all of the experiments, capturing more than one vortex across the range of sensors is still acceptable, especially since every vortex is reasonably of the same size and structure. However, for the current experiment, we are interested primarily with the active modes and mechanisms responsible for the breakdown of the crossflow vortices, not in tracking a particular vortex. Still, given the detailed mean-flow maps described in section 5.3 and the flow visualizations of section 5.2, we can be fairly confident that the hot-film sheet is appropriately aligned.

Figure 5.11 is a contour plot of the streamwise mean velocity acquired at $x/c = 0.50$ for $Re_c = 2.4 \times 10^6$ with 6:12 artificial surface roughness. The third sensor in the streamwise array is
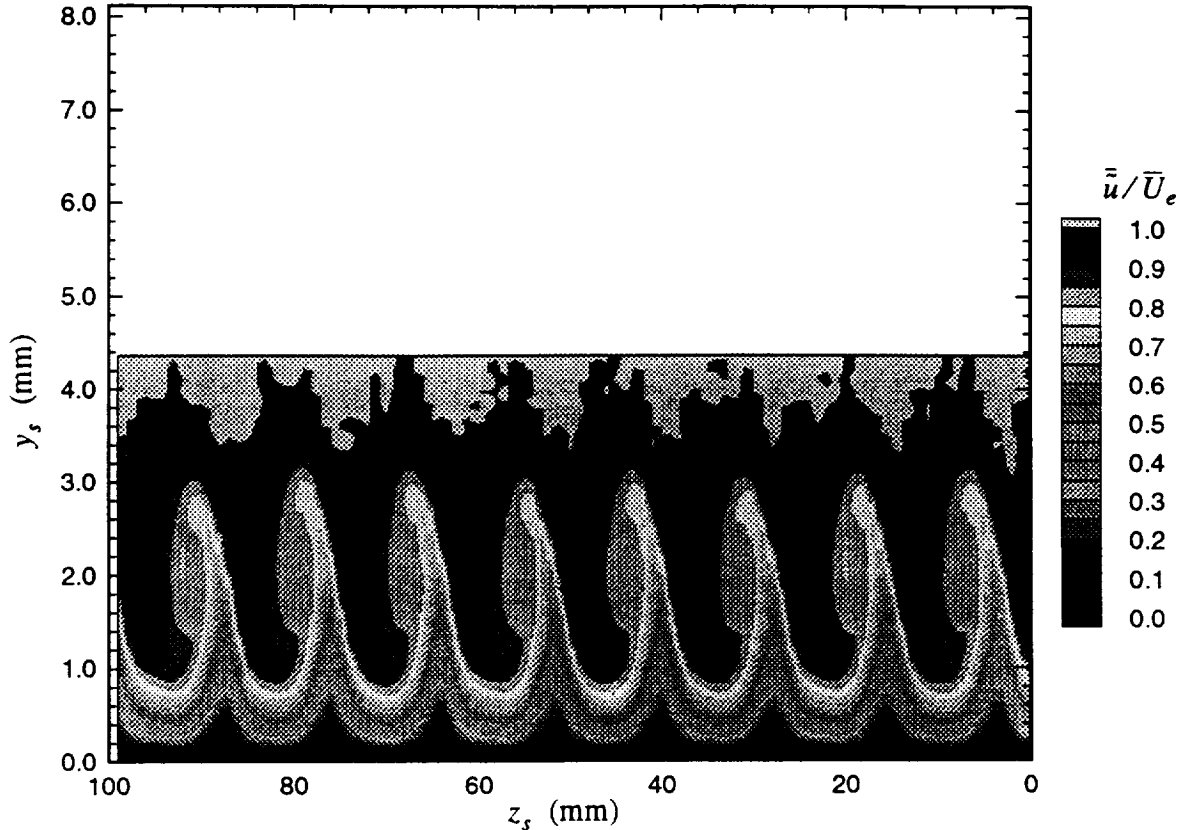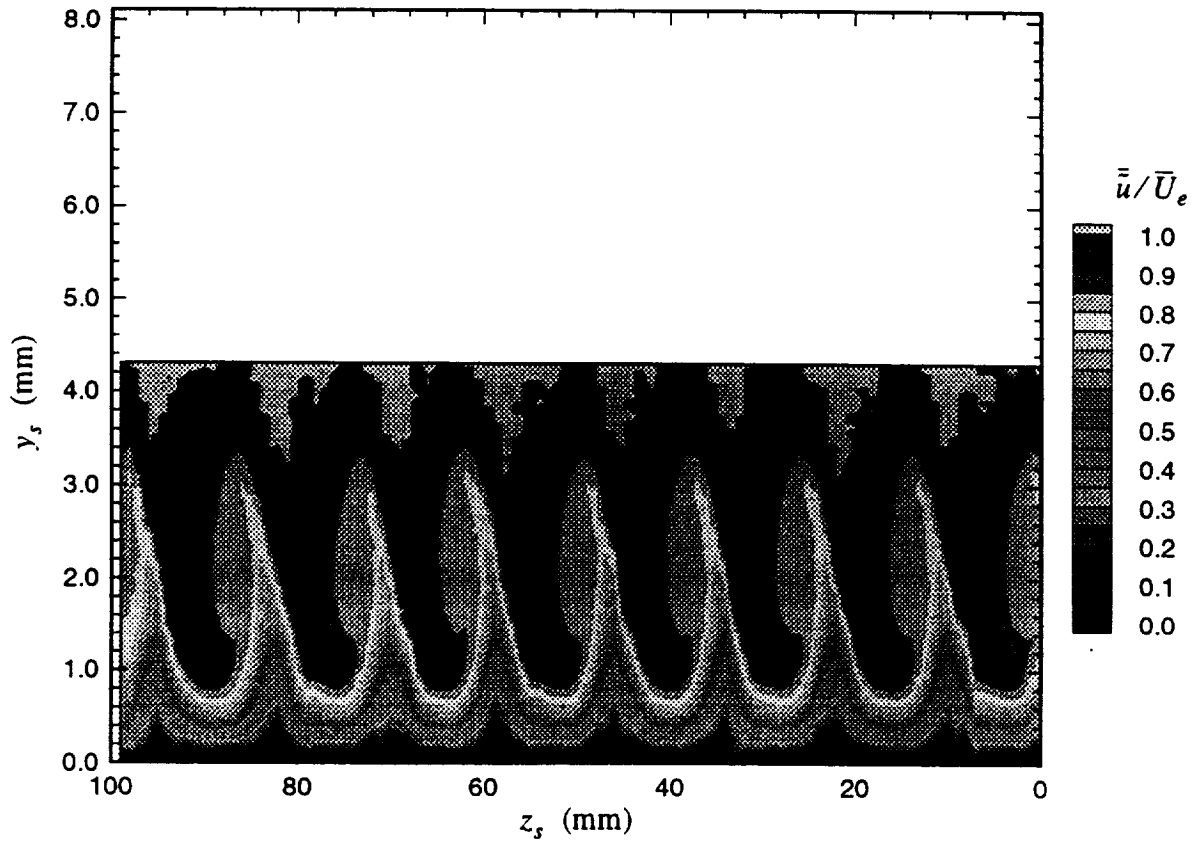
Figure 5.11: Streamwise velocity contours at $x/c = 0.50$, $Re_c = 2.4 \times 10^6$ with 6:12 artificial roughness.

placed at the precise location of 39 mm in figure 5.11. The sensors are aligned perpendicular to the center line of the vortex that resides between 29 mm and 41 mm. Thus, using the mean velocity boundary-layer scans to pin-point a single vortex and the surface flow visualization to mark the center line of that vortex, we can determine the appropriate alignment of the hot-film sheets.

One disadvantage to using the hot-film technology is the pseudo-permanent mounting technique. Once a sensor is destroyed by either burn-out or by being hit by a sizeable solid particle, it can no longer be used or replaced without removing the entire hot-film sheet. So, the experimentalist sometimes has to accept certain losses and make due with what data is available. In the present experiment, one sensor in the streamwise array near $x/c = 0.55$ (the 12th from the furthest upstream sensor) burned out. Thus, the data for the streamwise sheet consists of a total 15

sensors simultaneously sampled at 10 kHz for 10 blocks of 3 seconds each. The effects of the uneven spatial measurement grid are compensated in all of the analysis techniques which are dependent on the spacing between the sensors.

5.4.2 Crossflow Surface Shear-Stress Measurements

Crossflow hot-film sheets (shown in figure 4.3) are mounted at constant chord locations $x/c = 0.50$ and $x/c = 0.58$ such that the sensor elements (each parallel to one another) are perpendicular to their respective constant chord line as illustrated in figure 5.10. The sensing areas are placed close to the streamwise hot-film sheet sensing area so that the cable leads would not disturb the flow field near the sensors. The flow is confirmed to be undisturbed by the placement of the cable leads and sheets via the flow-visualization results in figure 5.3. The constant chord locations were chosen such that the transition front resides between the two crossflow hot-film sheets for the desired Reynolds number and that the sheets are mounted within the range of the traversing mechanism to allow for simultaneous hot- or cross-wire measurements.

The mean velocity contour plot shown in figure 5.11 provides a map typical of the mean flow above the hot-film sensors mounted at $x/c = 0.50$ in the laminar regime. The first sensor on the crossflow sheet at $x/c = 0.50$ resides precisely at the location 3 mm in figure 5.11. Unfortunately, the rest of the sensor array resides "to the right" of this location at 3 mm. This was necessary to accommodate the placement of all of the hot-film sheets. But because the 6:12 artificial roughness organizes the spanwise distribution so well, as long as the starting point of the sensor array is known, we can translate the usual mapping over to a corresponding portion of another vortex. For instance, the vortex position at 3 mm is nearly identical to that at 39 mm. So we can map the range of the sensor array to be roughly starting at location 39 mm and extending to 8 mm. Thus, the crossflow array ranges across approximately 2.5 crossflow vortices (based on the 12 mm forced wavelength and the contour map) starting at the rollover point (39 mm) of one vortex and ending near the center line of another (8 mm).

The other crossflow hot-film sheet is mounted downstream of the transition front in the turbulence regime at $x/c = 0.58$. It is aligned identically in the same manner as the other sheet with one exception. The flow visualization showed the center lines of the crossflow vortices to be angled approximately -6° from the x axis (before transition). Therefore, the first sensor on the

sheet in the turbulent regime is aligned on that -6° line to the first sensor on the sheet in the laminar regime, i.e., each corresponding sensor on the two sheets lies on a line -6° from the x axis. Thus, if the flow were completely laminar across both sensors, the same vortices would be captured by the two sensor arrays. By aligning the two sheets this way, we can see any spatial "deflections" caused by the transition process. This statement is based on the premise that the dominant large coherent structures in the turbulent flow field emerge from the strong vortex structure in the laminar regime. This point will be further discussed in light of the proper orthogonal decomposition results presented in chapter 8.

Not all of the crossflow sensors are used in the experiments. The linear stochastic estimation results of Chapman et al. (1994) show that a sensor spacing of up to 4 mm is adequate enough to resolve the spanwise structure of the crossflow vortices in the laminar regime. With this and the limitation of 16 anemometer channels for the hot films, only every other sensor is used in the experiments (starting with the very first sensor in the array closest to the streamwise sheet). All of the sensors used remained operational throughout the experiment for the sheet mounted at $x/c = 0.50$, however, four sensors were lost on the sheet in the turbulent regime (the 1st, 3rd, 11th and 21st from the start of the array closest to the streamwise hot-film sheet). Therefore, the crossflow surface shear-stress data at $x/c = 0.50$ consists of 16 channels simultaneously sampled at 10 kHz for 20 blocks of 3 seconds. The crossflow surface shear-stress data at $x/c = 0.58$ includes 12 channels simultaneously sampled at 10 kHz for 20 blocks of 3 seconds for each of the roughness cases (6:12 and 6:36).

Four sensors from each of the two crossflow sheets and eight sensors from the streamwise sheet are also sampled simultaneously to compare the entire measured field evolution. This experiment is designed with the use of linear stochastic estimation (LSE) in mind. LSE may be used to estimate an entire measured field from just a few sensors. Therefore, the entire field across the transition front may be estimated. This data set consists of 16 channels simultaneously sampled at 10 kHz for 20 blocks of 3 seconds for both roughness cases as well.

5.4.3 Two-Component Local Surface Shear-Stress Measurements

The local two-component surface shear stress is measured by two "T-array" hot-film sheets (shown in figure 4.5) mounted at constant chord locations $x/c = 0.50$ and $x/c = 0.58$. The

sheets are aligned such that the upper right corner and the lower left corner of the sensing area (as shown in figure 4.5) lie on the constant chord line as illustrated in figure 5.10. The appropriate alignment angles may then be computed to isolate the two components of local shear on the surface within the global or swept coordinate system. The sensors are so small that the entire sensing area may be considered relatively at the same chord location. Again, due to the limitations of only 16 anemometer channels, only certain sensors are used in the measurements simultaneously. Both data sets (6:12 and 6:36 artificial roughness cases) include 16 channels simultaneously sampled at 10 kHz for 20 blocks of 3 seconds for each chord location.

5.5 Two-Component Velocity Correlation Measurements

5.5.1 Cross-Wire Measurement Sites

Two-component velocity measurements are made within the internal flow of the boundary layer with the cross-wire probes (illustrated in figure 4.2) at the two constant chord locations $x/c = 0.50$ and $x/c = 0.58$. All cross-wire measurements are taken 3.0 mm directly above the crossflow hot-film sheets on a spanwise measurement grid that spatially corresponds to every fourth hot-film sensor as illustrated in figure 5.12. The height ($y_s = 3.0$ mm) of the cross-wires is the closest location to the surface obtainable given the size of the Auspex probes. The measurement site spacing of 4 mm is chosen as a compromise between satisfying the resolution criteria to resolve the large-scale flow structure (Chapman et al. 1994) and acquiring large amounts of data that result from such measurements. Only two cross-wire probes (requiring four anemometer channels) are used throughout these measurements. One is mounted directly to the surface of the wing, the other is mounted to the instrumentation sting (illustrated in figure 3.2) in the boundary-layer probe position with the probe axis fixed parallel to the test-section wall. This allows for one of the probes to be moved to various positions on the measurement grid, a necessity for correlation measurements (see section 5.5.2). Thirteen sensors from the crossflow hot-film sheet directly below the cross-wire measurement sites are sampled simultaneously with the cross-wires to later develop an estimate of the two instantaneous flow fields simultaneously. The theory behind this technique will be explained in chapter 6 with results shown in chapter 8.

91
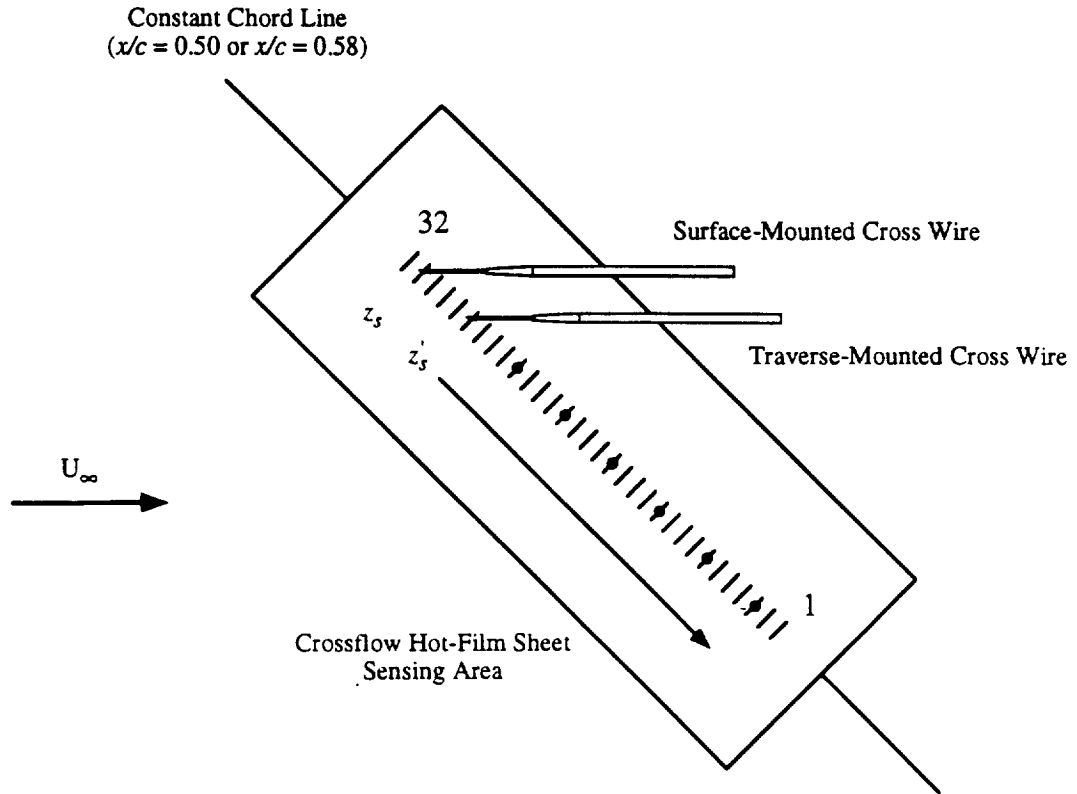
Figure 5.12: Schematic of cross-wire correlation measurements over a simultaneously sampled crossflow hot-film sheet. Dots represent other cross-wire measurement sites.

5.5.2 Correlation Measurements

In order to properly use the correlation analysis techniques described in chapter 6 (linear stochastic estimation and proper orthogonal decomposition), at least two measurements at different spatial locations must be made simultaneously. This is not typically an issue with the hot films because of the sheet technology. Several sensors may be placed on the surface without any significant flow disturbance. However, to measure two components of velocity, these types of measurements become somewhat involved. Only two cross-wire probes are used for any one measurement in the present experiment to minimize flow disturbance. Putting several probes in such a small boundary layer, so closely spaced (4 mm) could greatly influence the flow. Thus, the two probes are placed at various combinations of the measurement sites denoted by the dots in figure 5.12.

The one-dimensional velocity correlation tensor R_{ij} is mathematically defined as

$$R_{ij}(\hat{z}_s, \hat{t}) = \overline{u_i(z_s, t)u_j(z'_s, t')}$$ (5.2)

where the subscripts i and j denote the components in standard index notation, $\hat{z}_s = z_s - z'_s$ and $\hat{t} = t - t'$ denote the separation in span and time of the two velocities being correlated. The variables z'_s and t' simply denote another spatial position or another time, respectively. The spatio-temporal autocorrelation is obtained when $\hat{z}_s = 0$ and $\hat{t} = 0$. The measurements in the current experiment include the $\bar{u}$ and $\bar{w}$ components of velocity only, thus the subscripts i and j have a value of either 1 or 3 in equation 5.2. It should be clarified that the cross wires are aligned and calibrated in the current experiment to measure the $\bar{u}$ and $\bar{w}$ components of velocity in the global coordinate system. However, the grid that the cross wires measure upon, i.e., the center axis of the crossflow hot-film sensors, resides on the z_s axis of the swept coordinate system. This convention takes advantage of the structure repeatability in the spanwise flow and is actually required to properly compare the cross-wire measurements to the single hot-wire boundary-layer scans (which also measure $\bar{u}$ in the global coordinate system) and to the surface shear-stress measurements from the crossflow hot-film array (which measure τ_{z_s} in the swept coordinate system).

The correlation tensor of equation 5.2 is symmetric and may be acquired experimentally by sampling the cross wires at each single combination of spatial locations. For example, for the simple case of one component of velocity with three measurement sites and time suppressed, only three measurements are needed to compute all nine spatial values in the correlation tensor. First, the probes are placed at the first and second positions (giving $R(x, x') = R(1, 1)$, $R(1, 2)$ and $R(2, 1)$), then at the first and third positions (to produce $R(3, 3)$, $R(1, 3)$ and $R(3, 1)$) and then finally at the second and third positions (giving $R(2, 2)$, $R(2, 3)$ and $R(3, 2)$). The same technique is used for each cross-wire measurement grid of eight spatial locations illustrated in figure 5.12. The surface probe is first mounted above the 31st hot-film sensor in the crossflow sheet, the traverse-mounted probe is aligned above the 27th hot-film sensor and the data is acquired. The traverse-mounted cross-wire is then moved above the 23rd sensor and so on. When simultaneous
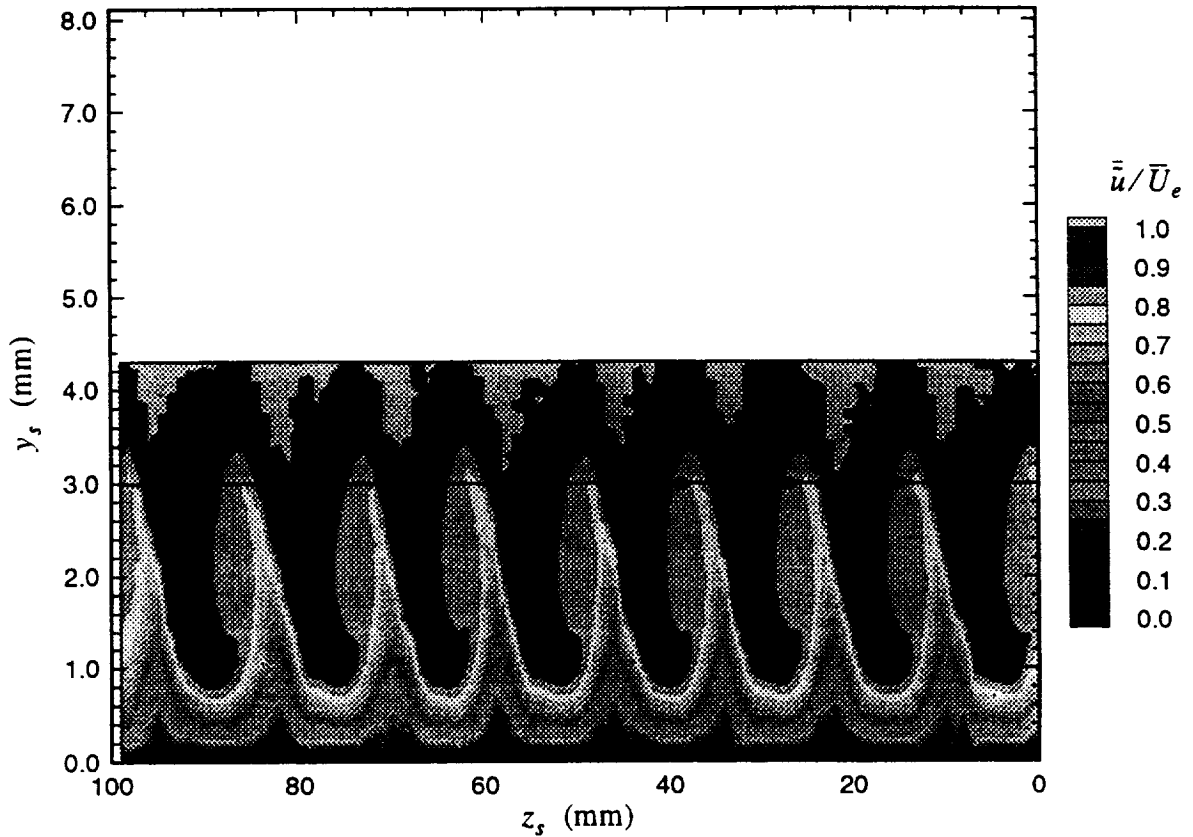
Figure 5.13: Cross-wire measurement locations mapped onto the streamwise velocity contours at $x/c = 0.50$, $Re_c = 2.4 \times 10^6$ with 6:12 artificial roughness.
Circles represent approximate cross-wire positions.

measurements at all of the position combinations in the z'_s direction (see figure 5.12) are acquired, the surface-mounted probe is then relocated to the 27th hot-film sensor and the traverse-mounted cross wire is moved to the 23rd sensor location. This progression is performed until all possible spatial combinations are acquired.

Using the translated mapping technique explained in section 5.4.2, we can map the cross-wire measurement grid at $x/c = 0.50$ to the mean streamwise velocity contour of figure 5.11. This mapping is shown in figure 5.13 where the circles represent the approximate locations of the cross-wire measurements. In most applications of the correlation analysis techniques described in chapter 6, the means are subtracted from each channel of data. Therefore, the analysis focuses on the disturbances and fluctuations of velocities and surface shear stresses. Figure 5.14, therefore

94
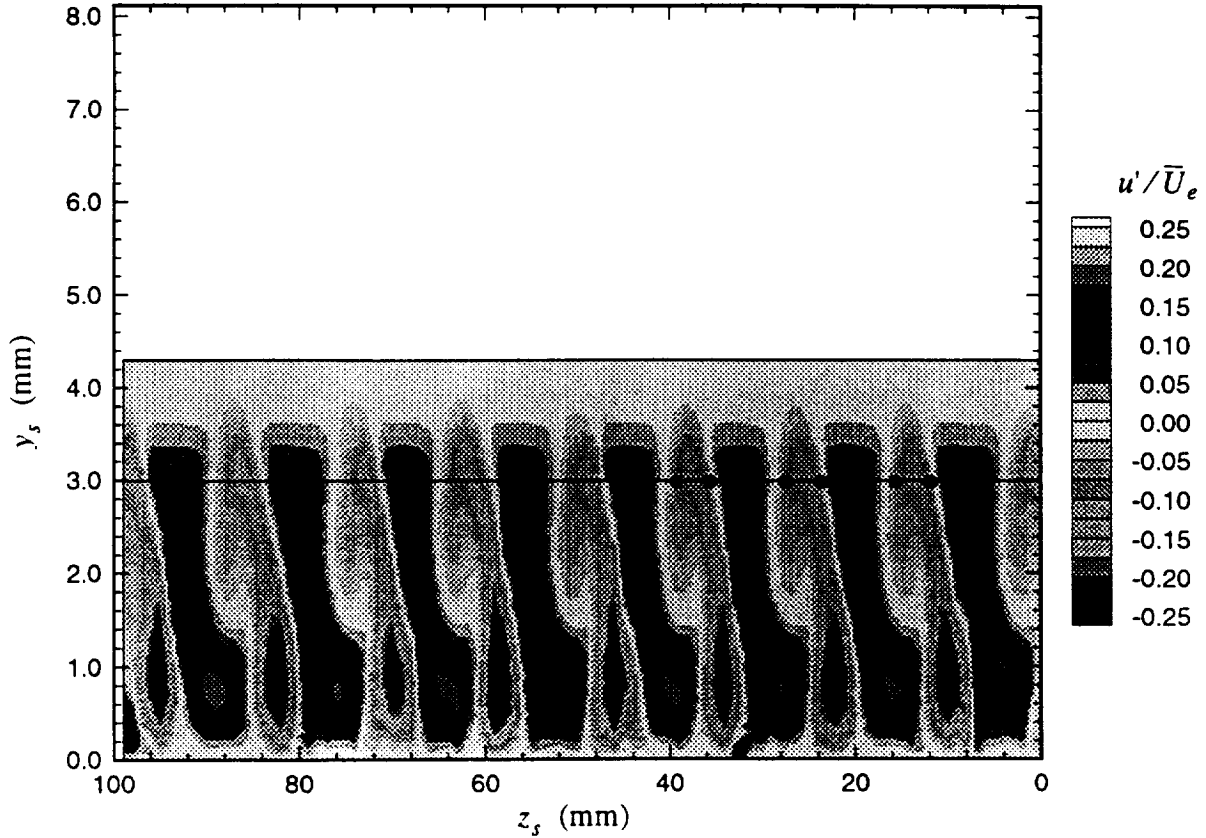
Figure 5.14: Cross-wire measurement locations mapped onto the streamwise disturbance velocity contours at $x/c = 0.50$, $Re_c = 2.4 \times 10^6$ with 6:12 artificial roughness. Circles represent approximate cross-wire positions.

uses the same mapping technique to display the cross-wire measurement locations over a streamwise velocity contour of the disturbances only. The spatial mean $\overline{U}(y_s)$ is subtracted from the total time-averaged streamwise velocity $\bar{u}$ data in figure 5.11 thus leaving the actual disturbance u' in the y_s-z_s plane in figure 5.14. This figure also illustrates the significant effect the disturbances have on the mean flow and whether the cross-wire measurements are made within a region of velocity deficit or surplus.

The cross-wire data is only acquired for the 6:12 artificial roughness case and consists of 4 channels (two two-component probes) simultaneously sampled with 13 channels of crossflow-aligned hot films at 10 kHz. The data set includes 5 blocks of 2 seconds for each spatial position

on the measurement grid at each constant chord location.

5.6 Data Summary

Below is a table that summarizes all the data acquired in the present experiment. The single hot-wire boundary-layer scans are excluded but are documented in detail by Reibert (1996a).

Table 5.1: Summary of data acquired in present experiment.

Section	Instrumentation	x/c	y_s (mm)	Artificial Roughness
5.4.1	Streamwise Hot-Film Sheet	0.49 - 0.58 Range		6:12
5.4.2	1 Streamwise & 2 Crossflow Hot-Film Sheets	0.49 - 0.58 0.50 & 0.58	0.0	
5.4.2	Crossflow Hot-Film Sheet	0.50 0.58		6:12 6:36
5.4.3	"T-array" Hot-Film Sheet			
5.5	Cross-Wire Probes		3.0	6:12

Instrumentation	Sample Rate (kHz)	# Channels	# Blocks	Record Length (s)
Streamwise Hot-Film Sheet		16		
1 Streamwise & 2 Crossflow Hot-Film Sheets		8 SW & 4 CF each		
Crossflow Hot-Film Sheet	10	16 12	20	3.0
"T-array" Hot-Film Sheet		16		
Cross-Wire Probes		4 XW & 13 CF	5	2.0

Correlation Analysis Techniques

Methods based on various calculated correlation tensors are used to identify the flow structure in the swept-wing boundary layer. These techniques take advantage of the statistical data inherent in the correlations to identify spatial structures within the boundary layer. Carefully selected instantaneous data is then projected upon those statistics to determine the spatio-temporal evolution of the flow structures before, through and after transition. The current experiment is specifically designed to accommodate the use of these multi-point correlation techniques through the correlation measurements of the two-component velocity and the various surface shear stresses explained in chapter 5. The background and theory is provided below for these analysis techniques which include observing the correlations themselves and the auto-spectra, linear stochastic estimation (LSE), proper orthogonal decomposition (POD) and a complimentary technique which takes advantage of the global aspects of POD and the locality of LSE.

6.1 Correlations and Spectra

6.1.1 Correlations

The heart of these analysis techniques lies within the various correlation tensors calculated for the measured velocity and surface shear-stress fields. Correlations define the statistical relationships between simultaneously measured quantities in both time and space and are mathematically defined in general as

$$R_{ij}(\hat{x}, \hat{t}) = \overline{u_i(\hat{x}, t)u_j(\hat{x}', t')} \tag{6.1}$$

for the full three spatial dimensions and time. As presented in section 5.5.2 for the one-dimensional case, the subscripts i and j denote the components in standard index notation and $\hat{x} = \dot{x} - \dot{x}'$ and $\hat{t} = t - t'$ denote the separation in three-dimensional space and time of the two quantities being correlated. (Velocities are shown in equation 6.1 but the relationship applies to all measured quantities in the current experiment.) The variables $\dot{x}'$ and t' simply denote another spatial position or another time, respectively. Refer to section 5.5 as to how the measurements relate to equations 6.1 and 5.2.

In the current analysis, only one-dimensional correlation tensors are computed. A one-dimensional, two-component correlation tensor is defined in equation 5.2 for the velocity measurements. A similar one-dimensional, one-component correlation tensor is defined as

$$\Re_{22}(\hat{z}_s, \hat{t}) = \overline{\tau_{z_s}(z_s, t)\tau_{z_s}(z'_s, t')} \qquad (6.2)$$

for the surface shear-stress measurements in the crossflow direction as described in section 5.4.2. The subscripts (22) denote the spanwise component of the surface shear within the swept coordinate system. Likewise, another one-dimensional correlation tensor is defined as

$$\Re_{11}(\hat{x}_t, \hat{t}) = \overline{\tau_{x_t}(x_t, t)\tau_{x_t}(x'_t, t')} \qquad (6.3)$$

for the surface shear-stress measurements in the streamwise direction as described in section 5.4.1 where the subscripts (11) denote the streamwise component in the boundary-layer coordinate system. The overbars in equations 5.2, 6.2 and 6.3 denote an ensemble block average with each block consisting of a uniform, predetermined record length. This amount of time is determined from inspecting the integral time scales within the boundary layer which are mathematically defined as

$$\mathcal{T} = \int_0^\infty \frac{R_{ii}(\hat{t})}{R_{ii}(0)} d\hat{t} \quad \text{or} \quad \mathcal{T} = \int_0^\infty \frac{\Re_{ii}(\hat{t})}{\Re_{ii}(0)} d\hat{t} \qquad (6.4)$$

where R_{ii} is the autocorrelation (the temporal relationship of a quantity with itself). Since an infinitely long record length cannot be obtained experimentally, an estimate of the integral time scale

is achieved by first computing the integral time scale for a very long record length. One can then determine the appropriate record length for the ensembled blocks based on when the variables become uncorrelated (i.e., when $R_{ii}(\hat{t}) = 0$). Since the current experiment involves three different flow regimes, a compromise is needed to accommodate the different characteristics of each flow regime, i.e., the three different locations of the first zero-crossing of equation 6.4. Another consideration is to make the number of samples within the determined record length a factor of 2 to accommodate the Fourier transforming procedure necessary for computing spectra (see section 6.1.2). This decision process for the current experimental data resulted in a record length of 512 samples which corresponds to a temporal block of 0.0512 seconds. This record length accommodates all three flow regimes to allow for appropriate comparisons between regimes and satisfies the factor of 2 criteria.

The spatial correlations are of particular interest in the current analysis since they include all the strictly spatial statistics used as the kernel in each of the more advanced multi-point correlation techniques. These spatial correlation tensors are obtained by simply setting $\hat{t} = 0$ in equations 5.2, 6.2 and 6.3. The spatial correlation tensors for each individual measurement used in the analysis are shown in chapter 7.

6.1.2 Spectra

It is often useful to inspect the spectral content of a time-dependent quantity in the frequency domain. By transforming a time-dependent quantity into the Fourier domain, one can observe active frequencies within the flow field. Also, the evolution of the energy in the measured quantity may be obtained across several spatial locations by observing the auto-spectra for each signal.

The Fourier transform pair of a velocity $u(t)$ (applicable also to shear $\tau(t)$) is expressed as

$$\hat{u}(f) = \int_{-\infty}^{\infty} e^{i2\pi ft} u(t) dt \qquad (6.5)$$

to transform the signal into the frequency domain (represented by $\hat{u}(f)$) and

$$u(t) = \frac{1}{2\pi} \int_{-\infty}^{\infty} e^{-i2\pi ft} \hat{u}(f) df \qquad (6.6)$$

99

for the inverse transform provided that the function $u(t)$ is smooth and vanishes at infinity. Unfortunately, these conditions are not satisfied by stationary random variables acquired experimentally. However, the required infinite length of the signal may be approached as a limit of a sequence of functions whose Fourier transforms do satisfy the criteria. Therefore, the Fourier transform of a stationary random signal may be represented by the limit of the Fourier transforms of the members of the sequence. The resulting Fourier coefficients are uncorrelated at different frequencies which may be mathematically expressed as

$$\overline{\hat{u}^*(f)\hat{u}(f')} = 0 \quad \text{for} \quad f \neq f' \tag{6.7}$$

where the star (*) represents the complex conjugate and must reside upon the first term for a rigorous mathematical definition (Ukeiley 1995). The overbar again denotes ensemble averaging over a number of blocks of a predetermined record length. If $f = f'$ then the correlation exists, is non-zero and is well defined mathematically from

$$\overline{\hat{u}^*(f)\hat{u}(f')}dfdf' = S(f)df \tag{6.8}$$

where $S(f)$ is the spectrum of the signal $u(t)$. By incorporating the Dirac delta function in the frequency domain with the combination of equations 6.7 and 6.8, a definitive relationship between the spectra and the Fourier transform of the correlation of the signal results and may be expressed as

$$\overline{\hat{u}^*(f)\hat{u}(f')} = S(f)\delta(f - f') \tag{6.9}$$

where $\delta(f - f')$ is the delta function (equal to 1 when $f = f'$ and 0 otherwise).

When transforming signals acquired experimentally into the Fourier domain, two conditions conflict with the requirements of equation 6.5. The acquired signal is obviously of a finite time and is discrete (i.e., sampled at finite intervals of time). These inflexible conditions are accommodated by defining a discrete Fourier transform determined from a discrete signal of a finite dura-

tion. Discretizing the variables $f = k\Delta f$ and $t = n\Delta t$ (where k and n are integers) results in the following definition for a discrete Fourier transform

$$\hat{u}(k\Delta f) = \Delta t \sum_{n=0}^{N-1} u(n\Delta t)e^{\frac{i2\pi nk}{N}} \tag{6.10}$$

where k and n range from 0 to $N-1$ and N is the number of data points acquired in the discrete signal $u(n\Delta t)$ at a uniform time interval Δt. This discrete form of equation 6.5 may then be used to develop the discrete form of the spectrum (equation 6.9) as

$$\frac{\overline{\hat{u}^*(k\Delta f)\hat{u}(k'\Delta f)}}{T} = S(k\Delta f) \tag{6.11}$$

where the delta function now takes the form of the signal's period $T = N\Delta t$. Equation 6.11 also demonstrates that the correlation function is indeed the Fourier transform of the spectrum, i.e.,

$$R_{ij}(\hat{t}) = \overline{u_i(t)u_j(t')} = \frac{1}{2\pi}\int_{-\infty}^{\infty} e^{-i2\pi f\hat{t}}S_{ij}(f)df \tag{6.12}$$

for continuous functions of infinite length. The discretized version of equation 6.12 for random stationary functions is given as

$$R_{ij}(\hat{t}) = \overline{u_i(n\Delta t)u_j(n\Delta t')} = \frac{\Delta t}{2\pi T}\sum_{n=0}^{N-1} S(f)e^{\frac{-i2\pi nk}{N}} = \frac{1}{2\pi N}\sum_{n=0}^{N-1} S(f)e^{\frac{-i2\pi nk}{N}} \tag{6.13}$$

The auto-spectra, simply the Fourier transforms of the auto-correlation functions, are used in chapter 7 to describe the frequency content distributed over spatial positions revealing the energetic nature of the structures present in the swept-wing boundary layer. This spatial evolution may be expressed as

$$S_{ii}(\hat{x}, f) = \frac{1}{N}\sum_{n=0}^{N-1} R_{ii}(\hat{x}, \hat{t})e^{\frac{i2\pi nk}{N}} \tag{6.14}$$

where there is no separation in space in the calculation of the auto-correlations. These calculations

also demonstrate the spatial transport of energy which is an important consideration in identifying a flow regime. The growth and/or decay of certain frequencies throughout this spatial evolution may also provide insight into the mechanisms responsible for transition. It may also expose the origins of large coherent structures within the turbulent boundary layer.

6.2 Linear Stochastic Estimation

6.2.1 Background

Stochastic estimation is a multi-point correlation technique that allows the estimation of a field of any quantity provided that the statistical data is known for the entire field to be estimated and that at least one conditional event is realized. Adrian (1975) introduced stochastic estimation to the study of turbulence by proposing that it could be applied to unconditional correlation data by defining a "conditional eddy" within the flow field as the required conditional event. Adrian (1979) defined these conditional eddies as recurrent flow patterns based on conditional averages defined by an event measured in the flow. He demonstrated that stochastic estimation could in fact provide excellent approximations for conditional averages using unconditional correlation data. Thus a method was developed which uses the conditional information specified about the flow at one or more locations with the statistical properties of all available locations to estimate the information at the remaining locations in the field.

Tung and Adrian (1980) supplemented Adrian's findings by concluding that low-order estimates qualitatively resolve the large-scale structure for all probable levels of the fluctuation intensity. They concluded that second-, third- and fourth-order estimates do not significantly improve the estimate, thus a linear stochastic estimation (LSE) is sufficient to identify coherent structures in turbulent flows.

Adrian et al. (1987) explored broader applications of LSE in the axisymmetric jet shear layer, the plane mixing layer and in turbulent pipe flow. They concluded that unconditional spatial correlations do indeed have the structures of the conditional fields imbedded within them. Adrian and Moin (1988) discovered results in their application of LSE to a direct numerical simulation of a turbulent shear flow. They used a new form of the conditional event which specifies the local kinematic state in terms of the velocity and deformation at a given location. Moin et al. (1987)

applied LSE to a numerically-simulated, turbulent channel flow to approximate the conditional vector fields associated with events that produce high Reynolds stress. Guezennec (1989) used LSE to identify coherent structures in a turbulent flat-plate boundary layer.

These past research efforts used various statistics such as the root mean square or a particular maximizing event as the conditional event. However, Cole (1991), Cole et al. (1992) and Cole (1996) have used the actual instantaneous time-history data of measured velocities as the conditional events, a technique used here in the current analysis of the swept-wing data. They also discuss the importance of specifically choosing which locations to use as reference for the conditional events and show that only one reference signal is not adequately representative of the measured field. Also, recent advances have been made by Cole (1996) who extends the theory of LSE to include two dimensions. Thus, a flow field may first be measured with at least two probes at all combinations of several locations to develop the needed correlation tensor. Then by choosing both of the actual time histories at the appropriate locations, one can estimate the instantaneous data at every other location producing a very good estimate of the instantaneous field. This is in place of measuring at every location simultaneously which may either significantly disturb the flow, require the acquisition of enormous amounts of data or require more instrumentation than what is available.

A distinct advantage to using stochastic estimation is that the experiment only needs to be performed once for each spatial location. Once the statistics are computed from all possible spatial combinations, the data used to compute the statistics is then used as the conditional event. Thus, when used to identify structures present in a flow field, stochastic estimation often requires less data than the conventional method of using conditional averages.

6.2.2 Theory

The theory of linear stochastic estimation (LSE) is briefly described below using velocity as the primary variable though other quantities such as shear stress or pressure may be used. LSE produces an estimate of the fluctuating velocity $u(x + \Delta x, t)$ provided that the velocity at some reference location (x, t) assumes some specified value $u(x, t)$. Mathematically, the one-dimensional LSE forms the estimate

$$u_i^{est}(x', t) = A_{ij}(x')u_j(x, t) \qquad (6.15)$$

103

where A_{ij} is a matrix of the estimation coefficients which are calculated from

$$\overline{u_j(x)u_k(x)}A_{ik}(x') = \overline{u_j(x)u_i(x')} \ . \tag{6.16}$$

where $\overline{u_j(x)u_k(x)}$ is the Reynolds stress and $\overline{u_j(x)u_i(x')}$ is the two-point correlation tensor. Expanding this system of equations for a two-probe estimate of the two-component velocity measurements taken in the swept-wing boundary layer results in a matrix form of equation 6.16 with two systems expressed as

$$
\begin{bmatrix}
\overline{u_{r1}^2} & \overline{u_{r1}w_{r1}} & \overline{u_{r1}u_{r2}} & \overline{u_{r1}w_{r2}} \\
\overline{w_{r1}u_{r1}} & \overline{w_{r1}^2} & \overline{w_{r1}u_{r2}} & \overline{w_{r1}w_{r2}} \\
\overline{u_{r2}u_{r1}} & \overline{u_{r2}w_{r1}} & \overline{u_{r2}^2} & \overline{u_{r2}w_{r2}} \\
\overline{w_{r2}u_{r1}} & \overline{w_{r2}w_{r1}} & \overline{w_{r2}u_{r2}} & \overline{w_{r2}^2}
\end{bmatrix}
\begin{bmatrix}
A_{11m}^{r1} \\
A_{13m}^{r1} \\
A_{11m}^{r2} \\
A_{13m}^{r2}
\end{bmatrix}
=
\begin{bmatrix}
\overline{u_{r1}u_m} \\
\overline{w_{r1}u_m} \\
\overline{u_{r2}u_m} \\
\overline{w_{r2}u_m}
\end{bmatrix}
\tag{6.17}
$$

for the first system and

$$
\begin{bmatrix}
\overline{u_{r1}^2} & \overline{u_{r1}w_{r1}} & \overline{u_{r1}u_{r2}} & \overline{u_{r1}w_{r2}} \\
\overline{w_{r1}u_{r1}} & \overline{w_{r1}^2} & \overline{w_{r1}u_{r2}} & \overline{w_{r1}w_{r2}} \\
\overline{u_{r2}u_{r1}} & \overline{u_{r2}w_{r1}} & \overline{u_{r2}^2} & \overline{u_{r2}w_{r2}} \\
\overline{w_{r2}u_{r1}} & \overline{w_{r2}w_{r1}} & \overline{w_{r2}u_{r2}} & \overline{w_{r2}^2}
\end{bmatrix}
\begin{bmatrix}
A_{31m}^{r1} \\
A_{33m}^{r1} \\
A_{31m}^{r2} \\
A_{33m}^{r2}
\end{bmatrix}
=
\begin{bmatrix}
\overline{u_{r1}w_m} \\
\overline{w_{r1}w_m} \\
\overline{u_{r2}w_m} \\
\overline{w_{r2}w_m}
\end{bmatrix}
\tag{6.18}
$$

for the second system where $r1$ and $r2$ refer to the two reference probe locations (i.e., measurement locations where the conditional instantaneous data originates) and m refers to the measurement location being estimated, an integer ranging from 1 to N_m, the total number of measurement sites. Equations 6.17 and 6.18 demonstrate that the LSE systems are independent of the condition being investigated. They are only dependent on the statistical information. The condition is applied in the actual calculation of the estimate using equation 6.15. This is expressed in

expanded form for the two-probe estimate of the two-component velocity data as

$$u_m^{est}(t) = A_{11m}^{r1}u_{r1}(t) + A_{13m}^{r1}w_{r1}(t) + A_{11m}^{r2}u_{r2}(t) + A_{13m}^{r2}w_{r2}(t) \qquad (6.19)$$

for the u component and

$$w_m^{est}(t) = A_{31m}^{r1}u_{r1}(t) + A_{33m}^{r1}w_{r1}(t) + A_{31m}^{r2}u_{r2}(t) + A_{33m}^{r2}w_{r2}(t) \qquad (6.20)$$

for the w component. The $u_{r1}(t)$, $w_{r1}(t)$, $u_{r2}(t)$ and $w_{r2}(t)$ velocities are the conditions used in the estimate and the subscript m again refers to each measurement site to be estimated, thus keeping the spatial distribution of the estimated signals. A one-probe estimate is obtained by setting all terms with $r2$ equal to zero. These equations may also be extended to include more reference probes as long as all reference signals are acquired simultaneously. In fact, an excellent way to validate LSE algorithms is to compare an estimated field using simultaneously sampled signals from all measurement locations as references to the originally measured field. If the LSE code is functioning properly, the two fields should be identical.

For the current analysis, LSE is used to estimate the entirely measured two-component velocity field using simultaneously sampled signals from the two best measurement locations (as qualified in chapter 8). LSE is also used to estimate the surface shear-stress field using the calibrated hot-film signals on the crossflow sheet sampled simultaneously with the cross-wire measurements made directly above the sheet. In this situation, certain shear-stress measurements are corrupted by the presence of the cross-wire probes. Those corrupted signals are estimated using LSE thus minimizing the flow disturbance effects on the measured field. In this unique application, the equations described above are extended to include the total number of reference signals used as the conditions and are reduced to one component of surface shear stress using the appropriate correlation tensor $\mathfrak{R}_{ij}$.

6.3 Proper Orthogonal Decomposition

6.3.1 Background

Proper orthogonal decomposition (POD) is a completely objective technique that is used to decompose a flow field into various modes based on energy. It is a powerful technique that provides the identification of the large-scale structures usually within a turbulent flow field but may be applied to other flow regimes to identify their dominant features as well.

This correlation-based technique was first introduced to the study of turbulence by Lumley (1967) who postulated that the large eddies within a turbulent flow are those structures within the flow that have the largest mean-square projection on the flow field. He developed this hypothesis through employing the Karhunen-Loeve expansion (Loeve 1955) to identify these large-scale structures resulting in what is now known as proper orthogonal decomposition, a mathematically unbiased method for extracting eigenfunctions characteristic of the flow structure through the solution of an integral eigenvalue equation that contains the appropriate correlation tensor as its kernel. The dominant mode resulting from the numerical solution of the POD identifies the spatio-temporal evolution of the large eddies imbedded within the flow.

POD was first applied to the wake behind a cylinder by Payne (1966) but revealed that the energy content in the dominant eddy was not significantly larger than that of subsequent eddies. More conclusive results were obtained by Bakewell and Lumley (1967) in their application of the POD to the near-wall region of a turbulent pipe flow. They determined that the dominant eddy contained 90% of the total streamwise turbulent energy. Since these early applications of POD, many research efforts have even extended the usefulness of this technique beyond the study of turbulent flows. The many applications of POD and significant contributions are further summarized by Berkooz et al. (1993) and Ukeiley (1995).

Other efforts particularly significant to the application of the POD to advanced experimental measurements and to transitional flows have greatly influenced the direction of the current analysis. Herzog (1986) applied POD to hot-film measurements taken in the near-wall region of a turbulent boundary layer and showed that the dominant mode contained approximately 60% of the total kinetic energy in the measured flow field, closely matching the POD results from a large eddy simulation of the same flow by Moin (1984). Leib et al. (1984) and Glauser et al. (1987) applied POD to the near-field region of a turbulent axisymmetric jet. They determined that an

accurate representation of the flow field may be obtained by reconstructing the measured velocity field with only the first three eigenmodes. They also determined a "life cycle" for the coherent structures in the flow through examination of the POD solutions.

Ukeiley (1991) and Ukeiley et al. (1993b) studied the complex flow field downstream of a lobed mixer and tracked the breakdown of large-scale vortical structures. Extensive studies by Delville et al. (1989), Delville (1993) and Delville and Ukeiley (1993) have also used POD in the plane mixing layer to determine the role of higher POD modes and higher degrees of complexity within the development of the kernel. Their results show that by including these complexities, more essential flow physics are recovered in the first POD mode. Ukeiley (1995) extends this research by using experimental POD results to develop a low-dimensional dynamical systems model of the plane mixing layer.

Aubry et al. (1994) used a technique similar to POD called the bi-orthogonal decomposition to study transitioning flow over a rotating disk. Rempfer and Fasel (1994) studied the spatio-temporal evolution of three-dimensional coherent structures in a transitional boundary layer using POD. They showed that the transitional characteristics, i.e., high-frequency, high-amplitude spikes within the signals, were linked to the higher order POD structures.

Thus, POD has a very broad history in application and development and is continually being applied in new ways. In the current analysis, POD is used primarily to identify spatially-varying structures in a three-dimensional boundary layer before, through and after transition. The dominant POD eigenmode is used to characterize the flow structure and to relate measurements taken on the surface to those taken internally within the boundary layer. The temporal evolution of the dominant modes are also inspected and related to the actual instantaneous data providing reductions in the amount of data needed to train future flow control strategies.

6.3.2 General Theory

Lumley (1967) first introduced the proper orthogonal decomposition technique as an objective and unbiased method of extracting coherent structures or dominant flow features from a flow field. He proposed that turbulent flows are dominated by large scale structures and that a descriptive candidate structure within that flow, $\tilde{\phi}$, should be selected such that it is the structure with the largest mean-square projection on the quantitative field (e.g., the velocity or surface shear-stress field). This projection maximizes the energy content of the candidate structure and is mathemati-

cally represented by

$$\frac{\overline{|\hat{u} \cdot \hat{\phi}|^2}}{|\hat{\phi} \cdot \hat{\phi}^*|} = \overline{|\alpha|^2} \qquad (6.21)$$

where $\hat{u}$ represents the three-dimensional fluctuating velocity field and α denotes the inner product of the velocity field with the candidate structure. The normalization with the inner product of the candidate structure with its complex conjugate (denoted by the *) is used to remove the system's dependence on amplitude. This technique focuses on the degree of projection, not the amplitude resulting from the projection.

Maximizing the mean-square of the energy projection in equation 6.21 is accomplished through the calculus of variations (Lumley 1981) or by defining a Hermitian operator (Berkooz 1991) resulting in the following integral eigenvalue problem

$$\iiiint R_{ij}(\hat{x}, \hat{x}', t, t') \phi_j(\hat{x}', t') d\hat{x}' dt' = \lambda \phi_i(\hat{x}, t) \qquad (6.22)$$

where the kernel R_{ij} is the two-point correlation tensor defined by equation 6.1, the eigenvalue λ is equal to $\overline{|\alpha|}^2$ and ϕ_i are the solved eigenfunctions or POD modes. Since the correlation tensor is symmetric, the solution of equation 6.22 may be described by Hilbert-Schmidt theory (Lumley 1967). The integrals in equation 6.22 may also be placed over a finite domain if the random vector field ($\hat{u}$ in this case) resides within a finite range. Such is the case for experiments thus providing for the following properties to apply.

1. There are a discrete set of solutions such that equation 6.22 may be expressed as

$$\int_D R_{ij}(\hat{x}, \hat{x}', t, t') \phi_j^{(n)}(\hat{x}', t') d\hat{x}' dt' = \lambda^{(n)} \phi_i^{(n)}(\hat{x}, t) \qquad (6.23)$$

where the integral operand D represents integration over a finite domain and the superscript (n) denotes an integer value corresponding to the finite number of POD modes ranging from 1 to N.

2. The eigenfunction solutions are indeed orthonormal, even for the discrete solution of

equation 6.23, and thus adhere to the following expression.

$$\int_D \phi_i^{(p)}(\hat{x}, t) \phi_i^{(q)}(\hat{x}, t) d\hat{x} dt = \delta_{pq} \tag{6.24}$$

Here, the superscripts (p) and (q) represent POD mode numbers and δ_{pq} is the Dirac delta function responding to those POD number indices.

3. The orthonormal solutions of equation 6.23 may be used in conjunction with the POD coefficients $a^{(n)}$ to reconstruct the original random vector field in the following manner.

$$u_i(\hat{x}, t) = \sum_{n=1}^{\infty} a^{(n)} \phi_i^{(n)}(\hat{x}, t) \tag{6.25}$$

The scalar POD coefficients $a^{(n)}$ contain the integrated effect of the spatio-temporal evolution within the flow and are calculated from the following equation.

$$a^{(n)} = \int_D u_i(\hat{x}, t) \phi_i^{(n)*}(\hat{x}, t) d\hat{x} dt \tag{6.26}$$

4. The POD coefficients calculated in equation 6.26 are random, uncorrelated and are representative of the eigenvalues in the mean-square sense, i.e.,

$$\overline{a^{(n)} a^{(m)}} = \lambda^{(n)} \delta_{nm} \ . \tag{6.27}$$

5. The kernel can also be reconstructed through equation 6.28 which uses a double series over the number of POD modes in $\phi_i^{(n)}$ that is uniformly and absolutely convergent.

$$R_{ij}(\hat{x}, \hat{x}', t, t') = \sum_{n=1}^{\infty} \sum_{n=1}^{\infty} \lambda^{(n)} \phi_i^{(n)}(\hat{x}, t) \phi_j^{(n)*}(\hat{x}', t') \tag{6.28}$$

6. The eigenvalues are positive since the kernel is positive definite, have a finite sum and have descending amplitudes with increasing POD mode number. These conditions are expressed

109

below in equations 6.29 through 6.31 respectively.

$$\lambda^{(n)} \geq 0$$

<div align="right">(6.29)</div>

$$\sum_{n=1}^{\infty} \lambda^{(n)} < \infty$$

<div align="right">(6.30)</div>

$$\lambda^{(1)} > \lambda^{(2)} > \lambda^{(3)} > \ldots > \lambda^{(n)}$$

<div align="right">(6.31)</div>

The general theory presented here is explained with infinite orthonormal solutions to equation 6.23, i.e., an infinite number of POD modes where n ranges from 1 to ∞. However, in real-world applications such as in all experimental investigations, only a finite number of solutions is possible. The number of modes available in the solution is ultimately determined by the order of the two-point correlation tensor. Thus, for a spatial correlation tensor with time suppressed, the number of modes is ultimately determined by the number of spatial locations (measurement sites) where the correlation is known.

POD provides a completely unbiased approach to decomposing a random vector field on an energy-weighted basis. As implied by equation 6.31, the first mode contains the most energy possible in the mean-square sense, extracted from the measured field. All subsequent modes then contain the most energy possible again in the mean-square sense, but at continuously decreasing levels. Thus, the method separates large-scale structures from the high-frequency small-scale structures due to the various energy levels residing within the flow.

6.3.3 One-Dimensional Equations

The analysis used in the current swept-wing experiment uses a one-dimensional version of the discrete POD in equation 6.23 for all measurements. Only spatial evolutions are computed from the POD solution and thus only require a spatial correlation tensor. The cross-wire application includes the two-components of velocity within one dimension (span) and the various hot-film analyses include one component of surface shear stress across one dimension (either span or streamwise direction).

<div align="center">110</div>

For the cross-wire application at each chord location, equation 6.23 may simplified to

$$\int_D R_{ij}(z_s, z'_s)\phi_j^{(n)}(z'_s)dz'_s = \lambda^{(n)}\phi_i^{(n)}(z_s)$$ (6.32)

where i and j have a value of either 1 or 3 corresponding to the u and w components of velocity as the spatial evolution occurs in the span direction of the swept coordinate system. This application requires that the POD coefficients be time dependent in order to properly restore the original flow field (which will actually be an estimated flow field - refer to section 6.4) since the time dependency is suppressed in the kernel and therefore in the eigensolutions as well. The resulting reconstruction equation then becomes

$$u_i(z_s, t) = \sum_{n=1}^{N_{eig}} a^{(n)}(t)\phi_i^{(n)}(z_s)$$ (6.33)

where N_{eig} is the total number of modes resulting from the POD solution. The number of modes is determined by the order of the spatial correlation tensor or ultimately by the number of measurement locations (N_m) multiplied by the total number of components (N_c). Thus, $N_{eig} = N_m N_c = 16$ for the cross-wire applications. The random, time-dependent POD coefficients are then calculated from the following simplified form of equation 6.26.

$$a^{(n)}(t) = \int_D u_i(z_s, t)\phi_i^{(n)}(z_s)dz_s$$ (6.34)

Note that the complex conjugate notation of the eigenfunctions has been dropped. This is due to the fact that the POD solutions are completely real for the swept-wing data.

The surface shear-stress solutions are obtained in a very similar manner. For the crossflow-aligned hot-film data, simply replace the two-component velocity u_i with the single-component spanwise surface shear stress τ_{z_j} in equations 6.33 and 6.34 using the appropriate spatial correlation tensor ($\Re_{22}$ defined in equation 6.2) in the governing POD equation (equation 6.32). For the POD solution of the streamwise surface shear stress, simply replace the two-component velocity

111

u_i with the single-component streamwise surface shear stress τ_{x_i} in equations 6.33 and 6.34 using the appropriate spatial correlation tensor ($\mathfrak{R}_{11}$ defined in equation 6.3) in the governing POD equation (equation 6.32). Also, replace the spatial variables and differentials containing z_s to x_i.

6.3.4 Numerical Approximations

The integration of the one-dimensional POD in equations 6.32 and 6.34 require the use of a quadrature rule (Glauser et al. 1987) to numerically solve the for the appropriate eigenvalues and eigenfunctions (equation 6.32) and the appropriate POD coefficients (equation 6.34). The current POD analysis of the cross-wire and crossflow hot-film data uses a trapezoidal rule which defines a spatially-dependent weighting function $W(m)$ as

$$W(m) = \begin{cases} (\Delta z_s)/2 & \text{for } m = 1, N_m \\ \Delta z_s & \text{for } 1 < m < N_m \end{cases} \tag{6.35}$$

where m is an integer index corresponding to the number of measurement sites ranging from 1 to N_m. The spatial difference in equation 6.35 is the numerical representation of the differential term in equations 6.32 and 6.34. The half scaling for the first and last elements is a result of the trapezoidal rule. A similar weighting function is obtained for use in the streamwise analysis by replacing Δz_s with Δx_i. Using the weighting function in equation 6.35 to approximate the POD eigenvalue problem, equation 6.32 may now be numerically represented as

$$\sum_{m=1}^{N_m} W(m) R_{ij}(m, m') \phi^{(n)}(m) = \lambda^{(n)} \phi^{(n)}(m') \tag{6.36}$$

where m' also ranges from 1 to N_m. The product of the spatial correlation tensor and the weighting function does not retain the Hermitian properties of R_{ij} and therefore loses all the advantageous properties of the POD technique. Therefore, it is necessary to separate the weighting

function (Baker 1977; Glauser 1987; Ukeiley 1995; Cole 1996) and rewrite equation 6.36 as

$$\sum_{m=1}^{N_m} \{ W(m)^{1/2} R_{ij}(m, m') W(m)^{1/2} \} W(m)^{1/2} \phi^{(n)}(m)$$

$$= \lambda^{(n)} W(m')^{1/2} \phi^{(n)}(m') \qquad (6.37)$$

to preserve the Hermitian properties. The resulting matrix is mathematically similar to that within equation 6.36 and therefore produces the same eigenvalues. The resulting eigenfunctions, however, must be scaled by $W(m)^{-1/2}$ to recover the appropriate solution.

6.4 Complimentary Technique

Glauser et al. (1993), Ukeiley et al. (1993a) and Bonnet et al. (1994) developed a technique which uses linear stochastic estimation (LSE) in conjunction with proper orthogonal decomposition (POD). This complimentary technique uses LSE to estimate the instantaneous flow field at all spatial positions of interest (provided that the statistical data is previously acquired) and then projects that estimated field onto the POD eigenfunctions. The result provides the experimentalist with temporal evolutions of the scalar POD modes without having prior knowledge of the full instantaneous flow field simultaneously. Application of the complimentary technique is especially useful in the current analysis in providing a way to examine the temporal evolution of the velocity-based POD modes simultaneously with the surface-shear-stress-based POD modes.

The complimentary technique first uses LSE to estimate the instantaneous flow field exactly as explained in section 6.2. Then, the spatial POD problem is solved using the statistical data in the form of the spatial correlation tensor as its kernel to obtain the spatially dependent eigenfunctions (theoretically using equation 6.32 or numerically using equation 6.37). The estimated field is then projected onto those eigenfunctions using a form of equation 6.34 expressed theoretically as

$$a_{est}^{(n)}(t) = \int_D u_i^{est}(z_s, t) \phi_i^{(n)}(z_s) dz_s \qquad (6.38)$$

or numerically as

$$a_{est}^{(n)}(t) = \sum_{m=1}^{N_m} u_i^{est}(m, t)\phi_i^{(n)}(m)W(m) \qquad (6.39)$$

to solve for the random, time-dependent POD coefficients. The coefficients may then be compared to the instantaneous field thus characterizing a full random vector field by a few dominant scalar modes. This allows a drastic reduction in the amount of data needed to accurately represent the flow field and makes the training of future flow control algorithms much simpler. These powerful analysis techniques are capable of quantifying a random flow field using an energy-based system of organization that minimizes human subjectivity and influence.

6.5 Analysis Summary

This section provides a summary to the data post-processing procedure used in the current analysis and demonstrates how one might use these correlation techniques to identify structures imbedded within a flow field.

First, the two-component velocity data is used to calculate the spatio-temporal correlation tensor using equation 5.2. From this the auto-spectra is computed in order to examine the spatial evolution of the frequency content of the autocorrelation data. The spatial correlation tensor is also formulated from the spatio-temporal correlations by setting $\hat{t} = 0$. The same is done independently for all of the surface shear-stress data. These results are detailed in chapter 7.

Next, the spatial POD problem is solved for each data set independently using equation 6.32 (or equation 6.37) and the appropriate spatial correlation tensors. These solutions provide the appropriate eigenvalues and eigenfunctions which are presented in chapter 8. The eigenvalues are used to determine the hierarchy of energy, i.e., how much relative kinetic energy is contained in each mode. The eigenfunctions, when properly scaled, expose the spatial evolution of the various modes which characterize the large-scale structure within the flow field.

The temporal POD coefficients are then calculated for the individual surface shear-stress data which were acquired independently of any cross-wire measurements. This is only possible

because the entire field is acquired simultaneously. These results are also presented in chapter 8 and reveal the temporal dynamics characteristic of the instantaneous data.

LSE is then used to estimate the two-component instantaneous velocity field from the statistical, spatial correlation data and only two instantaneous signals acquired at optimally chosen probe locations. The process of choosing the appropriate probe locations is discussed in chapter 8 along with the estimation results. LSE is also used to estimate the surface shear-stress fields acquired simultaneously with the cross-wire data to account for missing sensors and to relieve the flow disturbance caused by the presence of the cross-wire probes in the boundary layer.

Finally, the estimated fields are projected onto the corresponding eigenfunctions to determine the random, temporal POD coefficients for the two-components of velocity simultaneously with the surface shear stress coefficients. This allows a comparison of internal measurements to surface measurements and may prove very useful in training future flow control algorithms.

CHAPTER 7

Correlation and Spectra Results

It is often useful to examine the spatio-temporal evolution of the various correlation tensors mentioned in chapter 6. Here, the various spatial correlation tensors are presented and analyzed, demonstrating the spatial relationships of the flow field. The temporal information is actually better viewed in Fourier space (in the form of the auto-spectra) to identify the spatial evolution of the flow's frequency content. This is important in identifying specific scales within the flow with smaller scales residing at higher frequencies and large-scale structures existing at lower frequencies. It is also a very useful technique for identifying the *origins* of these scales. Many studies include this type of analysis to specifically identify structure. Some of the many similar analyses are included in Glauser (1987), Kohama et al. (1991), Ukeiley (1995), Cole (1996) and Yang et al. (1996).

7.1 Spatial Correlations

The spatial correlations are calculated for the two fluctuating components of velocity and one component of the crossflow-directed surface shear-stress fluctuations across the span at $x/c = 0.50$ in the laminar regime and $x/c = 0.58$ in the turbulent regime. The spatial correlation tensor for the streamwise evolution of the surface shear-stress fluctuations through the entire transition front is also presented. Equations 5.2, 6.2 and 6.3 are used to compute these correlations which are averaged over 195 blocks of 0.0512 seconds as discussed in section 6.1.1.

7.1.1 Velocity Spatial Correlations

Three-dimensional surface plots of the spatial correlations for the u and w velocity components at $x/c = 0.50$, 3.0 mm above the wing surface, are shown in figures 7.1 and 7.2, respectively. The cross-component spatial correlation for these two velocity components at $x/c = 0.50$ is shown in figure 7.3. The spatial autocorrelation, i.e., the trace of the spatial correlation tensors, varies quite radically in span for all three tensors.

Figure 7.1 demonstrates high amplitude peaks at all combinations of span positions 3 mm and 15 mm which denotes that the signals at these locations are very well correlated. In fact, the 12-mm, forced wavelength of the stationary vortices is captured in these peaks within the spanwise distribution of the streamwise velocity component. Referring back to the "flow map" of the disturbances shown in figure 5.14, we observe that the positions at 3 mm and 15 mm in figure 7.1 (which correspond to the first and fourth dots from the left in figures 5.13 and 5.14) reside in regions of high deficits in velocity while other positions lie on the outer fringes of the vortex disturbances, regions of nearly "balanced" velocity. Therefore, the 12-mm wavelength is only captured between the first two vortices while the third is completely undetected. This is due to the placement of the last few measurement sites which happen to lie between the vortices. Clearly, a finer measurement grid would provide better resolved features of the velocity field. However, one wavelength is indeed captured here and will be sufficient for analysis. The surface shear-stress measurements are taken at double the spatial resolution and will demonstrate better identification of the flow structure. Unfortunately, using only two cross-wire probes to make correlation measurements requires enormous amounts of data, significantly more than that produced from equivalent measurements taken with the hot-film sheets. This is due to the need for re-positioning the cross-wire probes which results in repeated data acquisition at certain positions. The hot-film technology permits all sensors to be acquired simultaneously therefore producing only one signal for each spatial location per experiment.

The spatial correlation of the w component shown in figure 7.2 demonstrates similar properties to that of the u component with a large correlation peak at the position of 15 mm. Evidence of the 12-mm wavelength also appears in the small-amplitude periodicity in the ridges of the surface close to either plot wall. Unfortunately, no "flow map" is available for the velocity in the z direction of the global coordinate system. However, based on the comparisons for figure 7.1 to the
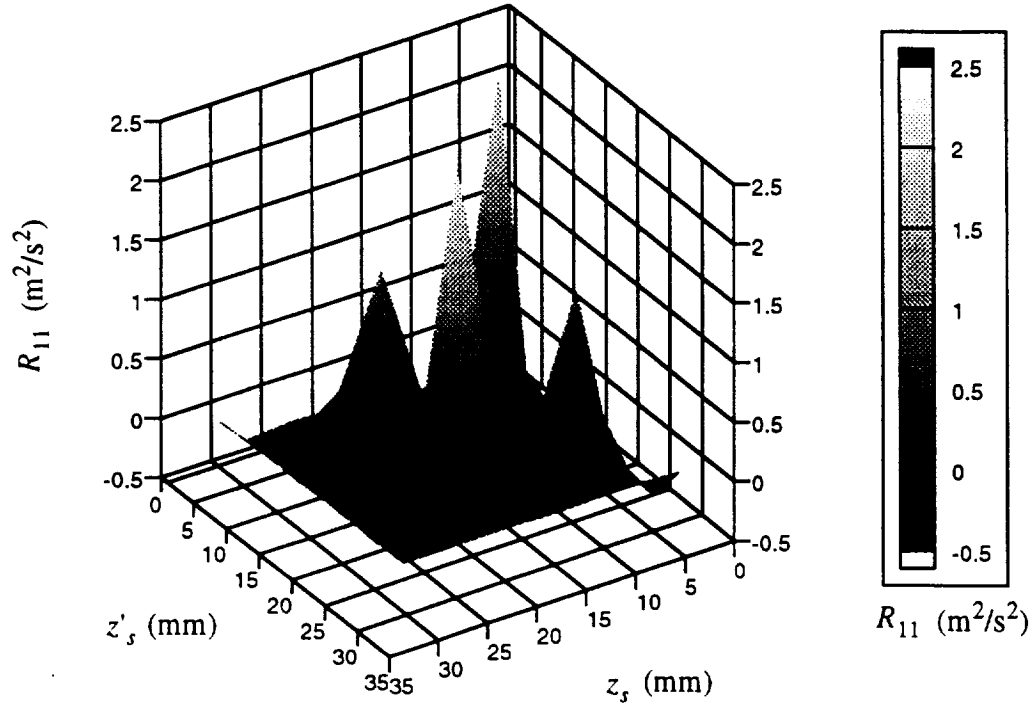
Figure 7.1: Spatial correlation tensor for the u component of velocity at $x/c = 0.50$, $y = 3.0$ mm.

Figure 7.2: Spatial correlation tensor for the w component of velocity at $x/c = 0.50$, $y = 3.0$ mm.

Figure 7.3: Cross-component spatial correlation tensor for the u and w components of velocity at $x/c = 0.50$, $y = 3.0$ mm.

available "flow map", one can infer that the measurements only capture one crossflow vortex of the forced 12-mm wavelength. Smaller peaks exist in the correlation trace at positions expected to contain the vortices, but due to the small size of these vortices and the relatively large spacing within the measurement grid, these measurements appear to be very close to the near "balanced" velocity region, i.e., the region between the vortices. Again, though, one wavelength is clearly captured and will be adequate for the analysis.

Figure 7.3 shows the cross-component spatial correlation tensor. This tensor is not symmetric, however it should be noted that $R_{13} = R_{31}$. A clear merging of the spatial correlations for the u and w in figures 7.1 and 7.2 appears in the cross-component correlation. Again, locations at 3 mm and 15 mm demonstrate high correlations. Even the smaller peaks near the ridges of figure 7.2 appear in figure 7.3. This demonstrates the coupled effect of the two-components of velocity whose interaction is very important in the boundary-layer breakdown to transition. Also, note the decrease in relative amplitude for the entire cross-component correlation which simply states that the components are better correlated with themselves than with each other at the peak locations.

Figure 7.4 provides wire-frame plots of the same data contained in figures 7.1, 7.2 and 7.3 to illustrate the differences in spatial structure and to present the data in another perspective.

Figures 7.5 and 7.6 show the three-dimensional surface plots of the spatial correlations for the u and w components in the turbulent regime at $x/c = 0.58$, 3.0 mm above the wing surface. The cross-component spatial correlation for these two velocity components at $x/c = 0.58$ is shown in figure 7.7.

Each of the spatial correlations in the turbulent regime exhibit similar behavior. The traces of each tensor grow to very large amplitudes (compared to the laminar cases) whereas the off-center combinations of spatial positions die off almost completely. This focusing on the autocorrelations is a typical characteristic of turbulent boundary layers and is due to the high degree of

Figure 7.4: Wire-frame illustrations of spatial correlation data for u and w components of velocity at $x/c = 0.50$ and $y = 3.0$ mm.

randomness produced by the transition process whereby the signals are far more correlated with themselves than with signals at any other location. The drastic increase in amplitude for the auto-correlations is a direct result of the mean-flow momentum transferring energy to the fluctuating flow.

The only significant difference between the u and w spatial correlations (shown in figures 7.5 and 7.6, respectively) is in amplitude. The trace of the w component correlation grows to a higher amplitude through transition than the u component, implying that more energy is being transferred to the w component during the transition process. As we will discover by inspecting the spectra, this is due to the secondary instability whose growth gives birth to small scales at high frequencies. Also, the vortex breakdown, critically induced by the streamwise growth of the disturbances in the laminar boundary layer, causes a great deal of mixing of the flow, so much so that the once laminar boundary layer is fully turbulent only 146 mm (8% chord) further downstream.

Another important observation is that the cross-component correlation shown in figure 7.7 is
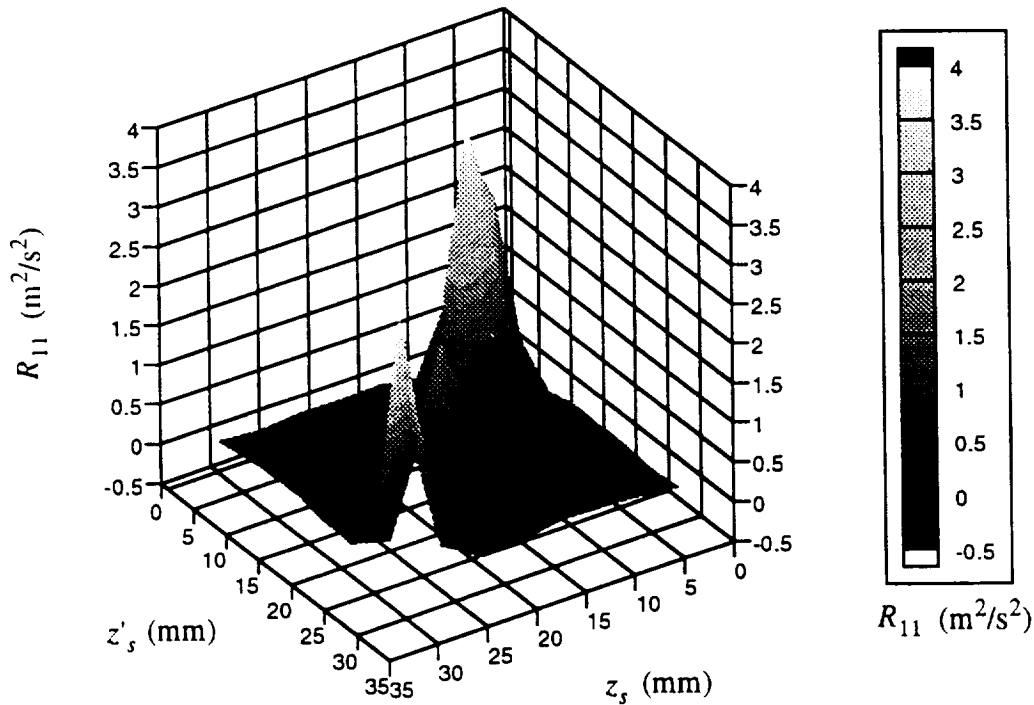
Figure 7.5: Spatial correlation tensor for the u component of velocity at $x/c = 0.58$, $y = 3.0$ mm.
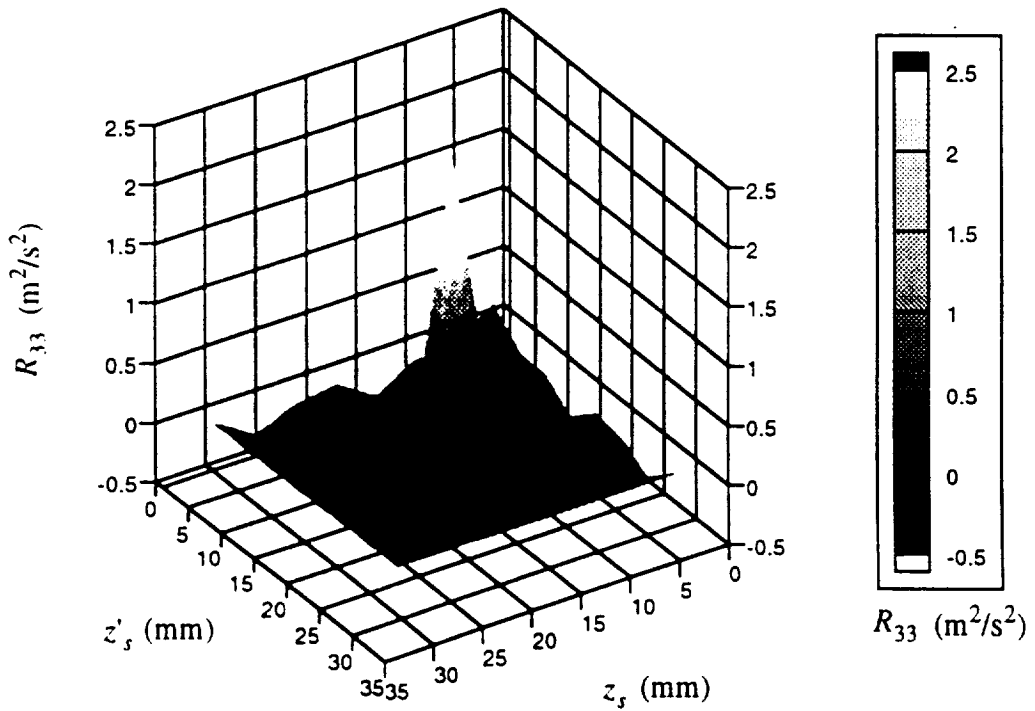
121
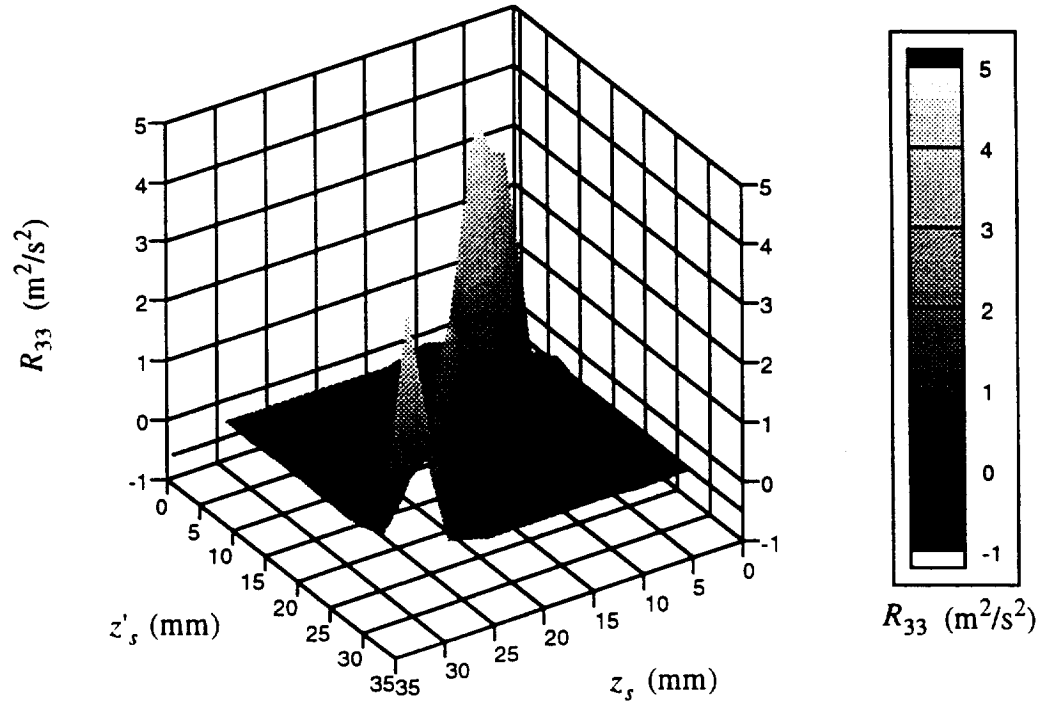
Figure 7.6: Spatial correlation tensor for the w component of velocity at $x/c = 0.58$, $y = 3.0$ mm.
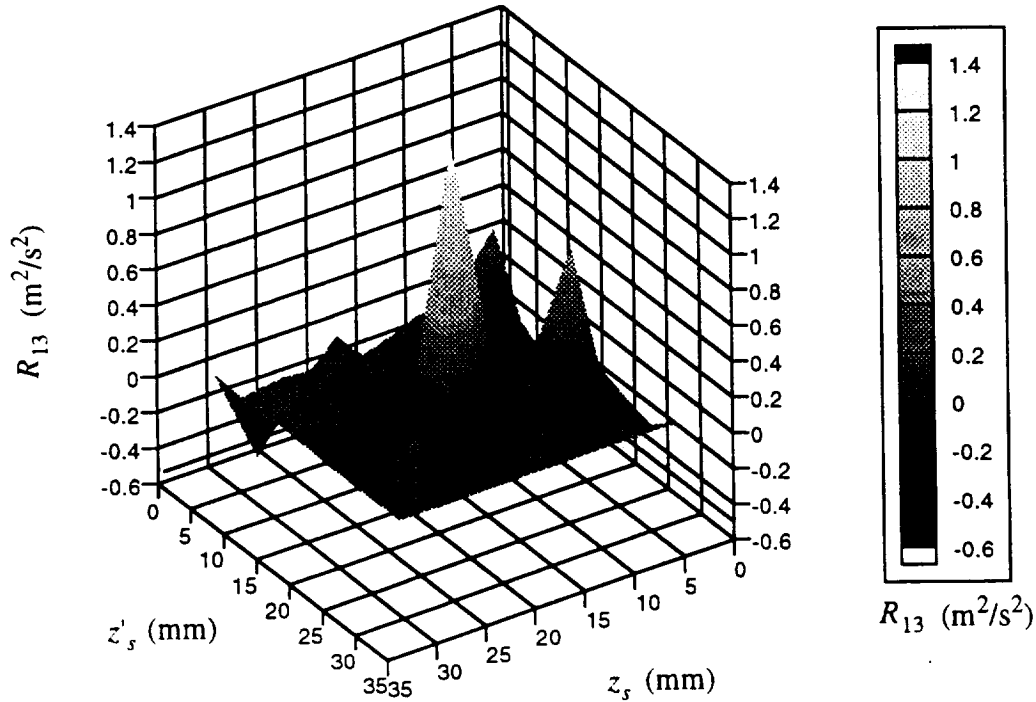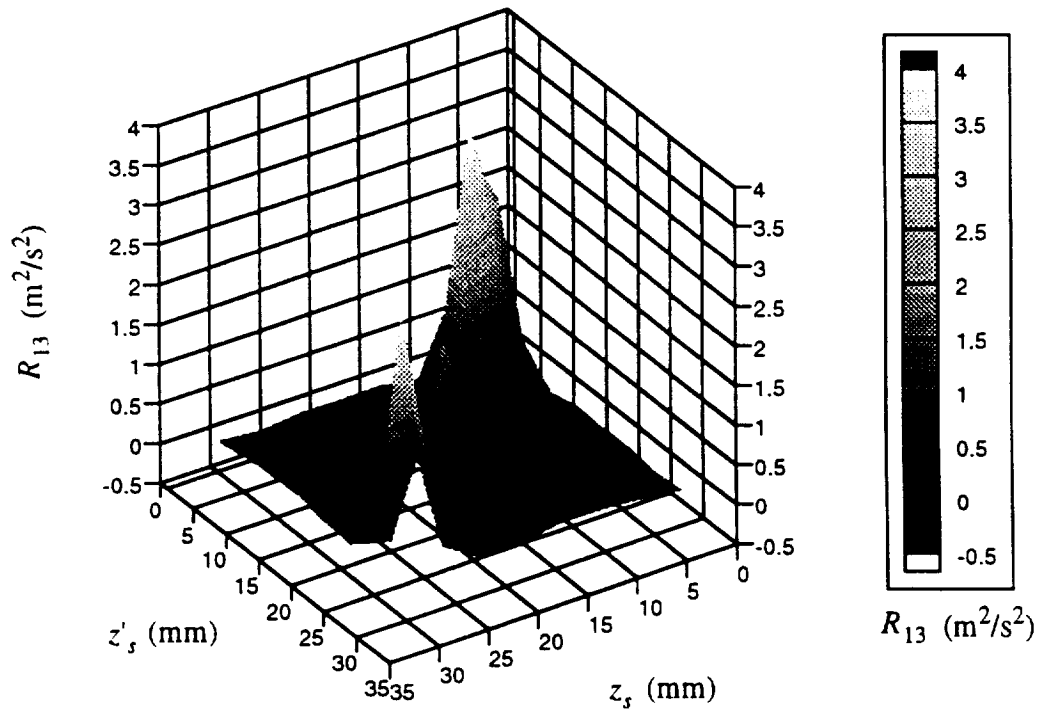

Figure 7.7: Cross-component spatial correlation tensor for the u and w components of velocity at $x/c = 0.58$, $y = 3.0$ mm.

extremely representative of either component's individual spatial correlation. This not only suggests that the velocity components remain coupled through transition but that they are actually more coupled in the turbulent regime than in the laminar regime. This increased coupling will become even more apparent in the dominant, spatially-evolving eigenfunctions resulting from the POD analysis (see chapter 8).

Figure 7.8 supplies the wire-frame plots of the same data presented in figures 7.5, 7.6 and 7.7 for relative structure comparisons. From these plots, we see that the small "ripples" present in the R_{11} off-center positions also show themselves clearly in the cross-component correlation. These small amplitude variations imply that remnants of the stronger periodic spanwise structures found in the laminar regime (shown in figure 7.4) survive transition in some form. The wavelength
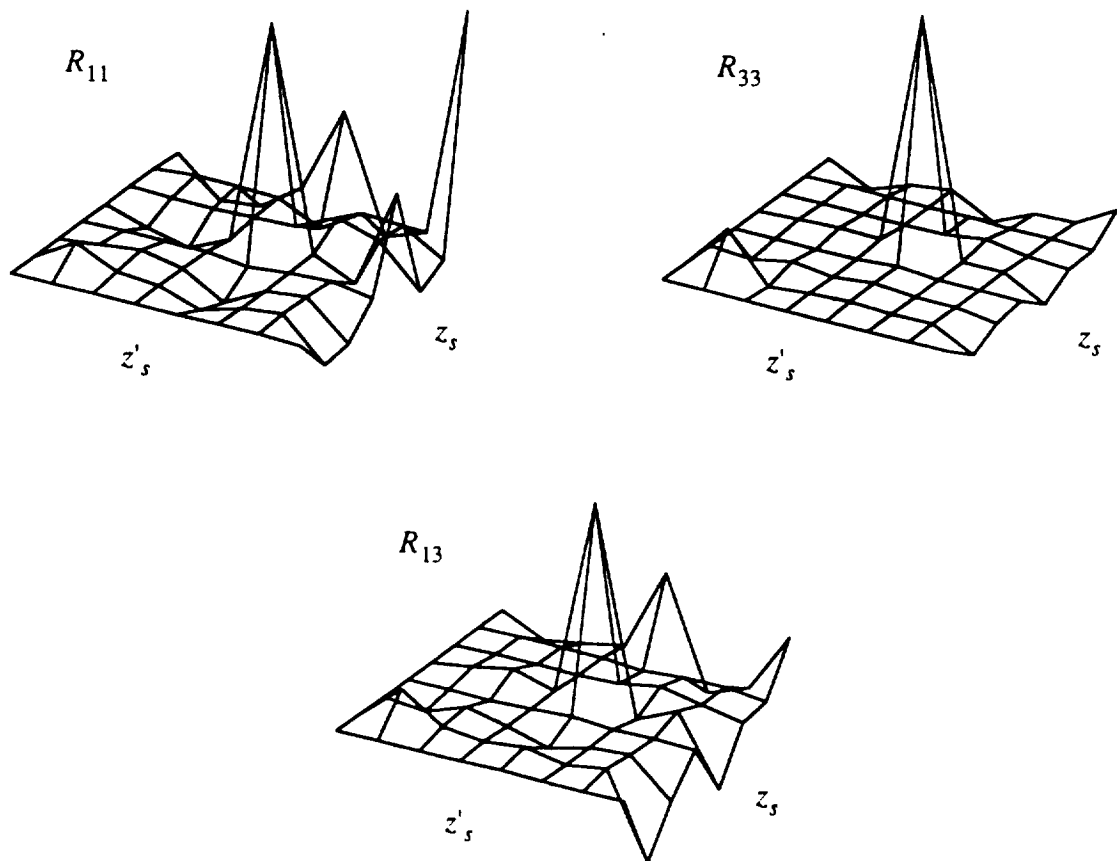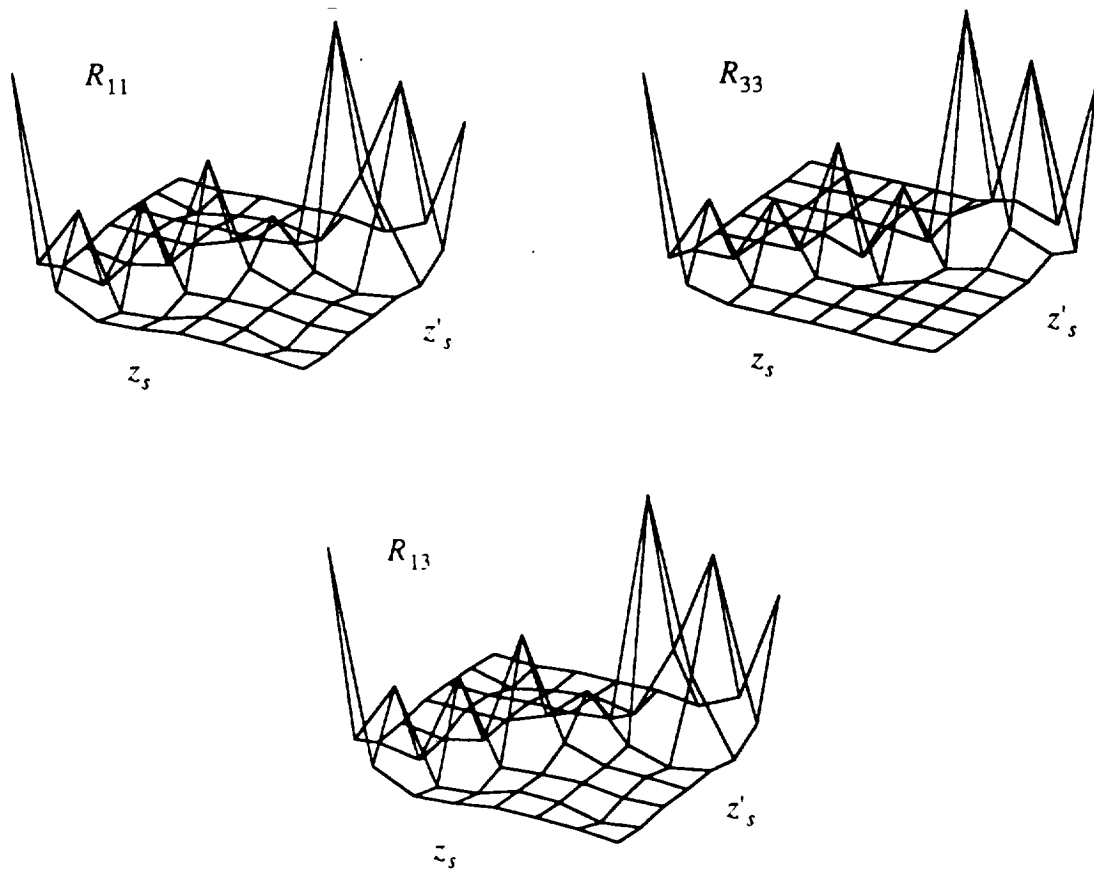

Figure 7.8: Wire-frame illustrations of spatial correlation data for u and w components of velocity at $x/c = 0.58$ and $y = 3.0$ mm.

of these "ripples" seems to have become broader in span but does in fact remain in the turbulent boundary layer. No evidence of these events are revealed in R_{33}. We will learn from inspection of the auto-spectra that these broad scales are generated from the primary instability. The small off-center variations which exist in the w-component correlation in the laminar regime (see R_{33} in figure 7.4) simply do not survive transition. This is again verified by the auto-spectra.

7.1.2 Crossflow Surface Shear-Stress Spatial Correlations

Similar spatial correlation calculations are made for the fluctuating surface shear stresses measured across the same span range as the velocity measurements. The measurement grid for the surface measurements, however, has double the spatial resolution of the velocity measurement grid. The spatial correlations are also calculated over the same number of blocks of the same record length to permit comparisons between the surface and internal measurements.

Figure 7.9 shows a three-dimensional surface plot of the one-dimensional, one component spatial correlation tensor for the spanwise-distributed surface shear stress at $x/c = 0.50$. The first apparent feature is the intense periodicity captured throughout the entire fluctuating flow field. Doubling the resolution of the measurement grid for the surface measurements clearly improves the structure identification of the stationary crossflow vortices. Also, by measuring the shear on the surface, the spatial correlations essentially capture the "foot-print" of the fluctuating internal flow, whereas the velocity spatial correlations are capturing the very top side of the crossflow vortices. Clearly, the added effects of increased measurement grid resolution and a completely submerged measurement location provide excellent detail in capturing the 12-mm forced wavelength of all three crossflow vortices in the laminar boundary layer. Also worth noting is the consistency of the peak amplitudes across the entire region verifying that the 6:12 artificial surface roughness elements do indeed statistically organize the crossflow-dominated flow uniformly.

Figure 7.10 shows the three-dimensional surface plot of the spatial correlation tensor for the spanwise-distributed surface shear stress at $x/c = 0.58$. The turbulent correlation shows a drastic increase in amplitude overall, but is concentrated at the 7-mm location and decreases over a rather broad range. This broad, high-shear region provides evidence that the crossflow vortices critically interact, thus starting the breakdown process giving way to the onset of turbulence. The additive effects of the fluctuating flow acquiring momentum from the mean flow and the merging
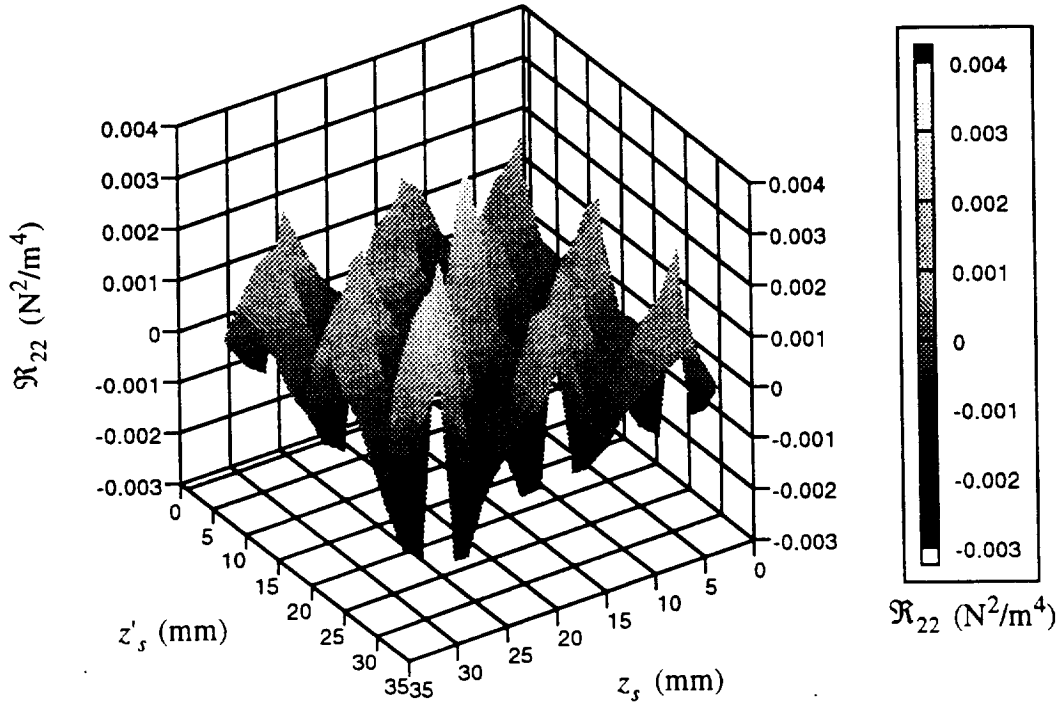
Figure 7.9: Spatial correlation tensor for the spanwise component of surface shear stress at $x/c = 0.50$.

of neighboring vortices produce rather large scales within the boundary-layer. The shear stress on the surface reflects the passing of these structures and creates regions of high shear. The streamwise location where the breakdown process actually begins, i.e., where the vortices start to interact and mix, demonstrate high-shear regions, particularly at spanwise locations where the doubly-inflected velocity profile once existed (refer to figure 5.13). It is at these locations where the greatest amounts of surface shear exist and where the mixing most likely starts since this is where the vortex structure is most unstable (Reibert 1996a). Directly beneath these sites of structure interaction, lies what we will refer to as the "spill region". These regions may be envisioned as locations where the stationary wave finally collapses upon itself and crashes onto the neighboring vortex, essentially eliminating the uniformity of the stationary field. The high-momentum fluid crashing to the surface (i.e., near-wall fluid within the spill region) will certainly generate large shear stresses which should propagate downstream. The slight shift in span should occur because of the small, but still significant, crossflow mean momentum (approximately 2.5% of the streamwise mean momentum).
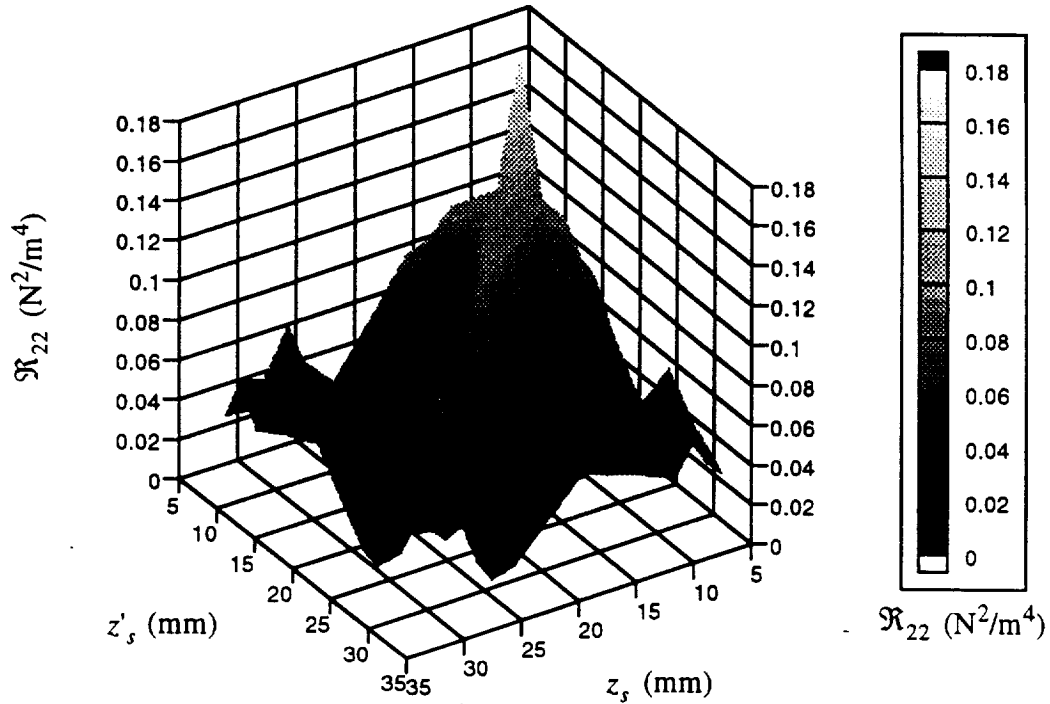
Figure 7.10: Spatial correlation tensor for the spanwise component of surface shear stress at $x/c = 0.58$.

Also note that the surface shear-stress measurements are acquired with the sensors aligned in the crossflow direction and therefore are predominantly measuring that component of surface shear. It is the author's interpretation that by the time the fluid within the *spill regions* propagate to $x/c = 0.58$ they are sensed as broad spanwise regions of high shear. Evidence of a broad high-shear region exists along the trace of the spatial correlation shown in figure 7.10 near 7 mm and yet again starting at 31 mm. It is interesting to note that the wavelength of this broad high-shear region is approximately twice the 12-mm forced wavelength of the stationary vortices in the laminar regime. Further evidence of the broad high-shear regions exist on the edges of the spatial correlation in figure 7.10. A clear structure of lesser amplitude than the trace exists ranging across approximately 24 mm from the right-hand plot wall. Thus, it appears that the breakdown process involves two vortices locally interacting and mixing to produce large-scale structures of a repeatable wavelength nearly double that of the original laminar structure wavelength. These large scales are accompanied by more random, smaller scales which are produced by the secondary
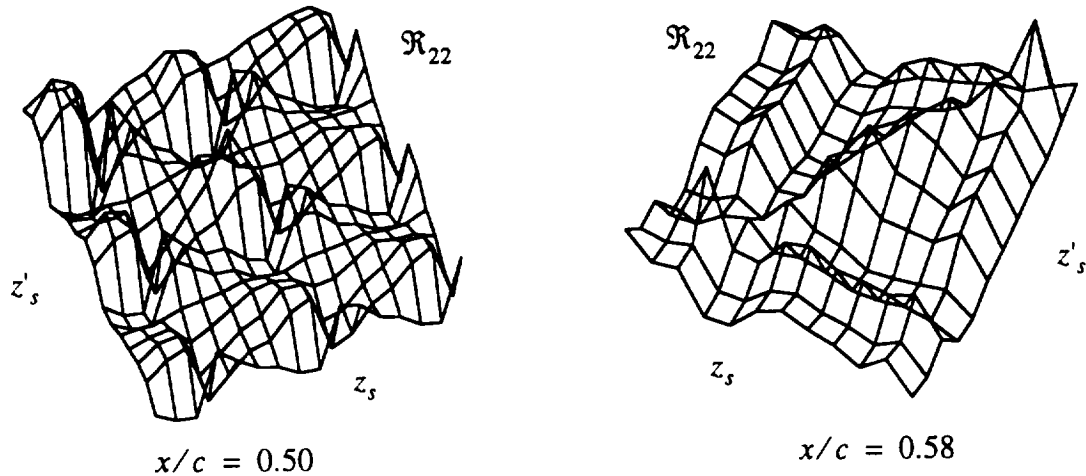
Figure 7.11: Wire-frame illustrations of spatial correlation data for the crossflow component of surface shear stress at $x/c = 0.50$ and $x/c = 0.58$.

instability mechanism.

Figure 7.11 displays the wire-frame versions of the data presented in figures 7.9 and 7.10 at different viewing angles to compare structural features before and after transition. The uniformity of the shear-stress correlation at the surface is evident at $x/c = 0.50$ through the periodic arrangement of the large spatial structures. At $x/c = 0.58$, broad, non-uniform, large-scale structures emerge extending over the spanwise direction providing further evidence of high span-wise shear regions resulting from the breakdown process. It is hypothesized that these regions are the result of the critical stationary wave interaction forcing fluid towards the surface.

7.1.3 Streamwise Surface Shear-Stress Spatial Correlations

The spatial correlation is also calculated for the surface shear-stress fluctuations evolving in the streamwise direction completely through the transition front ranging from $x/c = 0.49$ to just after $x/c = 0.57$. Figure 7.12 shows a three-dimensional surface plot of the spatial correlation for the streamwise evolving surface shear stress. The plot clearly shows rapid, yet smooth, growth in correlation amplitude as the flow progresses to downstream locations. By examining the edge of the plot surface, we see that the correlation first rapidly decreases then rises to a local maxi-
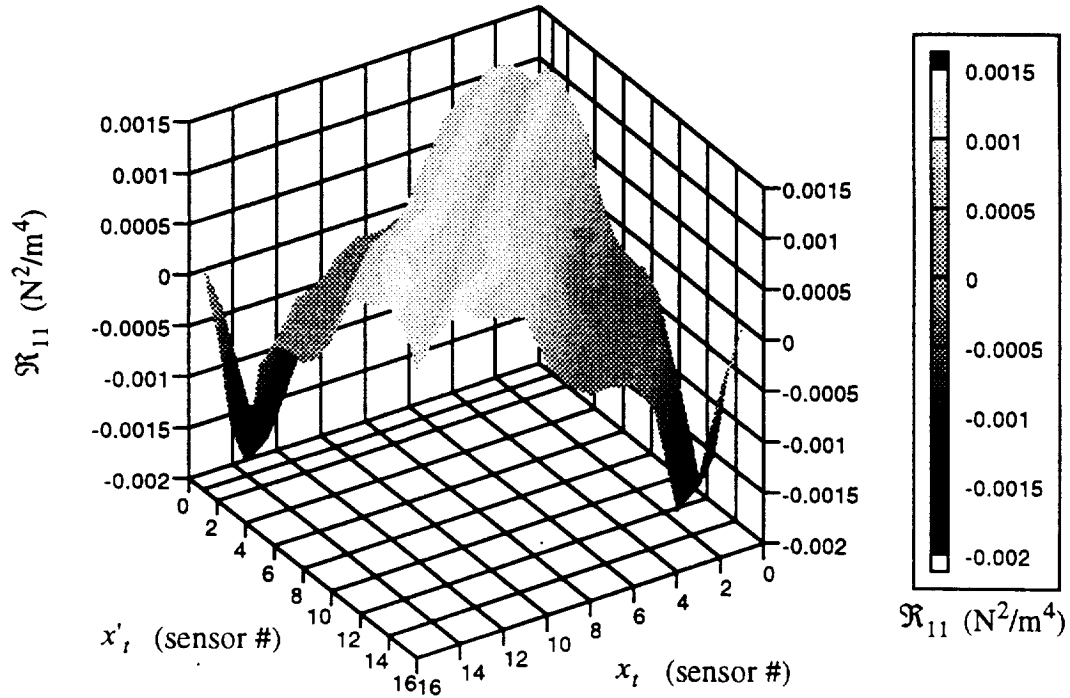
Figure 7.12: Spatial correlation tensor for the streamwise component of surface shear stress ranging from $x/c = 0.49$ to just before $x/c = 0.58$.

mum, slightly decreases again and then rises again to a second local maximum and then trails off further downstream. The local maxima in the correlations could be representative of the various instability mechanisms initiating the generation of turbulent scales. This is further supported by the auto-spectra. It is difficult to identify any definitive structure in this measured flow field from the spatial correlation tensor alone. However, it is clear that a significant amount of energy is being transferred as the fluid travels further downstream, thus providing evidence that the streamwise surface shear stress is indeed acquiring energy from the mean flow (mean shear stresses at the surface). This physically corresponds to the reshaping of the streamwise boundary-layer velocity profile. The slope of the streamwise velocity profile is becoming sharper as the flow travels downstream through the transition front and into the turbulent regime. This growth becomes very clear upon inspecting the spectra in section 7.2.3. The POD solutions also reveal some very interesting dynamics involved with the transition process (see chapter 8).

Figure 7.13 shows the corresponding wire-frame plot of the same data presented in figure 7.12 in a different perspective. The figure demonstrates a relatively high degree of spatial period-

128
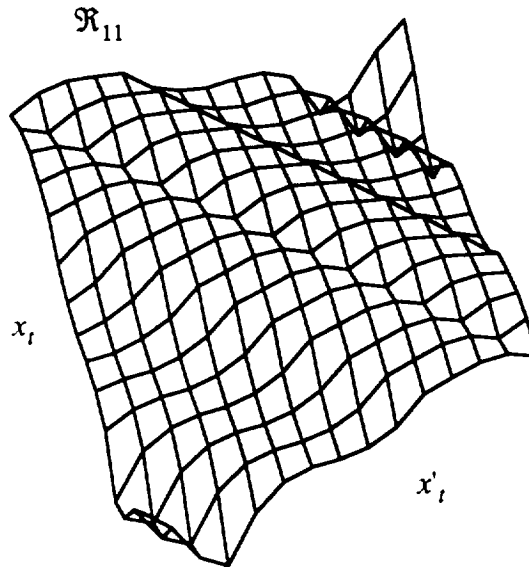
Figure 7.13: Wire-frame illustration of spatial correlation data for the streamwise component of surface shear stress through transition ranging from $x/c = 0.49$ to just before $x/c = 0.58$.

icity as the amplitude grows in the streamwise direction. This periodicity is most likely due to the secondary instability mechanism since the hot-film sensors are closely aligned to the center of a single crossflow vortex and lie beneath a doubly-inflected streamwise velocity profile (the 39-mm location in figure 5.13). We will look to the auto-spectra and to the POD solution for further insight into this periodicity and what mechanisms may lie imbedded within the measured flow field.

7.2 Auto-Spectra

As seen from the spatial correlation analysis, the trace contains the most significant structure. Therefore, we concentrate the spectral analysis on these autocorrelations. By Fourier transforming the spatially distributed autocorrelations in time, we can identify important features in the frequency domain and examine the levels of kinetic energy present in the measured flow fields. The auto-spectra are hence calculated for the two components of velocity and one component of the crossflow-directed surface shear stress across the span at $x/c = 0.50$ in the laminar regime and

at $x/c = 0.58$ in the turbulent regime. The auto-spectra for the streamwise surface shear stress through the transition front is also presented. Appropriate forms of equation 6.14 are used to compute the spectra which are also essentially averaged over 195 blocks of 0.0512 seconds since they are simply calculated by Fourier transforming the autocorrelations. The appropriate formulations of equation 6.14 are listed below for the two-component velocity (equation 7.1), the crossflow surface shear stress (equation 7.2) and the streamwise surface shear stress (equation 7.3). The two-component velocity auto-spectra is calculated from

$$S_{ii}(z_s, f) = \frac{1}{N} \sum_{n=0}^{N-1} R_{ii}(\hat{z}_s, \hat{t})e^{\frac{i2\pi nk}{N}} \tag{7.1}$$

where i has values of either 1 or 3 representing the u and w components, respectively. The auto-spectra for the crossflow-oriented surface shear stress is computed from

$$S_{22}(z_s, f) = \frac{1}{N} \sum_{n=0}^{N-1} \Re_{22}(\hat{z}_s, \hat{t})e^{\frac{i2\pi nk}{N}} \tag{7.2}$$

and from

$$S_{11}(x_r, f) = \frac{1}{N} \sum_{n=0}^{N-1} \Re_{11}(\hat{x}_r, \hat{t})e^{\frac{i2\pi nk}{N}} \tag{7.3}$$

for the streamwise surface shear stress

The auto-spectra is presented below in two plotting formats for each measured flow field. A three-dimensional surface plot similar to that used for the spatial correlation analysis is used with the three axes being space, frequency and spectra. The actual frequency content is then inspected more closely by plotting all velocity components at both chord positions together for each spanwise position on a standard X-Y log-log plot. This allows inter-regime comparisons of the relative energy and its evolution in span. The same plotting style is used for the surface shear stresses with slight differences (see their respective sections).

7.2.1 Velocity Auto-Spectra

3-D Surface Plots

The spanwise evolution of the auto-spectra at $x/c = 0.50$, 3.0 mm above the wing surface, is shown in the surface plots of figures 7.14 and 7.15 for the u and w components of velocity, respectively. The spanwise periodicity of the kinetic energy from the crossflow vortices clearly emerges from the auto-spectral surface of both components. This provides very clear evidence of the uniformity of the laminar vortex structure and verifies the measurement grid mapping to the mean velocity boundary-layer contours performed in section 5.5.2. A notable observation is that all three vortices known to exist within the range of measurement from that mapping process are well captured and are actually measured at nearly identical energy levels for the lower frequencies at corresponding vortex locations in span. Referring back to the spatial correlation plot for the same data (figures 7.1 and 7.4), we see that only one of the three existing structures is strongly

Figure 7.14: Auto-spectral surface for the u component of velocity at $x/c = 0.50$, $y = 3.0$ mm.
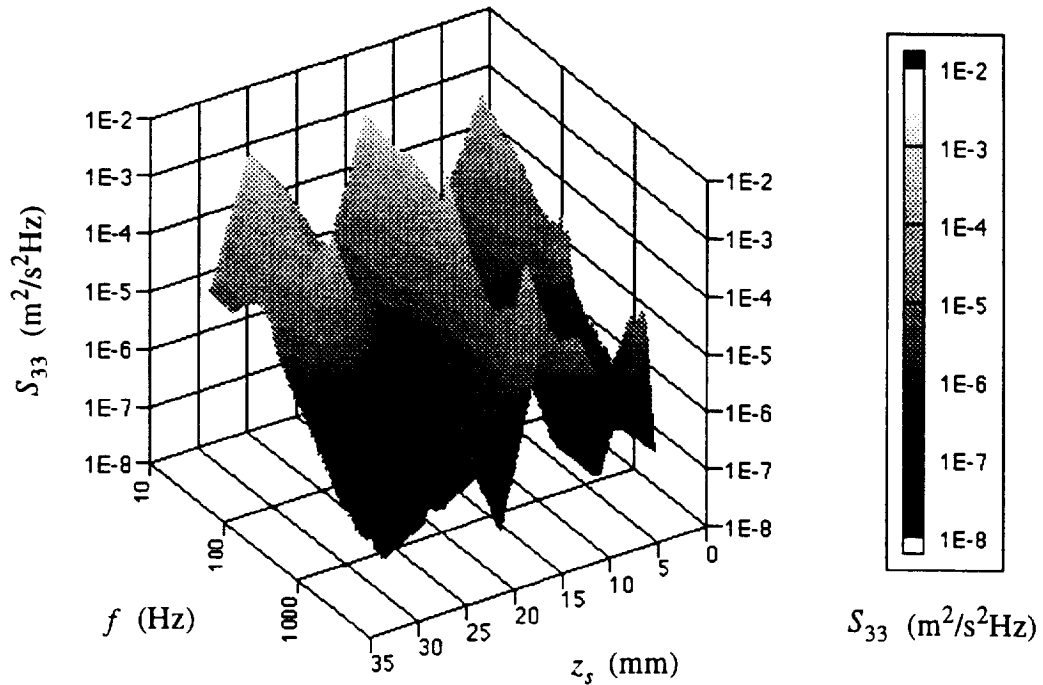
Figure 7.15: Auto-spectral surface for the w component of velocity at $x/c = 0.50$, $y = 3.0$ mm.

identified. The other two are recognizable due to our prior knowledge of their existence but are only weakly identified through the spatial correlation analysis alone. This reveals the true strength of auto-spectral analysis, the ability to identify structure based on the measured energy content of the flow.

The energy contained within the flow field certainly provides excellent identification of structure in the laminar velocity field when viewed in spectral space. Also note that the one vortex which is well captured by the spatial correlation analysis (the one centered about the 15-mm location) has significantly more spectral information than the other two. The higher frequencies display higher amplitudes for this structure than for the other two. Simply more information is measured at this location where the measurement site is known to exist within the high-velocity region of a vortex, as opposed to between the stationary structures, as is the case for other measurement sites near the other two vortices. Thus the spatial resolution problem experienced in the correlation analysis may be overcome by inspecting the data in the frequency domain.

Significant events at some higher frequencies exist within the peak spectra for each vortex. These span locations at 3 mm, 15 mm and 27 mm correspond to the first, fourth and seventh dots (from the left) in the mean velocity contour map shown in figure 5.13. All three measurement sites are located above doubly-inflected velocity profiles, especially the location at 15 mm. The spanwise location of these peak events at higher frequencies suggest that they are the spectral signatures of the secondary instability mechanism produced by the inflection of the mean velocity profile. In fact, Kohama et al. (1991) show similar spectral events to occur over the doubly-inflected velocity profiles within the swept-wing boundary layer over the same airfoil. This hypothesis will be further discussed upon closer inspection of the auto-spectra plots at individual span locations.

The spanwise evolution of the turbulent auto-spectra at $x/c = 0.58$, 3.0 mm above the wing surface, is shown in figures 7.16 and 7.17 for the u and w components, respectively. Here, we see that the entire flow field has gained a great deal of energy in both components. This drastic energy increase through transition suggests that the fluctuating velocity field has acquired a significant amount of energy from the mean flow. That energy transfer appears to have been focused on the span locations that lie between the vortices in the laminar flow field, i.e., the "valleys" in figures 7.14 and 7.15. The spectra did not significantly increase in the high-energy regions of the laminar regime. Energy is specifically being transferred to those valley span locations, regions of high surface shear in the laminar regime, by the transition process. As a vortex collapses, it supplies kinetic energy to the low-energy regions previously located between the vortex structures.

Another interesting observation is that the auto-spectra of the streamwise component in the turbulent regime has very little variation in span, whereas the w component still exhibits some significant spanwise structure. Thus, it seems that some turbulent structure is produced directly from the remnants of the strong crossflow in the laminar regime. Coherent structures in the turbulent velocity field are originating from the periodic structure of the crossflow vortices despite the destructive mixing process of transition.

133

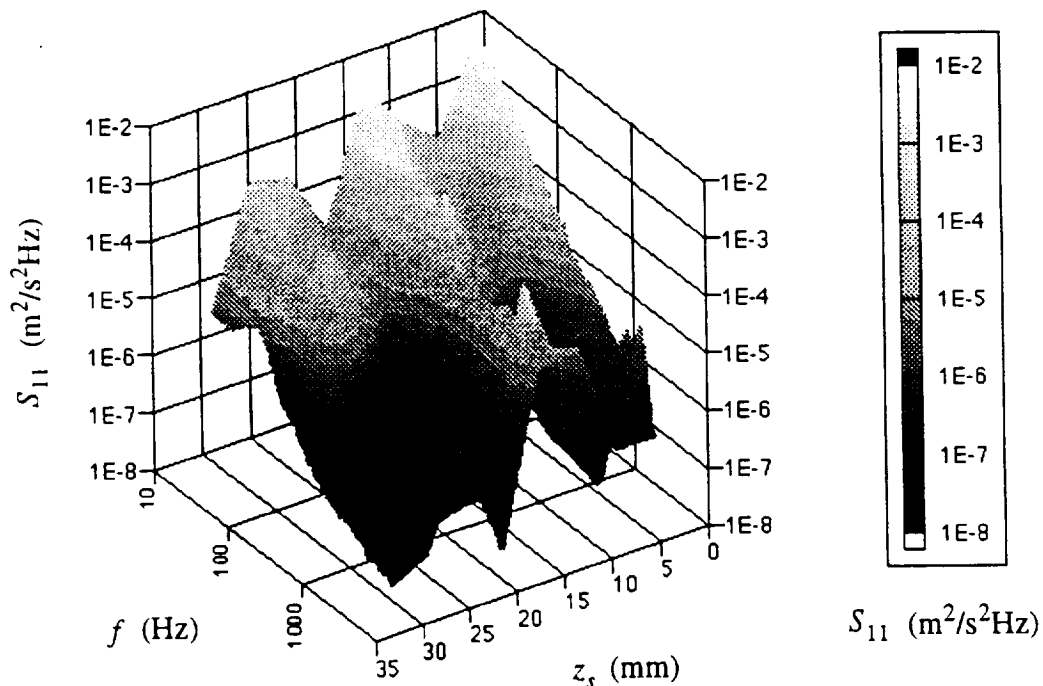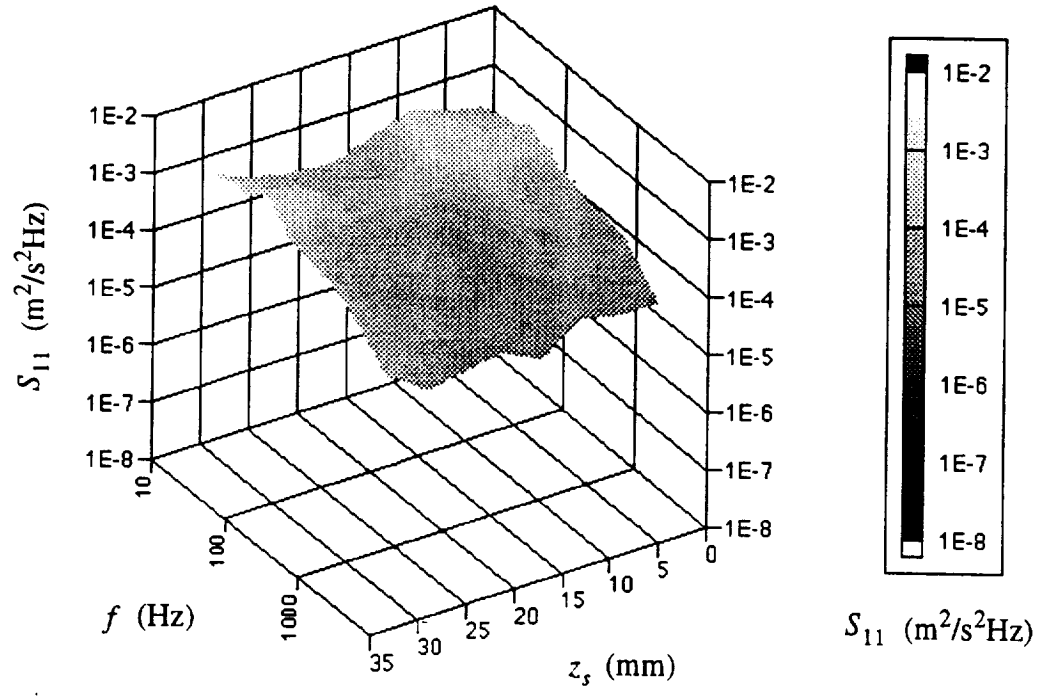Figure 7.16: Auto-spectral surface for the u component of velocity at $x/c = 0.58$, $y = 3.0$ mm.
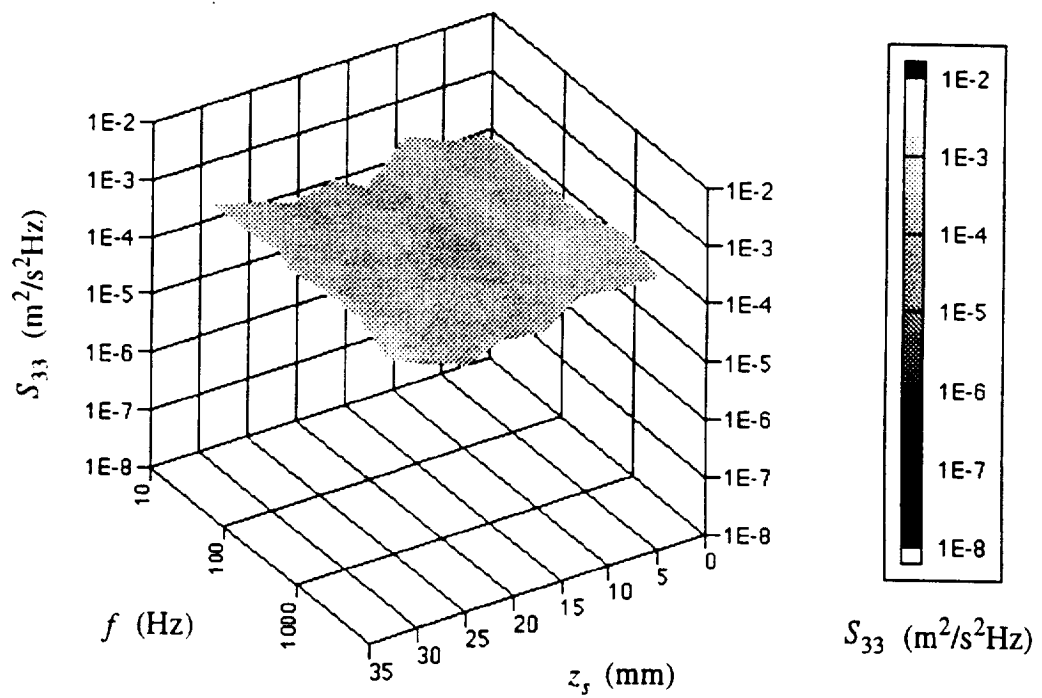
Figure 7.17: Auto-spectral surface for the w component of velocity at $x/c = 0.58$, $y = 3.0$ mm.

After arriving at the spatial results of the auto-spectra for the two components of velocity before and after transition, we take a closer look at the actual frequencies excited by the flow by examining traditional X-Y log-log plots (auto-spectra versus frequency) comparing the two chord locations for both components at each spanwise location. Figures 7.18 through 7.25 display these data sets with both components for each chord location plotted together at each span location for the sake of evolutionary comparisons. The u component auto-spectra are plotted using thinner lines and data for the velocities acquired at $x/c = 0.58$ are grayed to avoid confusion. Plotting these quantities on the same graph allows us to identify the effects of transition on various spectral events at specific frequencies.

Kohama et al. (1991) observed two distinct spectral peaks in their analysis of the streamwise component of velocity in the boundary layer over the same airfoil in the laminar regime. They discovered a peak centered at 350 Hz and a second peak at 3.5 kHz for spectra acquired at span locations just above a doubly-inflected mean-velocity profile. Their analysis attributes the first peak as the spectral signature of the primary instability mechanism of the travelling wave. They attribute the second peak to the secondary instability (a form of Rayleigh instability) which, according to Kohama (1987), is a streamwise inflectional instability appearing on top of each of the streamwise crossflow vortices. Poll (1985) first discovered these spectral signatures of the secondary instability at very high frequencies (near 17.5 kHz) for the flow over a swept cylinder.

We see very similar spectral events in the laminar velocity shown in figures 7.18, 7.21 and 7.24 to that of Kohama et al. (1991). These figures display the auto-spectra acquired directly above a doubly-inflected profile area (refer to figure 5.13 and the appropriate mapping of the corresponding measurement sites). A definitive double-peak event resides near 300 Hz for the laminar cases in figures 7.18, 7.21 and 7.24 with the first peak at 255 Hz and the second at 315 Hz. The very slight difference in frequency between these results (300 Hz) and those of Kohama et al. (350 Hz) is most likely due to the fact that these measurements are made at $y/\delta = 0.75$ (where δ is the boundary-layer thickness) whereas Kohama et al. acquired their data at $y/\delta = 0.50$. An additional observation is that these events occur in both components and are at relatively equivalent energy levels per span location. The same spectral events also occur in figures 7.20, 7.22 and 7.23 for $x/c = 0.50$ but are not as well defined. These span locations correspond to positions

Figure 7.18:
location at 3 mm
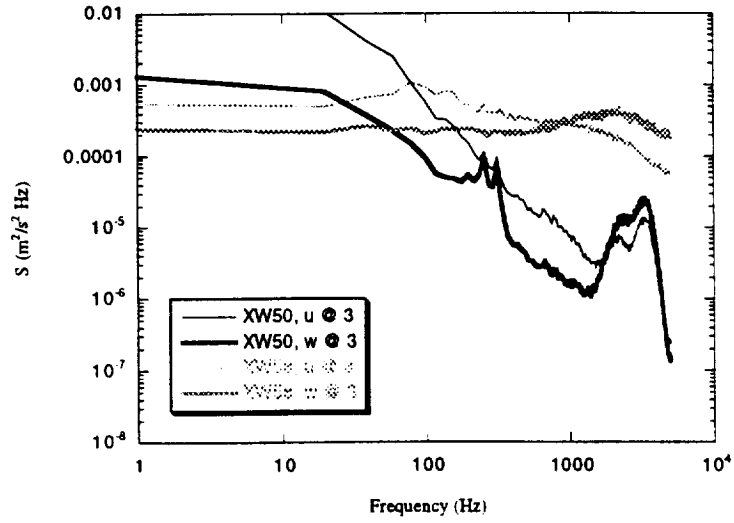
Figure 7.19:
location at 7 mm
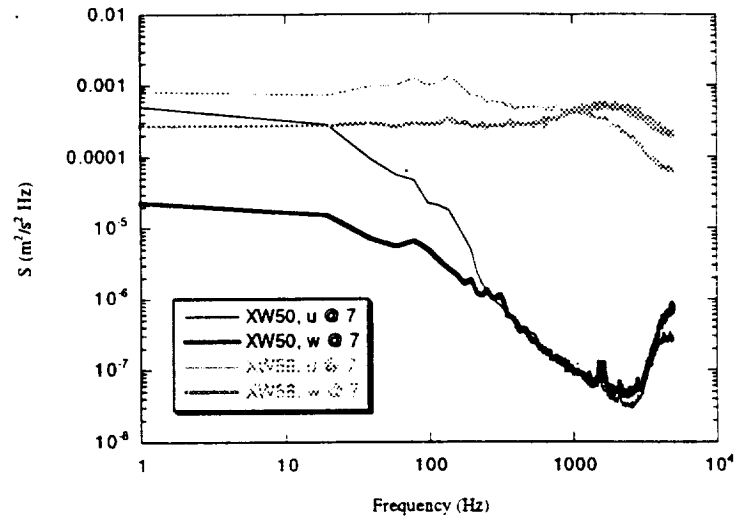
Figure 7.20:
location at 11 mm
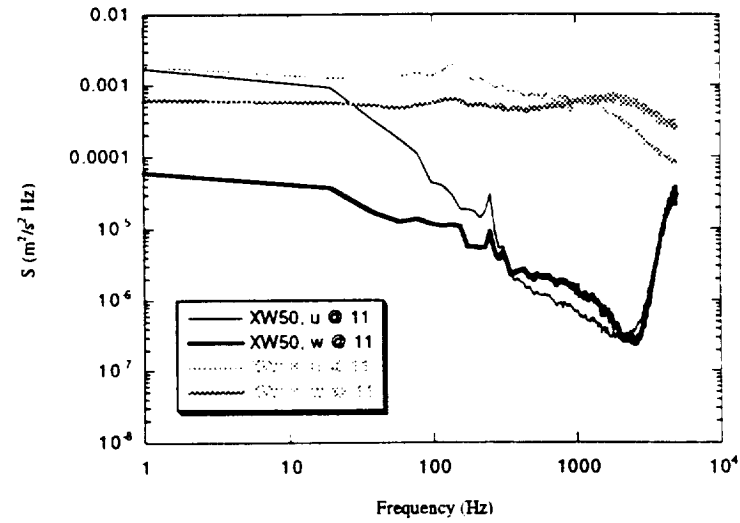
Figures 7.18, 7.19 and 7.20: Auto-spectra on log-log axes for both velocity components at $x/c = 0.50$ and $x/c = 0.58$, $y = 3.0$ mm at $z_s = 3, 7$ and 11 mm, respectively.

Figure 7.21:
location at 15 mm
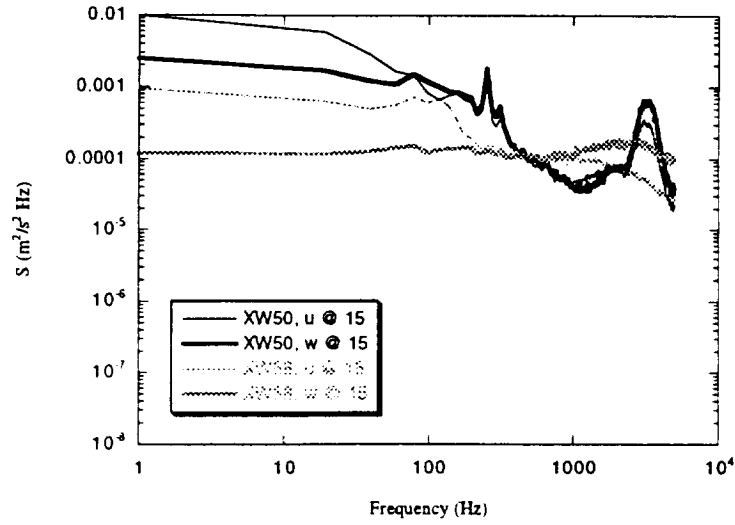
Figure 7.22:
location at 19 mm
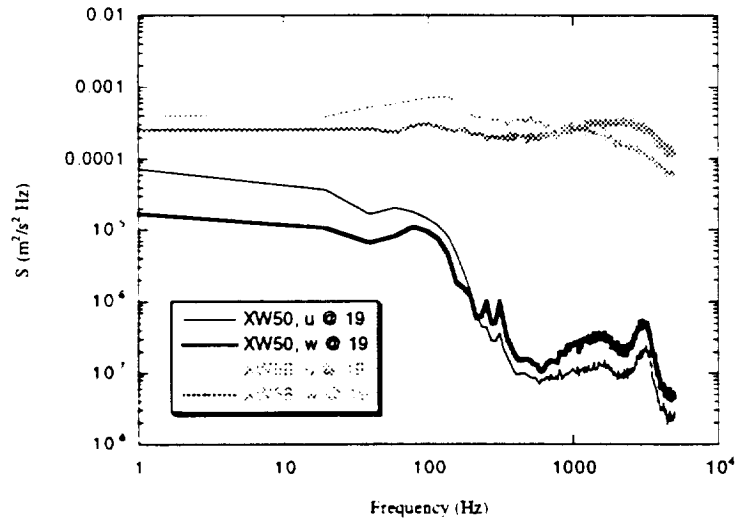
Figure 7.23:
location at 23 mm
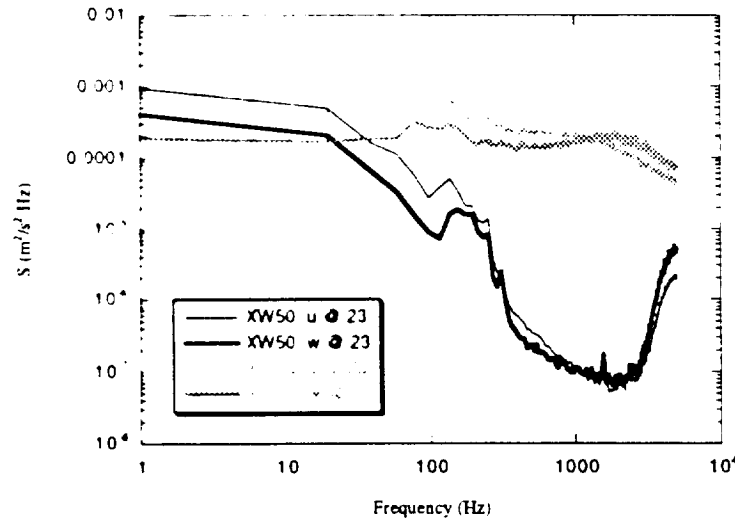
Figures 7.21, 7.22 and 7.23: Auto-spectra on log-log axes for both velocity components at $x/c = 0.50$ and $x/c = 0.58$, $y = 3.0$ mm at $z_s = 15$, 19 and 23 mm, respectively.

Figure 7.24:
location at 27 mm
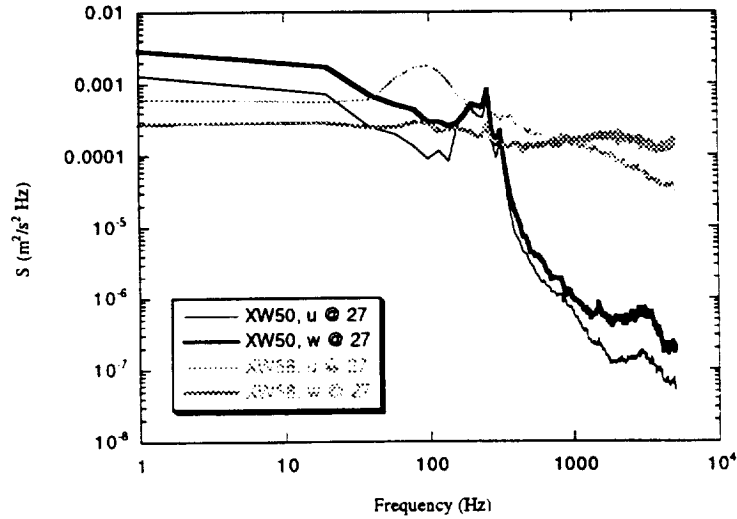
Figure 7.25:
location at 31 mm
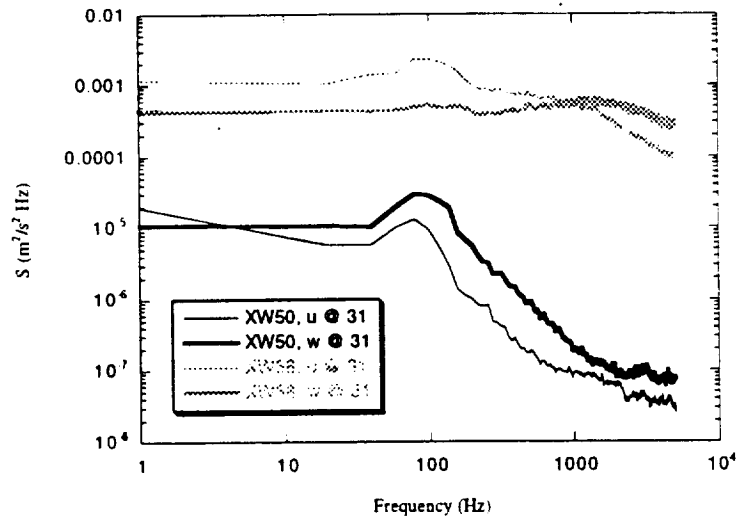
Figures 7.24 and 7.25: Auto-spectra on log-log axes for both velocity components at $x/c = 0.50$ and $x/c = 0.58$, $y = 3.0$ mm at $z_s = 27$ and 31 mm, respectively.

neighboring the doubly-inflected velocity profile areas and apparently contain remnant signatures of the travelling wave.

Another low-frequency event occurs in the span locations between the vortices. Figures 7.22 and 7.23 contain this event at a frequency near 100 Hz. Figure 7.19 contains a weaker event at this frequency. Each of these spanwise locations corresponds to the areas where the up-swelling of fluid occurs, i.e., above regions of low surface shear stress. This is most likely the spectral signature of the travelling wave's mechanism responsible for transferring low-momentum fluid away

from the wing surface.

The secondary instability is identified in the laminar regime at the higher frequency peak in figures 7.18, 7.21 and 7.24. This very broad peak is centered near 3.0 kHz and displays very similar features observed by Kohama et al. (1991). The peak is only observed at spanwise locations corresponding to measurements made directly above the doubly-inflected velocity profile. Looking at the higher frequency range at different locations in span, one sees that the peak shifts past 5.0 kHz and then reappears at 3.0 kHz as the location shifts back over the doubly-inflected portion of the mean velocity contours. Each position that exhibits the +5.0 kHz event is located directly between the vortices and therefore could be a result of the interaction between up-swelling fluid particles from one vortex and down-swelling fluid particles from the neighboring vortex.

A very interesting feature of the turbulent auto-spectra emerges for every span location. The u component exhibits a low-frequency event centered at 100 Hz which qualitatively corresponds to the same laminar peaks seen in span locations which reside between two vortices (demonstrated in the laminar cases in figures 7.23 and 7.25). These events are not observed in any of the w components for the turbulent case (with the exception of figure 7.23). The w component does display the higher frequency event characteristic of the secondary instability in the turbulent regime. However, its center appears shifted to approximately 2.0 kHz and extends over a broader band. These features are not seen at all in the u components. Thus, we have seen the origins of two important scales in the turbulent swept-wing boundary layer. Two events in the laminar regime (the 100 Hz and 3.0 kHz peaks) seen in both components separate through transition. The 100 Hz event attributed to remnants from the primary instability survives transition in the streamwise velocity but is eradicated in the w component. The 3.0 kHz peak attributed to the secondary instability present in both laminar components only remains in the w component after transition but only after becoming broader and acquiring more energy from the mean flow thus providing significant small-scale turbulence. Therefore, it can be stated that the large-scale structure in the turbulent regime originates from the primary instability mechanism for the streamwise component of velocity. Likewise, the small-scale structures in the turbulent regime originate from the secondary instability mechanism for the w component and are a direct result of the doubly-inflected velocity profile.

7.2.2 Crossflow Surface Shear-Stress Auto-Spectra

3-D Surface Plots

The auto-spectra for the surface shear stress measured with the crossflow-oriented hot-film sheets are displayed in figures 7.26 and 7.27 for $x/c = 0.50$ and $x/c = 0.58$, respectively. The better spatial resolution of these measurements improves the identification of the crossflow vortices in the laminar regime. The surface plot is much smoother in span and the energy present in each vortex is observed in a more uniform manner. The surface plots show few features at higher frequencies compared to that seen by the velocity measurements. This is due in part to the weaker frequency response of these sensors. In addition, the technique used to calibrate the hot-film sensors limits the frequency response to 3.0 kHz thus minimizing our ability to appropriately capture the high-frequency effects of the secondary instability. Thus, we find a limitation with the hot-film technology. The hot-films are certainly appropriate for spatial measurements but filter much of the higher frequency information used to quantify the highly nonlinear instability mechanisms. We
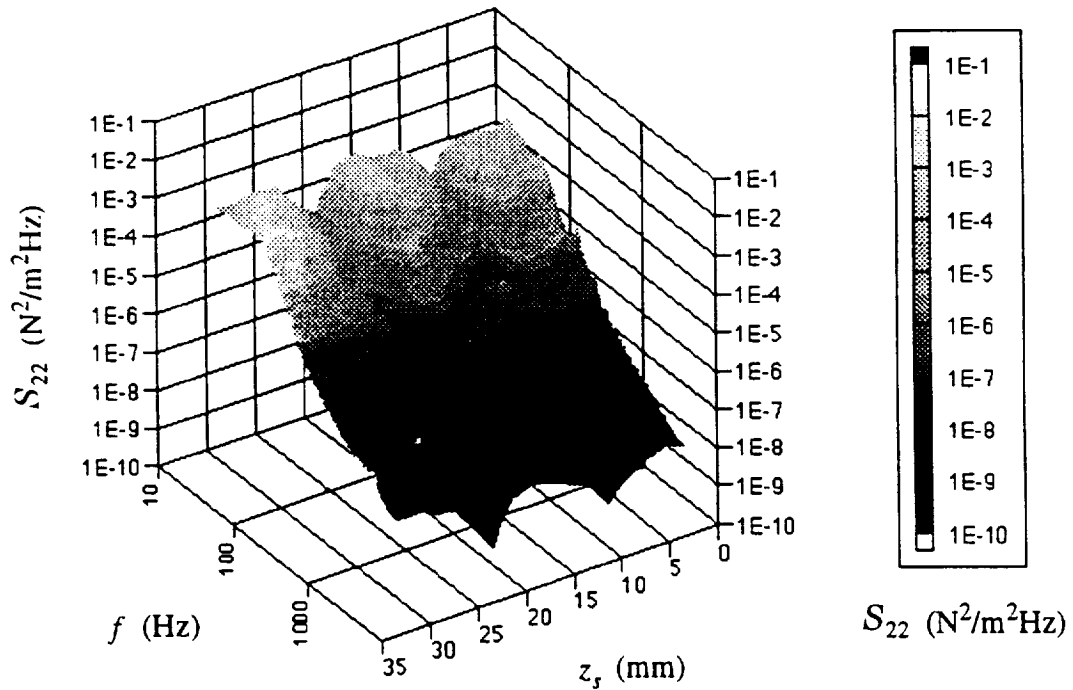
Figure 7.26: Auto-spectral surface for the crossflow-oriented surface shear stress at $x/c = 0.50$.
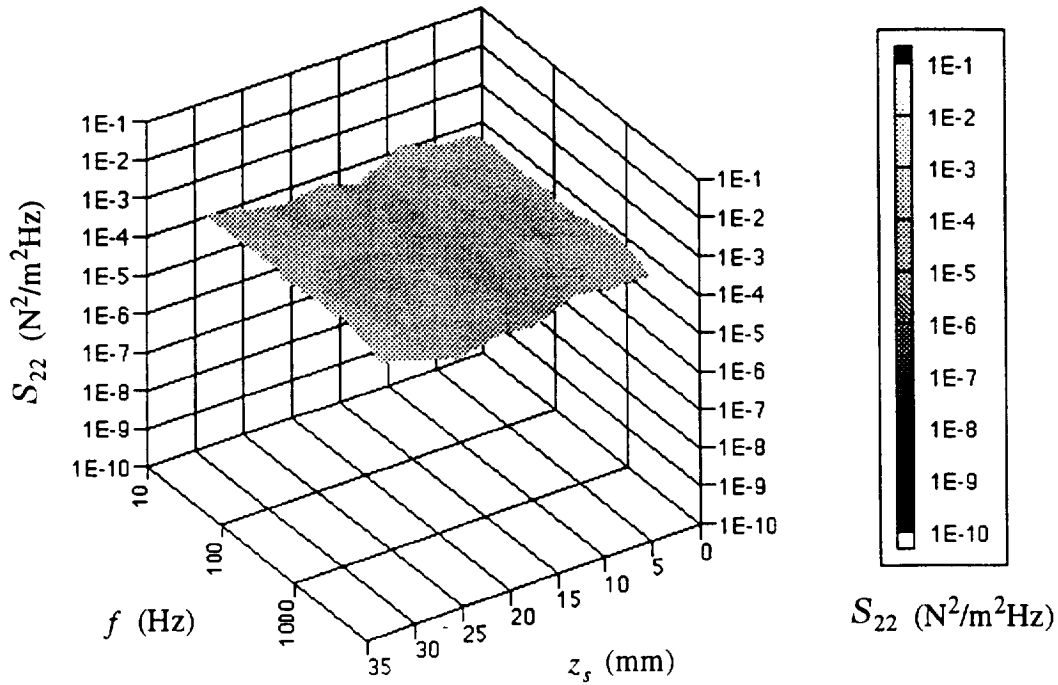
Figure 7.27: Auto-spectral surface for the crossflow-oriented surface shear stress at $x/c = 0.58$.

will look for evidence of the travelling waves in the X-Y log-log plots since little evidence of their existence is seen in the surface plots. The turbulent auto-spectra reveal similar results in that spatial information is again retained but very little high frequency information is observed. The spatial information shows that some of the spatial periodicity seen in the laminar regime survives the transition process and creates large spatial structures in the spanwise direction.

X-Y LOG-LOG Plots

The X-Y log-log plots for the crossflow surface shear stress are plotted in figures 7.28 through 7.39. Not all spatial locations are available for the crossflow measurements in the turbulent regime due to the few failed sensors on that hot-film sheet (as discussed in section 5.4.2). Therefore, the "extra" locations for the laminar regime are plotted on the same graph as their neighbors to allow for some comparison to a "nearby" measurement in the turbulent regime.

Upon closer inspection of the frequency content present in the auto-spectra, we see that the two instabilities detected in the velocity measurements are indeed also identified in some form for the surface shear stress measurements in span. The surface shear-stress measurements are compa-

Figure 7.28:
locations at
1, 3, 5 mm
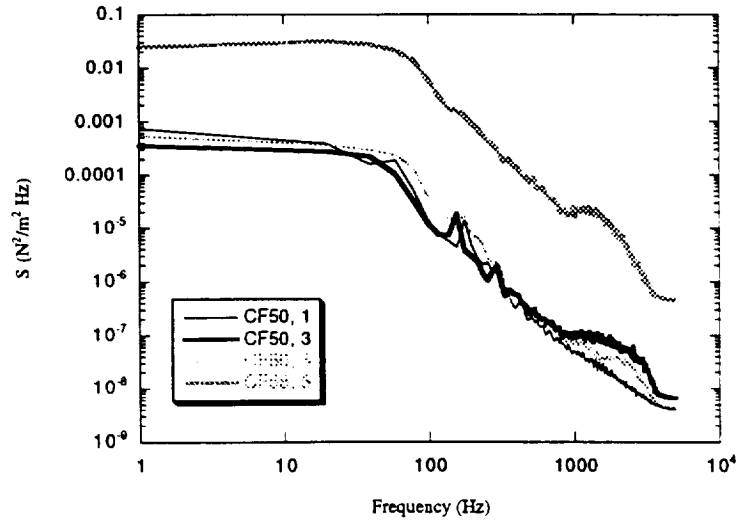
Figure 7.29:
locations at
7, 9 mm
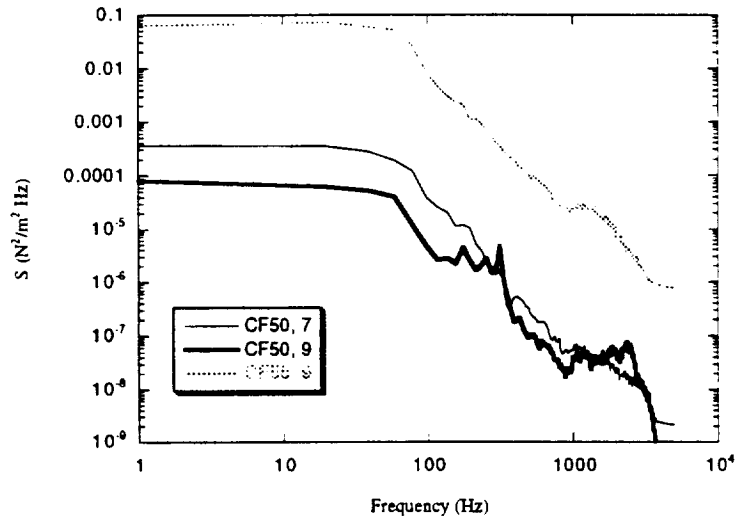
Figure 7.30:
locations at
11, 13 mm
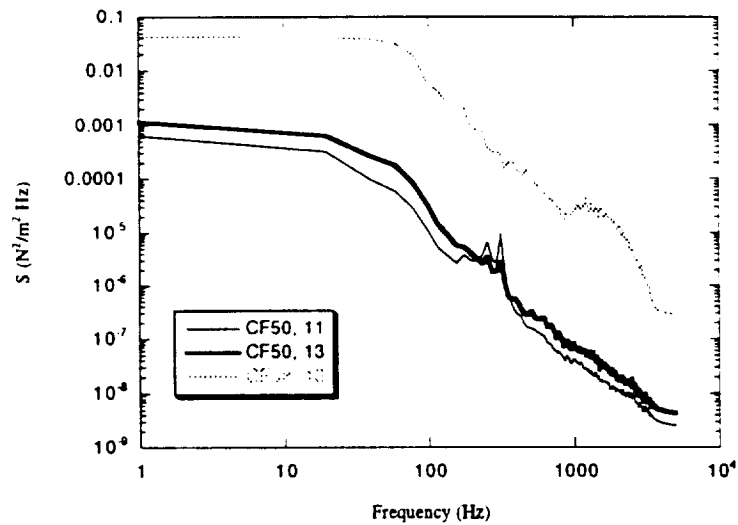
Figures 7.28, 7.29 and 7.30: Auto-spectra on log-log axes for the crossflow surface shear stress at $x/c = 0.50$ and $x/c = 0.58$ at $z_s = 1-5, 7-9$ and $11 - 13$ mm, respectively.

Figure 7.31:
location at 15 mm
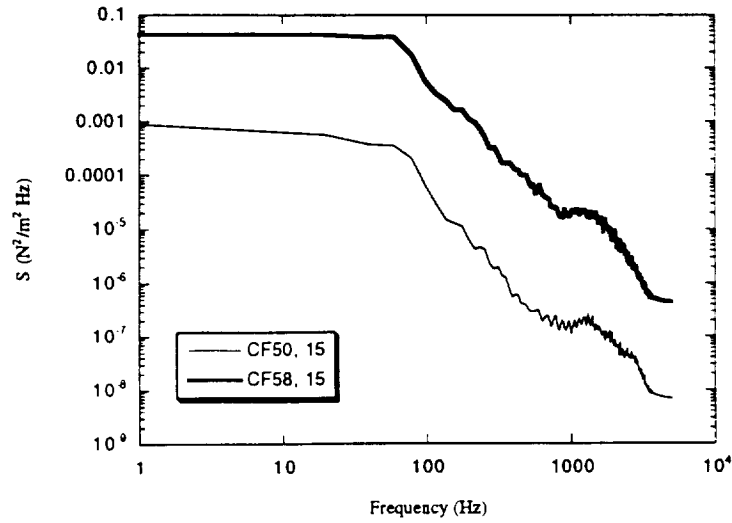
Figure 7.32:
location at 17 mm
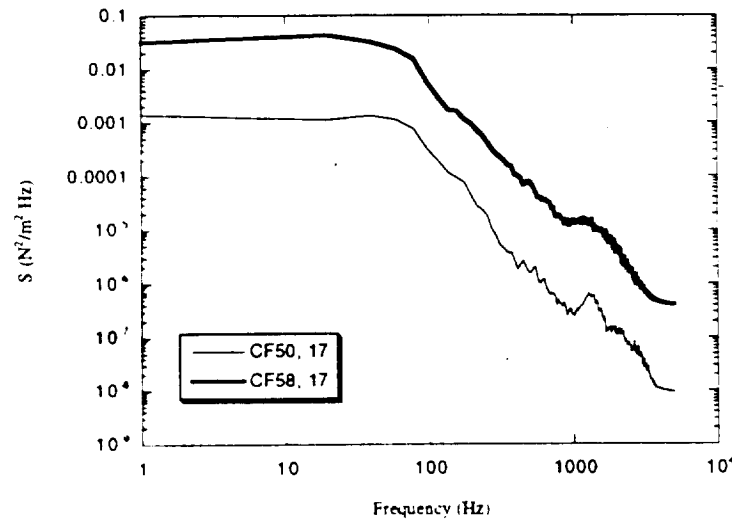
Figure 7.33:
location at 19 mm
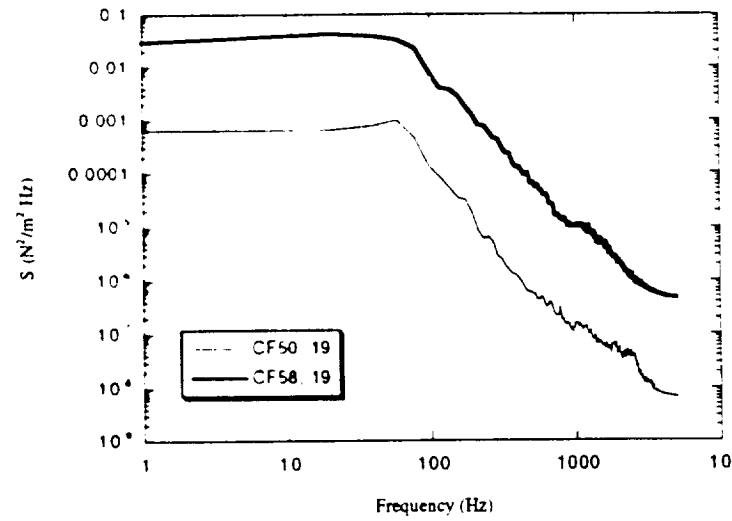
Figures 7.31, 7.32 and 7.33: Auto-spectra on log-log axes for the crossflow surface shear stress at $x/c = 0.50$ and $x/c = 0.58$ at $z_s = 15, 17$ and 19 mm, respectively.

Figure 7.34:
location at 21 mm
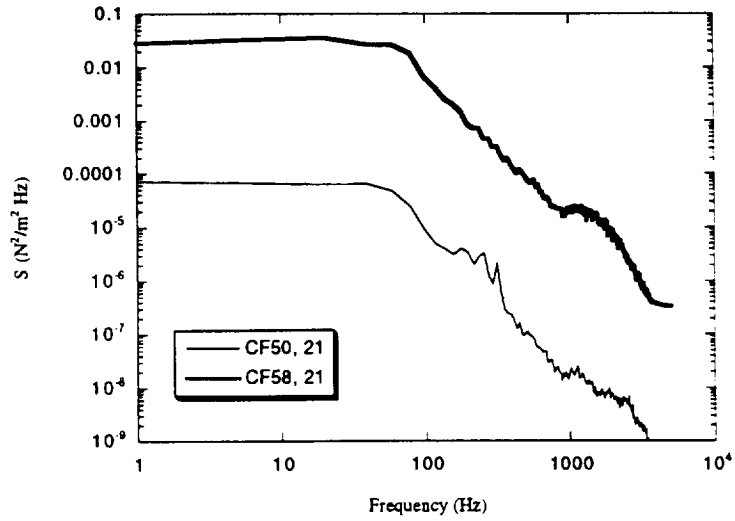
Figure 7.35:
location at 23 mm
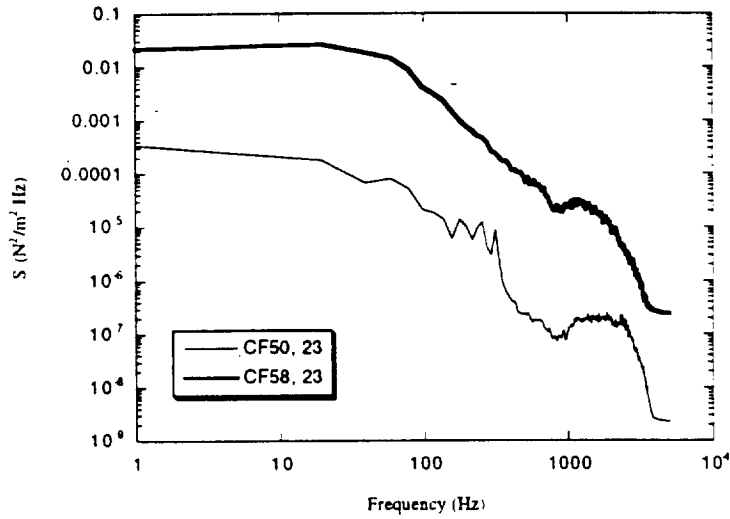
Figure 7.36:
location at 25 mm
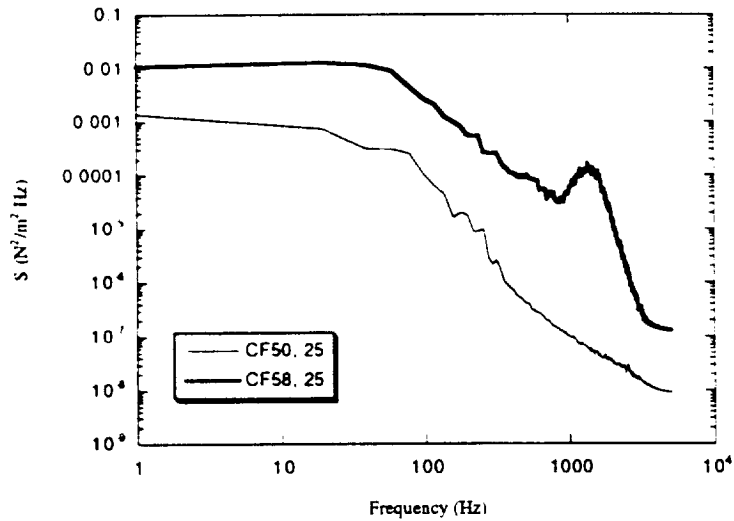
Figures 7.34, 7.35 and 7.36: Auto-spectra on log-log axes for the crossflow surface shear stress at $x/c = 0.50$ and $x/c = 0.58$ at $z_s = 21, 23$ and 25 mm, respectively.

144

Figure 7.37:
location at 27 mm
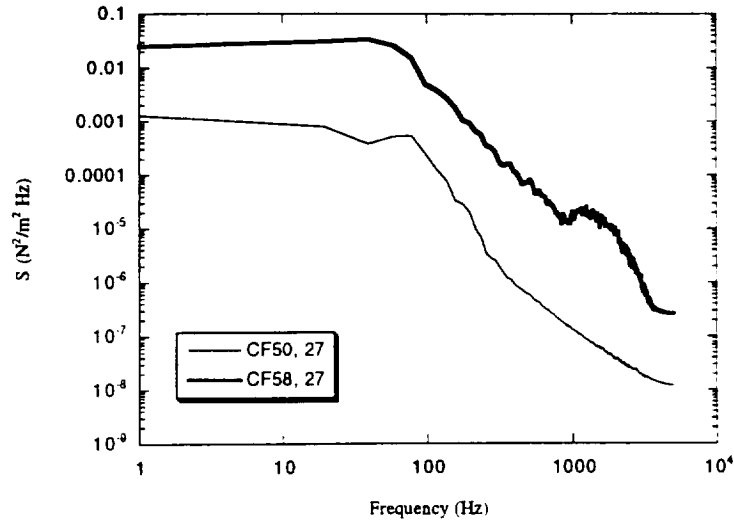
Figure 7.38:
location at 29 mm
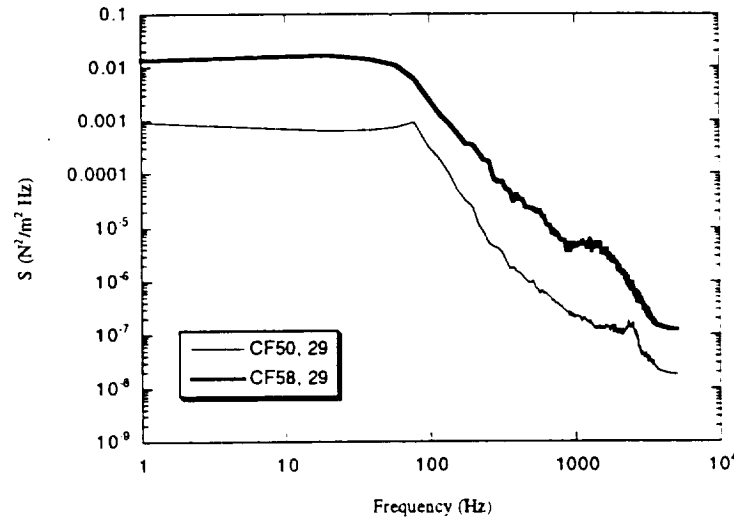
Figure 7.39:
location at 31 mm
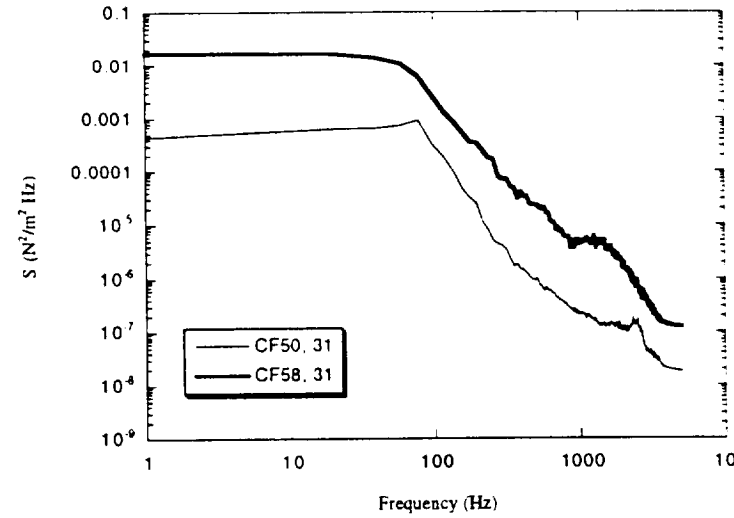
Figures 7.37, 7.38 and 7.39: Auto-spectra on log-log axes for the crossflow surface shear stress at $x/c = 0.50$ and $x/c = 0.58$ at $z_s = 27, 29$ and 31 mm, respectively.

rable to the w component of the velocity measurements. In particular, the primary instability is identified at similar frequencies on the surface (near 300 Hz). The laminar cases in figures 7.29 (location at 9 mm), 7.30 (location at 11 mm), 7.34 and 7.35 display these same events including the double-peak feature. These locations again correspond to the regions between the vortices, i.e., in regions of high shear where the fluid is being forced to the surface by the vortical motions. None of these signatures are present in the turbulent cases which is consistent with the velocity spectra results where these events were only found in the u component. We might expect to see some form of these low-frequency travelling-wave effects in the streamwise component of surface shear stress based on the streamwise velocity spectra observations.

The secondary instability is not detected as well as in the velocity measurements but is somewhat identifiable based on our prior knowledge. The limitations of the instrumentation and calibration technique become obvious here where the high frequency data is somewhat filtered. Despite these faults, figures 7.28 (locations at 3 and 5 mm), 7.29 (location at 9 mm), 7.31, 7.32, 7.34, 7.35, 7.38 and 7.39 each display high frequency events typically centered near 2.0 kHz or 2.5 kHz. Thus, the secondary instability does leave a "foot-print" on the surface but is better detected by the internal measurements due to the sensor limitations. However, with ever improving hot-film technology, the frequency response may possibly be increased in the future to properly identify these high-frequency instabilities from the surface. For now, we at least know that the spectral signature is indeed contained within the surface shear stress. As expected, the crossflow shear component in the turbulent regime displays the second instability as well. Aside from the increased energy level, figures 7.31, 7.32 and 7.33 show very little difference in frequency content between the laminar and turbulent cases. The high-frequency peak in the turbulent cases at almost every span location are centered near 1.3 kHz. Thus, we again see the shift of the secondary instability signature through transition. However, the bandwidth is not significantly broader than the secondary instability event seen in the laminar flow field as was the case with the velocity measurements. Therefore, although the hot-film sensors do not pick up as much detail as the internal velocity measurements, they do display the fundamental characteristics of the instability mechanisms which is an important result when considering in-flight applications where internal measurements are typically not feasible.

146

7.2.3 Streamwise Surface Shear-Stress Auto-Spectra

3-D Surface Plot

Figure 7.40 displays the three-dimensional surface plot for the streamwise evolution of the surface shear-stress field through the transition front. Again, only spatial structure is truly observable from this plotting technique. We see that there is a significant jump in the energy level as the flow progresses downstream. There appears to be a gradual, underlying build-up of energy as the flow approaches the transition front which then rapidly increases through the actual transition region and settles once the turbulent regime is engaged. Not much information is available at higher frequencies, although a significant increase in energy is again witnessed. We should expect to see the evolution of the instability mechanisms through transition upon closer inspection of the auto-spectra.
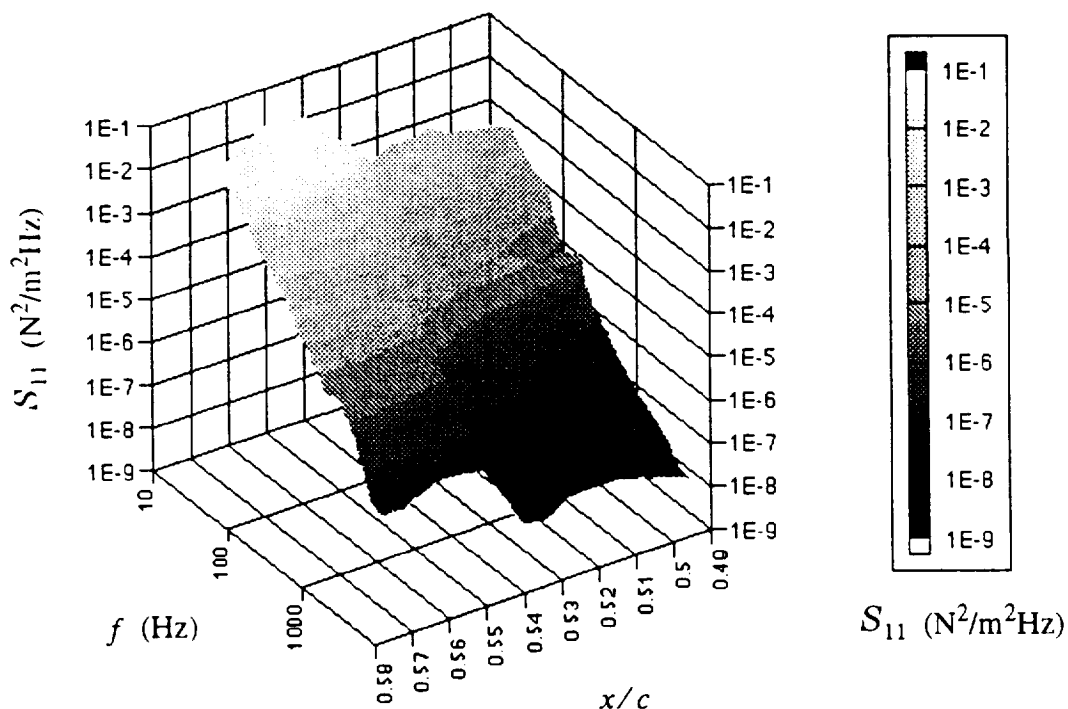
Figure 7.40: Auto-spectral surface for the streamwise-oriented surface shear stress through transition from $x/c = 0.49$ to just past $x/c = 0.57$.

147

Figure 7.41 demonstrates the dramatic increase in energy in the streamwise surface shear stress as the flow progresses downstream through transition. The streamwise-oriented hot-film sheet is closely aligned to the center axis of a crossflow vortex such that it resides beneath a doubly-inflected mean velocity profile. Therefore, as expected, the auto-spectra exhibits the typical signatures of the travelling wave near 300 Hz and the secondary instability near 3.0 kHz.

In figure 7.41 we see a rare streamwise evolutionary picture captured by the hot-film sensors. The spectra in the laminar regime first display a definitive peak near 175 Hz at $x/c = 0.49$ which gives way to the dominant double-peak signature typically associated with the primary instability of the travelling wave near 300 Hz. The travelling wave signature starts with a small amount of energy and then rapidly grows further downstream through the start of the breakdown region and then quickly dissipates leaving very little trace of its existence in the turbulent regime.
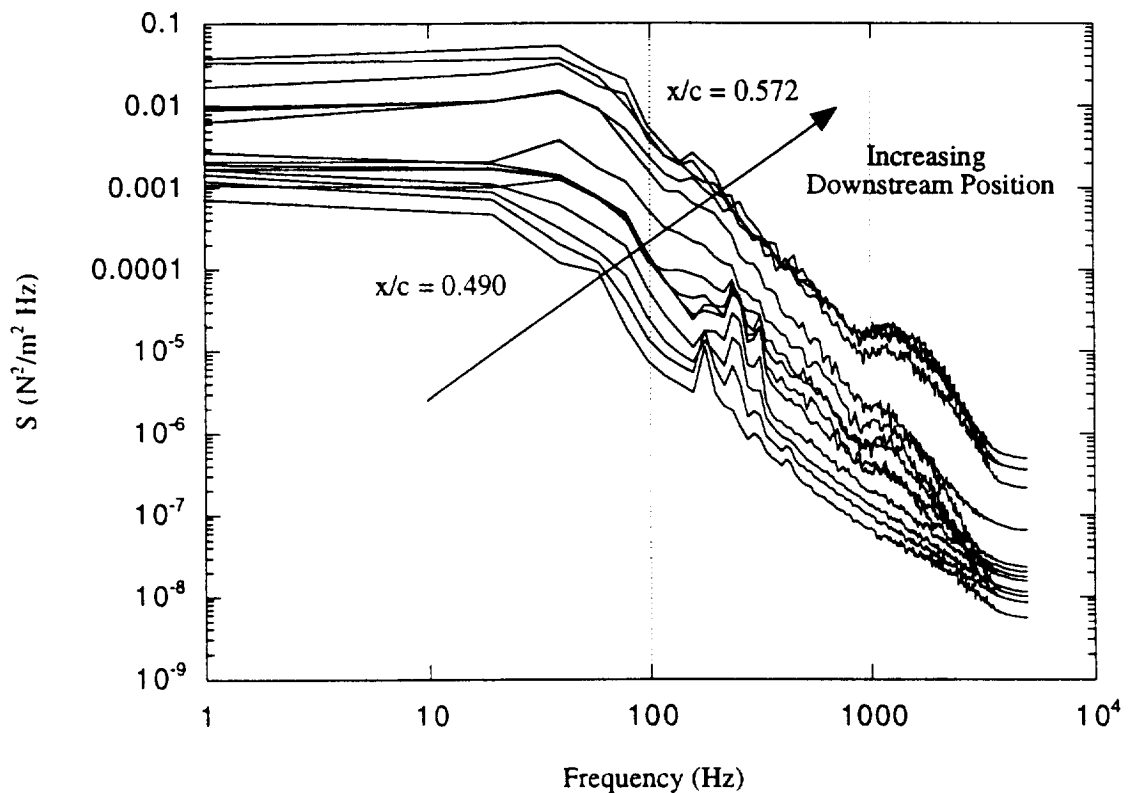
Figure 7.41: Evolution of auto-spectra for the streamwise surface shear stress through transition from $x/c = 0.49$ to just past $x/c = 0.57$.

The secondary instability is also captured despite the hot-film instrumentation limitations. In fact, the secondary instability signature, i.e., the broad-band, high-frequency event, grows and emerges through the transition process. The presence of the secondary instability is not particularly identifiable in the laminar regime from these measurements due to the cut-off frequency in the hot-film calibration. However, as the flow progresses through the transition region, a small peak emerges near 2.0 kHz and then grows and shifts to approximately 1.3 kHz as the boundary layer becomes fully turbulent. This presents excellent insight into the transfer of energy between the two instability mechanisms and provides us with a definitive answer as to where the small-scale structures in the turbulent regime originate. It is clear that they are produced by the highly nonlinear secondary instability.

The streamwise auto-spectra reveal important dynamics in the transitioning swept-wing boundary-layer. The sudden streamwise growth of the primary instability just before transition suggests its dominant role in supplying energy to the transition process. It seems to actually be driving the breakdown of the crossflow vortices. The secondary instability due to the inflectional mean velocity profile is also known to contribute to the breakdown process. This is supported by the presence of the secondary instability signatures observed in some of the crossflow-oriented surface shear-stress spectra. For the case studied in the streamwise evolution, the secondary instability signature remains weak until transition commences. We will look to more advanced analysis techniques such as the proper orthogonal decomposition to determine the growth of the secondary instability and its causal effects on transition. We will then be able to quantify the growth of the individual mechanisms and where the energy transfer occurs.

Results of Advanced Correlation Techniques

This chapter focuses on the results from applying the advanced correlation analysis techniques discussed in chapter 6. In particular, linear stochastic estimation (LSE) is used to estimate the instantaneous velocity field from just two available simultaneously sampled signals which are chosen based on specific qualifications. LSE is also used to estimate a surface shear-stress field disturbed by the presence of cross-wire probes. This will allow in-phase comparisons of the estimated internal velocity field to the underlying estimated surface shear-stress field instantaneously. Proper orthogonal decomposition (POD) is used to determine the spatial evolution of energy-based eigenfunctions characteristic of the structure present in the flow field. POD is also used to determine the temporal evolution of the dominant modes which provides scalar information about the entire measured flow field. This, in turn, may be used to train future flow control algorithms which could include the use of neural networks. Using the condensed field data contained in the POD coefficients would make training these flow control modules much easier.

8.1 Linear Stochastic Estimation Results

LSE (explained in section 6.2) is used primarily to estimate the full instantaneous velocity field from just the instantaneous signals available to us at any two positions and the full two-component spatial correlation tensor (investigated in section 7.1.1). Equations 6.19 and 6.20 are used to compute the estimates for the two velocity components across the entire measured field. Due to the cross-wire technique used to acquire the correlation measurements (as explained in section

5.5), only two measurement locations are acquired simultaneously per experiment run. Since solving for the POD coefficients requires a completely instantaneous measurement field, LSE is first used to generate this data from the simultaneously sampled data that is available to us. Certainly, many combinations of the measured spatial locations are available which presents us with a choice of which positions to use as the basic reference for the full-field estimation. Typically, some locations will produce better estimates than others. An objective method has been devised to select the appropriate reference signals to produce the best estimate possible. This is illustrated below first by subjectively picking any two locations in the measured field. The estimate is calculated and then compared to the objective method of selection to demonstrate the importance of properly selecting the reference signals.

8.1.1 Random Reference Selection

For demonstration purposes, we choose any two locations in the measured field as the reference signals to calculate the full-field estimate. Referring to figures 5.12, spatial locations at 19 mm and 11 mm (the third and fifth dots from the left in figure 5.13, also shown in figure 8.20) are chosen as reference locations. The "flow map" in figure 5.13 shows that one location resides between two stationary vortices and the other is very close to a vortex. Performing the two-component LSE for two reference locations, equations 6.17 and 6.18 are used with the appropriate spatial correlation tensor to solve for the LSE coefficients. Equations 6.19 and 6.20 then provide the actual estimates for each spatial location resulting in an entire estimated instantaneous field.

The estimated u-component and w-component velocity fields in the laminar regime at $x/c = 0.50$ are shown in figures 8.1 and 8.2, respectively. The signals are offset along the ordinate axis to allow visual comparisons. Amplitudes are therefore relative to one another. From simple observation of the estimated time histories in the laminar regime, we see some form of the spatial presence of the stationary crossflow vortices in the u component. Signals at locations of 3, 15 and 27 mm demonstrate higher amplitudes than those at other locations showing some spatial periodicity. The w-component estimate does not show any sense of spatial periodicity. In fact, only the signal at the location of 15 mm is of sizable amplitude. This seems uncharacteristic of what is expected and reflects some disparity in the estimation performance.

Figures 8.3 and 8.4 contain the estimated fields of the u and w component at $x/c = 0.58$.
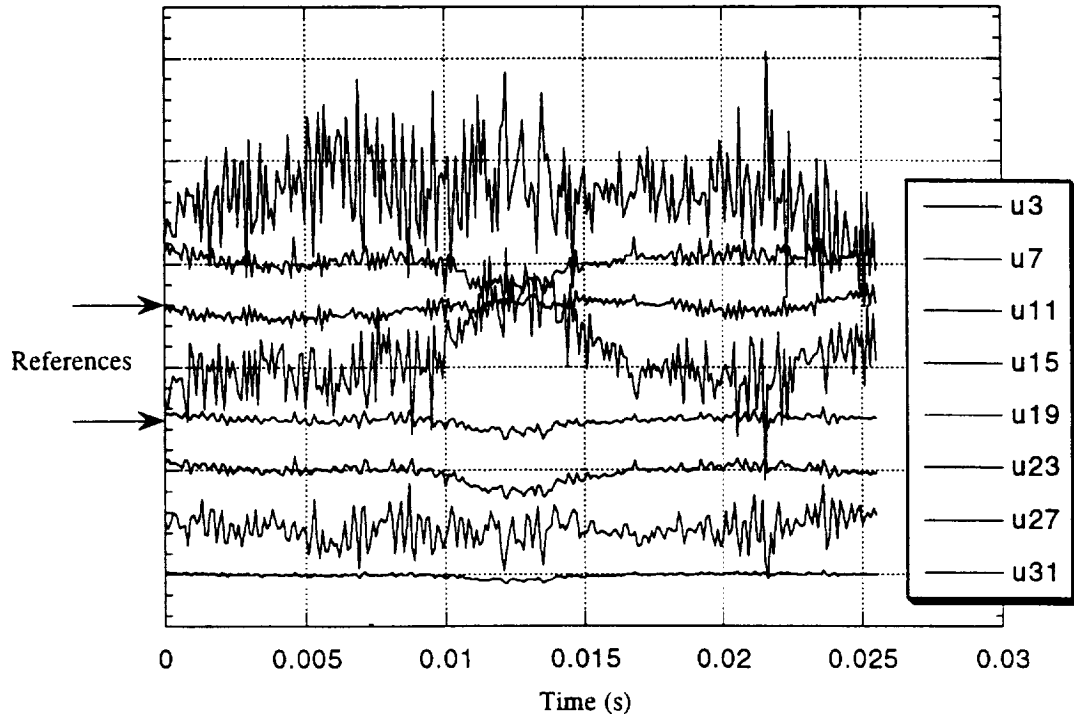
Figure 8.1: Linear stochastic estimate of the u-component velocity field at $x/c = 0.50$ using signals from locations at 19 mm and 11 mm as reference.
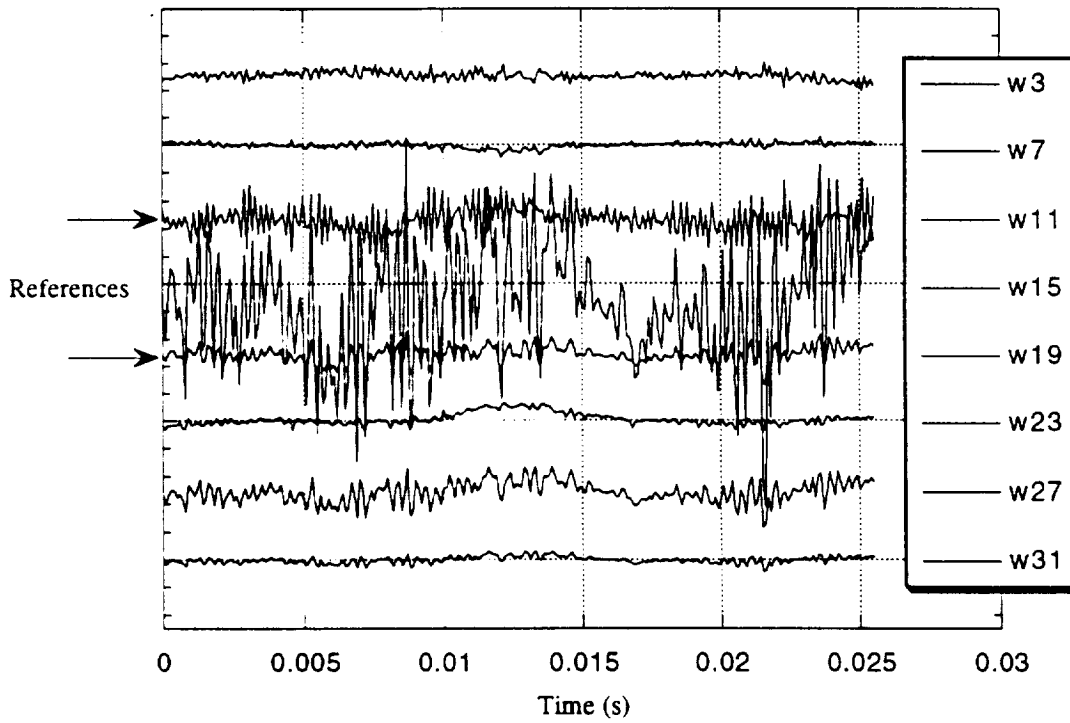
Figure 8.2: Linear stochastic estimate of the w-component velocity field at $x/c = 0.50$ using signals from locations at 19 mm and 11 mm as reference.
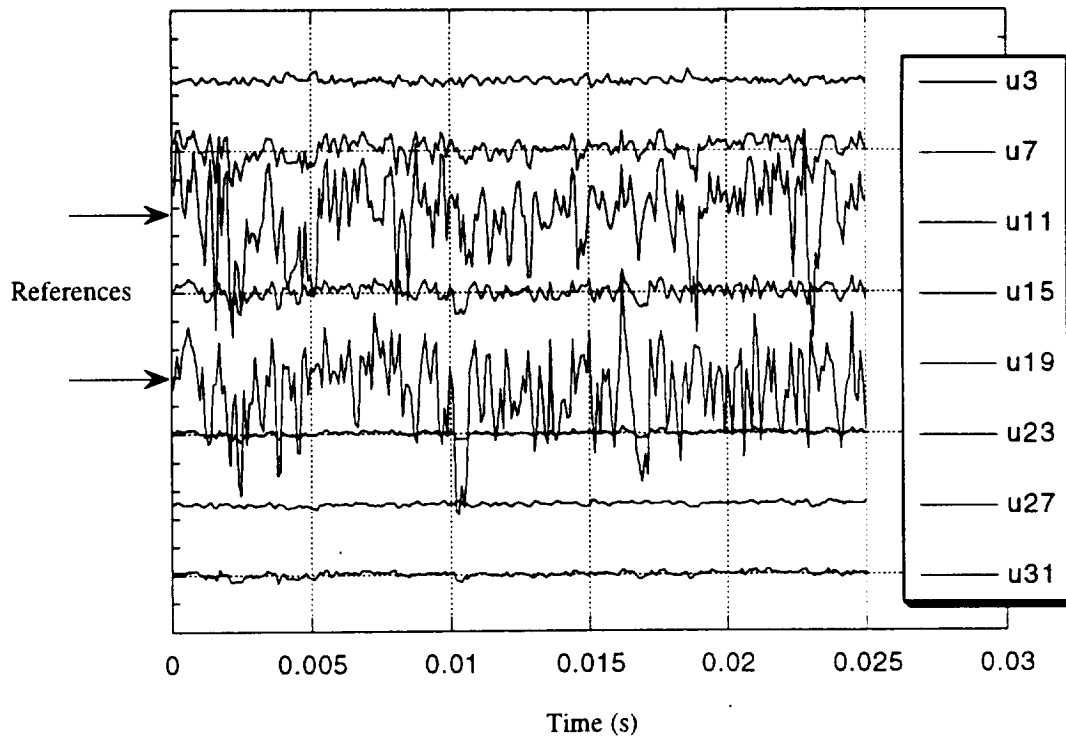
Figure 8.3: Linear stochastic estimate of the u-component velocity field at $x/c = 0.58$ using signals from locations at 19 mm and 11 mm as reference.
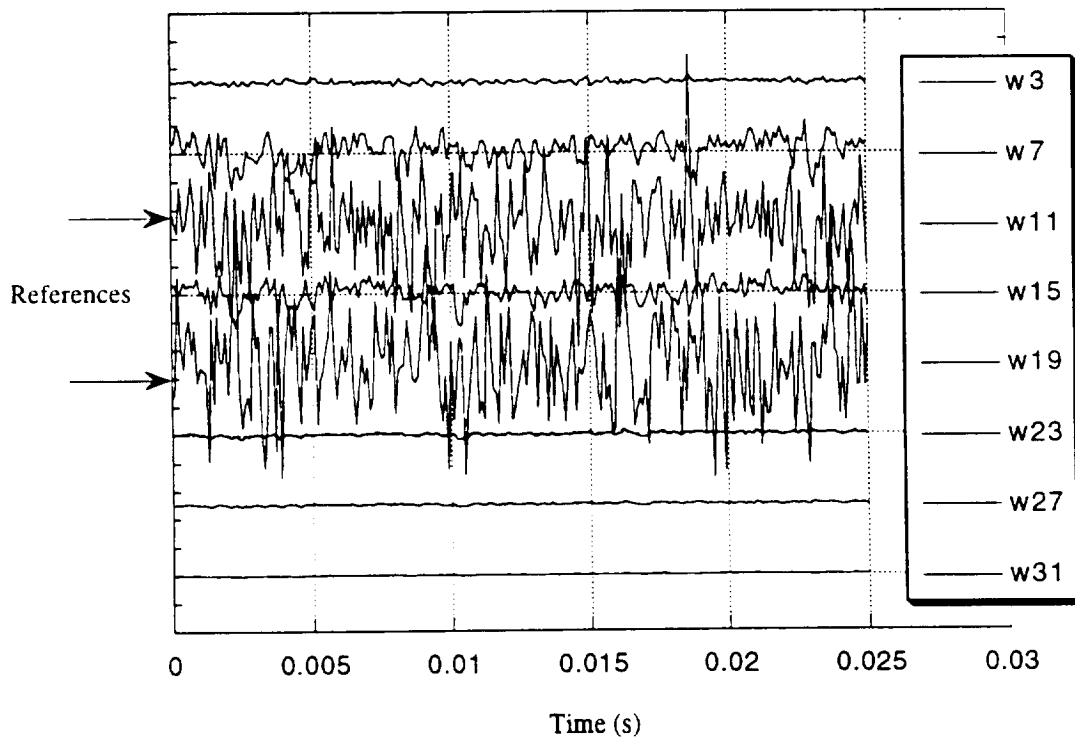
Figure 8.4: Linear stochastic estimate of the w-component velocity field at $x/c = 0.58$ using signals from locations at 19 mm and 11 mm as reference.

The estimation clearly does not perform as well in the turbulent regime. This is due to the lack of correlation away from the trace of the corresponding spatial correlation tensors shown in figures 7.5, 7.6 and 7.7. The estimated signals in close proximity to the reference sensors do retain some of the amplitude of the reference signals but still not at levels near the actual measurements. Signal amplitudes at spatial locations furthest away from the reference locations are simply not well estimated.

Since the velocity field was never sampled at every span location simultaneously, we cannot quantify exactly how well the estimate is performing on a point-to-point basis. Therefore, we compare the single-point statistics, i.e., the root-mean-square (RMS) values, at each span location from actual measurements to those of the estimated field. Hence, figure 8.5 displays the RMS values of the actual measured data for the u - and w -component velocity fields in both flow regimes. The presence of the stationary vortices is identified in the laminar case where the peak RMS values correspond to measurements made within the rollover of the vortices (refer to figure 5.13 or
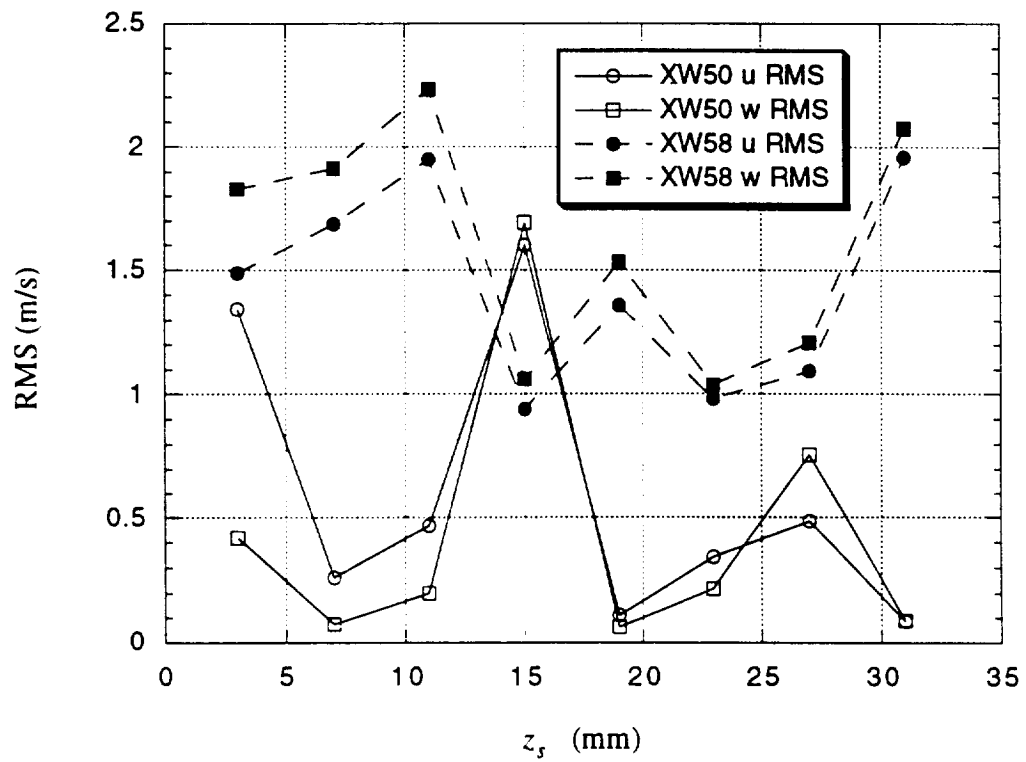
Figure 8.5: Root-mean-square values for the u and w components of velocity for actual measurements at x/c = 0.50 and x/c = 0.58.

figure 8.20). The turbulent RMS plot shows some sense of spatial structure as well reminiscent of the laminar vortex structure. Even the single-point statistics support the hypothesis that the large-scale structure present in the turbulent regime originates from the stationary vortical structures in the swept-wing boundary layer before transition.

Figure 8.6 shows the RMS of the estimated field using locations at 19 mm and 11 mm as reference compared to the actual measured RMS values for the u and w components in the laminar regime. Figure 8.7 shows the similar RMS comparisons of the estimated field to the actual field for both components in the turbulent regime. There are drastic disparities between the estimate and the actual RMS. In fact, one would completely mis-identify the spanwise location of the vortices by observation of the estimated RMS values for the laminar regime. Even the trends of relative amplitude are not accurate. The turbulent estimate places the reference RMS values near the proper amplitudes but does not accurately determine the appropriate RMS relationship between the spatial positions. It is clear that the estimated field is not appropriately representative of the what truly exists instantaneously in the measured field. Therefore, we now need a method of choosing the appropriate reference signals to produce the best estimate possible which consists of both reasonable amplitudes and proper relative amplitudes, i.e., appropriate spatial trends. Some losses in amplitude are expected for the estimated signals but, in general, the shape of the RMS
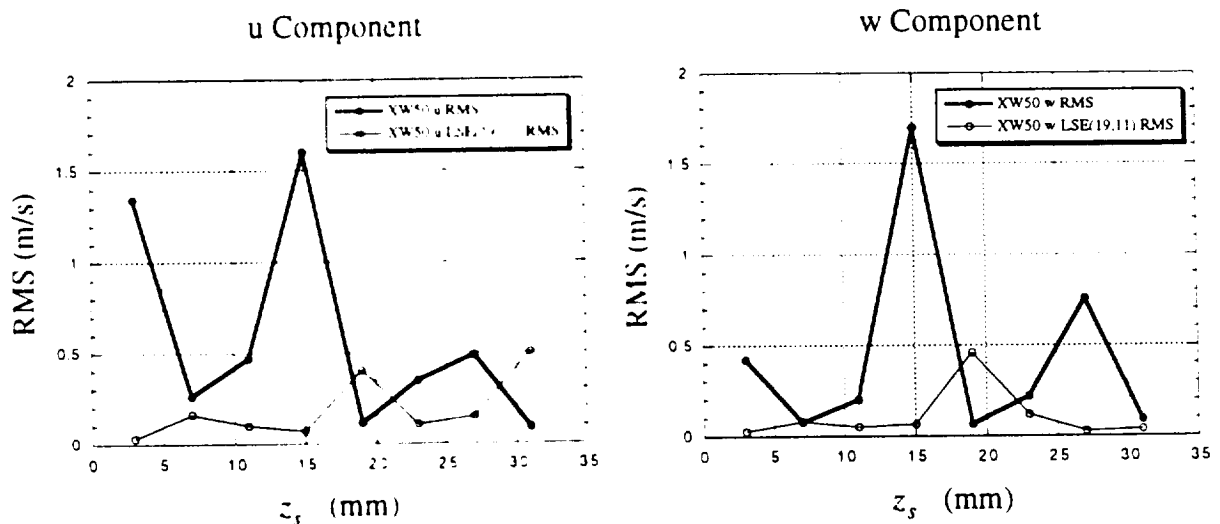
Figure 8.6: Comparison of root-mean-square values between estimated and actual fields for the u and w components of velocity at $x/c = 0.50$.
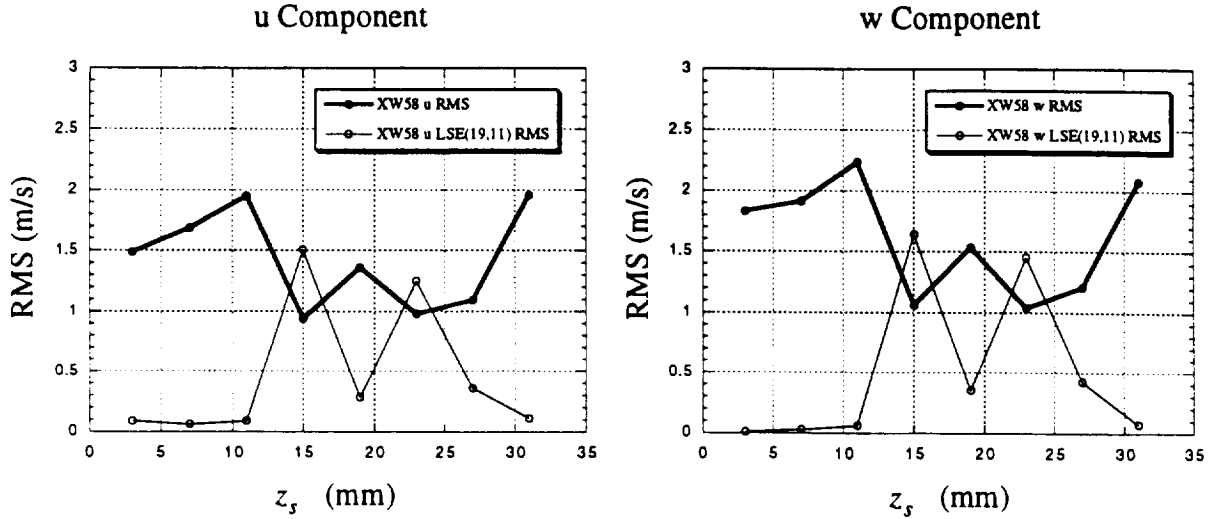
Figure 8.7: Comparison of root-mean-square values between estimated and actual fields for the u and w components of velocity at $x/c = 0.58$.

profile should retain the same features as the actual velocity field. An objective method of reference selection is presented in the next section.

8.1.2 Objective Reference Selection

Cole (1991) selected reference signals from an axisymmetric jet mixing-layer experiment based on their high RMS values for a linear stochastic estimate. He showed that locations with high RMS values produce the best estimates in a turbulent velocity field. The same principle is applied here. By selecting the two reference locations with the maximum RMS values, we assure that an adequate amount of "signal energy" (i.e., a relatively high amplitude signal with rich spectral content characteristic of the entire measured flow field) is available to provide the best possible two-probe estimate. Figure 8.5 shows that the maximum RMS values differ for the two components in the laminar regime. The u component displays locations at 3 mm and 15 mm as the maximum and the w component shows locations at 15 mm and 27 mm as maximum RMS values. The w component shows very little RMS at the 3-mm location, but the u component does show significant amplitude at the 27-mm location. Therefore, the reference signals are chosen at the 27-mm and 15-mm positions. Components of a measured quantity will often provide conflicting reference selection results based on the maximum RMS criteria. To allocate the greatest amount of coupled

"signal energy" available to the estimation procedure, the spatial positions with the maximum RMS values summed over all components should be selected.

Figures 8.8 and 8.9 show the estimated u and w velocities, respectively, for the laminar regime calculated from the two-point, two-component LSE equations with reference signals from spatial locations at 27 mm and 15 mm. The result is a completely different looking flow field. Significant amounts of periodicity are produced with the RMS-maximized-reference estimates at locations previously unstructured with the randomly selected reference estimates. The broad periodicity is in fact due to the travelling wave that resides with the stationary spatial wave. Very little evidence of travelling waves is observed in the random-reference estimates in figures 8.1 and 8.2. The random estimate also creates numerous high-frequency events in the signals that later display the periodicity of the travelling waves (in the estimates of figures 8.8 and 8.9). The laminar estimates in figures 8.1 and 8.2 actually display features typical of turbulent flows, further contributing to the downfall of the random selection process. Figures 8.8 and 8.9 display laminar swept-wing flow characteristics such as the clean periodicity and relatively low frequency content.

The RMS-maximized reference estimates even reveal specific flow physics in the time histories previously undetected in the random-reference estimates. The presence of the travelling waves, the low frequency events in locations at 3, 23 and 27 mm, is certainly evident. The effects of the secondary instability mechanism is also observed. Kohama et al. (1991) refer to the temporal signature of the secondary instability as those events which exhibit "top-hat-like" peaks, i.e., flat peaks that contain a few "kinks" in the top portion of the structure. Similar time-trace features, particularly in the location at 15 mm of the streamwise component, exist where we see high frequency events within the top portions of the "top-hat-like" events. One of these possible "top-hat" structures is pointed out in figure 8.8. These events only appear strongly in the one position at 15 mm which, as we know from the spatial correlation analysis, is the only measurement site directly above a doubly-inflected velocity profile, the source of the secondary instability. These temporal observations agree with the past correlation and spectra analyses and therefore gives us a further sense of confidence in the RMS-maximized-reference estimates.

To quantify just how well these estimates are actually performing, we again look to the RMS comparisons of actual to estimated fields. Figure 8.10 shows these RMS comparisons for the laminar LSE solution. Clearly we have achieved a much better estimate in the mean-square sense by choosing the signals at the maximum-RMS locations. The estimated streamwise RMS profile

Figure 8.8: Linear stochastic estimate of the u-component velocity field at $x/c = 0.50$ using signals from locations at 27 mm and 15 mm as reference.
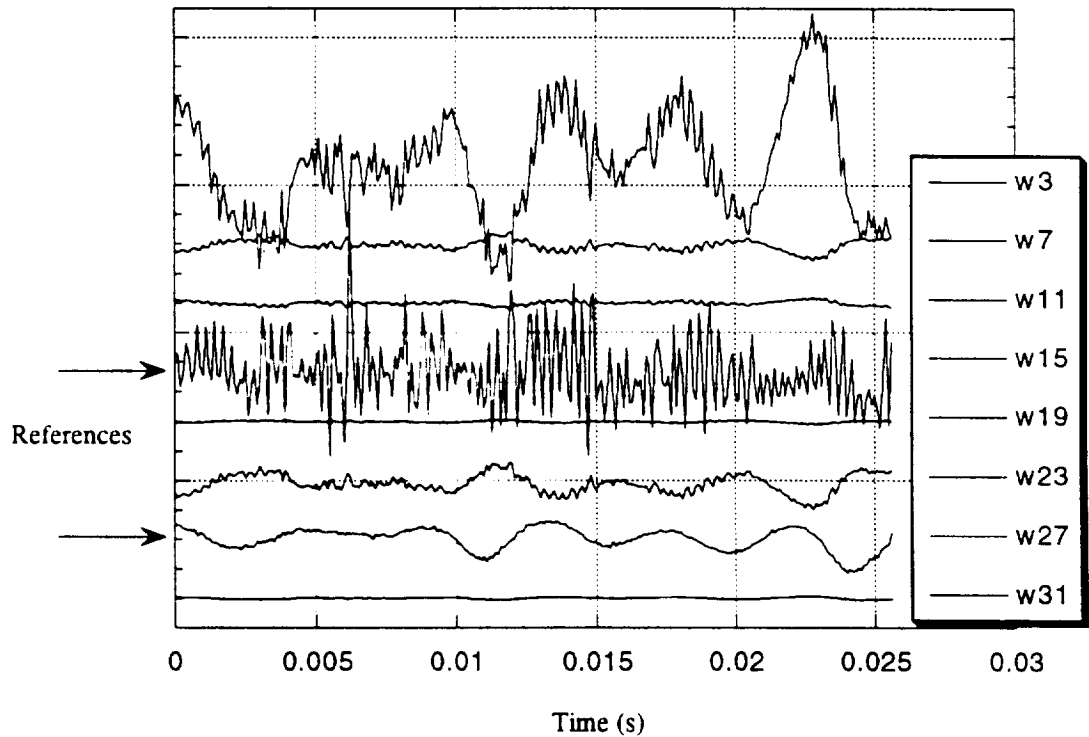
Figure 8.9: Linear stochastic estimate of the w-component velocity field at $x/c = 0.50$ using signals from locations at 27 mm and 15 mm as reference.
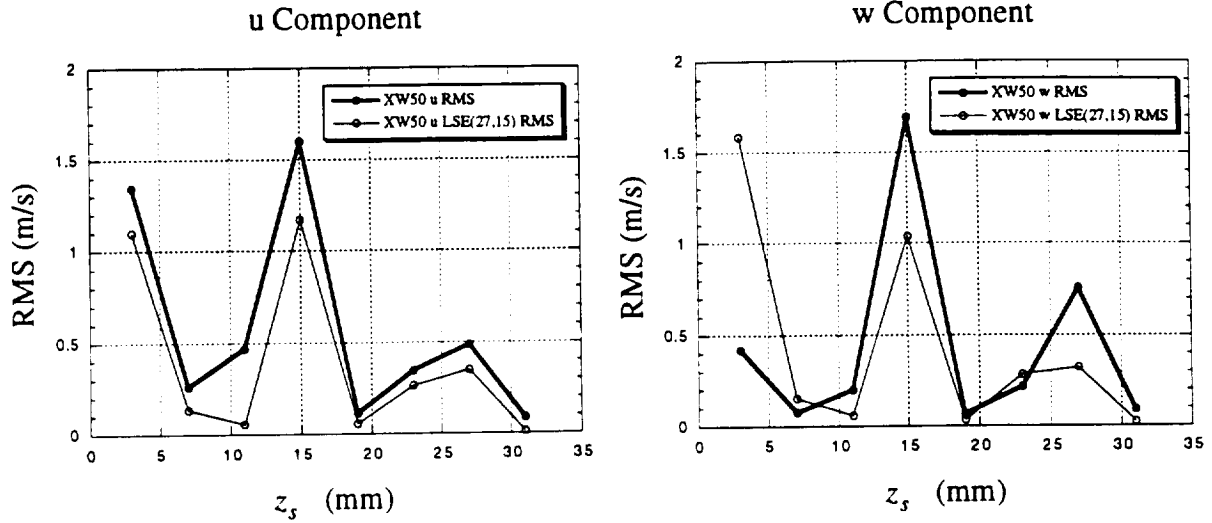
Figure 8.10: Comparison of root-mean-square values between actual and RMS-maximized-reference estimated fields for the u and w components of velocity at $x/c = 0.50$.

agrees quite well with the actual measured profile. The spatial structure is well preserved with only a slight loss in amplitude. The w component also exhibits the appropriate spatial structure but has an amplitude anomaly at the 3-mm location. Here the estimate is exaggerated from the actual measurement which is most likely due to the higher amplitudes of the reference signals in the actual RMS profile. LSE treats the estimation of the components as a coupled problem and therefore cross-component information from the reference signals is used to estimate both components (see equations 6.19 and 6.20). Hence, the higher amplitude in the u-component reference has affected the estimate of the w component. Despite this over-estimated signal, the estimated field is, in general, quite representative of the actual measurements.

The LSE is also performed to estimate the instantaneous turbulent fluctuating velocity field. From figure 8.5, we see that the maximum RMS values have relocated to new spatial positions through transition. If the references determined from the laminar case are used in the turbulent regime the estimate again fails to capture the trends of the actual measured field. The RMS comparison for this case is shown in figure 8.11. New references should be chosen to obtain the best possible estimate.

It is clear that the turbulent case must be treated as an independent problem and that new reference signals based on the maximum turbulent RMS values must be determined. Figures 8.12

159
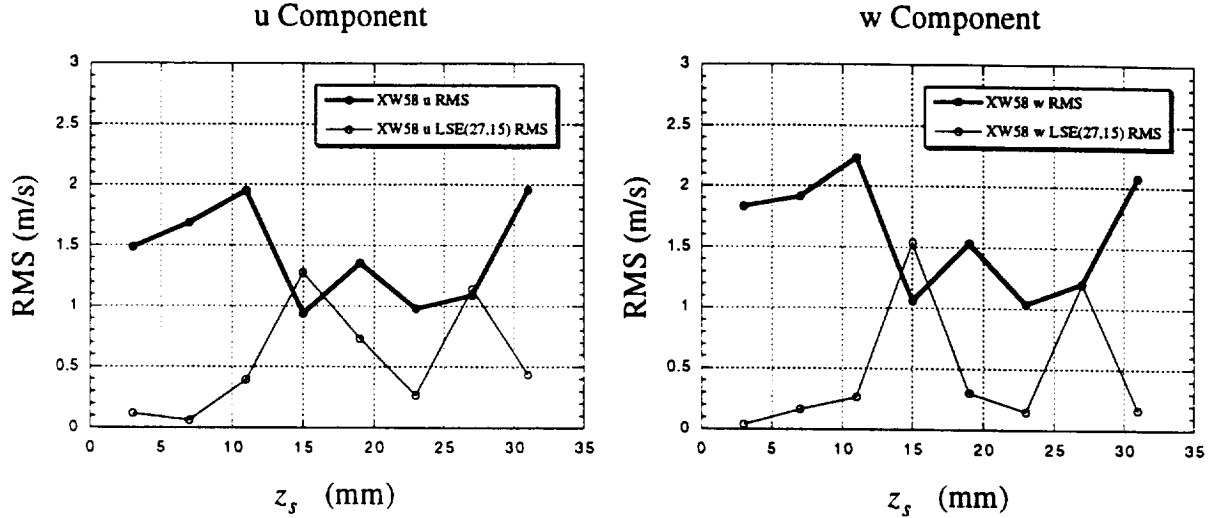
Figure 8.11: Comparison of turbulent root-mean-square values between actual and laminar-RMS-maximized-reference estimated fields for the u and w components of velocity.

and 8.13 display the two estimated velocity components in the turbulent regime using signals from 11 and 31 mm as reference. In general, the turbulent swept-wing boundary layer is very difficult to accurately estimate (Chapman et al. 1994). This is reflected in the poor amplitude recovery of the estimated field in figures 8.12 and 8.13 and is due to the fact that the turbulent flow field is not well correlated. Cole (1991, 1996) shows that a three-probe estimate is a minimum requirement for appropriately estimating in most turbulent flows.

Despite these shortcomings, we look to the standard RMS comparison (shown in figure 8.14) for a true picture of the LSE performance. Certainly, the amplitudes are significantly lower than the actual measurements. This must be considered when analyzing the POD results through use of the complimentary technique. Only a very limited number of eigenmodes will be considered appropriately descriptive. Aside from the amplitude discrepancy, the spatial trends are somewhat accurate in the mean-square sense. We must consider that the flow field is severely more complex and not as well correlated as the laminar regime. However, we have insured that the best possible estimate is obtained for the measured flow field given our limitation of a two-probe estimate.
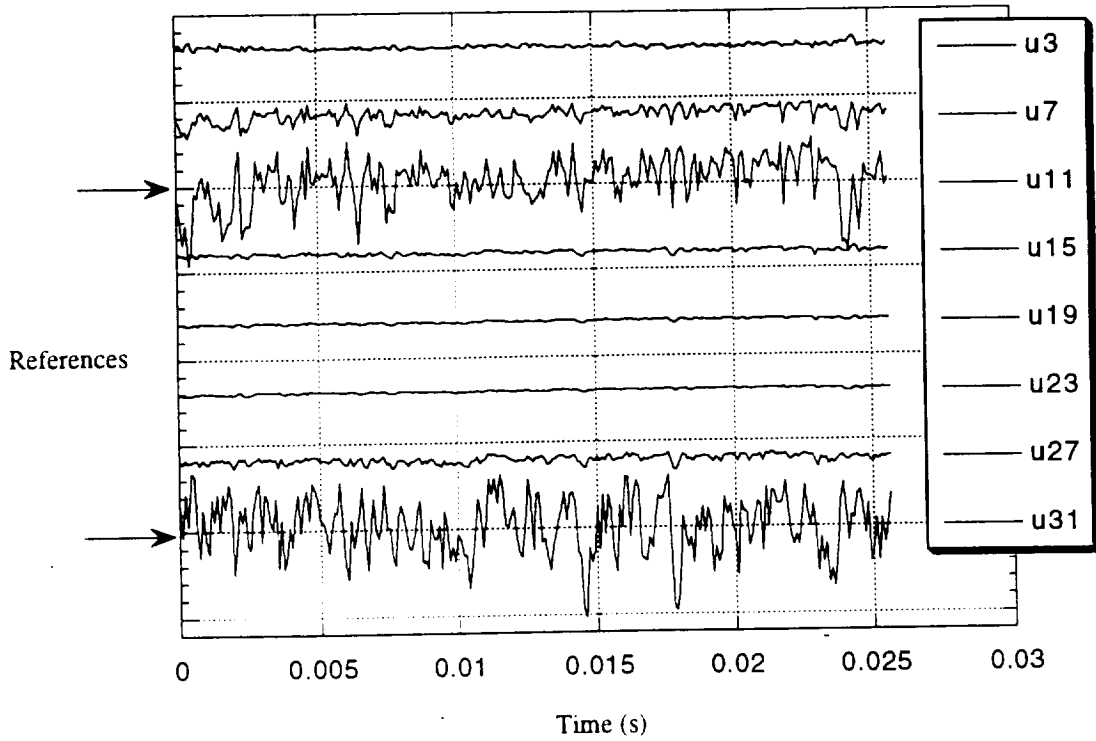
Figure 8.12: Linear stochastic estimate of the u-component velocity field at $x/c = 0.58$ using signals from locations at 31 mm and 11 mm as reference.
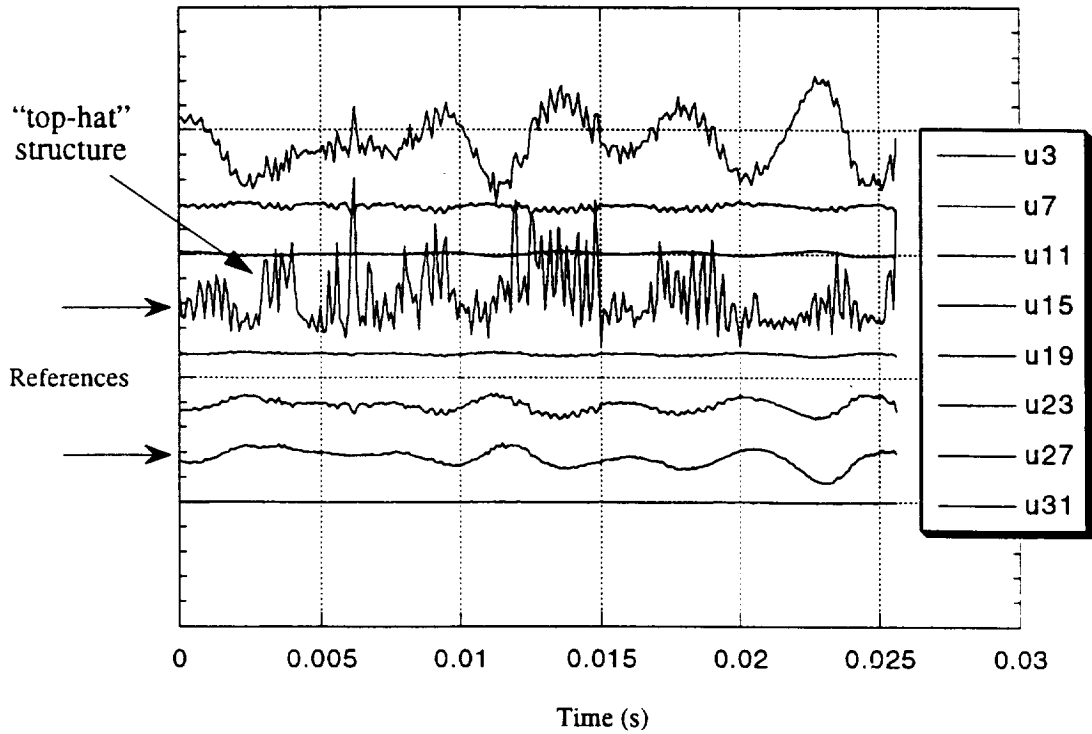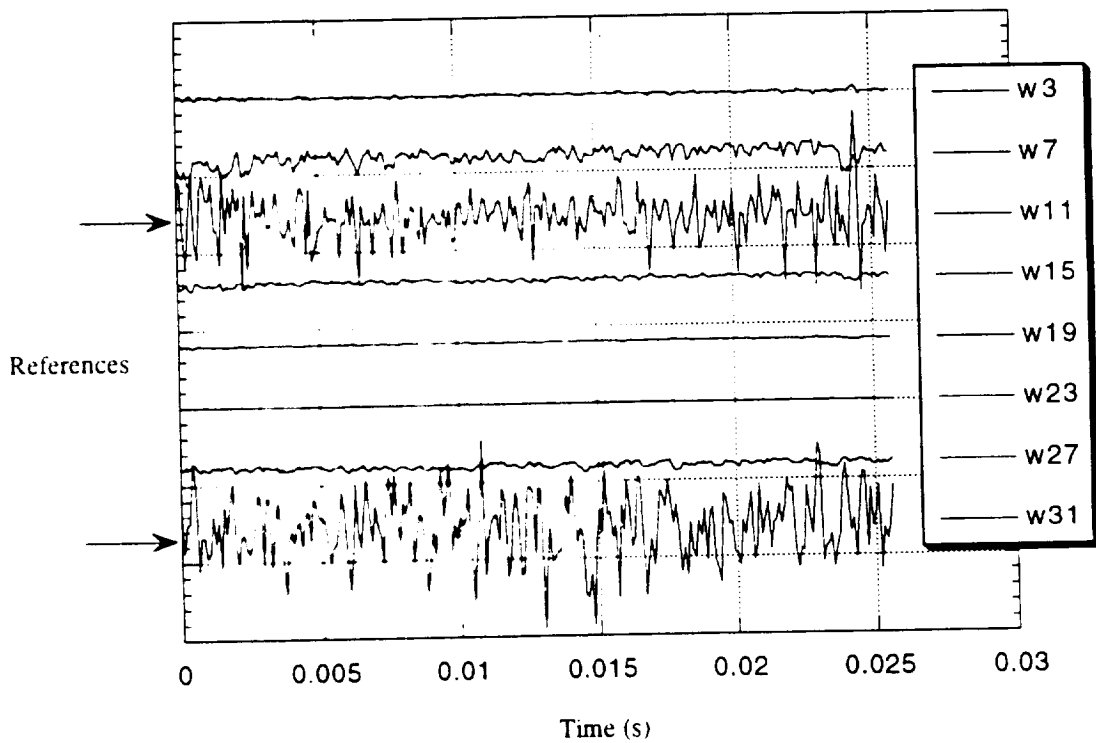

Figure 8.13: Linear stochastic estimate of the w-component velocity field at $x/c = 0.58$ using signals from locations at 31 mm and 11 mm as reference.
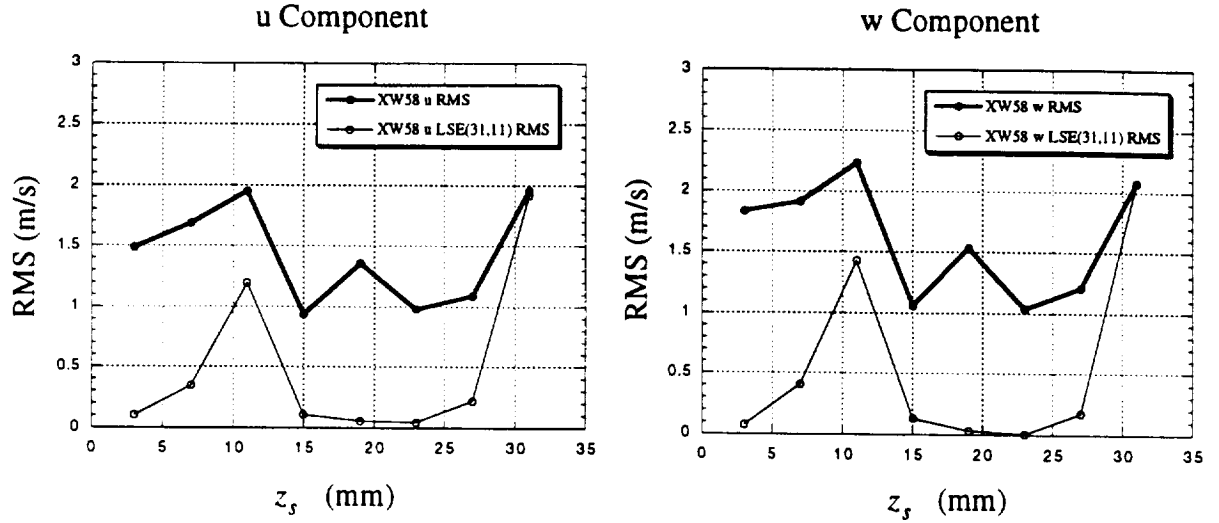
Figure 8.14: Comparison of root-mean-square values between actual and RMS-maximized-reference estimated fields for the u and w components of velocity at $x/c = 0.58$.

8.1.3 Uses of Estimated Fields

Now that the instantaneous fields are appropriately estimated with the best possible selections for the reference signals, they may be used in conjunction with the spatial POD solutions (presented in section 8.2) through the complimentary technique discussed in section 6.4. The estimates also display the temporal structures within the flow field instantaneously at all spatial positions. This allows for simple structure recognition which is demonstrated above in recognizing the presence of the travelling wave and the effects of the secondary instability mechanism. To obtain the POD coefficients, the estimated fields are effectively used with equation 6.38 (as the $u_i^{est}(z_s, t)$ term where the subscript i is either 1 or 3 for the u and w components, respectively) to determine the POD coefficients. The temporal evolution of each mode may then be examined and used to train future flow control algorithms. This would not be possible without the full instantaneous measured velocity field provided by the LSE. Keeping in mind that the POD coefficients are derived from an estimated field, we must be careful as to how many modes are truly representative of the actual flow field. This will be further discussed in section 8.4.

8.2 Spatial Proper Orthogonal Decomposition Results

POD is used to decompose each of the measured flow fields into eigenfunctions that represent the spatial evolution of characteristic flow structure at specific energy levels determined through maximizing the mean-square projection of a candidate structure onto the quantitative field. These solutions provide the analyst with a method to identify spatial structure within a flow field. This is important in understanding the effects of transition and in deciphering the origins of coherent structures in the turbulent regime. This identification technique simply requires the two-point spatial correlation tensor and use of equation 6.32. The eigenvalues from this solution represent the relative kinetic energy contained within each POD mode. The eigenfunctions or spatial modes reveal characteristic structures in space. The magnitude of the various modes identify structural shape and the sign of the function values represent relative phase within that solution. For example, a negative peak does not denote specific phase information other than that it is out of phase with a positive peak within the same POD solution.

8.2.1 Eigenvalues

The eigenvalues, $\lambda^{(n)}$ in equation 6.32, for all measured flow fields are shown in figure 8.15. For comparisons of relative energy content within modes, the eigenvalues have been normalized by the first eigenvalue which is known to contain the most kinetic energy as stated in equation 6.31. It should also be noted that the velocity solution contains the coupled effects of the two components of velocity whereas the surface shear-stress solutions are determined by only one component.

Figure 8.15 shows that the higher modes contain more energy for the velocity measurements than for the surface shear stresses. This could be a result of a number of factors. First, the velocity measurements include the two-component information which could add energy to the higher modes. Some additional low-energy, high-frequency scales within the flow may be captured by including the second, coupled component. Secondly, the cross-wire sensors are known to have a broader-band frequency response than that of the hot-film sensors. This permits better measurement of higher frequencies within the flow, scales that tend to have lower energy content and would therefore appear in the higher modes.

Another interesting feature of the energy distributions is the effect of transition. The velocity
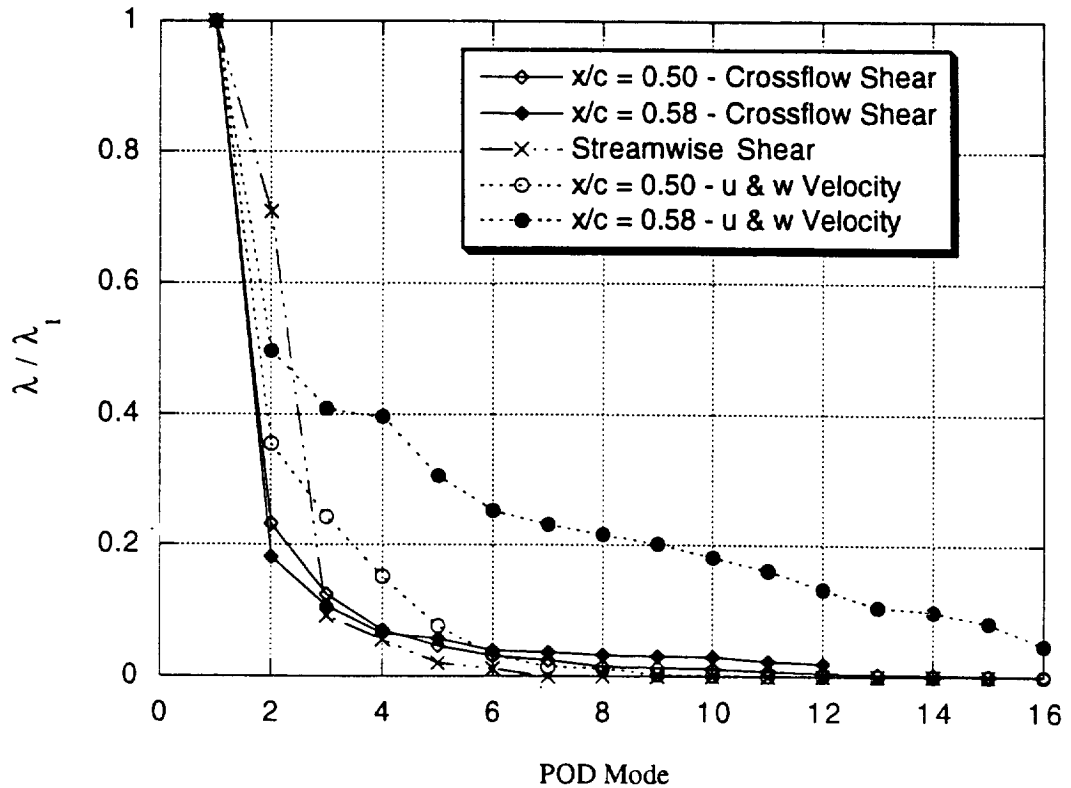
Figure 8.15: Eigenvalues for each measured flow field including both flow regimes.

eigenvalues are significantly higher in the turbulent solution at higher modes. This is due to the presence of small scale structure generated through the breakdown process. More modes are needed to appropriately described the turbulent velocity field. The effect is not as drastic in the surface shear-stress solutions. These levels are not perfectly comparable however, since the measured shear field in the turbulent regime consists of fewer measurements due to the loss of a few sensors. However, there is still evidence of more energy at higher modes, particularly in modes 6 through 12, again attributed to the presence of small-scale structure.

The streamwise surface shear-stress eigenvalues determined through the transition front show an enormous amount of energy within the first two modes. Higher modes really contribute very little to the flow structure. In fact, there is almost no modal energy after mode 5. This states that there are two very specific high-energy modes that exist within the transition process. Upon inspection of the eigenfunctions, we will see that these modes are in fact capturing the spatial effects of the primary and secondary instability mechanisms.

Past POD applications in turbulent flows often quantify the importance of the first few modes by observing the percentage of kinetic energy contained within those modes. Therefore, for comparison, figure 8.16 shows the various percentages of kinetic energy for the first few significant modes in each measured flow field. The crossflow shear measurements retain approximately 60% of the total measured kinetic energy in both flow regimes with significant contributions only from the next two modes. Therefore, we can appropriately represent the surface shear stresses at the two chord locations with only the first three modes (85% of the total measured kinetic energy in the laminar regime and 79% in the turbulent regime). The velocity eigenvalues reveal a different energy distribution in that only 53% of the total measured kinetic energy is retained in the first mode within the laminar regime and only 23% is contained in the first mode for the turbulent regime. The first three modes in the laminar case provide nearly 85% of the total energy and only 45% in the turbulent regime. Clearly, higher modes are needed to appropriately describe the turbulent velocity field. The streamwise surface shear-stress solution shows that 53% of the energy is contained within the first mode and nearly 38% within the second mode. Subsequent modes provide very little information. Thus, the first three modes in the streamwise shear through transition contain approximately 95% of the entire measured kinetic energy. Obviously, the mechanisms in the first two modes dominate the transition process and govern the origins of the turbulent scales.

8.2.2 Two-Component Velocity: Spatial Modes

The one-dimensional POD eigenfunctions are solved for the two components of velocity measured at $x/c = 0.50$ and $x/c = 0.58$ using equation 6.32 with the full two-component spatial correlation tensor. Because this is a coupled solution including two components, the POD solution for the eight measurement sites in span actually results in 16 total modes for each component (ϕ_1 corresponds to the u component and ϕ_3 to the w component). Referring to the reconstruction equation of the correlation tensor, i.e., equation 6.28, we see that in order to relate these eigenfunctions to actual measured quantities, they must be appropriately scaled by $\lambda^{1/2}$. In loose mathematical terms, the correlation tensor is to $\lambda^{(n)}\phi^{(n)}\phi^{(n)*}$ as the velocity (or shear stress) is to $(\lambda^{(n)})^{1/2}\phi^{(n)}$. Therefore, all the spatial modes are plotted with the appropriate eigenvalue scaling.

165
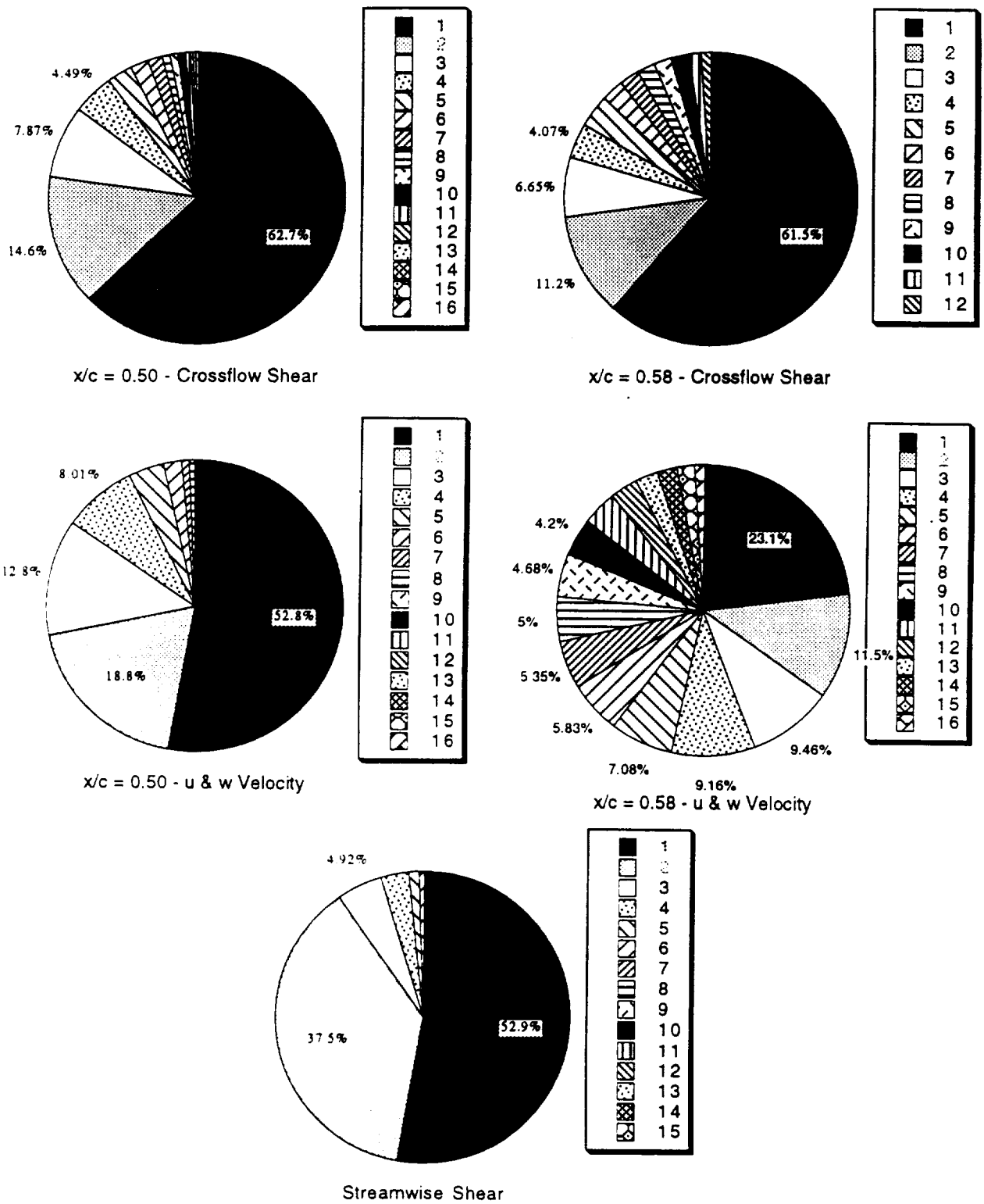
Figure 8.16: Percentage of kinetic energy in first few modes for all measured flow fields.

Laminar Modes

The first six modes (since higher modes are fairly insignificant in the mean-square sense) for the two components of velocity in the laminar regime are presented in figure 8.17 and are appropriately scaled by their corresponding eigenvalue. The data is cubic splined across the span range to expose possible trends of the functions.

The first modes in figure 8.17 exhibit a strong peak at the 15-mm span location where the measurement is known to reside within the high-velocity region of a stationary vortex from the "flow map" in figure 5.13 (also shown in figure 8.20). Those measurement sites which lie on the outer "fringes" of the vortex structure (locations at 3, 7, 27 and 31 mm) do not exhibit much amplitude in the first mode. This gives the appearance that only one stationary structure is present when, in fact, three structures exist in the measured span range. This clearly demonstrates the advantage of better measurement grid resolution. As we saw in the spatial correlation analysis, only one wavelength is identifiable. However, if the spatial evolution of the auto-spectra and the spatial correlation tensor is examined prior to the interpretation of the POD analysis, we can identify the large-scale structures that exist within the flow field. Thus, the first mode is tracking the spatial distribution of the stationary structures in both components, as evidenced by the bandwidth of the peaks in the first modes being approximately 12 mm. If the higher modes in figure 8.17 are included in our analysis, we see smaller amplitude events at locations near the doubly-inflected portions of the boundary-layer profiles. It is also interesting to note that the higher modal events at 15 mm are completely out of phase with the first mode in the streamwise solution but are in phase with the first mode in the w component. Also, modes 2 and 4 of both components denote the weak presence of another stationary structure at the 27-mm location, a site known to reside very near the doubly-inflected portion of that vortex. Weak amplitudes are also seen at the 3-mm location near the inflected portion of a third stationary vortex in modes 1 through 4 for the u component. These events also occur in the w component but at much weaker amplitudes. So even with the limited measurement grid resolution, the POD still detects important spatial structure representative of the stationary vortices known to exist within that spatial range. Also, the energy percentages derived from the eigenvalues in figure 8.16 show that only the first four modes are significant. And by observation, the first four eigenfunctions do identify the presence of all three stationary vortices despite the limited spanwise resolution.

Figure 8.17: First six spatial POD modes of the two components of velocity at $x/c = 0.50$, $y = 3.0$ mm.

Further observations of the higher modes show that small periodic swells in modes 5 and 6 in the streamwise component occur in locations at 11 mm and 23 mm, precise locations of measurements made between the vortices (refer again to figure 5.13 or figure 8.20). This could possibly be spatial evidence of very weak Tollmein-Schlichting (T-S) waves which do indeed propagate downstream within the "valleys" of the stationary structures. The T-S waves, a streamwise instability, are known to exist in this crossflow-dominated boundary layer (Saric et al. 1990a). However, these waves are not amplified due to the airfoil configuration (see section 3.3.1). Also, the measurements are taken 3.0 mm above the wing (approximately at $y/\delta = 0.75$) where the T-S velocity profile is generally fairly weak (approximately 20% of the maximum disturbance velocity as seen in two-dimensional flat-plate studies by Krutckoff (1996)). So, the presence of the T-S waves should be very weak. The fact that the periodic low-amplitude swells occur in very low-energy modes of the *streamwise component only* supports these specific T-S properties. Due to the powerful energy-based decomposition of the POD technique, it is certainly possible that such small disturbances could be detected in the higher modes. The evidence indeed presents itself in the higher modes but further investigations should be performed before a commitment is made in labeling these swells as T-S instability effects.

Turbulent Modes

Figure 8.18 displays the first six spatial modes from the one-dimensional POD solution for the two coupled components of velocity in the turbulent regime. The first POD mode contains a large spatial structure at the 11-mm location which originates from the stationary crossflow vortex in the laminar regime. This large-scale structure exists in a spanwise location that previously was between two stationary structures in the laminar regime, i.e., within a "valley". The breakdown process produces, via the crossflow instability, a large coherent structure from the remaining energy of the vortical motion. The combined effects of spanwise momentum from the strong crossflow and the breakdown of the vortex structure forcing high-momentum fluid towards the surface, effectively "spilling" high-momentum fluid into the "valleys", could account for the shifted position. This "spill" effect also gives rise to smaller scale structures witnessed in modes 3 and 4 in both components at the 19 mm position. Higher modes contain the small-scale structure known from the auto-spectra analysis to originate from the secondary instability induced by the doubly-inflected profile.
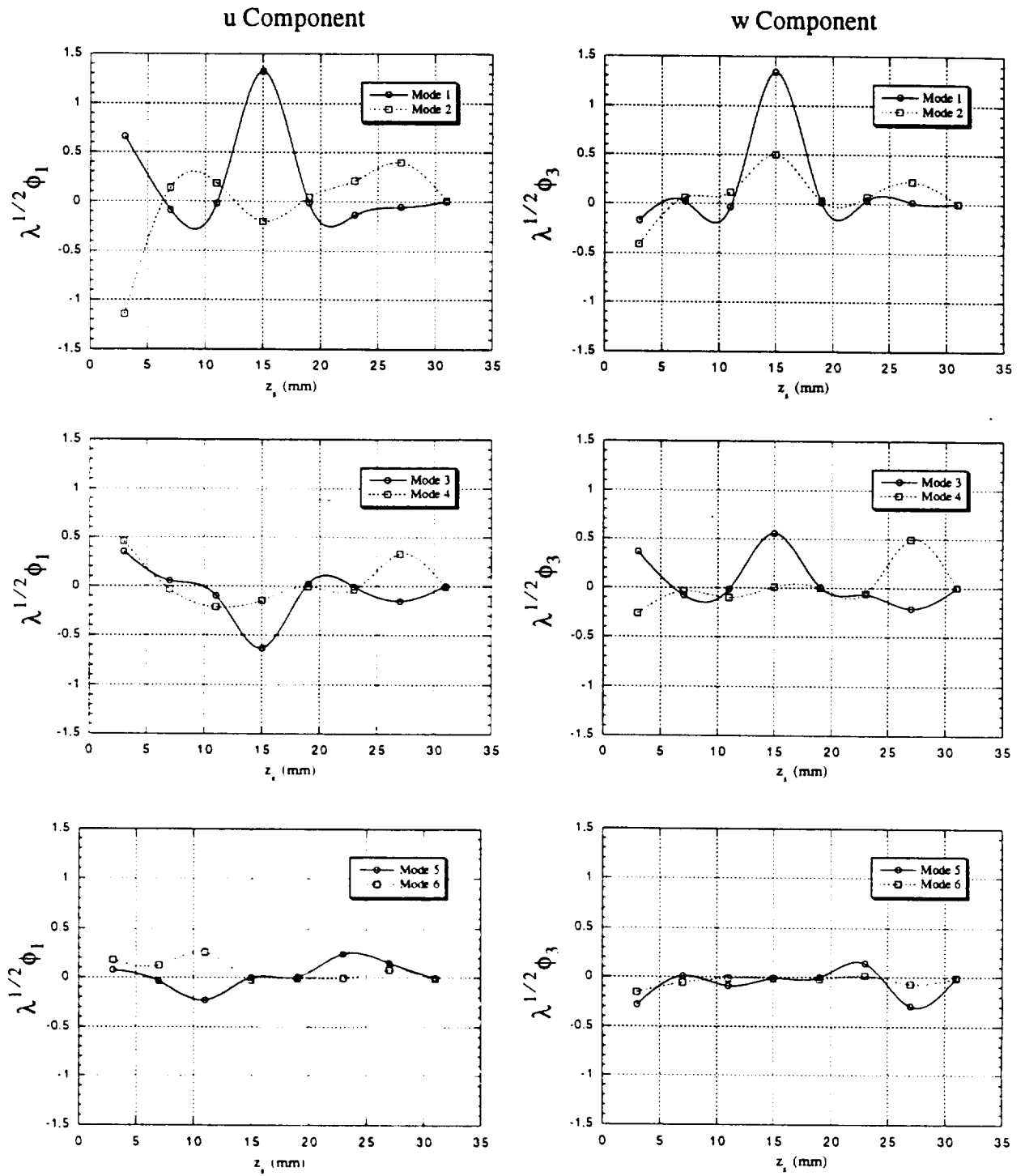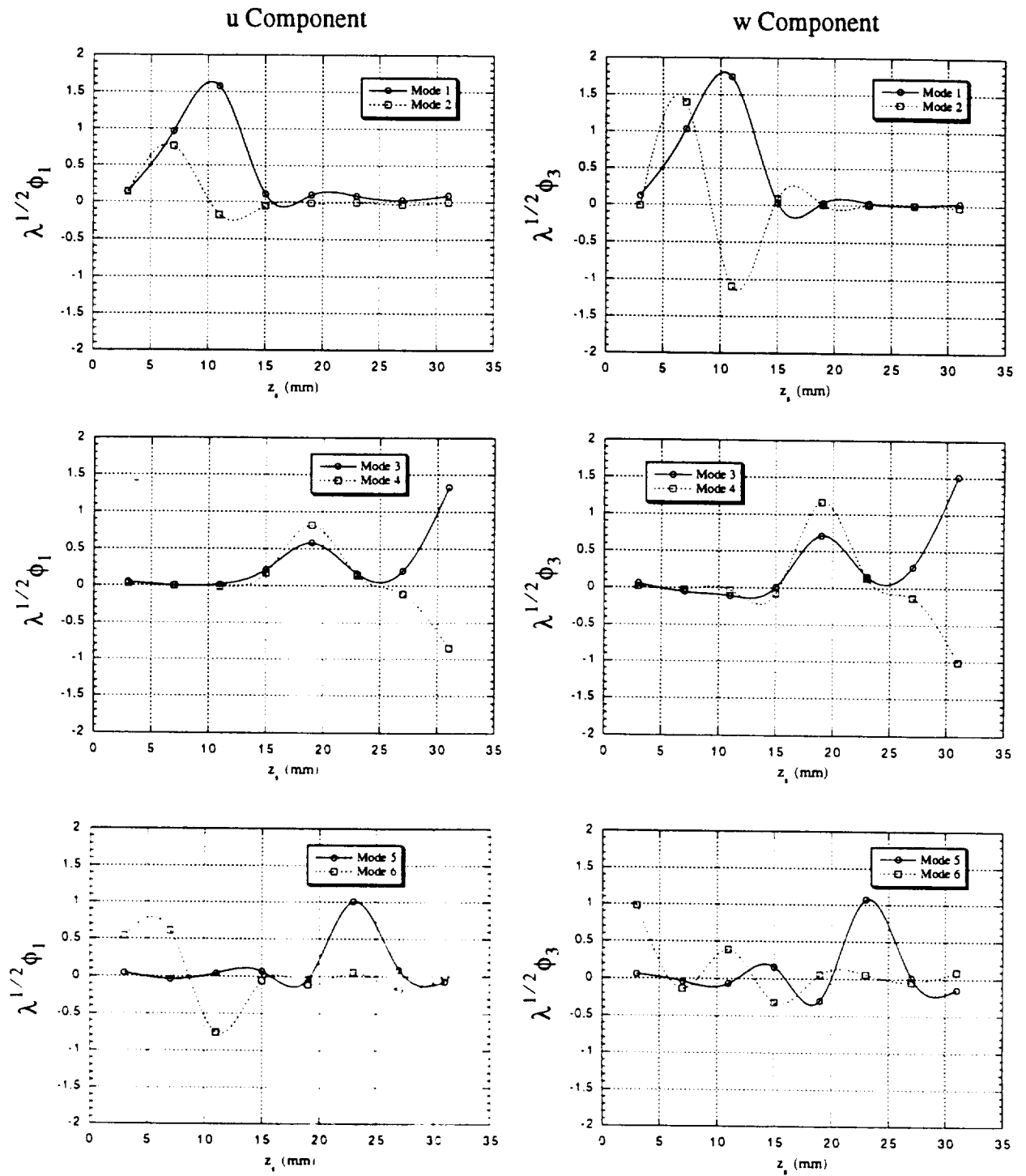
Figure 8.18: First six spatial POD modes of the two components of velocity at $x/c = 0.58$, $y = 3.0$ mm.

The amplitudes of the first modes have increased suggesting that the fluctuations have gained momentum from the mean flow through the transition process. Also, the second modes contain an almost equal event in amplitude near the same region as the corresponding first mode but is out of phase. The peaks at the 7-mm location in the second mode may be caused by the same crossflow mechanism determined to produce the large structure in the first mode. The 7-mm location is originally located on the up-swelling portion of a stationary vortex and the 11-mm position is in the "valley" region in the laminar regime. The positive peak at 7 mm and the negative peak at 11 mm in the turbulent second mode could correspond to a large structure produced by a specific mixing process. This process may occur when the vortex centered at the 15-mm position in the laminar regime collapses towards the surface and is met with the up-swelling fluid of the neighboring vortex centered between the 3-mm and 7-mm laminar positions. This predominantly spanwise flow feature would account for the significant growth in the w component's second mode (compared to the u component) in this region.

Evidence of this process occurring at the 31-mm position is viewed in modes 3 and 4 which are, again, stronger in the w component. Although there is not enough experimental evidence here, it is hypothesized that these structures are somewhat periodically recurring in span. The significant rise in amplitude at the 31-mm position suggests that this is the case. If we could consider the origin of the large-scale structure sensed in the first two modes as a result of neighboring, co-rotating, stationary vortices colliding then the resulting structure in the turbulent boundary layer should reappear approximately 24 mm away in span. With the one such turbulent structure sensed at 11 mm, this would place the next similar event at a span location 24 mm away in span placing the center of that second structure at 35 mm. Clearly, the event in the third and fourth modes at 31 mm is a significant rise in amplitude and could possibly be the outer edge of the next large-scale structure produced by the crossflow instability. If this is the case, then their presence in modes 3 and 4 may be attributed to the fact that only the edge of the structure resides within the measurement range. The measured kinetic energy would certainly not be comparable to a structure that is completely captured within the spanwise range of measurements but would overpower the smaller scales that normally exist in higher modes. Again this theory of spanwise periodicity in the turbulent boundary layer is a hypothesis and requires further investigation. A measurement grid of the same or better resolution extended across five or six stationary vortex wavelengths would deter-

mine if in fact the large coherent structures in the turbulent regime have some sense of spanwise periodicity with a spacing approximately twice the stationary vortex spatial wavelength.

8.2.3 Crossflow Surface Shear Stress: Spatial Modes

The one-dimensional POD eigenfunctions are solved for the single crossflow component of surface shear stress measured at $x/c = 0.50$ and $x/c = 0.58$ using equation 6.32 with the appropriate spatial correlation tensor of equation 6.2. The single-component POD solution for the 16 (12 in the turbulent regime) measurement sites in span results in 16 total modes (12 in the turbulent regime). The spatial POD modes (where φ_2 corresponds to the crossflow component eigenfunctions of the surface shear stress) are again plotted here with the appropriate eigenvalue scaling as explained in section 8.2.1. It should also be noted that these solutions are for the fluctuating surface shear stress. No mean flow is included within any of the POD analyses.

Laminar Modes

Figure 8.19 shows the first six POD modes of the crossflow-oriented surface shear stress in the laminar regime. The first mode is capturing the surface shear "foot-print" of the stationary vortices which exist within the boundary layer directly above the wing surface. The large spatial events are periodic with a spatial bandwidth of approximately 12 mm, matching the wavelength forced by the 6:12 artificial roughness elements placed at $x/c = 0.023$. The positive peaks of the first POD mode coincide with those spanwise locations where there begins an up-swelling of fluid from near the surface into the vortex structure. The location of the positive peaks in mode 1 are denoted on the "flow map" by the arrows in figure 8.20. Here the near-wall fluid particles are being drawn upwards into the vortex structure only to be forced to the surface again just before the spanwise wavelength is reached in span. The down-forcing of the fluid occurs at locations where the first mode exhibits negative peaks. Thus the relative direction of fluid motion above in the boundary layer, sensed in the spanwise component of surface shear stress, manifests itself in the opposition of positive and negative peaks, i.e., the phase relationship between spatial events in the POD eigenfunctions.

The first modes of the u-component velocity solution and the crossflow surface shear-stress solution are superimposed upon a local portion of the "flow map" in figure 5.13 and are shown in
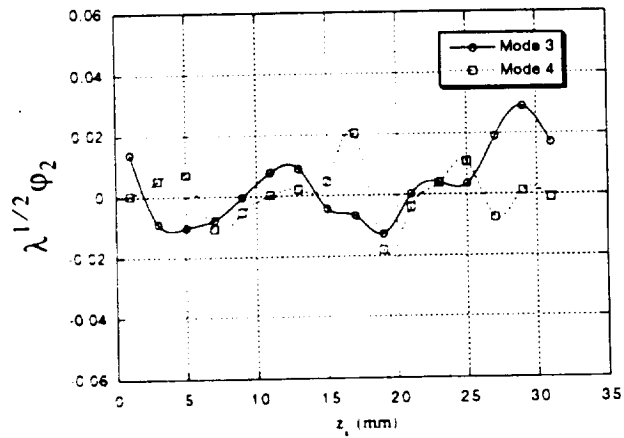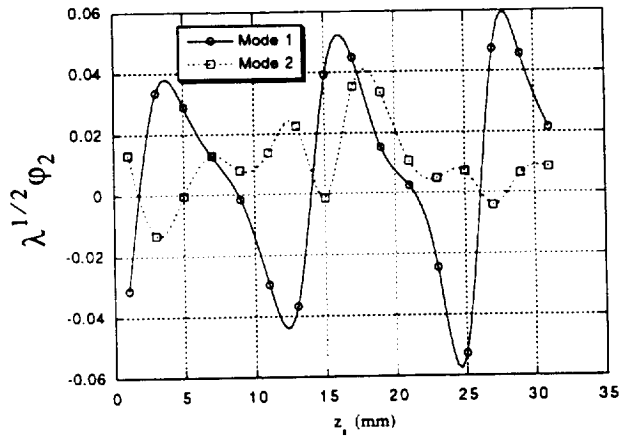
Figure 8.19: First six spatial POD modes of the crossflow component of surface shear stress at $x/c = 0.50$.
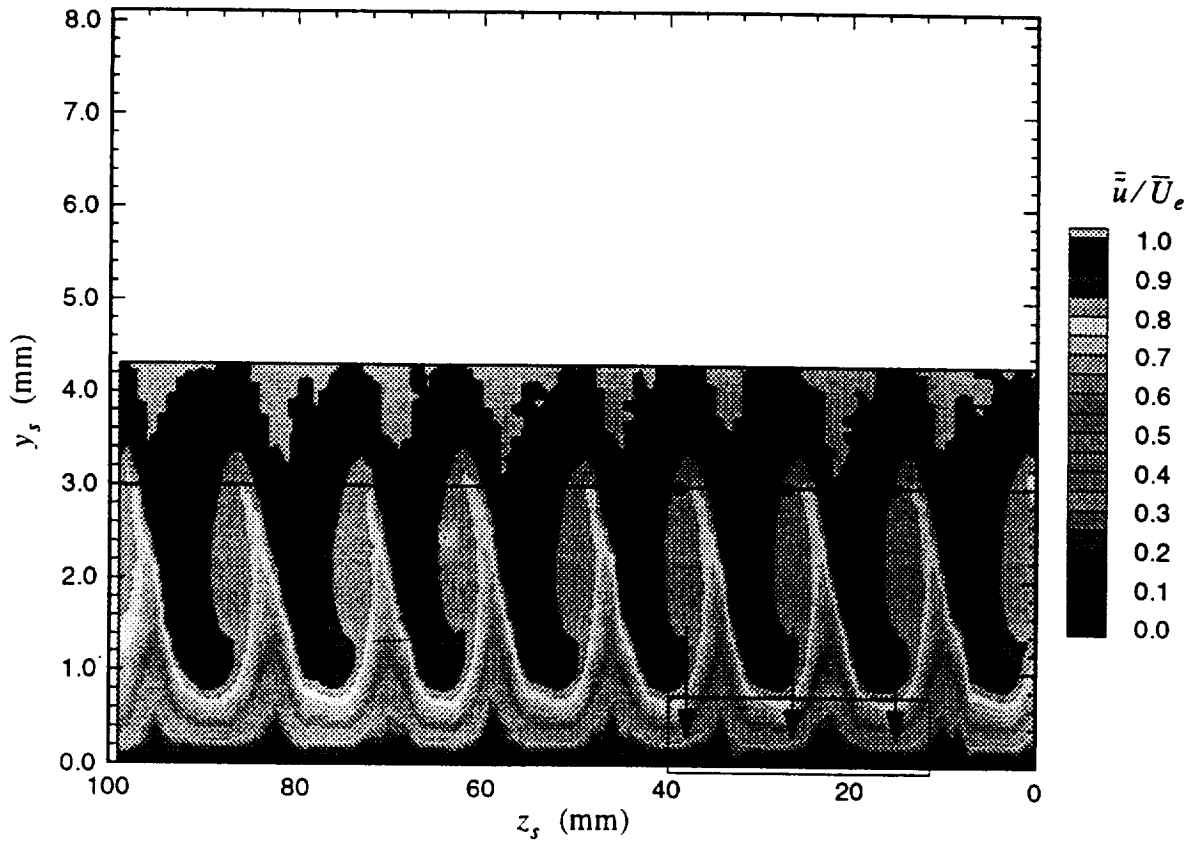
Figure 8.20: Peak identification for first mode of surface shear stress in crossflow direction by arrows on the streamwise velocity contour at $x/c = 0.50$.
Circles represent approximate cross-wire positions.
Rectangle represents approximate span range of hot-film measurements.

figure 8.21. It is clear that the increased resolution of the hot-film measurement grid captures more structural information of the stationary vortices. The dominant shear mode provides excellent identification of the near-wall fluid motion which of course is linked to internal vortical motions measured by the cross-wires 3.0 mm above the surface. However, this vortical structure is only captured if the cross-wire grid is fine enough or if the measurement sites happen to fall in regions of down-swelling or up-swelling such as the measurement site at 15 mm (see figure 8.17). Thus, surface measurements actually provide the necessary spatial information with significantly less amounts of data. The surface measurements spatially identify the dominant flow structure in the first POD mode and with prior knowledge of the swept-wing boundary layer can provide detailed information about the internal flow. This is a very important result for flight applications
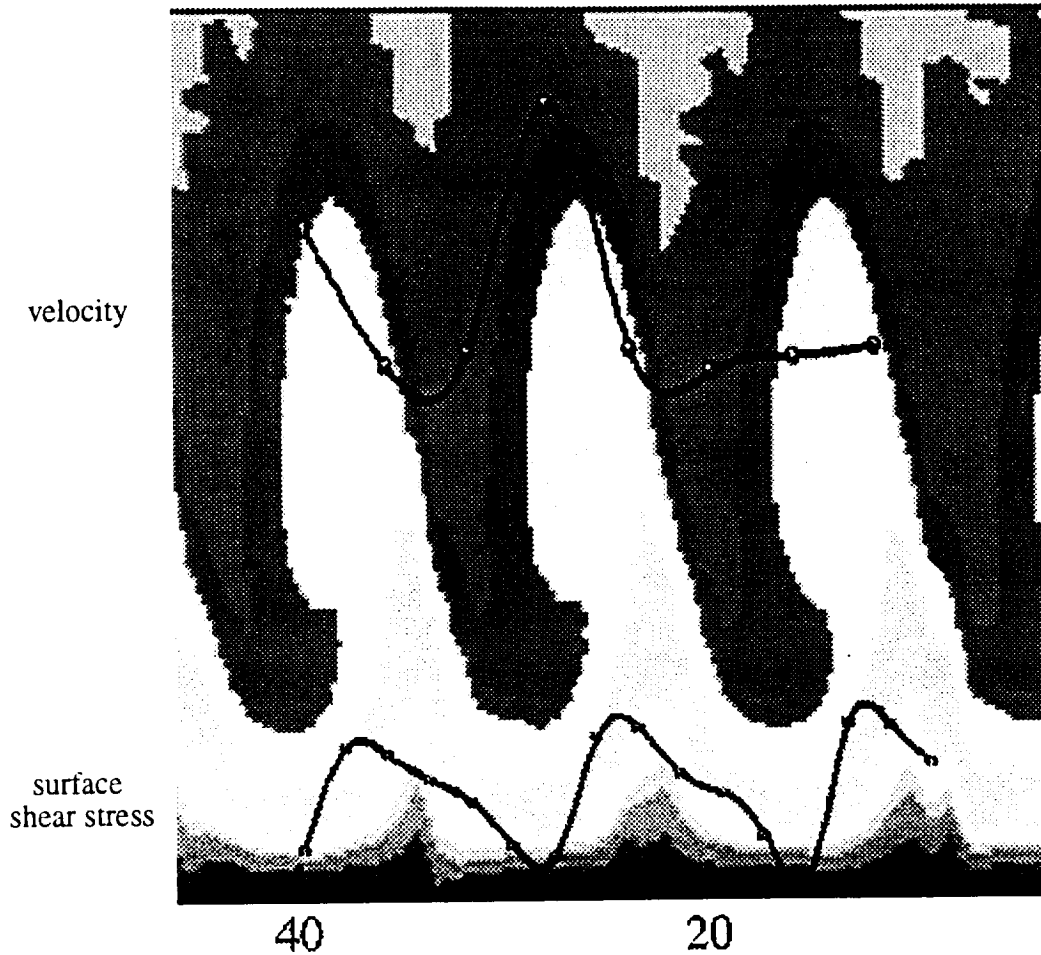
Figure 8.21: First POD modes of the u component of velocity and the spanwise component of surface shear stress superimposed onto the streamwise velocity contour of figure 5.13.

where internal measurements are not easily obtained. Simply using the surface-mounted hot-film technology in flight, appropriately on any control surface, should reveal some important internal structural data about the boundary layer.

The higher modes in figure 8.19 appear very nonlinear spatially and show a little sense of broad periodicity as smaller events are found at several spanwise locations, particularly near the doubly-inflected portion of the boundary layer velocity profiles. For instance, modes 3, 4 and 5 all demonstrate small spatial events near the 3-, 15- and 27-mm positions, locations directly below doubly-inflected velocity profiles. So, these relatively low-amplitude, low-energy events are most likely spatial surface shear effects of the secondary instability growth mechanism. One may

attribute these events to the slope of the double inflection which has a very different profile than accelerated or decelerated profiles. (Refer to Reibert (1996a) for further information on these three categorized mean velocity profiles.)

Turbulent Modes

Figure 8.22 displays the POD modes in the turbulent regime solved from the one-dimensional, one-component surface shear-stress version of equation 6.32. The first POD mode demonstrates a very high-energy distribution across the spanwise direction. The entire first mode resides above zero and is completely in phase across the measured span range. Remnants of the stationary structure emerge through transition as previously witnessed in the turbulent velocity solutions of figure 8.18. The shear structure on the surface, however, is much broader than that sensed by the velocity measurements at 3.0 mm above the wing surface. This large, broad structure in the first mode ranges from 5 mm to 25 mm which is most likely not coincidental. This is most likely further evidence that a spatial wavelength near double that of the stationary structure before transition exists in the turbulent regime. (The structure may extend the full 24 mm but cannot be confirmed without an extended measurement grid in the spanwise direction.) The difference between the shear solution and the velocity solution is that the large-scale shear structure *extends* over the proposed 24 mm wavelength whereas the velocity structure has a significantly narrower bandwidth but possibly re-occurs every 24 mm (supported by the large event in modes 3 and 4 at the 31-mm position in figure 8.18). The presence of the broad-band shear structure further supports the double-wavelength theory described in section 8.2.2 which states that the origin of the large-scale structures in the turbulent regime are a result of neighboring, co-rotating, stationary vortices colliding. The resulting spatial structure in the turbulent boundary layer should then re-occur 24 mm further in span. We see similar evidence of that in the first two modes of the surface shear stress. However, more concrete evidence by extending the measurement grid further in span is required to verify this hypothesis.

Higher modes for the turbulent shear solution in figure 8.22 reveal spatially nonlinear relationships reminiscent of the higher modes in the laminar regime. In fact, mode 3 of the turbulent shear solution is extremely similar to mode 5 in the laminar regime. Likewise, the spatial trends of mode 5 in the turbulent regime are similar to the spatial evolution of mode 3 in the laminar regime. These similarities are most likely attributed to the secondary instability producing the
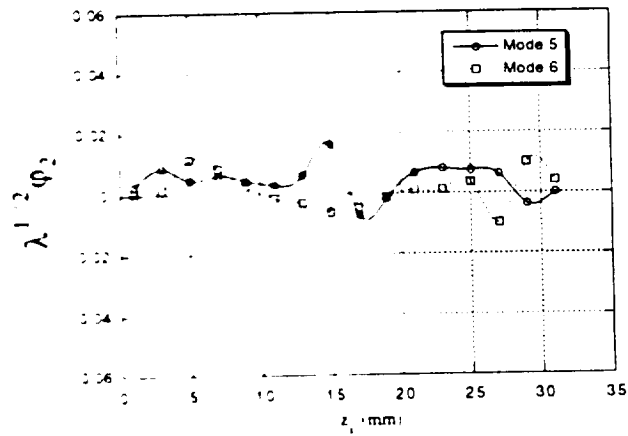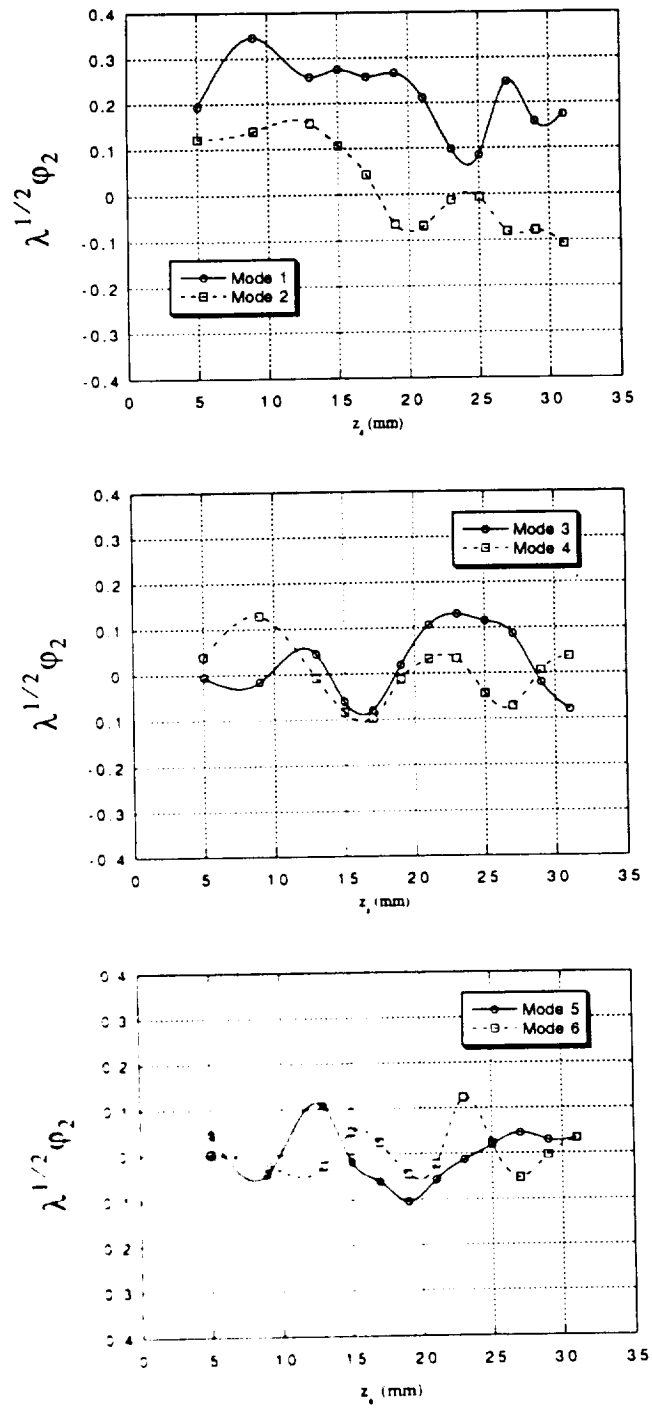
Figure 8.22: First six spatial POD modes of the crossflow component of surface shear stress at $x/c = 0.58$.

small-scale turbulent structure as observed through the auto-spectral analysis of sections 7.2.2 and 7.2.3. The higher modes in the laminar shear solution are identified as effects of the secondary instability growth which is supported by their structural features and their spatial coincidence with the doubly-inflected velocity profile. Similar low-energy, small-scale structure exists in the turbulent regime and therefore most likely originate from the secondary instability.

8.2.4 Streamwise Surface Shear Stress: Spatial Modes

The one-dimensional POD eigenfunctions are also solved for the fluctuating streamwise component (from sensors closely aligned parallel to the stationary vortex center-lines) of surface shear stress measured through transition from $x/c = 0.49$ to just after $x/c = 0.57$ using equation 6.32 with the spatial correlation tensor of equation 6.3. This single-component POD solution for the 15 measurement sites in span results in 15 total modes (φ_1 corresponds to the streamwise component of surface shear stress). The spatial POD modes are again plotted here with the appropriate eigenvalue scaling as explained in section 8.2.1.

The measured streamwise shear-stress field through transition is a very rich environment for physical mechanisms which emerge from the first six eigenfunctions (shown in figure 8.23). Because of the abundance of information involved, the analysis is separated into two sections. The first discusses the first two POD modes and the second section discusses higher modes.

Modes 1 and 2

Figure 8.23 shows the first six modes from the streamwise shear solution. Some very exciting flow physics are captured particularly within the first two modes. The first mode shows growth until a local maximum is reached near $x/c = 0.52$ and then a steady decrease as the flow progresses downstream into the turbulent regime. The second mode also grows but surpasses the first mode in downstream position before reaching a local maximum at $x/c = 0.56$. The second mode then also decreases as the flow progresses further into the turbulent regime. Referring to figure 7.41, the auto-spectra of the streamwise surface shear stress, we see a growth in the spectral signature of the primary instability (the crossflow instability near 250 Hz) upstream of the transition front. This spectral event disappears as transition gives way to the onset of turbulence. As transition starts, we also see a growth in the spectral signature of the secondary instability (near
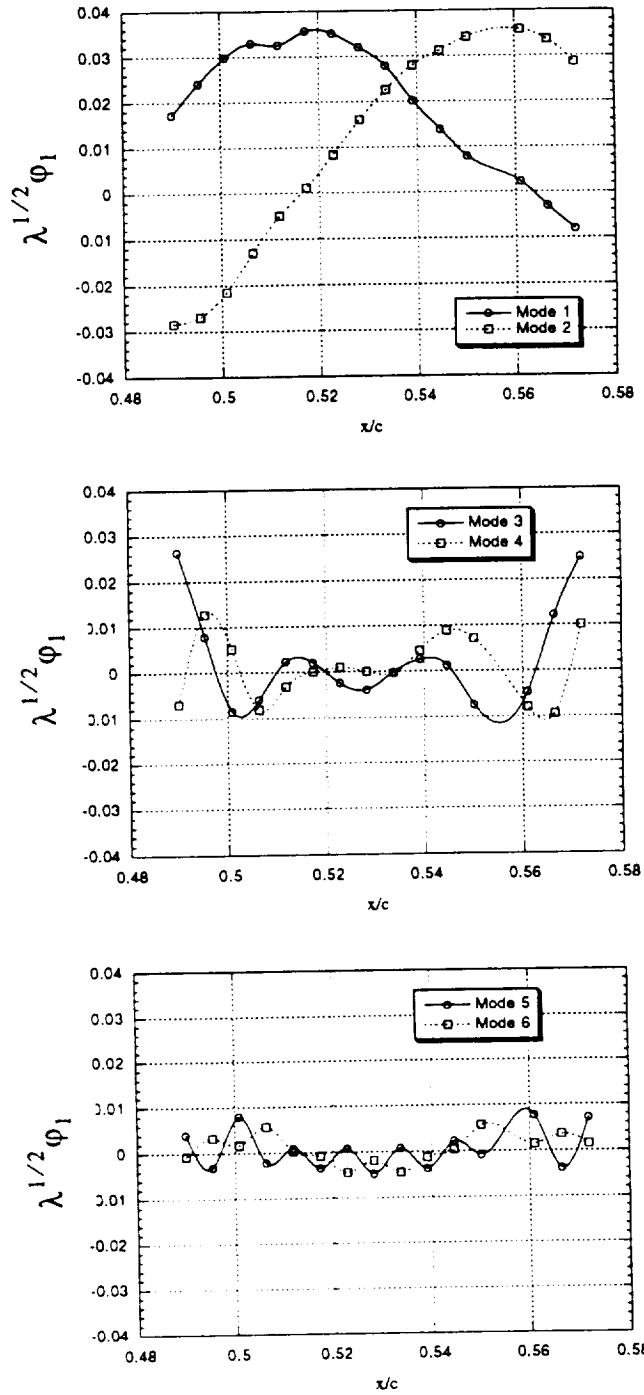
Figure 8.23: First six spatial POD modes of the streamwise component of surface shear stress through transition from $x/c = 0.49$ to just after $x/c = 0.57$.

1.3 kHz) and then a slight decrease further into the turbulent region. Therefore, the spatial POD solution is clearly capturing the two instability mechanisms individually within the first two modes. The growth and decay of the primary crossflow instability mechanism is isolated in the first mode and the spatial growth and decay of the secondary instability mechanism (due to the doubly-inflected velocity profile) is captured within the second mode. This is a remarkable result in that it *objectively* identifies the transition region, not just the start of transition, but the entire region from the breakdown of the stationary vortices in the laminar regime to the full onset of turbulence.

Several transition detection techniques have been used in the past including flow visualization or signal-processing-based analyses which set intermittency thresholds or spectral thresholds. Appropriate flow-visualization techniques often supply a decent "image" of the transition front as seen in figures 5.1 and 5.2 but they do not provide quantitative information on the onset of turbulence or how far downstream the transition front extends. Flow visualizations serve their purpose in providing global understanding of the flow patterns but rarely provide enough quantitative results. Signal processing techniques used to detect transition are often very subjective. Typical techniques which are based on intermittency or kinetic energy levels rely on thresholds chosen by the analyst. Here, the POD, a mathematically unbiased method, provides a completely objective transition detection method through simple analysis of the first two spatially-evolving POD modes. The entire transition front may be identified by the activation and deactivation of specific mechanisms between the first two modes. In other words, the transition region is identified between the two maxima of the first two POD modes.

The primary instability becomes critical at the peak of the first mode and then subsides as large-scale turbulence emerges. The secondary instability continues to grow and eventually reaches a maximum completing the transition process. It is at this peak in the second mode that full turbulence starts, a location where the critical growth of the secondary instability creates very small scales within the boundary layer. These claims are verified by the flow visualizations in figures 5.1 and 5.2 which show the transition front starting near $x/c = 0.52$. This transition-detection technique is also supported more quantitatively by the auto-spectral results in figure 7.41 where the evolution of the instability mechanisms coincides with the transition limits determined by the POD maxima in the first two modes.

From this analysis, we see that the primary instability is appropriately named since it is

indeed the dominant instability which, as the first POD mode and the auto-spectra show, initiates the breakdown process as its growth becomes critical. The fact that this mechanism resides within the first POD mode also states that this mechanism has higher energy content than any other in the measured flow field. This mechanism physically corresponds to the collapse of the rollover structure seen in the streamwise mean velocity contour in figure 5.13 as the disturbances become critical. This collapse along with the momentum transfer from the mean flow to the fluctuations creates the large-scale structures within the turbulent regime which are identified in the first few spanwise POD modes of the streamwise velocity at $x/c = 0.58$.

The secondary instability mechanism, evident in the second mode of the streamwise shear solution, still grows through transition and loses energy only when the flow continues to propagate in the turbulent regime. This supports the fact that the small-scale structures in the turbulent regime originate directly from the secondary instability. This physically corresponds to the doubly-inflected velocity profile effectively becoming more "S" shaped and finally creating a mixing process similar to an internal shear layer where low-velocity fluid resides between the accelerated portion of the boundary-layer fluid near the wall (which starts forming a sharp slope familiar to turbulent boundary layers) and the high-velocity fluid near the outer edge of the boundary layer. Through transition, the spectral event caused by the secondary instability still grows (as also seen in the second POD mode) and gives way to small-scale turbulence. These small scales are generated by the highly nonlinear terms in the equations of motion (Tennekes and Lumley 1972) which further identifies with the secondary instability, a highly nonlinear process involving an inflectional boundary-layer profile. Within the turbulent regime, these small scales start to dissipate due to the effects of viscosity which accounts for the decrease seen in the second mode within the fully turbulent region.

Higher Modes

The higher modes also contain significant physical information even though these modes contain very little energy in comparison to the first two modes as evidenced by the eigenvalue-based modal percentage of kinetic energy shown in figure 8.16. The streamwise structures present in the higher modes certainly do not dominate the flow field or cause the breakdown process but do reveal the well-identified signatures of specific mechanisms that do govern transition.

There exists a great deal of periodicity in the higher modes. Modes 3 and 4 demonstrate long

181

streamwise wavelengths while modes 5 and 6 exhibit very short spatial wavelengths. The "mirrored" periodic structure ranging from $x/c = 0.49$ to approximately $x/c = 0.53$ in mode 3 has a spatial wavelength of approximately 70 mm (sensor spacing is 10 mm in the x_t direction). Thus, for a freestream velocity of 26 m/s which is typical of the current experiment (where $Re_c = 2.4 \times 10^6$ and $x/c \approx 0.50$), this spatial wavelength corresponds to a wave frequency of approximately 375 Hz. This very closely agrees with the spectral signature associated with the primary instability mechanism which typically resides between 200 and 350 Hz as seen in the spectral analysis in chapter 7. Saric et al. (1990a) have shown that the travelling wave (i.e., the primary instability mechanism) spectral signature may extend as high as 400 Hz for similar flow conditions on the same airfoil. Thus, the third mode most likely represents some form of the streamwise evolution of the travelling wave. Similar wavelengths are detected in the fourth mode but appear less periodic.

Modes 5 and 6 demonstrate high degrees of periodicity and evolve with the same spatial wavelength of approximately 20 mm which, for the same flow conditions used above, corresponds to a wave frequency of 1.3 kHz. This is identified in the auto-spectra of figure 7.41 as the spectral signature of the secondary instability. The fact that these waves are in the fifth and sixth modes implies that these evolutions contain low amounts of kinetic energy, consistent with the characteristics of the small-scale structure in the turbulent regime. Both modes 5 and 6 show a longer wavelength in the laminar regime and then again in the fully turbulent regime with a shorter wavelength in the transition region. These events spatially correspond to the growth of the secondary instability in the laminar regime (the first longer wavelength), the growth through transition and the generation of small-scale turbulence (the shorter wavelength), and the decay due to viscous dissipation in the fully turbulent regime of the small scales (the second longer wavelength). Also note that mode 5 is completely out of phase with mode 6. As seen in section 8.2.2 in the laminar POD solution of the crossflow surface shear stress, phase information can sometimes infer relative fluid motion. If this indeed applies to the streamwise modal evolution (not yet proven), then the phase difference between modes 5 and 6 could represent the relative fluctuations produced in the mixing process previously described in the discussion of the first two streamwise POD modes. This mixing was attributed to the doubly-inflected velocity profile effectively becoming more "S" shaped and generating an internal shear layer giving way to the production of small-scale turbu-

lence. Regardless of the possibility of phase determination of relative fluid motion, the important result here is that the secondary instability mechanism is being tracked by the higher modes and shows changes in wavelength as the flow enters or exits specific flow regimes.

8.3 Temporal Proper Orthogonal Decomposition Results

Now that important mechanisms and spatial flow structures have been identified by the solution of the POD near and through the transition region, we can consider the temporal evolution of the dominant modes which are very useful for developing flow control strategies. The first few modes are seen to contain most of the kinetic energy within the flow field as witnessed by the eigenvalue-based modal energy percentages in figure 8.16. Therefore, we hope to characterize the temporal evolution of the entire measured flow field by considering only the first two POD modal coefficients. These temporal coefficients are scalar quantities still based on the mean-square energy projection described in section 6.3.2 and contain an integrated effect of the spatial distributions within the field. In general, the POD coefficients are solved using equation 6.26 or, for the one-dimensional POD solution, using equation 6.34. Equation 6.38 is used if the complimentary technique is needed. Using these coefficients to describe the flow field has many advantages. There is a greatly reduced amount of data needed to appropriately characterize the flow field. Also, as demonstrated in the streamwise surface shear-stress POD solution in section 8.2.3, specific mechanisms can be isolated. Looking at the temporal evolution of these individual mechanisms contained within specific dominant modes may reveal control possibilities otherwise unseen.

Therefore, if we are concerned with the global characteristics of a flow field, we look to the first two POD modes, spatially through the eigenfunctions and temporally through the coefficients. Most boundary-layer flow-control strategies, particularly ones for flight applications, are concerned with reducing the growth of the disturbances and effectively the dominant structures in the laminar flow field. Thus, our focus is on the dominant modes. If we are concerned with the small-scale structure, particularly in the turbulent boundary layer, then we need to include higher modes in our analysis. However, one has to be very careful with incorporating higher modes into the temporal analysis when the complimentary technique is used. Recall that the complimentary technique uses the estimated instantaneous field from the LSE solution to compute the time-

dependent POD coefficients. (The spatial POD solution is only dependent on the correlation tensor.) Bonnet et al. (1994) have shown that the complimentary technique converges on the estimated field when higher modes are included. This potentially corrupts the analysis and is strongly dependent on the performance of the LSE. As we saw in section 8.1, LSE shows some significant limitations in capturing amplitude in the turbulent regime. We also saw that in the laminar regime, the higher spatial modes really do not add significant detail or energy to the flow field. Because of these two stipulations, this entire analysis is limited to just the first two modes.

8.3.1 Two-Component Velocity: Temporal Modes

The coupled POD coefficients are solved for the two-component velocity measurements using the two-component form of the complimentary technique shown in equation 6.38. Note that these solutions contain the integrated effect of the cross-component spatial information.

Laminar Solution

Figure 8.24 shows the first two temporal modes, i.e., the coefficients, for the POD solution

Figure 8.24: Temporal evolution of the first two POD modes for the two-component velocity measurements at $x/c = 0.50$, $y = 3.0$ mm.

obtained at $x/c = 0.50$ using the estimated instantaneous fields (shown in figures 8.8 and 8.9) calculated with the appropriate references (using locations at 15 and 27 mm). The first mode demonstrates some periodicity associated with the travelling waves and large high-frequency spikes characteristic of the secondary instability mechanism. The second mode produces a very laminar-looking signal with broad periodicity again attributed to the presence of the travelling wave and the integrated effects of the stationary wave which has significant spanwise periodicity.

The important result here is how descriptive these scalar signals are of the two-component velocity fields in figure 8.8 and 8.9. The POD coefficients of the first mode are very characteristic of the velocity components at the 15-mm location. This is due to the structural event at this location captured in the first spatial POD mode in figure 8.17. The dominance of this event appears in the coefficients as well. Also, the high degree of periodicity seen at other locations in the flow field are well described by the second mode.

Using both scalar signals to describe the entire two-component velocity field seems very reasonable when concerning the global applications discussed above, particularly with in-flight applications. Thus, we have reduced the amount of needed information from 16 two-component signals to 2 scalar signals. The beauty of this technique is that the dominant-energy events anywhere in the measured field are contained within these two scalar signals. The entire field may even be reconstructed using these two temporal modes and all of the spatial modes. These reconstructions are demonstrated for the surface shear-stress solutions in section 8.4.

This technique is not without its limitations, however. As mentioned above, the velocity fields used to compute the temporal modes in figure 8.24 are indeed estimated from just two cross-wire probes. Higher modes are not to be trusted due to the high degree of dependency on the performance of the LSE.

However, we have shown that very characteristic signals can be obtained through the complimentary technique as long as the limitations are considered. The result allows us to possibly train neural networks with these scalar signals in the future. We allow the networks to "learn" how to change a control feature on an aircraft surface in reaction to the global events in the flow field as determined through the complimentary technique. Once fully-automated, this could provide previously unobtainable levels of dynamic flow control.

The POD coefficients for the coupled velocity components are also computed in the turbulent regime at $x/c = 0.58$ and are shown in figure 8.25. Here we see that the two modes display turbulent characteristics with high frequencies and no real detectable periodicity. This is very descriptive of the reference signals in the estimated velocity fields of figures 8.12 and 8.13. The remaining locations in the velocity fields are not well represented but this entirely due to the poor performance in estimating the signal amplitudes by the LSE in the turbulent regime. So a further advantage to using the dominant POD coefficients to describe the flow field emerges. If we look at the statistical information from the auto-spectra and the spatial correlation tensor in the turbulent regime and any actual measured signals we see that there is very little discrepancy in signal characteristics across the span. This is not what we see in the estimated field. Clearly, there are amplitude problems. However, by using this limited information to determine characteristic scalar signals that are to represent the entire field, we effectively do not corrupt any control algorithms. The scalar, time-dependent functions in figure 8.25 contain the high-energy-based structures. It is these large coherent structures that are the focus of control strategies. The smaller scales dissipate
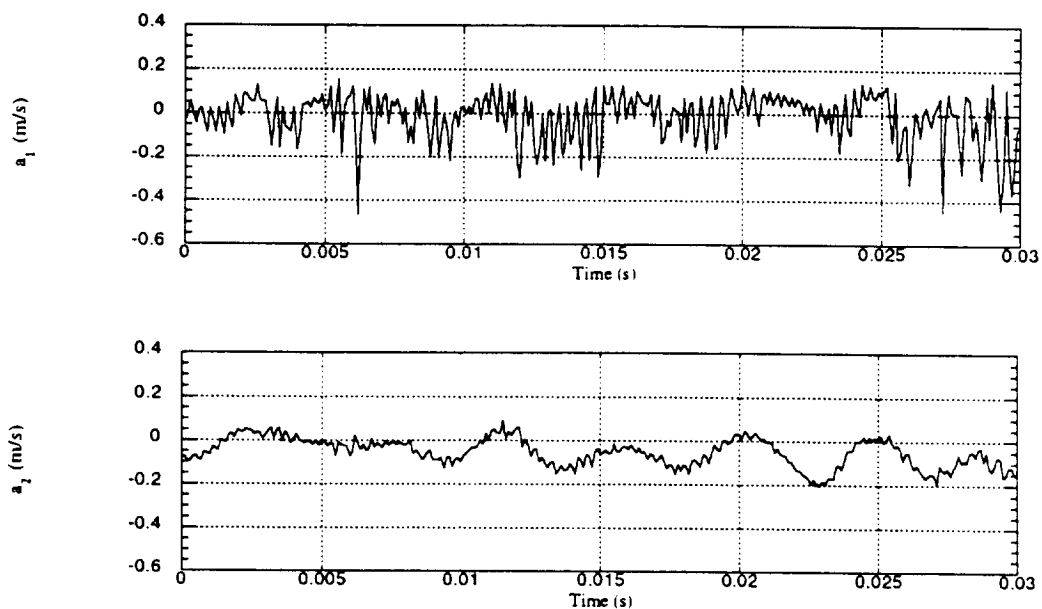

Figure 8.25: Temporal evolution of the first two POD modes for the two-component velocity measurements at $x/c = 0.58$, $y = 3.0$ mm.

rather quickly due to the viscous effects (as witnessed in the streamwise surface shear stress solutions). Thus we actually improve our available information about the instantaneous flow field by using the POD coefficients as opposed to the estimated velocity fields. This is encouraging if we consider the ultimate goal of bringing these techniques to actual flight applications.

8.3.2 Crossflow Surface Shear Stress: Temporal Modes

Similar calculations are performed for the crossflow component of the surface shear stress. The hot-film sensors are used to simultaneously measure this shear field with the velocity measurements. Thus, through these simultaneous measurements and the advanced correlation techniques discussed in chapter 6, the surface shear-stress POD coefficients are calculated such that they are in phase, i.e., instantaneous, with the velocity modes discussed in the previous section.

Simultaneous Laminar Solutions of Surface Shear and Velocity

To check for any flow disturbance, the RMS profiles of the surface shear stresses acquired simultaneously with the velocity measurements are compared to the RMS profiles of the same shear field acquired without the cross-wire probes in the flow (shown in figure 8.26). There is a discrepancy in the shear values at span locations close to the surface-mounted cross-wire which is apparently locally disturbing the shear measurements on the surface. Therefore, LSE is used to estimate the disturbed surface shear-stress field and reclaim appropriate RMS values. The choice
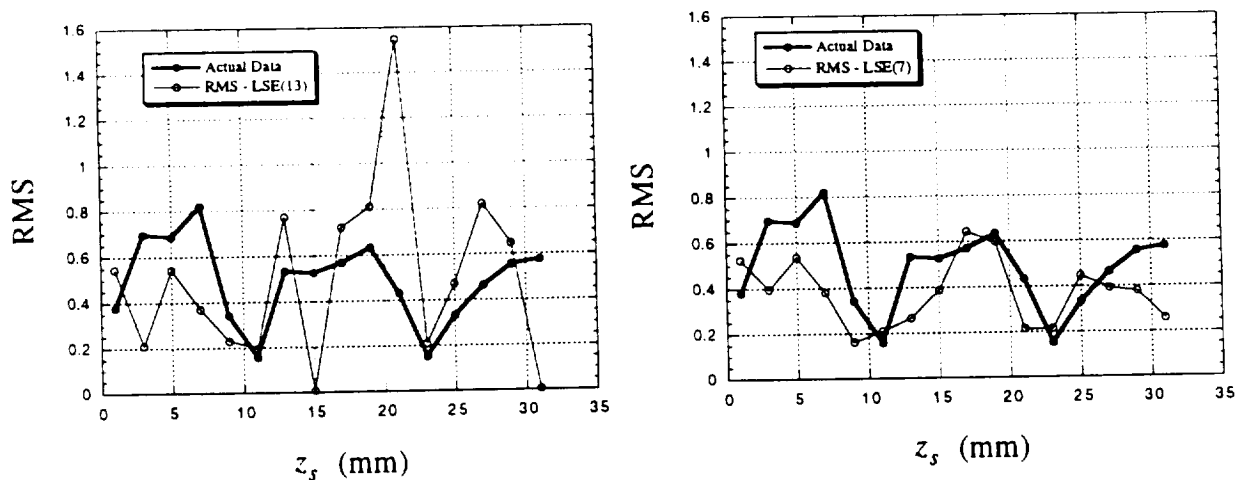
Figure 8.26: RMS comparison of the probe-disturbed crossflow surface shear-stress field in laminar regime to the same undisturbed field. RMS matching is demonstrated through use of LSE to estimate the disturbed field.

187

of reference sensors is determined through a trial-and-error process until the best RMS-profile match to the undisturbed field is obtained. The results of this process are shown in figure 8.26. LSE with a seven-sensor reference is used to reclaim the previously disturbed shear field to within reasonable statistical characteristics. When using the POD coefficients calculated from this field, we must again consider that this is now an estimated field and that higher modes are not to be trusted.

Now that the shear field is corrected as best as possible, we examine the crossflow shear coefficients from the POD solution which are instantaneous with the velocity coefficients of figure 8.23. The first two modes of the crossflow surface shear in the laminar regime are shown in figure 8.27. The coefficients are plotted here on a longer time scale to show the structure within the scalar signals. The calibration of the hot-film sensors acts again as a filter and removes some of the smaller events. Because of this, there is little we can infer about internal measurements from the surface measurements, at least when examining the POD coefficients. This is obvious when the velocity coefficients (shown in figure 8.28) are considered on the same time scale as the shear coefficients. The structural content is even visibly on a different scale. The velocity coefficients
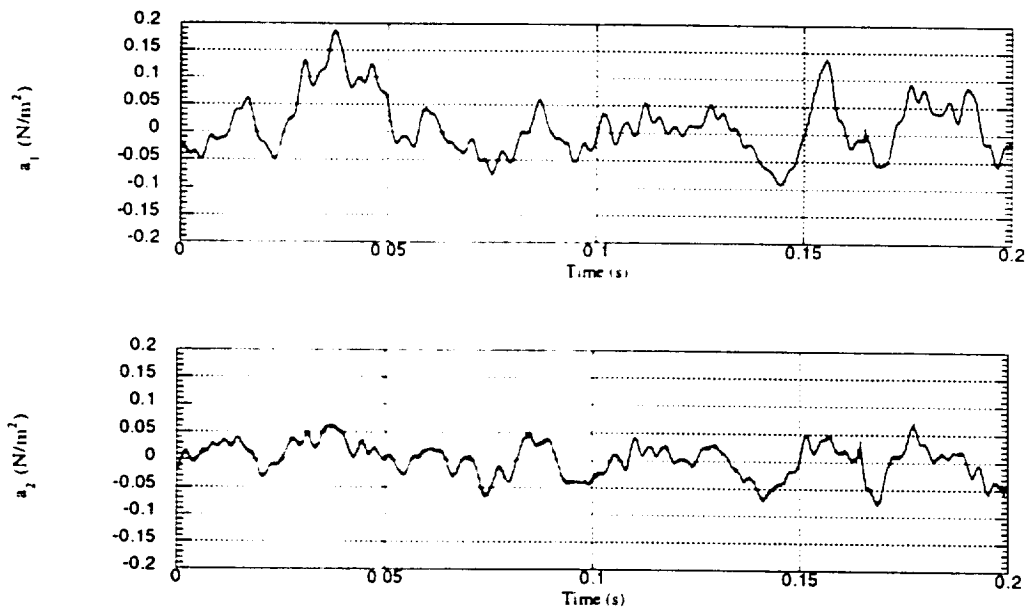
Figure 8.27: Temporal evolution of the first two POD modes for the estimated crossflow surface shear-stress field, instantaneous with the velocity modes (figure 8.28), at $x/c = 0.50$.
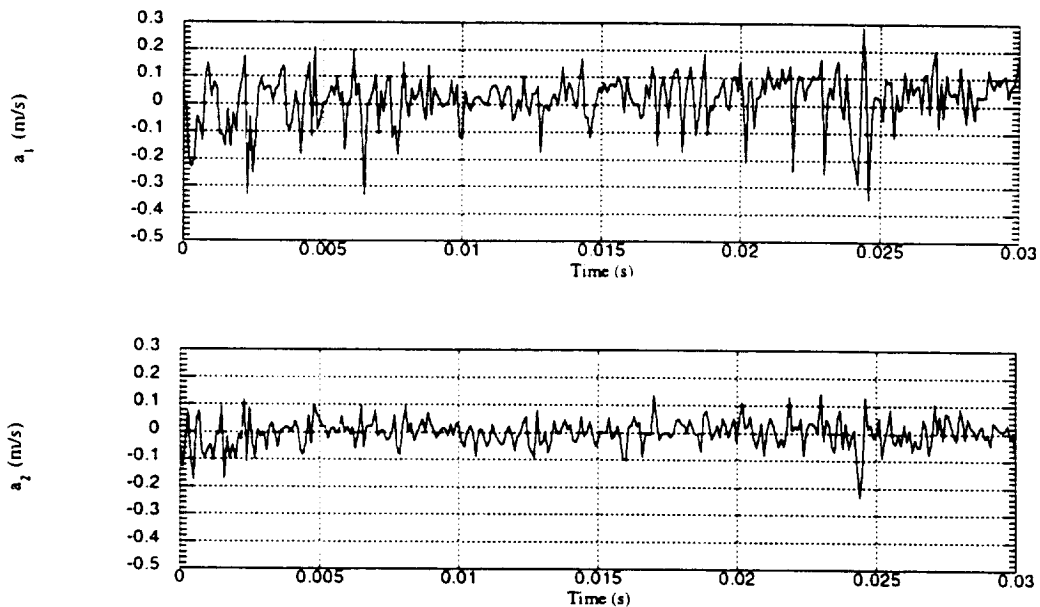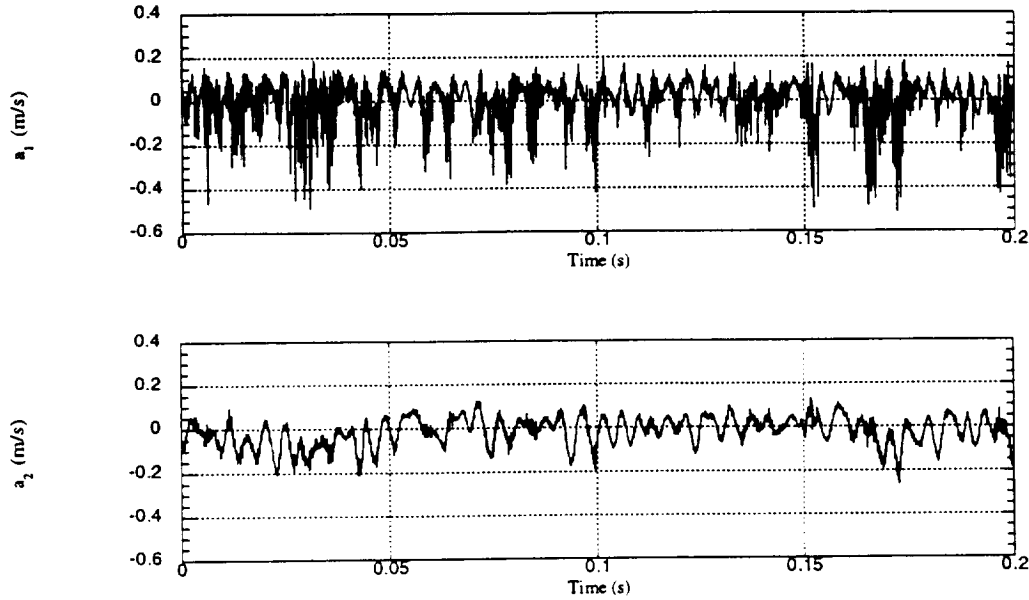
Figure 8.28: Temporal evolution of the first two POD modes for the two-component velocity measurements at $x/c = 0.50$, $y = 3.0$ mm on the same time scale as the shear in figure 8.27.

display high degrees of periodicity at higher frequencies than the shear coefficients. The spatial POD solution showed significant relations between these measurements, but the temporal solution clearly does not at this time. Many different approaches may be taken to improve the temporal relationship. These include but are not limited to attempts at better hot-film calibrations, clever use of digital filtering on the velocity coefficients to match the filtering effect of the hot-films or use of spectral comparisons. The development of these methods is beyond the scope of the current research effort, but should be considered in future work as using these coefficients for flow control and training of neural networks is realized. Another concern is that these measurements may be too separated in the y direction for appropriate temporal relationships to be realized. Thus, in future attempts at identifying the temporal relationship between the surface shear and the internal velocity, it is recommended that the velocity measurements be made closer to the wall. Unfortunately, this was not feasible for the current experiment.

Still, we focus on the positive results of this analysis. The POD coefficients contain scalar information representative of the entire measured field which is important for flow control. The comparisons of the instantaneous POD coefficients have been attempted and much has been

learned from this first attempt. However, the study of the temporal relationship is inconclusive at this point and is left for future investigations. The remainder of the current analysis will then focus on just the surface shear-stress coefficients from the undisturbed fields and how they compare across and through the transition front. Further comparisons to the originally measured shear stress fields are made through reconstructions of those fields using a few dominant POD modes in section 8.4.

Laminar Solutions

Figure 8.29 shows the first three POD modes of the crossflow surface shear-stress POD solution in the laminar regime. These coefficients are computed using data from the undisturbed shear-stress

Figure 8.29: Temporal evolution of the first three POD modes for the crossflow surface shear-stress measurements at $x/c = 0.50$ with no cross wires in the flow.

field, i.e., no cross-wire probes were in the flow. Equation 6.34 is used to calculate these coefficients since the entire field is measured simultaneously and so no estimation is needed. Hence, higher modes may be observed. The third mode is included here. Higher modes do not contain much kinetic energy as portrayed by figure 8.16 and are thus neglected in the analysis since only the dominant modes are significant to most flow control strategies.

The first and third modes demonstrate a high degree of periodicity showing evidence of the travelling wave and the integrated effect of the stationary vortices. The periodicity is very clear in these modes presumably more than the velocity solution because the sensors are aligned in the crossflow direction and are on the surface. The second mode shows less periodic events and has a few sharp peaks scattered throughout time perhaps due to the secondary instability. This could be confirmed through spectral analysis of these modes which is reserved for subsequent studies. How characteristic these scalar signals are of the original shear field is determined in section 8.4.

Turbulent Solutions

Figure 8.30 displays the first three POD modes of the crossflow surface shear-stress POD solution in the turbulent regime using the undisturbed data. The scalar signals appear filtered compared to typical turbulent signals (and to the raw voltages). This is again attributed to the limitations of the hot-film calibration procedure. The periodicity seen in the laminar regime is still evident which supports the theory that large-scale structures in the turbulent regime originate from the large vortical structure in the laminar regime. Despite the breakdown of these vortices, very strong remnants remain in the turbulent flow field. The periodicity is now seen in all three dominant modes suggesting that though the smaller scales are indeed present (as witnessed by the auto-spectra results), they are overpowered by the presence of larger scales. Smaller scales are becoming more evident in the third mode which is capturing smaller, high-frequency events. Another interesting observation is that the second mode is almost completely out of phase with the first mode. This may again be representative of relative fluid motion, however, further investigation is required to confirm this.

8.3.3 Streamwise Surface Shear Stress: Temporal Modes

The POD coefficients are also determined for the streamwise surface shear stress through transition. As the spatial POD solution showed, the first two modes isolate the effects of the two insta-
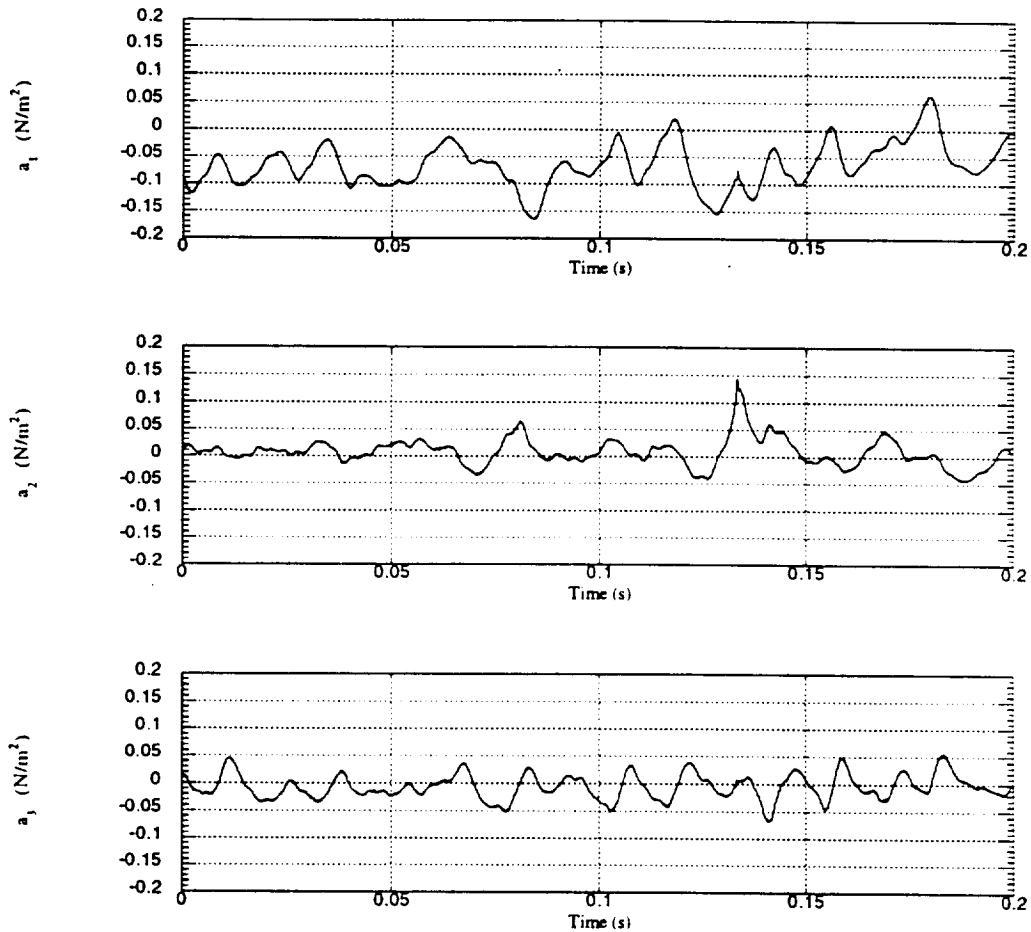
191
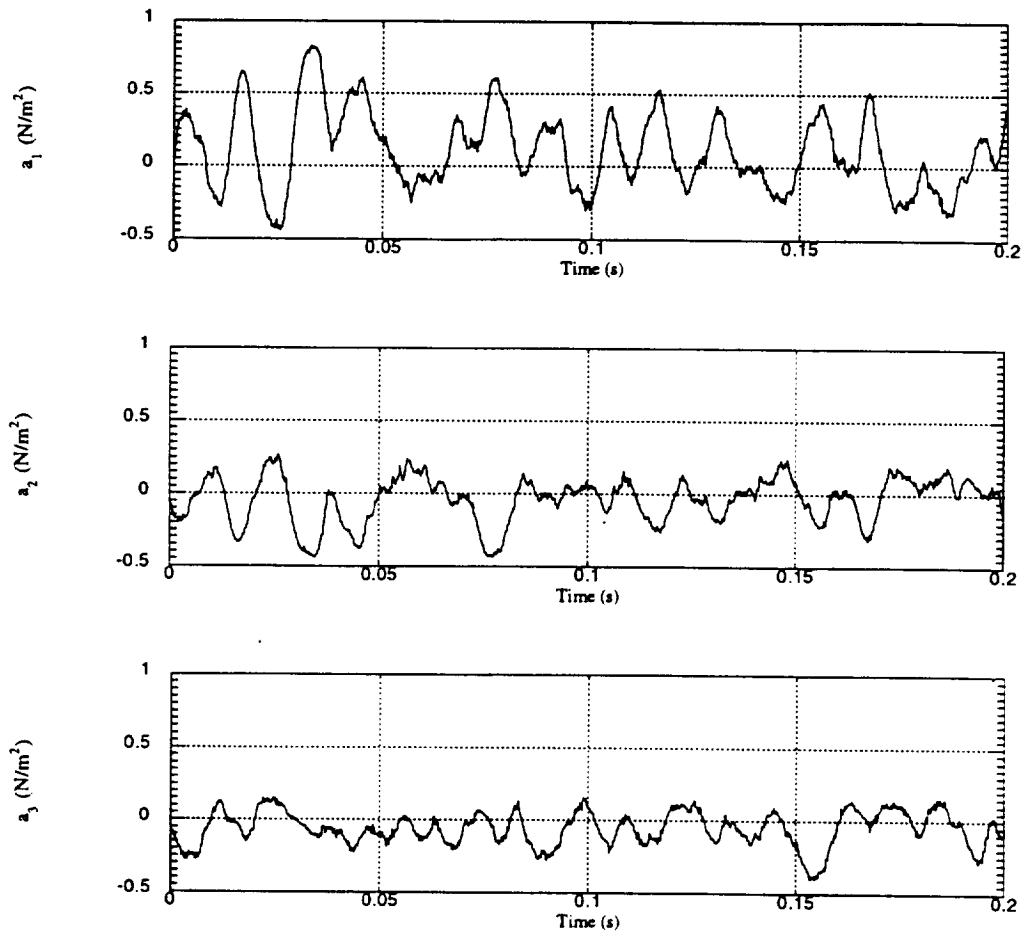
Figure 8.30: Temporal evolution of the first three POD modes for the crossflow surface shear-stress measurements at $x/c = 0.58$ with no cross wires in the flow.

bility mechanisms and so the temporal evolution of these modes is shown in figure 8.31. The first mode, attributed to the effects of the primary instability, exhibits relatively low frequency propagation consistent with the auto-spectra (where signatures are at low-frequencies) and spatial POD (where the crossflow instability is isolated) results. The second mode demonstrates higher frequency content which is consistent with the secondary instability signature already assigned to the second mode from the previous results. It is interesting to note that the events in both modes are extremely consistent. This is expected since the primary instability is coupled by the secondary instability. The secondary instability exists only because the crossflow instability (i.e., the primary instability) exists. Thus, the fact that the events coincide in time is not surprising.
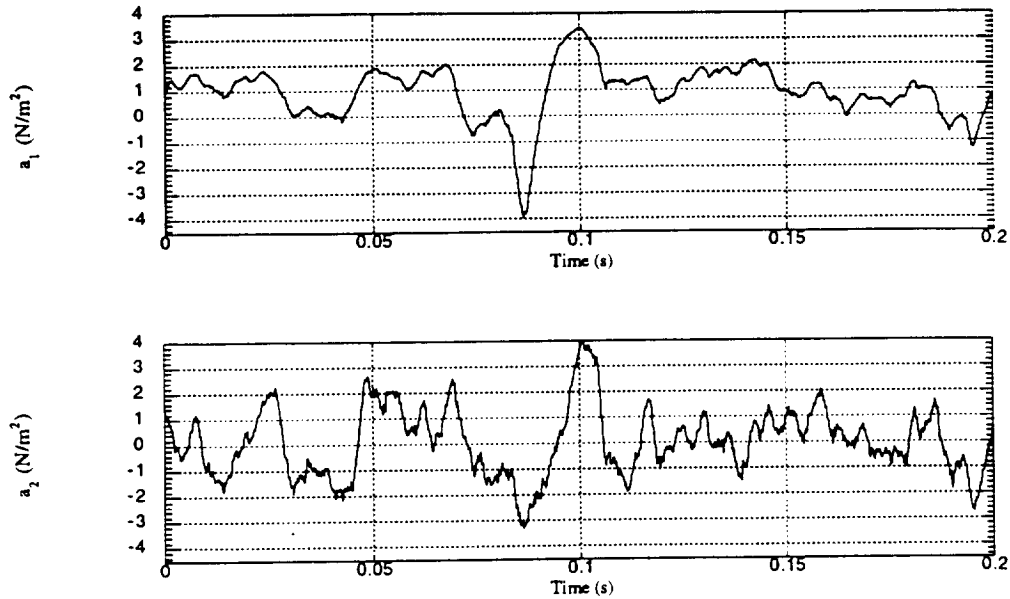
Figure 8.31: Temporal evolution of the first two POD modes for the streamwise surface shear-stress measurements through transition from $x/c = 0.49$ to just after $x/c = 0.57$.

Figure 8.31 presents a rather unique solution since the spatial measurements are in the predominant direction of the flow. This means that the coefficients contain the integrated effect of all measured downstream positions *and* the temporal evolution which is also representative of the downstream progression of fluid if an appropriate convection velocity is used to convert time to space. The result is a modal isolation of each mechanism as it might progress downstream. The spatial POD solutions, i.e., the eigenfunctions, provide a statistical downstream evolution whereas the temporal POD coefficients provide an instantaneous picture in some spatially averaged sense. Thus, if a significant event occurs in the temporal evolution of the POD coefficients, it could represent local activity (local in time) of a specific instability anywhere in the measured spatial range. Thus a properly trained flow-control system could react to these events and perhaps make appropriate changes to the flow field. These streamwise temporal modes essentially become signatures of the transition process.

These scalar signals could be used to train a neural network attempting to control the location of the transition front. For example, the large event just before 0.1 seconds in the first mode in figure 8.31 could be interpreted as a local breakdown somewhere in the measured range. When a

similar event is detected by a trained control algorithm in a similar flow situation, slight changes to the flow could be made to prevent further such events from occurring, thereby delaying transition which was identified through education from the events in the streamwise POD coefficients.

8.4 Dominant-Mode Reconstructions of Surface Shear Stresses

The POD coefficients for the surface shear stress fields determined in the previous section may now be used to reconstruct their respective shear fields. Using only the dominant modes to do this, we effectively see qualitative evidence of how much energy each mode contributes to the originally measured field, an important examination when considering the possibility of training control algorithms. Only the undisturbed surface shear stresses are reconstructed since other fields would converge towards the estimated field. This convergence creates difficulty in assessing the importance of dominant modes due to the strong dependency on the LSE performance. With the simultaneously sampled data from the hot-films, we can be confident that the reconstructions converge towards the original field. Each field is reconstructed using 1, 2 and 3 modes with equation 6.33 and the entire eigenfunction solution (to recover spatial information) to demonstrate the structural information contained within the coefficients.

8.4.1 Laminar Crossflow Reconstructions

For comparisons, the originally measured surface shear-stress field is shown in figure 8.32 in the crossflow direction at x/c = 0.50. The fluctuating signals are "stacked" and display only relative amplitudes. The spatial location of the stationary vortices is even identifiable here in the time-history data at locations near 3, 15 and 27 mm (denoted by the legend). Figure 8.33 shows the reconstruction of the surface shear-stress field in the crossflow direction at x/c = 0.50 using the first POD mode. The spatial location of the stationary vortices is captured by using the first POD mode. The travelling wave is also apparent (due to the temporal periodicity) near the locations of the stationary vortices. This implies that the travelling wave is most amplified in regions near the stationary vortical structures. The reconstructions using the first two POD modes and first three POD modes are displayed in figures 8.34 and 8.35, respectively. Adding the second mode tends to

add the periodic structure of the travelling wave to those locations in the general vicinity of the vortices. Adding the third mode fills in regions even further from the stationary vortices particularly near the 31-mm location. So we see that using the dominant modes really does capture a significant amount of the flow field's structure. Amplitudes are accurate in regions close to the stationary structures and the phase information has been well recovered. Thus, if we are concerned with global field structure then even perhaps the first mode would suffice. If we are concerned with the evolution of the entire field (not just the dominant wave-like structures) then we may opt to use a three mode representation of the entire field. Again, with estimated fields, one has to be careful when incorporating higher modes. However, with the advantage of simultaneously sampling an entire field with the non-intrusive hot-film technology we are able to use higher modes with confidence.

8.4.2 Turbulent Crossflow Reconstructions

Figure 8.36 shows the originally measured surface shear-stress field in the crossflow direction at $x/c = 0.58$. The high degree of periodicity is still present in the turbulent regime but is more consistent across spanwise locations. This shows the remnants of the travelling wave surviving the transition process near the surface and propagating in span with some high frequencies indicative of small-scale turbulence above the viscous sublayer. The first POD mode reconstruction shown in figure 8.37 isolates the high-energy large-scale structural mode that dominates approximately 60% of the shear-stress field. The phase information is not well captured, however. The large-scale events in the first mode reconstruction are out of phase with the originally measured field and continue to be through the first two and three mode reconstructions (shown in figures 8.38 and 8.39, respectively). Higher modes are required to retain the appropriate phase information. This suggests an important role for the small-scale structures and a need for higher modes to be included in the turbulent regime. Just within the addition of two other modes, we see the large events being altered and slightly moved into better phase agreement. However, in the sense of flow control, the amplitude information, i.e., the large-scale structure, is what will determine a control decision.

8.4.3 Streamwise Reconstructions

The originally measured surface shear-stress field in the streamwise direction through transition is

195

Figure 8.32: Temporal evolution of the originally measured crossflow surface shear-stress field at $x/c = 0.50$.

Figure 8.33: Temporal evolution of the reconstructed crossflow surface shear-stress field at $x/c = 0.50$ using the first POD mode.

Figure 8.34: Temporal evolution of the reconstructed crossflow surface shear-stress field at $x/c = 0.50$ using the first 2 POD modes.

Figure 8.35: Temporal evolution of the reconstructed crossflow surface shear-stress field at $x/c = 0.50$ using the first 3 POD modes.

presented in figure 8.40. The downstream propagation of specific events in the laminar field are shown to give rise to very large events through transition and generate large coherent structures upon entering the turbulent regime. Examples of this structural evolution is pointed out by the arrows in figure 8.40. Here the small amplitude swells in the laminar regime propagate downstream and are greatly amplified by the instability mechanisms and ultimately create the large structures, one of which exists between 0.02 seconds and 0.03 seconds.

The first POD mode reconstruction is shown in figure 8.41. The evidence of the primary instability is seen here. The growth of the travelling wave is apparent as the flow propagates downstream until transition is initiated when the growth of the disturbances becomes critical. The decay of the effects of the travelling wave is seen in the turbulent regime as indicated earlier by the streamwise spatial POD solution. By incorporating the second mode into the reconstruction (shown in figure 8.42) we see the severe level of influence the secondary instability has on the fluctuating shear stress. The isolation of the two instability mechanisms clearly show growth until the initiation of the transition process where the secondary instability effects seem to completely turn off and resume in the turbulent regime. This is a very unique way of viewing the isolated effects of the instability mechanisms. The growth of the fluctuations is clearly affected by the particular mechanisms and thus provide excellent characteristic information about the instability of the boundary layer. Using these modes to train a control algorithm could alert the system to these unstable trends. Control surfaces or devices could then perhaps alter the flow through some feedback system such that the effect of these mechanisms could be reduced, effectively delaying transition.

Another interesting observation within the first two mode reconstruction is the loss of phase information once the turbulent regime is encountered. This again stresses the important role of the small scales if phase information is considered important to control possibilities. By including the third mode in the reconstruction (shown in figure 8.43), we see better resolved detail of the large coherent structures which emerge from the breakdown process. The phase information is starting to improve with the addition of higher modes in the turbulent regime. Also, a slight reduction in the amplitude of the two instability effects is seen in the laminar portion of the field suggesting that higher modes have some form of a stabilizing effect. The smaller scales that evolve in the transitioning boundary layer and are identified in higher modes act as a "sink" and resist the instability growth by dissipating energy due to viscous effects. This is another advantage of the POD
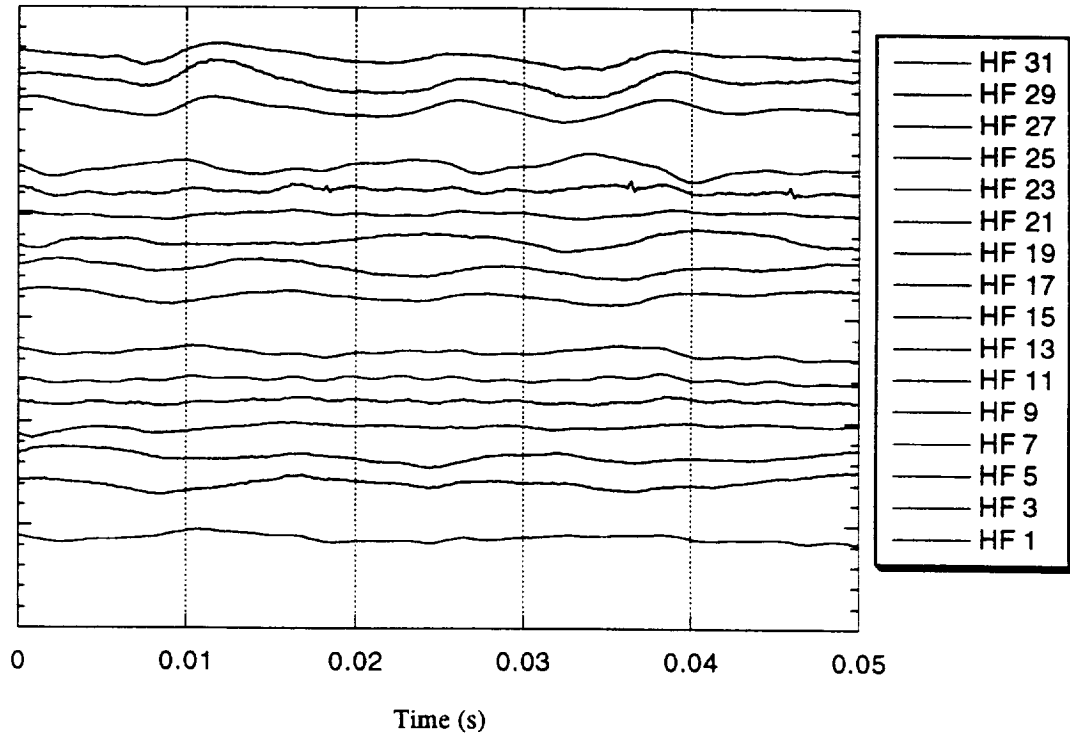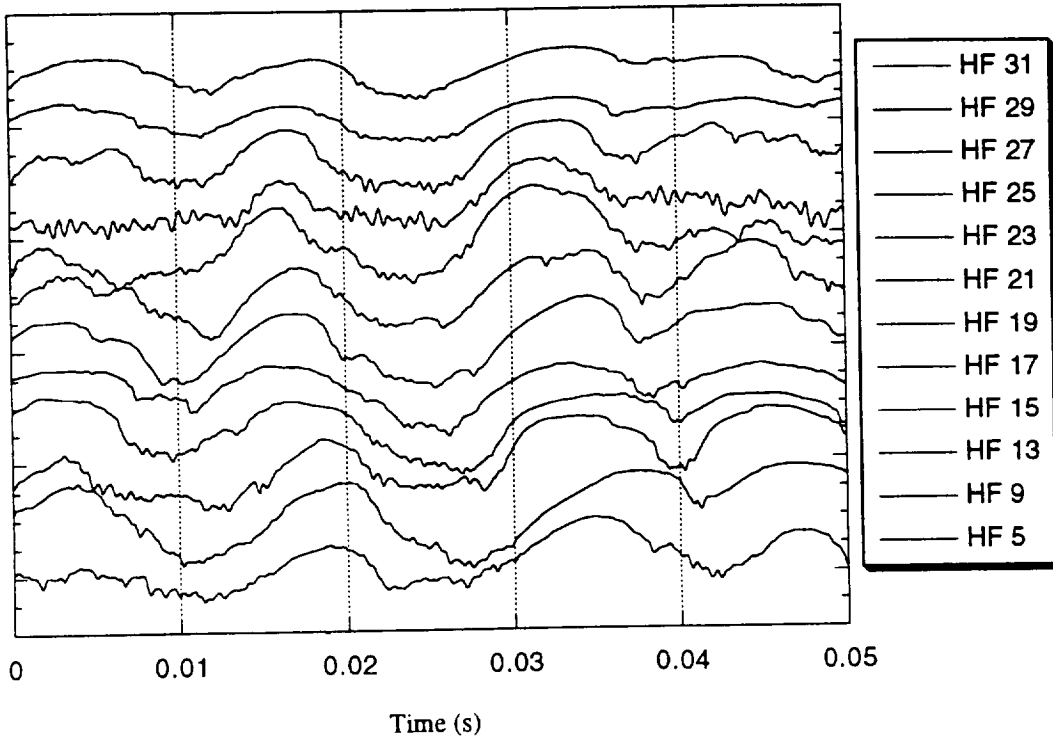
Figure 8.36: Temporal evolution of the originally measured crossflow surface shear-stress field at $x/c = 0.58$.
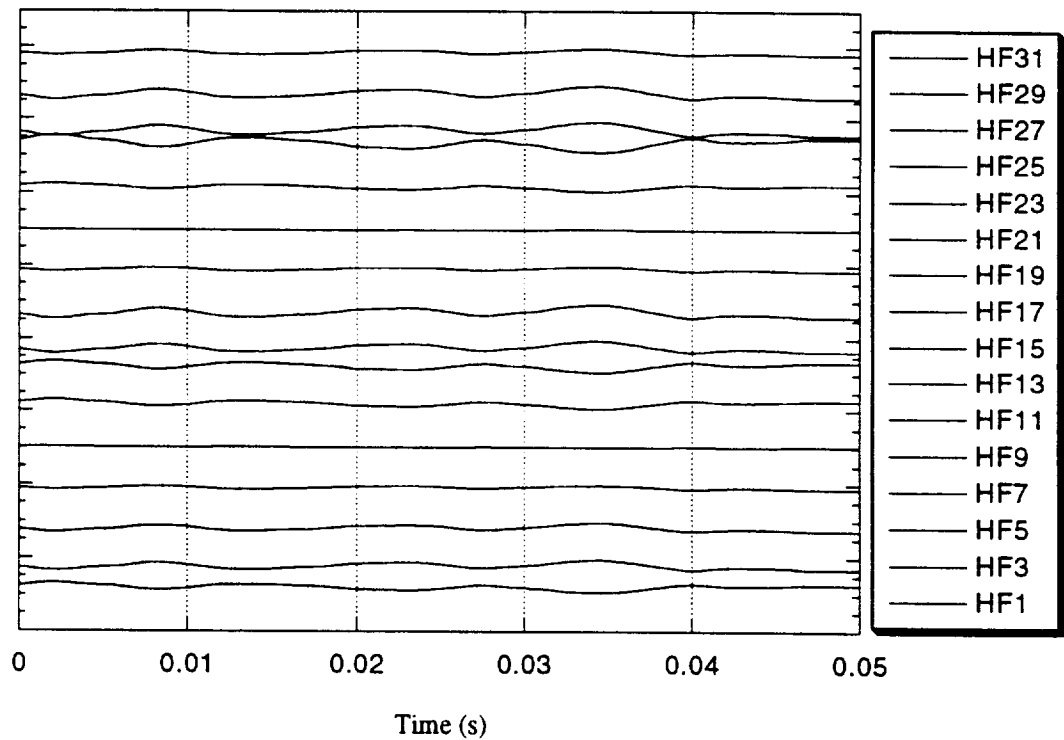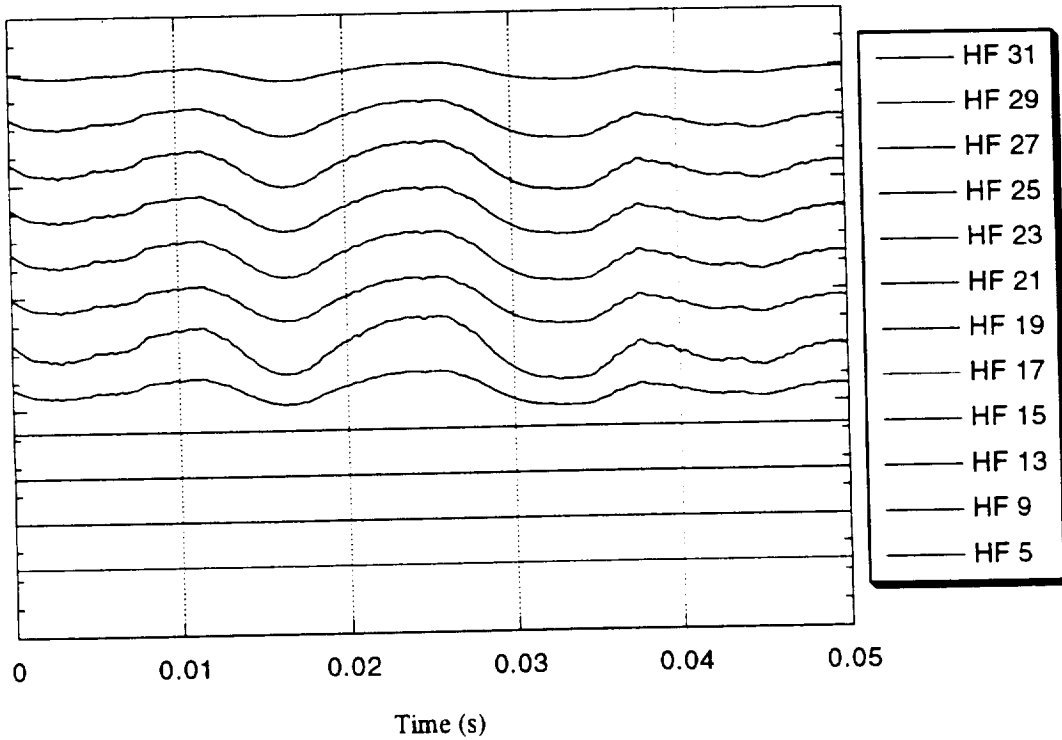

Figure 8.37: Temporal evolution of the reconstructed crossflow surface shear-stress field at $x/c = 0.58$ using the first POD mode.
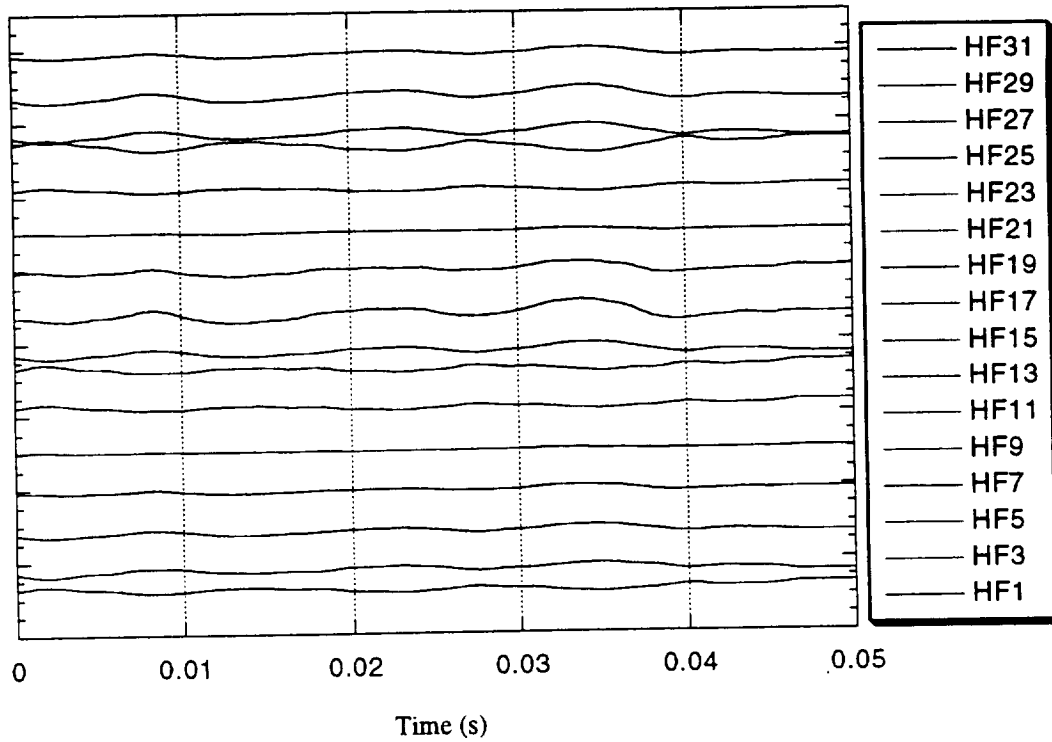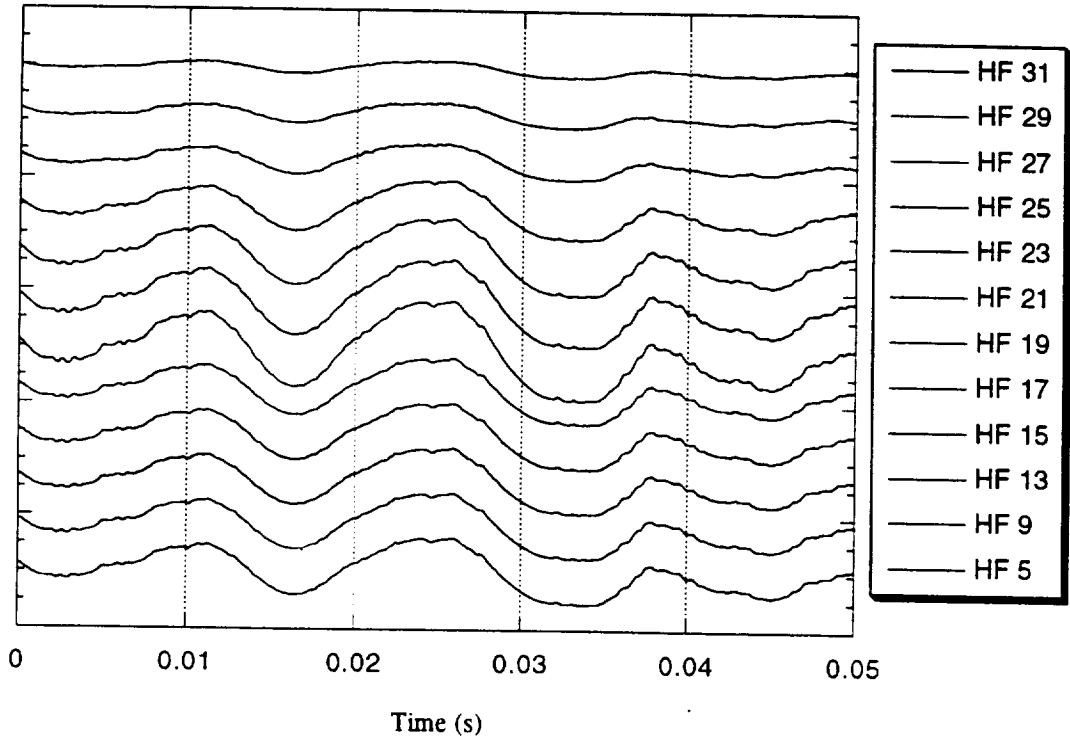
Figure 8.38: Temporal evolution of the reconstructed crossflow surface shear-stress field at $x/c = 0.58$ using the first 2 POD modes.
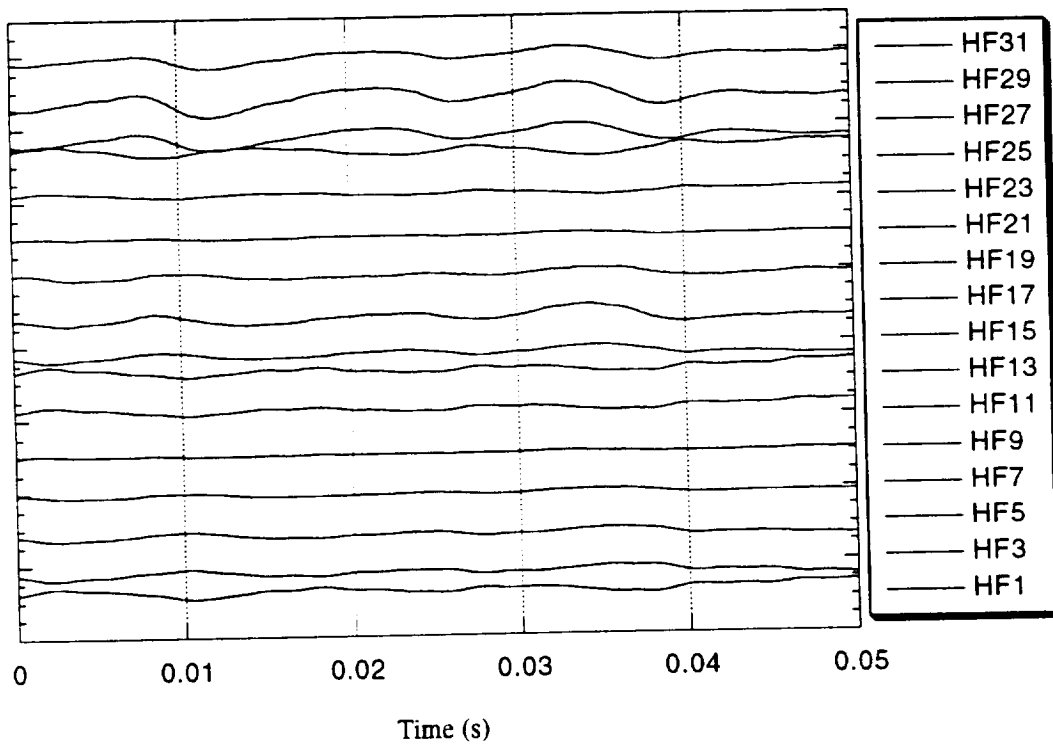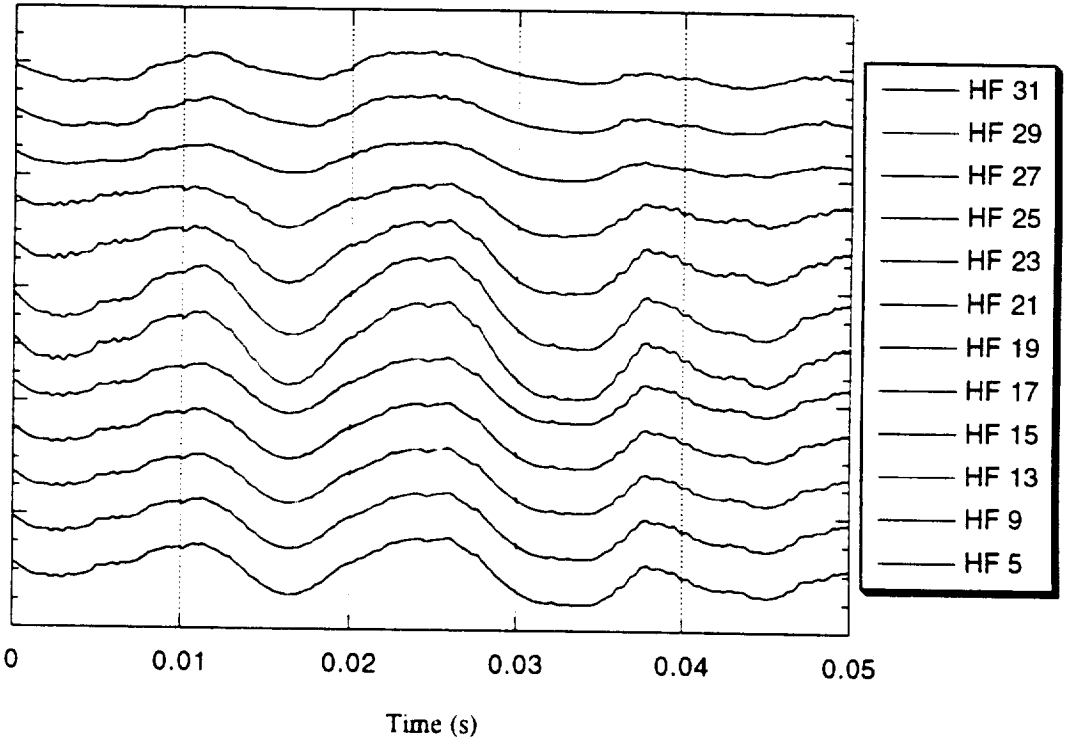

Figure 8.39: Temporal evolution of the reconstructed crossflow surface shear-stress field at $x/c = 0.58$ using the first 3 POD modes.
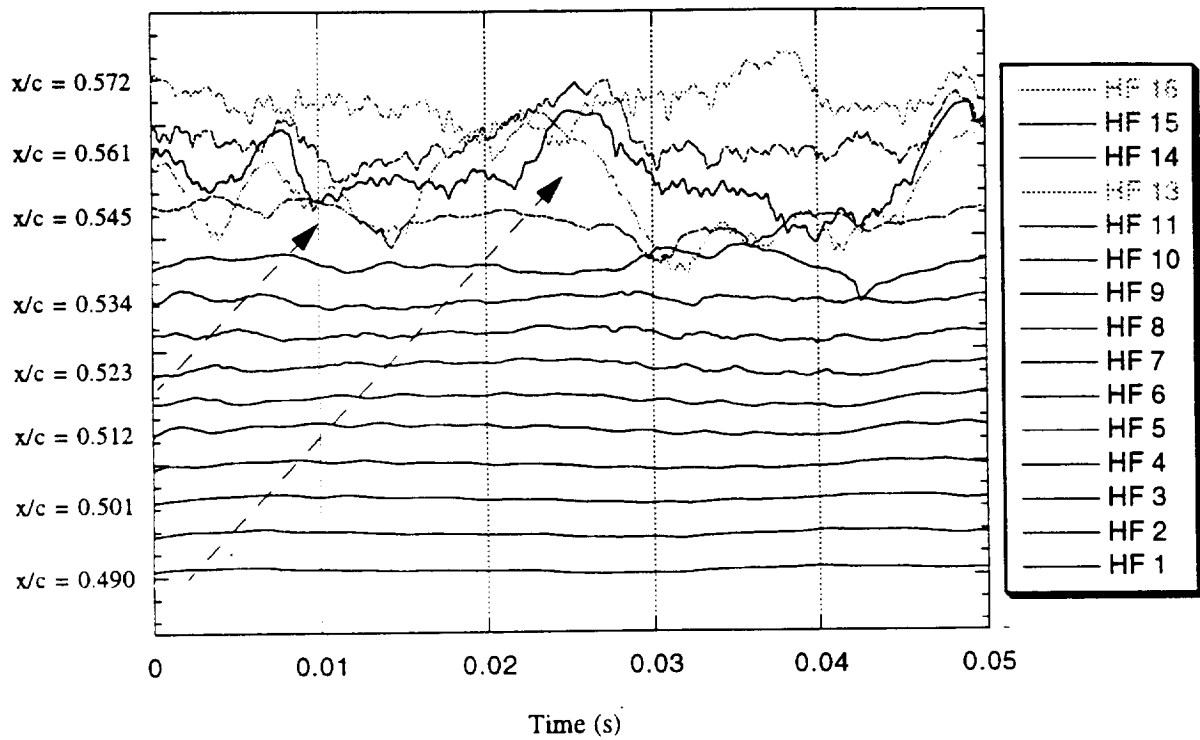
Figure 8.40: Temporal evolution of the originally measured streamwise surface shear-stress field from $x/c = 0.49$ to just after $x/c = 0.57$.
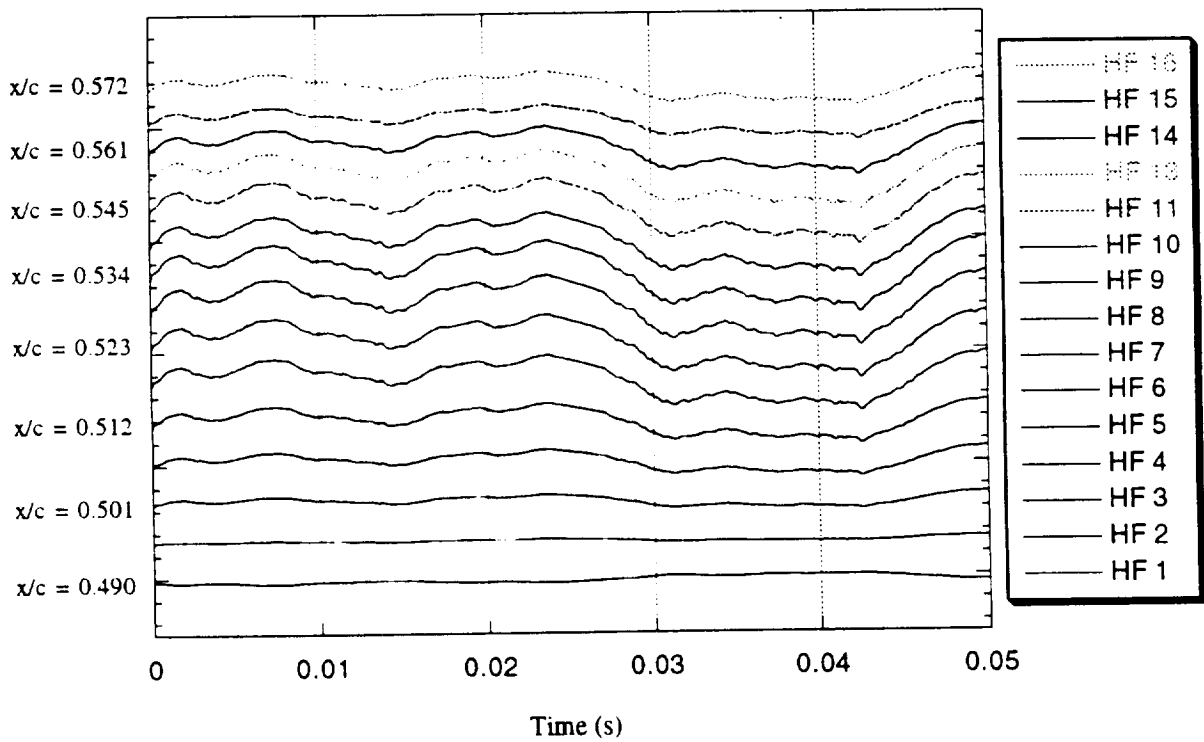
Figure 8.41: Temporal evolution of the reconstructed streamwise surface shear-stress field from $x/c = 0.49$ to just after $x/c = 0.57$ using the first POD mode.
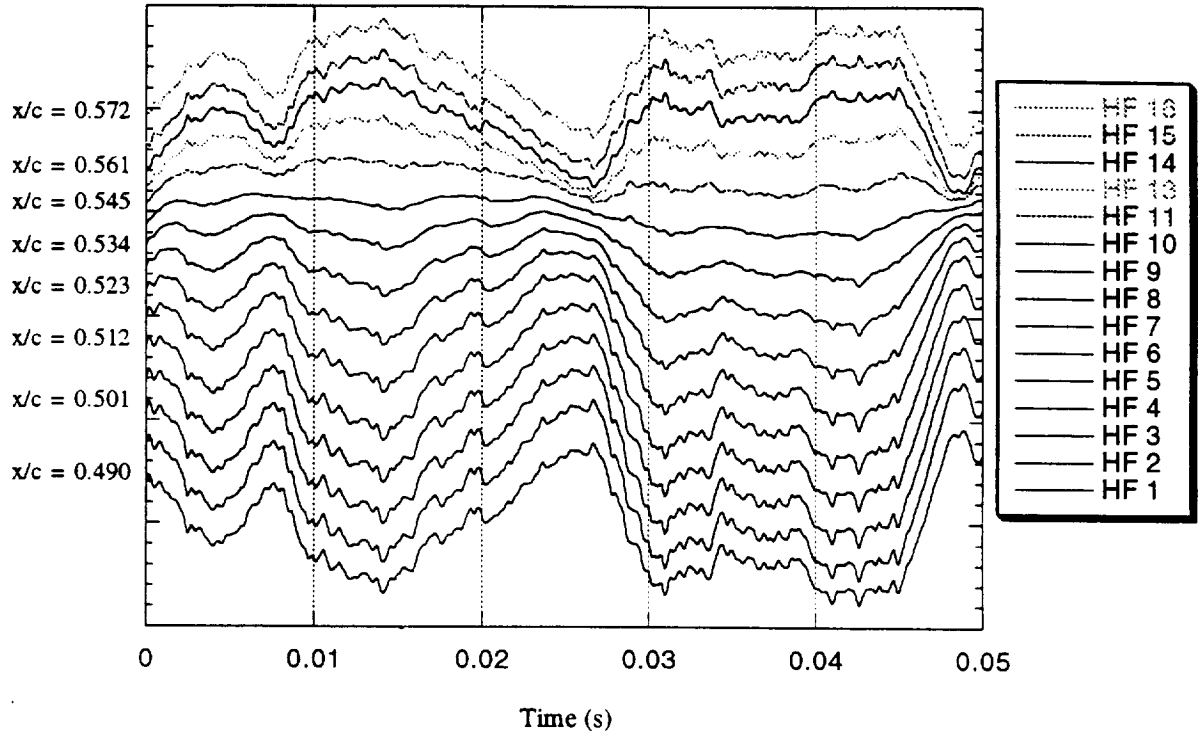
Figure 8.42: Temporal evolution of the reconstructed streamwise surface shear-stress field from $x/c = 0.49$ to just after $x/c = 0.57$ using the first 2 POD modes.
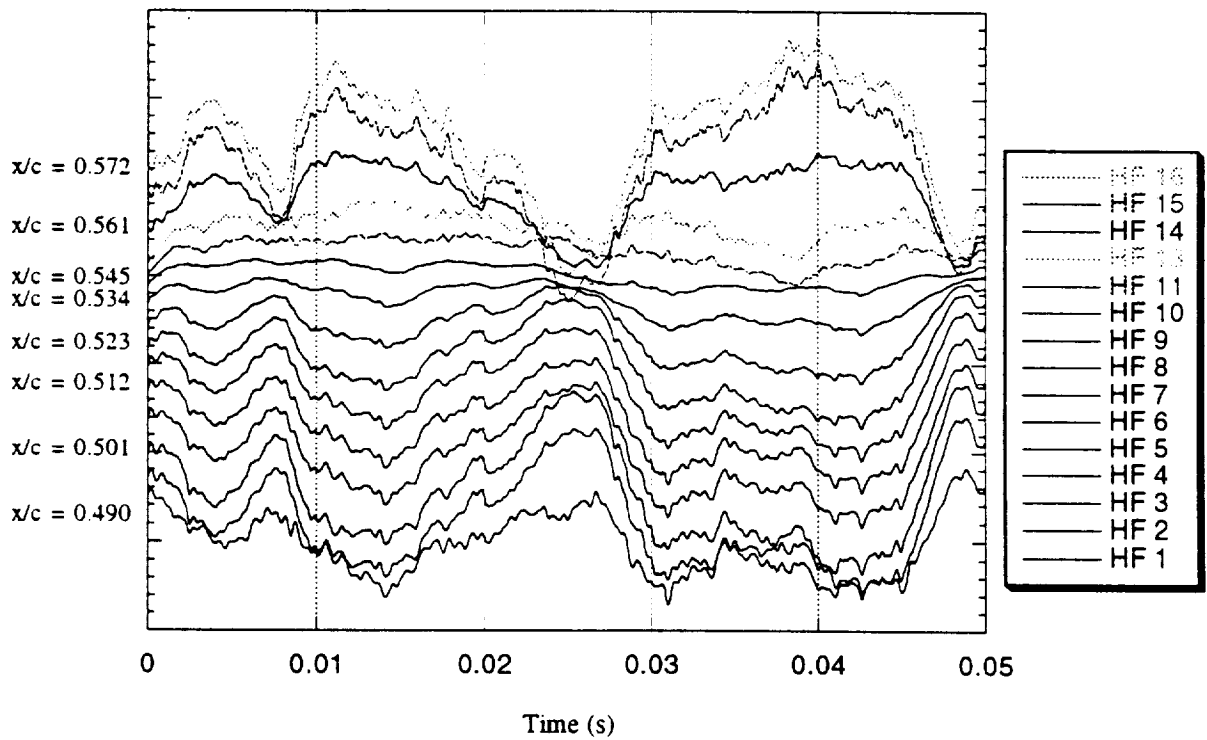
Figure 8.43: Temporal evolution of the reconstructed streamwise surface shear-stress field from $x/c = 0.49$ to just after $x/c = 0.57$ using the first 3 POD modes.
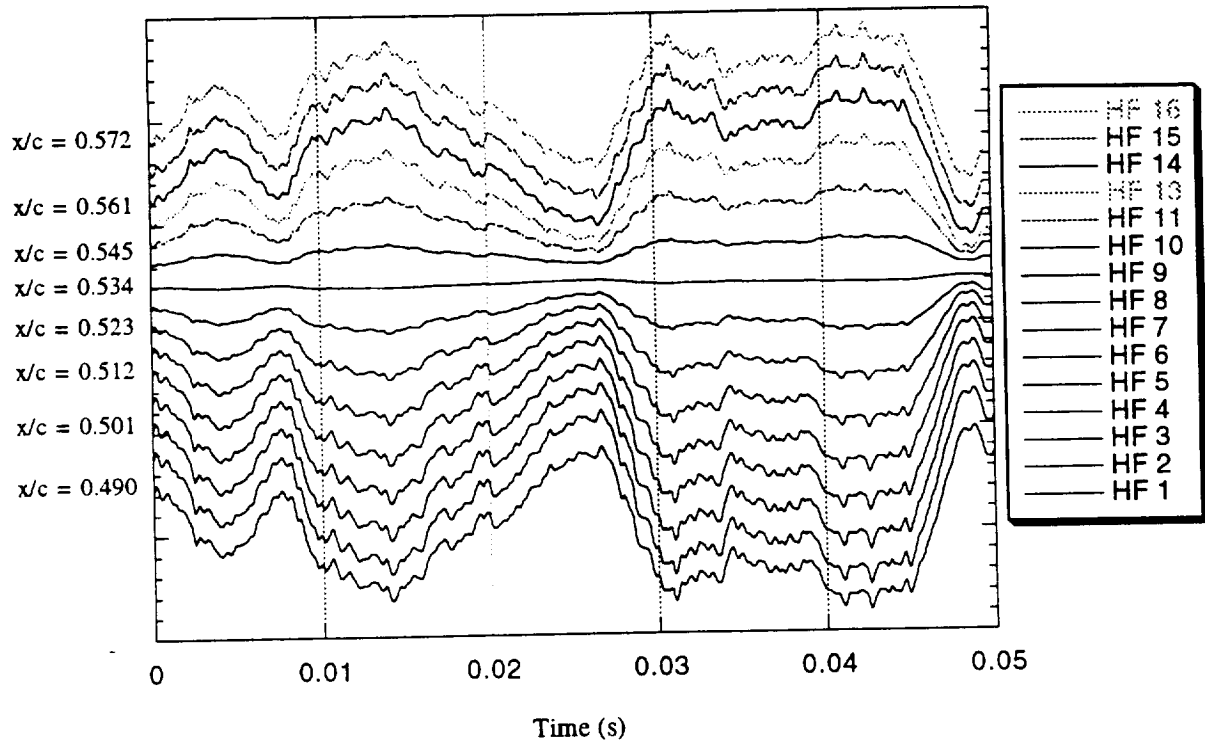
Figure 8.44: Temporal evolution of the reconstructed streamwise surface shear-stress field from $x/c = 0.49$ to just after $x/c = 0.57$ using just the second POD mode.

technique. It separates the high-energy modes from the low-energy modes allowing us to view the mechanisms that create an unstable boundary layer within the low mode numbers. At the same time, we can look to the higher POD modes and recognize how also the boundary layer resisted the instabilities up until breakdown.

Figure 8.44 shows the reconstructed time histories using only the second mode, thus isolating the effects of the secondary instability. The secondary instability demonstrates considerable alteration of the signals yet is second in energy content to the primary instability as witnessed by the POD spatial mode solution. Again, the higher modes resist the growth of the instabilities, especially the secondary instability. The secondary instability has a strong presence in the reconstructions without higher modes and shows very little growth in the originally measured data. So, by isolating these instabilities we may be able to train control algorithms and determine appropriate methods of delaying their growth.

CHAPTER 9

Conclusions and Future Directions

The advantages of using advanced correlation techniques in conjunction with traditional correlation and spectra analyses are summarized in this chapter along with significant results when applied to the swept-wing boundary layer to identify structure. The application of these methods to the data acquired in the current experiment leaves many further details to be explored. These possible future endeavors are also discussed with suggestions and recommendations. Also in this chapter are discussions regarding possible uses of these correlation techniques in flight applications and other laboratory-based experiments.

9.1 Summary

Many detailed measurements are made near the transition region in the crossflow-dominated boundary layer of a swept-wing using hot-film, cross- and hot-wire anemometry techniques. Artificial roughness elements are placed near the leading edge to amplify the dominant spatial wavelength of the stationary vortices known to exist in the laminar boundary layer. A very large database is constructed through extensive correlation measurements. Several hot-film sensor sheets allow simultaneous spatio-temporal measurement of surface shear-stress fields in the spanwise direction. Two independent experiments measure this field separately at two chord locations, one in the laminar regime and the other in the turbulent regime. Cross-wire measurements at a height of 3.0 mm off the surface are used to measure the u and w components of velocity across the span at constant chord locations (above the hot-film measurement grid) in the laminar and tur-

bulent regimes. Flow visualizations, single hot-wire boundary-layer scans and past research efforts are used to map out the flow field in the laminar regime. This provides a reference foundation for the analysis through transition and into the turbulent regime.

Various analysis techniques are used to identify structure within in the swept-wing boundary layer before, through and after transition. These include observation of field time histories, spatial correlation analysis, examination of spatial distributions of auto-spectra, linear stochastic estimation (LSE), proper orthogonal decomposition (POD) and the complimentary technique which incorporates the advantages of both LSE and POD. Time histories provide insight to the local evolution of structures within the various measured flow fields. The spatial correlation analysis provides statistical relationships between all measured spatial locations and determine which locations have significant spatial flow structure. The study of the auto-spectra and its distribution over the measured spatial range provides spectral signature of specific instability mechanisms known to exist within the flow. It also provides detailed information on the spatial evolution of these mechanisms. Levels of kinetic energy contained within the flow field are also determined. The origin of large- and small-scale turbulence is also identified by comparing the streamwise evolving surface shear-stress spectra.

The advanced correlation techniques provide a closer look at the various mechanisms causing transition and the structures that evolve through the complete transition process. LSE uses the measured velocities at two spatial positions to estimate the rest of the field producing an entire velocity field that is now instantaneous. POD is used to determine the spatial evolution of various modes within the measured flow field based on energy levels. Important dominant structures present in the flow are isolated and identified in the laminar and turbulent regimes. The growth of the two instability mechanisms that cause transition in the crossflow-dominated boundary layer are isolated. An objective transition detection method is devised using these results. POD is also used in conjunction with the LSE results in a complimentary technique analysis that provides the temporal evolution of the dominant modes in each velocity field. Similar calculations are made for the simultaneously sampled fields of surface shear stress where an estimate is not needed. These POD coefficients are determined with the goal of training flow control algorithms with one or two scalar signals that are characteristic of the entire measured field. LSE is also used to estimate corrupted signals within a disturbed shear-stress field containing cross-wire probes. Finally, the dominant shear-stress temporal modes are used with the spatial modes of the entire field to reconstruct

the shear-stress fields. This reveals the structure contained within the dominant modes as the reconstructed fields are compared to the actually measured flow fields.

9.2 Significant Results

Below is a list of significant results and corresponding sections within the text which summarizes the accomplishments of this research effort.

Experiment

- An extensive 45° swept-wing experiment (chapter 5) at $Re_c = 2.4 \times 10^6$ is performed with the use of artificial roughness elements (sections 3.3.3 and 5.3.3) mounted near the leading edge to isolate the most amplified wavelength of the stationary vortices known to exist within the boundary layer.

- Extensive correlation measurements (section 5.5) are made with two cross-wire probes at two chord locations, one in the laminar regime, the other in the turbulent regime.

- Surface flow visualizations (section 5.2) are performed to determine locations of the stationary vortices and the transition front (figure 5.1) for appropriate sensor placement. Flow visualizations are also used to determine if the flow is disturbed by the presence of the surface-mounted hot-film sheets in the measurement regions. This flow visualization showed no change in the transition front in the measurement regions (figure 5.2).

- Streamwise mean velocity contours (section 5.3) acquired with a single hot-wire probe by Reibert et al. (1996) are used as "flow maps" (section 5.3.2) to assist in sensor placement and in the analysis (chapters 7 and 8), especially in the laminar regime. These scans are also used to explain the streamwise evolution of the stationary vortices (section 5.3.4).

Instrumentation

- Three hot-film sensor sheets (section 4.1.3) have been designed and used to measure the surface shear-stress fields in the spanwise direction, in the streamwise direction across a broad range and locally in a very small area for both components of surface shear stress (section 5.4).

- A calibration technique has been developed for the hot-film sensors (section 4.3). This technique uses the advantages of flat-plate receptivity experiments (section 4.3.1) to drive Toll-mein-Schlichting waves at individual frequencies with acoustic forcing (section 4.3.2). The frequency response of a typical hot-film sensor is acquired for a range up to 3.0 kHz. As a first attempt, this method needs improvement but did provide an adequate approximation at surface shear-stress quantities (section 4.3.3). Recommendations for improvements are made (section 4.3.4).

Spatial Correlation Analysis

- Evidence of the 12-mm forced vortex wavelength appears in the laminar spatial correlation tensors of both components of velocity (sections 6.1 and 7.1.1) but more readily in the cross-flow surface shear-stress spatial correlations (sections 6.1 and 7.1.2) due to the doubled measurement grid resolution.

- Velocity spatial correlations in the turbulent regime are near identical for each component combination (section 7.1.1) implying a fully turbulent boundary layer. Only the tensor trace positions, i.e., the auto-correlations, show strong correlation.

- Surface shear-stress spatial correlations in the turbulent regime (section 7.1.2) show evidence of large structures originating from the stationary vortices in the laminar regime. These large turbulent structures happen to be double the spatial wavelength of a single stationary vortex in the laminar regime. It is hypothesized that two neighboring vortices interact in a highly nonlinear fashion through the breakdown process and create these large scales in the turbulent regime.

- The growth of the secondary instability in the streamwise direction is identified in the surface shear-stress spatial correlation tensor through transition (section 7.1.3). Two local maxima in the spatial correlations denote the start and end of the transition region. These are the effects of the primary and secondary instabilities.

Auto-Spectral Analysis

- The spatial distributions of the auto-spectra from both velocity components (sections 6.1 and 7.2.1) and from the crossflow surface shear stress (sections 6.1 and 7.2.2) provide excellent identification of the stationary vortices in the laminar regime. Identification of the structures is drastically improved over the spatial correlation analysis for the velocity measurements. Their

correlations appear more dependent on the location of the measurement site relative to the location of the crossflow vortices. Their spectra displays the measured kinetic energy captured in each measurement and allows better spatial structure identification. The finer resolution of the hot-film measurement grid provides better spatial identification of structure whereas the better response of the cross-wire sensors allow for better identification of the spectral events.

- Turbulent spatial distributions of the velocity (section 7.2.1) and crossflow surface shear-stress (section 7.2.2) auto-spectra reveal the remnants of the stationary structures which survive the transition process. Again, a wavelength double the 12-mm forced wavelength is observed for these large coherent structures suggesting the interaction of two neighboring vortices through breakdown.

- Individual auto-spectra plots for the velocity (section 7.2.1) and the shear stress (section 7.2.2) in the laminar regime reveal the spectral signatures of the primary and secondary instabilities at 300 Hz and 3.0 kHz, respectively, which is consistent with the findings of Kohama et al. (1991). These events are strongest near regions of high velocities within the vortices, particularly at locations where the fluid is being forced towards the surface. At locations between the vortices, the secondary instability signature in the velocity spectra shifts to higher frequencies (higher than 5.0 kHz) and is perhaps due to the up-swelling motion. This is not captured by the hot-film sensors due to their limited frequency response.

- The turbulent auto-spectra for the velocity data (section 7.2.1) show that the secondary instability, present in both components in the laminar regime, is only present in the w component after transition. The primary instability effects, also present in both components in the laminar regime, are only present in the u component after transition. This suggests that the secondary instability creates small-scale turbulence strongest in the w component of velocity after transition and the primary instability, i.e., the crossflow instability, creates the large-scale structure in the turbulent regime which is observed predominantly in the u component. The secondary-mechanism creation of smaller scales is further supported by the crossflow surface shear-stress auto-spectra results (section 7.2.2). No primary instability effects are witnessed in the turbulent shear-stress spectra again consistent with the velocity spectra results.

- The streamwise auto-spectra results (section 7.2.3) reveal the evolution of the two, instability mechanisms as the flow propagates downstream. In the laminar regime, the primary insta-

bility grows and causes transition. Through the transition front, energy is transferred from this mechanism into the generation of the large-scale structures found in the turbulent regime. The secondary instability is seen to grow through the transition front and eventually produce the small-scale turbulence seen at higher frequencies.

Linear Stochastic Estimation

• Linear stochastic estimation (sections 6.2 and 8.1) is used to estimate the instantaneous velocity field at all spatial locations measured in the correlation experiments from just two measurements sites and the appropriate two-component spatial correlation tensor.

• An objective method of selecting the two reference locations for the estimate (section 8.1.2) is determined such that the best estimate possible is obtained in the mean-square sense. This technique selects the reference locations as those with the largest root-mean-square (RMS) values (summed over all components) in order to provide enough energy for estimates characteristic of originally measured data at locations relatively far from the reference locations. This method drastically improves the estimation of the velocity fields and recovers some flow physics not seen in estimated fields using randomly selected reference signals.

• A method involving RMS matching is developed to estimate a flow field disturbed by the presence of cross-wire probes in the flow, thus ridding the field of corrupted signals (section 8.3.2). The RMS profiles of the disturbed field are compared to that of the same undisturbed field, i.e., measurements acquired with no cross-wire probes in the flow. The RMS profiles are matched as best as possible through a trial-and-error approach thus minimizing the effect of the cross-wire flow disturbance.

Proper Orthogonal Decomposition

• Proper orthogonal decomposition (section 6.3) is used to separate the measured flow field into various modes at similar energy levels in the mean-square sense thus isolating specific structures within the flow field. This is accomplished through the solution of an integral eigenvalue problem. Spatial solutions (sections 6.3.3 and 8.2) are realized and used to identify spatial structures within the laminar and turbulent regimes. Eigenvalues (section 8.2.1) represent the relative kinetic energy distribution across POD modes. Temporal evolutions of the dominant modes (section 8.3) are determined through solution of the POD coefficients for the surface shear stresses. A

complimentary technique (sections 6.4) which uses LSE is used to determine similar temporal results for the estimated instantaneous velocity fields. Surface shear-stress fields are reconstructed using only the few dominant modes (section 8.4) to identify structure captured within those dominant modes.

• The eigenvalues (section 8.2.1) of the velocity solutions show 53% of the total measured kinetic energy is contained in the first mode for the laminar regime and 23% in the turbulent regime. Higher modes are required to appropriately characterize the turbulent flow field whereas the laminar regime is well characterized by the first two modes. The crossflow shear-stress eigenvalues demonstrate 63% of the measured kinetic energy within the first mode in the laminar regime and 62% in the turbulent regime. Both fields are well characterized by the first three modes. The streamwise shear-stress eigenvalues show that the first mode contains 53% of the energy through transition and 38% in the second mode. Thus, this flow field is well characterized by the first two modes.

Spatial POD Solutions

• The spatial POD solutions for the laminar velocity measurements (section 8.2.2) reveal the presence of one stationary vortex in the first mode. Others exist but are not captured due to the sparse resolution of the measurement grid. Both components contain similar modal structure. The turbulent solutions reveal the presence of a similar large spatial structure as seen in the laminar regime in the first mode. This structure is a remnant of the stationary vortices after breakdown, is shifted in span and has a broader bandwidth. This is most likely due to the interaction of neighboring vortices through the transition process as evidenced by the auto-spectra and spatial correlation analyses.

• The spatial POD solutions for the crossflow surface shear stress in the laminar regime (section 8.2.3) capture the presence of all three stationary vortices in the first mode. The large positive peaks in these structures correspond to regions beneath the doubly inflected velocity profile just before where the fluid is drawn away from the surface into the vortex structure. The turbulent solution again reveals the remnants of the vortical structure surviving transition in the first few modes. The double-wavelength of the stationary vortices is again seen in the first turbulent POD mode.

• The spatial POD solutions for the streamwise surface shear stress through transition (sec-

tion 8.2.4) displays remarkable separation of the two instability mechanisms that cause transition. The first POD mode is found to capture the growth of the primary instability up until the transition region initiates. The effects of this crossflow mechanism then decays through transition and into the turbulent region. Thus the peak of the first mode is used to detect the starting streamwise location of the transition front. The second mode has been determined to contain the secondary instability growth through the laminar and transition region. The mode then peaks at the onset of turbulence and decays thereafter giving way to small-scale turbulence. Thus the entire transition region may be *objectively* detected based on the growth and decay of the instability modes. These interpretations are fully supported by flow visualizations and the auto-spectra analysis.

- Further evidence of the travelling wave and the secondary instability are captured in the higher modes of the spatial streamwise POD solution. It is hypothesized that distinct phase differences in the higher modes represent relative fluid motion highly characterized by measured quantities near an "inner" shear layer resulting from the breakdown of the doubly-inflected profile.

Temporal POD Solutions

- Temporal modes (section 8.3) of the velocity fields are calculated using the complimentary technique (sections 6.4 and 8.3.1). The estimated instantaneous field is used to determine the POD coefficients for the first two modes. Higher modes are not to be trusted since they converge onto the estimated field not the actual measurements.

- The laminar and turbulent velocity solutions (section 8.3.1) result in scalar signals very characteristic of their respective two-component velocity fields. These signals may then be used to train flow control algorithms. Advantages to using temporal modes include greatly reduced amounts of data required to describe the entire flow field and isolation of instability mechanisms upon which control strategies may focus.

- POD coefficients simultaneous with the velocity coefficients are calculated for the crossflow surface shear stress in both regimes (section 8.3.2). Very few relationships are visible between the internal and surface measurements. This is in part due to the calibration procedure and the significant distance between the two sets of measurements.

- Temporal POD modes are also computed for the undisturbed surface shear stress fields in the crossflow direction for both regimes (section 8.3.2). The first and third modes of the laminar solution contain a high degree of periodicity indicative of the travelling wave. The turbulent solu-

tion still displays high degrees of periodicity providing further evidence that the large temporal structures in the turbulent regime originate from the travelling wave present in the laminar regime.

- The two instability mechanisms are isolated in the first two temporal modes of the streamwise surface shear-stress solution (section 8.3.3). These coefficients may be used to train control algorithms to identify the growth signatures of these instabilities with the hopes of identifying transition and altering the flow in such a way that transition is delayed.

Shear-Stress POD Reconstructions

- Temporal evolutions of the surface shear stresses are reconstructed using only the first, first two and first three modes (section 8.4) to identify the spatio-temporal evolution of the dominant structures in the flow.

- Laminar reconstructions of the crossflow shear-stress (section 8.4.1) reveal that the periodicity in space and time is captured near the high-velocity regions of stationary vortex using just the first POD mode. Other spatial locations start showing periodicity when higher modes are included in the reconstructions.

- Turbulent reconstructions (section 8.4.2) show that the first mode contains the dominant large-scale structures but is failing to capture the phase information. Including higher modes improve the phase recovery and add detail to the dominant structures.

- Streamwise reconstructions (section 8.4.3) demonstrate the spatio-temporal evolution of the primary instability mechanism when using just the first POD mode. Adding the second mode shows the combined effect of the isolated instabilities. Including higher modes stabilizes their growth in the laminar regime and demonstrates the important role of the smaller scales in the flow.

9.3 Future Directions

9.3.1 Immediate Issues

There are many avenues, sometimes even seemingly endless, to explore within this type of research. Still, there are immediate issues that should be considered in regards to the current experiment and the resulting database. Many sets of data have yet to be analyzed. Below is a list of immediate issues that could be addressed in the near future.

- Perform a full spectral POD analysis on the streamwise surface shear-stress data. Only the spatial POD was solved here using the spatial correlation tensor. The POD analysis may include the full frequency spectra such that the correlation tensor used as the kernel in the POD is a function of spatial separation *and* frequency. This results in the eigenvalues being a function of frequency as well. Thus, these eigenspectra should reveal isolated spectral signatures of the primary instability in the first eigenspectrum and of the secondary instability in the second eigenspectrum. This is complete validation that the transition region may be detected in its entirety through the use of POD and simultaneous streamwise surface shear-stress measurements.

- Improve the hot-film calibration technique. More ensembles are needed to determine statistically accurate frequency responses. A follow-up experiment is already scheduled to advance the accuracy of this technique. The first attempt, presented here, is a good starting place but has significant short-comings. Thus, this is a rich area for expanding the calibration concept. There are also plans to possibly perform a similar calibration on the actual wing model. By taking advantage of the amplified streamwise instability at slightly positive angles of attack, we can again use the receptivity mechanism of the boundary layer to calibrate each hot-film sensor without removing it from the surface or using other similar sensors.

- Perform a full analysis on the local two-component surface shear-stress measurements. This data set, acquired by the "T-array" hot-film sensors, was not analyzed here due to time constraints. However, the advanced analysis techniques described in chapter 6 should reveal very interesting dynamics between the two components and may shed light on how the instability mechanisms locally interact. Comparisons may also be made across the transition region.

- Perform a full analysis on the experiments acquired with 36-mm forcing by artificial roughness elements placed near the leading edge. This adds complexity to the flow field by adding harmonics of the most amplified wavelength. Now that the 12-mm forcing problem is better understood, results from the 36-mm forcing experiments may be properly interpreted.

- Improve the linear stochastic estimate of the velocity fields by implementing a type of RMS scaling. By using the objective reference selection technique (i.e., using the maximum RMS values as reference), we capture the appropriate trends. This additional step would investigate the effects of multiplying the estimated signals by a ratio of the actual RMS value to the estimated RMS value. This could possibly eliminate the amplitude recovery problem.

- Perform additional hot-film and/or cross-wire measurements in the turbulent regime

across a larger span range to verify the hypothesis that the large-scale turbulent structures origi-
nate from the interaction of two neighboring stationary vortices in the laminar regime. The
hypothesis that these turbulent large-scale structures are somewhat periodic in span at approxi-
mately double the stationary vortex wavelength could also be verified.

- Examine the spectra of the POD coefficients. This would essentially provide a modal
decomposition of the auto-spectra presented in chapter 7. Spectral signatures of specific mecha-
nisms, particularly in the streamwise surface shear-stress solutions, could be identified and possi-
bly affect the future of flow control approaches.

- Examine the spectra of the reconstructed surface shear-stress fields. This is merely an
extension of the previous suggestion.

- Improve the relationship between the simultaneously sampled cross-wire and hot-film
data. This is important for future flight applications where internal measurements cannot be
readily made. To obtain the instantaneous POD coefficients for both measured quantities, one
could apply a digital filter to the velocity data that simulates the filtering effect observed in the
hot-film data. Perhaps a second experiment could be performed with single hot-wire probes in
place of the cross wires to allow closer measurements to the wall. A major concern is the limita-
tion of the hot films not being able to capture the high frequency information. If a relationship
between the surface and internal measurements can be established then flow control algorithms
could be better trained. Knowledge of the internal flow from surface measurements provides a
non-intrusive way of determining flow control strategies.

9.3.2 Future Issues

The ultimate goal of this line of research is to bring these advanced correlation techniques to flight
with the hopes of dynamically training neural networks which effectively apply some form of
flow control. The difficulty is often bringing a technique from the laboratory to actual flight appli-
cations. To aid this vision, figure 9.1 shows a flow chart of typical applications for these correla-
tion techniques in the current state. Here the flow control module has not been developed, but is at
the heart of the immediate goal. Figure 9.2 shows a flow chart of how these techniques might be
applied to a feedback flow control system in the laboratory. This could eventually turn into a
dynamic flow control experiment and then be brought to flight. Figure 9.3 shows how these tech-
niques might be applied to actual flight situations while incorporating computer simulations of the
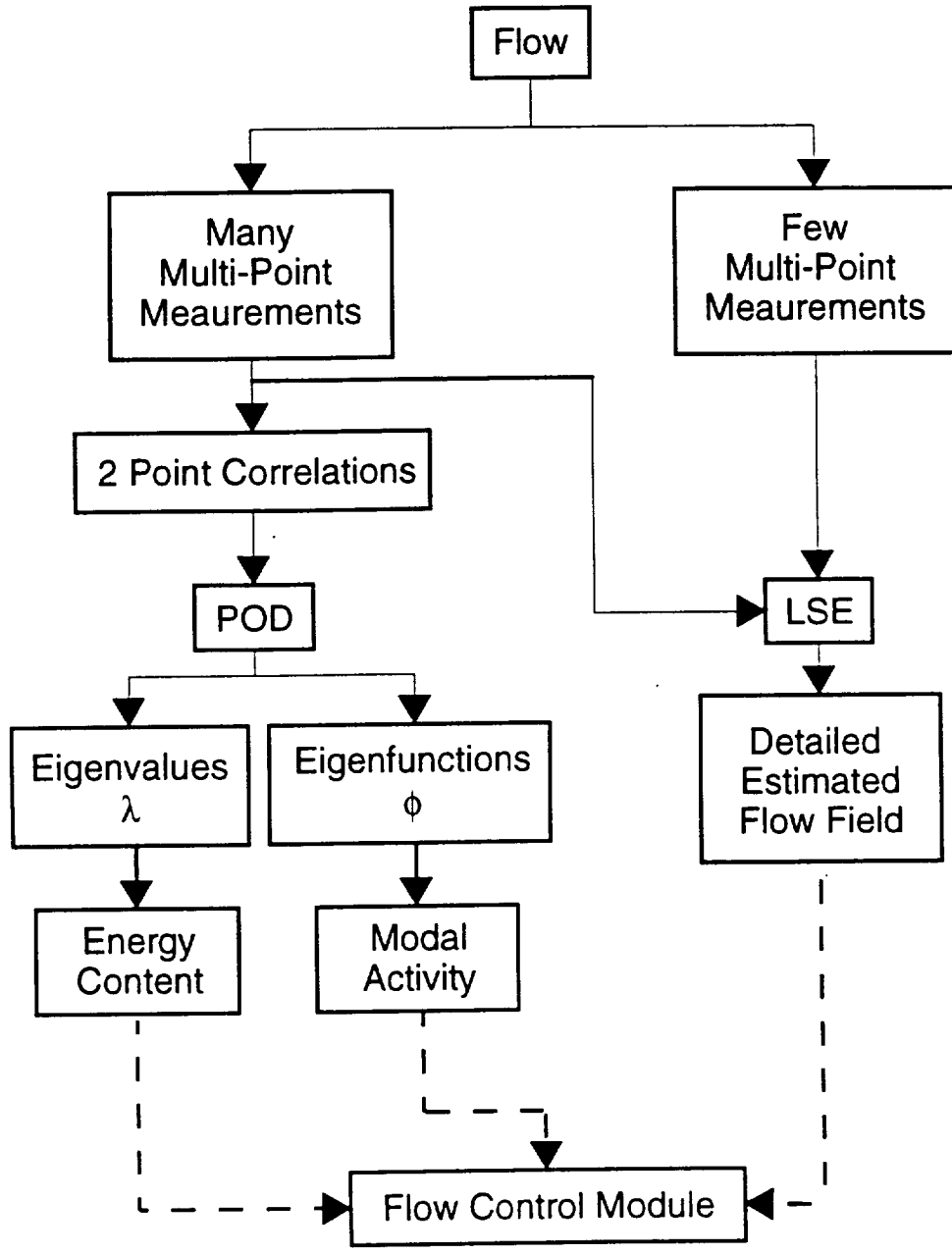
Figure 9.1: Typical uses of multi-point correlation techniques in current state of research.

swept-wing boundary layer. By keeping the long-term goals in focus and advancing the use of these techniques in the laboratory, these types of research efforts could greatly affect the future of flight by incorporating environment-induced decisions on how to reduce drag or control the boundary layer in some other desired fashion.
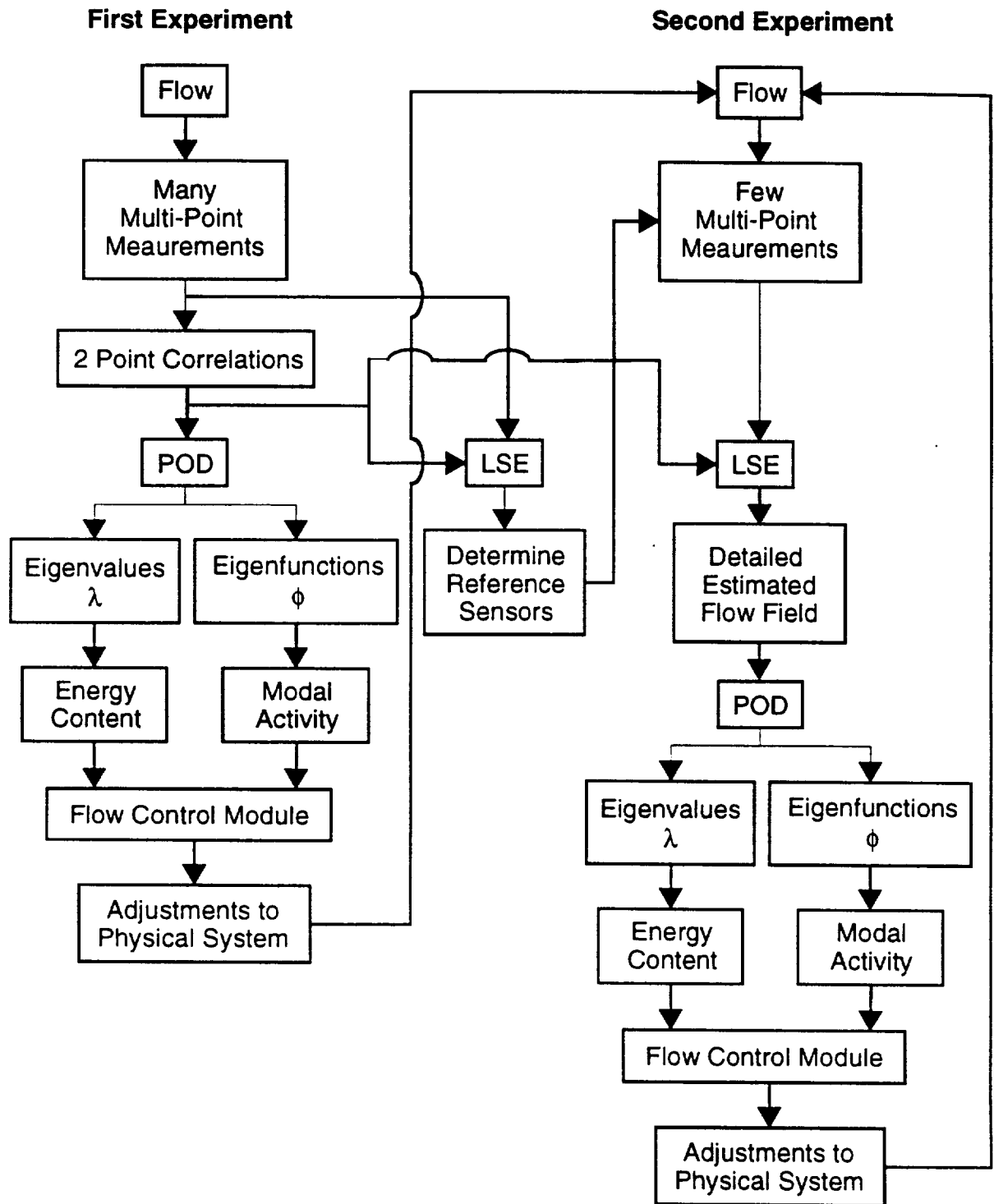
Figure 9.2: Possible uses of correlation techniques for a flow control experiment in the laboratory.
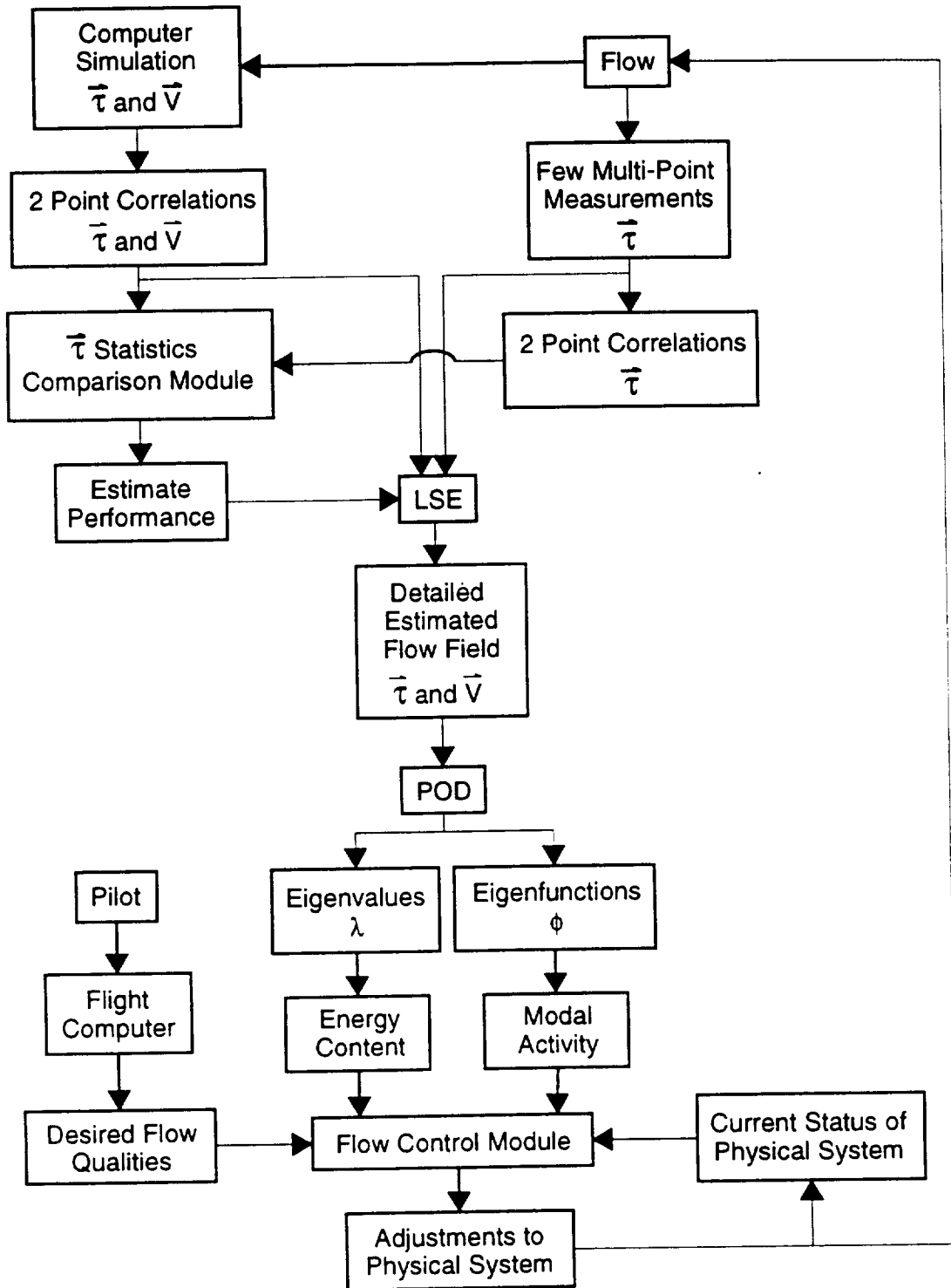
Figure 9.3: Possible uses of correlation techniques in actual flight scenarios.

Bibliography

Adrian, R. J. (1975) On the role of conditional averages in turbulence theory. In *Proc. 4th Biennial Symp. on Turbulence in Liquids*.

Adrian, R. J. (1979) Conditional eddies in isotropic turbulence. *Phys. Fluids*, vol. 22, no. 11, p. 2065.

Adrian, R. J., M. K. Chung, Y. Hassan, B. G. Jones, C. K. Nithianandan and A. T.-C. Tung (1987) Experimental study of stochastic estimation of turbulent conditional averages. In *Proc. 6th Symp. Turbulent Shear Flows*. Toulouse, France.

Adrian, R. J. and P. Moin (1988) Stochastic estimation of organized turbulent structure. *J. Fluid Mech.*, vol. 190, p. 531.

Agarwal, N. K., D. V. Maddalon, S. V. Mangalam and F. S. Collier Jr. (1991) Cross-flow vortex structure and transition measurements using multi-element hot films. AIAA Paper 91-0166.

Arnal, D. (1984) Description and prediction of transition in two-dimensional incompressible flow. In *Special Course on Stability and Transition of Laminar Flows*. AGARD Rep. 709.

Arnal, D. (1986) Three-dimensional boundary layers: Laminar-turbulent transition. In *Special Course on Calculation of Three-Dimensional Boundary Layers with Separation*. AGARD Rep. 741.

Arnal, D. (1992) Boundary-layer transition: Prediction, application to drag reduction. In *Special Course on Skin Friction Drag Reduction*. AGARD Rep. 786.

Arnal, D., G. Casalis and J. C. Juillen (1990) Experimental and theoretical analysis of natural transition on infinite swept wing. In *Laminar-Turbulent Transition* (eds. D. Arnal and R. Michel), vol. 3, pp. 311-325. Berlin: Springer-Verlag.

Aubry, N., M.-P. Chauve and R. Guyonnet (1994) Transition to turbulence on a rotating flat disk. *Phys. Fluids*, vol. 6, no. 8, pp. 2800-2814.

Baker, C. T. H. (1977) *The Numerical Treatment of Integral Equations*. New York: Oxford.

Bakewell, P. and J. L. Lumley (1967) Viscous sublayer and adjacent wall region in turbulent pipe flow. *Phys. Fluids*, vol. 10, no. 3, pp.1880-1889.

Bearman, P. W. (1971) Corrections for the effect of ambient temperature drift on hot-wire measurements in incompressible flow. DISA Information #11, pp. 25-30.

Bellhouse, B. J. and D. L. Schultz (1966) Determination of mean and dynamic skin friction, separation and transition in low speed flow with a thin-film heated element. *J. Fluid Mech.*, vol. 24, no. 2, pp. 379-400.

Benmalek, A. and W. S. Saric (1994) Effects of curvature variations on the nonlinear evolution of Goertler vortices. *Phys. Fluids*, vol. 3, no. 10, pp. 3353-3367.

Berkooz, G. (1991) *Turbulence, Coherent Structures and Low Dimensional Models*. Ph.D. Thesis, Cornell University.

Berkooz, G., P. Holmes and J. L. Lumley (1993) The proper orthogonal decomposition in the analysis of turbulent flows. *Ann. Rev. of Fluid Mech.*, vol. 25, pp. 539-575.

Beuther, P. D., A. Shabbir and W. K. George (1987) X-wire response in turbulent flows of high intensity turbulence and low mean velocities. *ASME Symposium on Thermal Anemometry*, vol. 53, pp. 39-42.

Bippes, H., B. Müller and M. Wagner (1991) Measurements and stability calculations of the disturbance growth in an unstable three-dimensional boundary layer. *Phys. Fluids*, vol. 3, no. 10, pp.2371-2377.

Bonnet, J. P., D. R. Cole, J. Delville, M. N. Glauser and L. S. Ukeiley (1994) Stochastic estimation and proper orthogonal decomposition: Complimentary techniques for identifying structure. *Exp. in Fluids*, vol. 17, pp. 307-314.

Brown, W. B. (1959) Numerical calculation of the stability of crossflow profiles in laminar boundary layers on a rotating disk and on a swept wing and an exact calculation of the stability of the Blasius velocity profile. Northrop Rep. NAI-59-5 (BLC-117).

Champagne, F. H., C. A. Sleicher and O. H. Wehrmann (1967a) Turbulence measurements with inclined hot wires: Part 1. Heat transfer experiments with inclined hot-wire. *J. Fluid Mech.*, vol. 28, pp. 153-175.

Champagne, F. H., C. A. Sleicher and O. H. Wehrmann (1967b) Turbulence measurements with inclined hot wires: Part 2. Hot-wire response equations. *J. Fluid Mech.*, vol. 28, pp. 177-182.

Chapman, K.L., J. R. Dagenhart, M. N. Glauser and W. S. Saric (1994) Application of multi-point correlation techniques to aerodynamic flows. AIAA Paper 94-2279.

Chapman, K. L., M. N. Glauser, M. S. Reibert and W. S. Saric (1996) A multi-point correlation analysis of a crossflow-dominated boundary layer. AIAA Paper 96-0186.

Cole, D. R. (1991) *Utilizing Stochastic Estimation to Determine the Role of Large Eddies in the Axisymmetric Jet Mixing Layer*. M.S. thesis, Clarkson University.

Cole, D. R. (1996) *Utilizing a Flying Hot-Wire System to Study the Flow in an Axisymmetric Sudden Expansion*. Ph.D. diss., Clarkson University. Also Clarkson Report MAE-315.

Cole, D. R., M. N. Glauser and Y. G. Guezennec (1992) An application of stochastic estimation to the jet mixing layer. *Phys. Fluids, A*, vol. 4, no. 1.

Crouch, J. D. (1994) Receptivity of boundary layers. AIAA Paper 94-2224.

Dagenhart, J. R. (1992) *Crossflow Stability and Transition Experiments in a Swept-Wing Flow*. Ph.D. diss., Virginia Polytechnic Institute and State University. Also NASA TM-108650.

Dagenhart, J. R., W. S. Saric, M. C. Mousseux and J. P. Stack (1989) Crossflow vortex instability and transition on a 45-degree swept wing. AIAA Paper 89-1892.

Dagenhart, J. R., W. S. Saric, J. A. Hoos and M. C. Mousseux (1990) Experiments on swept-wing boundary layers. In *Laminar-Turbulent Transition* (eds. D. Arnal and R. Michel), vol. 3, pp. 369-380. Berlin: Springer-Verlag.

Delville, J. (1993) Characterization of the organization in shear layers via proper orthogonal decomposition. In *Eddy Structure Identification in Free Turbulent Shear Flows*. (eds. J. P. Bonnet and M. N. Glauser). Kluwer Academic.

Delville, J., S. Bellin and J. P. Bonnet (1989) Use of proper orthogonal decomposition in a plane turbulent mixing layer. In *Turbulence and Coherent Structures*. (eds. O. Metais and M. Lesieur). Kluwer Academic. pp. 75-90.

Delville, J. and L. S. Ukeiley (1993) Vectorial proper orthogonal decomposition, including span-wise dependency, in a plane fully turbulent mixing layer. In *Proc. 9th Symp. on Turbulent Shear Flows*. Kyoto, Japan.

Deyhle, H. and H. Bippes (1996) Disturbance growth in an unstable three-dimensional boundary layer and its dependence on environmental conditions. To appear in *J. Fluid Mech.*

Deyhle, H., G. Höhler and H. Bippes (1993) Experimental investigation of instability wave propagation in a 3-D boundary-layer flow. *AIAA J.*, vol. 31, no. 4, pp. 637-645.

Eaton, E. L. (1995) *An Examination of a Hot-Film Response Using Flush Mounted Probes in a Turbulent Jet Mixing Layer*. M.S. thesis, Clarkson University.

Floryan, J. M. (1991) On the Görtler instability of boundary layers. *Prog. Aero. Sci.*, vol. 28, pp. 235-271.

Gault, D. E. (1960) An experimental investigation of boundary layer control for drag reduction of a swept-wing section at low speed and high Reynolds numbers. NASA TN-D-320.

George, W. K., P.D. Beuther and A. Shabbir (1987) Polynomial calibrations for hot-wires in thermally varying flows. *ASME Symposium on Thermal Anemometry*, vol. 53, pp. 1-6.

Glauser, M. N. (1987) *Coherent Structures in the Axisymmetric Turbulent Jet Mixing Layer.* Ph.D. diss., University at Buffalo, SUNY.

Glauser, M. N., S. J. Leib and W. K. George (1987) Coherent structures in the axisymmetric jet mixing layer. In *Turbulent Shear Flows 5.* Berlin: Springer-Verlag.

Glauser, M. N. and W. K. George (1992) Application of multipoint measurments for flow characterization. *Exp. Thermal and Fluid Science,* vol. 5, pp. 617-632.

Glauser, M. N., D. R. Cole, L. S. Ukeiley, J. P. Bonnet and J. Delville (1993) Stochastic estimation and the proper orthogonal decomposition: Complimentary techniques for identifying structure. In *Proc. 9th Symp. on Turbulent Shear Flows.* Kyoto, Japan.

Gray, W. E. (1952) The effect of wing sweep on laminar flow. RAE TM Aero. 255.

Gregory, N., J. T. Stuart and W. S. Walker (1955) On the stability of three-dimensional boundary layers with application to the flow due to a rotating disk. *Phil. Trans. Roy. Soc.*, Series A, vol. 248, no. 943.

Guezennec, Y. G. (1989) Stochastic estimation of coherent structures in turbulent boundary layers. *Phys. Fluids, A,* vol. 1, no. 6, p. 1054.

Hall, P. and M. R. Malik (1986) On the instability of a three-dimensional attachment-line boundary layer: Weakly nonlinear theory and a numerical approach. *J. Fluid Mech,* vol. 163, pp.257-282.

Hall, P., M. R. Malik and D. I. A. Poll (1984) On the stability of an infinite swept attachment-line boundary layer. *Phil. Trans. Roy. Soc. Lon.*, Series A, vol. 395, pp. 229-245.

Haynes, T. S. (1996) *Nonlinear Stability and Saturation of Crossflow Vortices in Swept-Wing Boundary Layers.* Ph.D. diss., Arizona State University.

Haynes, T. S. and H. L. Reed (1996) Computations in nonlinear saturation of stationary crossflow vortices in a swept-wing boundary layer. AIAA Paper 96-0182.

Heinrich, R. A., M. Choudhari and E. J. Kerschen (1988) A comparison of boundary-layer receptivity mechanisms. AIAA Paper 88-3758-CP.

Hinze, J. O. (1959) *Turbulence*. New York: McGraw-Hill.

Holmes, B. J., C. C. Croom, P. D. Gall, G. S. Manuel and D. L. Carraway (1986) Advanced transition measurements methods for flight applications. AIAA Paper 86-9786.

Johnson, C. B. and D. L. Carraway (1989) A transition detection study at mach 1.5, 2.0, and 2.5 using a micro-thin hot-film system. 13th ICIASF, Gottingen, West Germany.

King, L. V. (1915) On the precision measurements of air velocity by means of the linear hot-wire anemometer. *Phil. Mag.*, vol. 29, pp. 556-577.

Kohama, Y. (1987) Some expectation on the mechanism of crossflow instability in a swept-wing flow. *Acta. Mech.*, vol. 66, pp. 21-38.

Kohama, Y., W. S. Saric and J. A. Hoos (1991) A high-frequency secondary instability of cross-flow vortices that leads to transition. In *Proc. R.A.S. Boundary Layer Transition and Control*, Cambridge, U.K.

Krutckoff, T. K. (1996) *Experiments on Boundary-Layer Receptivity to Sound*. M.S. thesis, Arizona State University.

Lerche, T. and H. Bippes (1995) Experimental investigation of cross-flow instability under the influence of controlled disturbance generation. In *Proc. Colloquium of the Royal Netherlands Academy of Arts and Sciences on Transitional Boundary Layers in Aerodynamics: State-of-the-Art and Future Directions of Research*, Amsterdam: Elsevier.

Liepmann, H. and G. Skinner (1954) Shearing stress measurements by use of a heated element. NACA TN-3268.

Loeve, M. (1955) *Probability Theory*. Van Nostrand.

Ludwieg, H. (1950) Instruments for measuring the wall shearing stress of turbulent boundary layers. NACA TM-1284.

Lumley, J. L. (1967) The structure of inhomogenous turbulent flows. In *Atmospheric Turbulence and Radio Wave Propagation*. (eds. A. M. Yaglom and V. I. Tatarsky), Moscow: Nauka. pp. 166-178.

Lumley, J. L. (1981) Coherent structures in turbulence. In *Transition and Turbulence*. (ed. R. E. Meyer), New York: Academic Press. pp. 215-242.

Mack, L. M. (1984) Boundary-layer linear stability theory. In *Special Course on Stability and Transition of Laminar Flows*. AGARD Rep. 709.

Mangalam, S. M., D. V. Maddalon, W. S. Saric, and N. K. Agarwal (1990) Measurements of crossflow vortices, attachment-line flow, and transition using microthin hot films. AIAA Paper 90-1636.

Michel, R., D. Arnal, E. Coustols and J. C. Juillen (1985) Experimental and theoretical studies of boundary layer transition on a swept infinite wing. In *Laminar-Turbulent Transition*. (ed. V. V. Kozlov), vol. 2, pp. 553-561. Berlin: Springer-Verlag.

Moin, P., R. J. Adrian and J. Kim (1987) Stochastic estimation of organized structures in turbulent channel flow. In *Proc. 6th Symp. Turbulent Shear Flows*. Toulouse, France.

Morkovin, M. V. (1969) On the many faces of transition. In *Viscous Drag Reduction* (ed. C. S. Wells), pp. 1-31. New York: Plenum.

Mousseux, M. C. (1988) *Flow-Quality Improvements in the Arizona State University Unsteady Wind Tunnel*. M.S. thesis, Arizona State University.

Myers, G., J. Schauer and R. Eustis (1963) Plane turbulent wall jet flow development and friction factor. *ASME J. Basic Engineering*, vol. 85, p.47.

Owen, P. R. and D. J. Randall (1952) Boundary-layer transition on the swept wing. RAE TM Aero. 277.

Payne, F. R. (1966) *Large Eddy Structure of a Turblent Wake*. Ph.D. diss., Pennsylvania State University.

Perry, A. E. (1982) *Hot-Wire Anemometry*. New York: Oxford University Press.

Pfenninger, W. (1957) Experiments on a 30° 12% thick symmetrical laminar suction wing in the 5 x 7 foot michigan tunnel. Northrop Rep. NAI-57-317 (BLC-93).

Pfenninger, W. (1977) Laminar flow control - laminarization. In *Special Course on Concepts for Drag Reduction*. AGARD Rep. No. 654.

Pfenninger, W. and J. W. Bacon Jr. (1961) About the development of swept laminar suction wings will full chord laminar flow. In *Boundary Layer and Flow Control* (ed. G. V. Lachmann), vol. 2, pp. 1007-1032. New York: Pergamon.

Poll, D. I. A. (1979) Transition in the infinite swept attachment line boundary layer. *Aeronaut. Q.*, vol. 30, pp. 607-629.

Poll, D. I. A. (1984) Transition description and prediction in three-dimensional flows. In *Special Course on Stability and Transition of Laminar Flows*. AGARD Rep. 709.

Poll, D. I. A. (1985) Some observations of the transition process on the windward face of a long yawed cylinder. *J. Fluid Mech.*, vol. 150, pp. 329-356.

Press, W. H., S. A. Teukolsky, W. T. Vetterling and B. P. Flannery (1992) *Numerical Recipes in C: The Art of Scientific Computing*. New York: Cambridge University Press, 2nd ed.

Radeztsky, R. H. Jr. (1994) *Growth and Development of Roughness-Induced Stationary Crossflow Vortices*. Ph.D. diss., Arizona State University.

Radeztsky, R. H. Jr., M. S. Reibert, W. S. Saric and S. Takagi (1993a) Effect of micron-sized roughness on transition in swept-wing flows. AIAA Paper 93-0076.

Radeztsky, R. H. Jr., M. S. Reibert and S. Takagi (1993b) A software solution to temperature-induced hot-wire voltage drift. In *Proc. Third Symposium on Thermal Anemometry*, vol. 167, pp. 49-55. ASME-FED.

Radeztsky, R. H. Jr., M. S. Reibert and W. S. Saric (1994) Development of stationary crossflow vortices on a swept wing. AIAA Paper 94-2373.

Ramaprian, B. R. and S. W. Tu (1983) Calibration of a heat flux gage for skin friction measurement. *J. Fluids Engineering*, vol.105, pp. 455-457.

Rasmussen, B. K. (1993) *Boundary-Layer Receptivity: Freestream Sound on an Elliptical Leading Edge*. M.S. thesis, Arizona State University.

Reed, H. L. and W. S. Saric (1989) Stability of three-dimensional boundary layers. *Ann. Rev. Fluid Mech.*, vol. 21, pp. 235-284.

Reed, H. L., W. S. Saric and D. Arnal (1996) Linear stability theory applied to boundary layers. *Ann. Rev. Fluid Mech.*, vol. 28, pp. 389-428.

Reibert, M. S. (1996a) *Nonlinear Stability, Saturation, and Transition in Crossflow-Dominated Boundary Layers*. Ph.D. diss., Arizona State University.

Reibert, M. S. (1996b) *Standard C Libraries and Codes: A Guide to Programming at the ASU Unsteady Wind Tunnel*. Arizona State University. Unsteady Wind Tunnel Internal Documentation.

Reibert, M.S., W. S. Saric, R. B. Carrillo Jr. and K.L. Chapman (1996) Experiments in nonlinear saturation of stationary crossflow vortices in a swept-wing boundary layer. AIAA Paper 96-0184.

Rempfer, D. (1996) Investigations of boundary layer transition via Galerkin projections on empirical eigenfunctions. *Phys. Fluids*, vol. 8, no. 1, p. 175.

Reshotko, E. (1984) Environment and receptivity. *Special Course on Stability and Transition of Laminar Flows*. AGARD Rep. 709.

Reshotko, E. (1994) Boundary layer instability, transition and control. AIAA Paper 94-0001.

Saric, W. S. (1992a) The ASU transition research facility. AIAA Paper 92-3910.

Saric, W. S. (1992b) Laminar-turbulent transition: Fundamentals. In *Special Course on Skin Friction Drag Reduction*. AGARD Rep. 786.

Saric, W. S. (1994a) Görtler vortices. *Ann. Rev. Fluid Mech.*, vol. 26, pp. 379-409.

Saric, W. S. (1994b) Physical description of boundary-layer transition: Experimental evidence. In *Special Course on Progress in Transition Modeling*. AGARD Rep. 793.

Saric, W. S. (1994c) Low-speed boundary-layer transition experiments. *Transition: Experiments, Theory & Computations*. Eds. T. C. Corke, G. Erlebacher, M. Y. Hussaini, Oxford.

Saric, W. S. and L. G. Yeates (1985) Experiments on the stability of crossflow vortices in swept-wing flows. AIAA Paper 85-0493.

Saric, W. S., S. Takagi and M. C. Mousseux (1988) The ASU Unsteady Wind Tunnel and fundamental requirements for freestream turbulence measurements. AIAA Paper 88-0053.

Saric, W. S., J. R. Dagenhart and M. C. Mousseux (1990a) Experiments in swept-wing transition. In *Numerical and Physical Aspects of Aerodynamic Flows IV* (ed. T. Cebeci), pp.359-371. Berlin: Springer-Verlag.

Saric, W. S., T. K. Krutckoff and R. H. Radeztsky, Jr. (1990b) Visualization of low-Reynolds-number flow fields around roughness elements. *Bull. Amer. Phys. Soc.*, vol. 35, p.2262.

Saric, W. S. and B. K. Rasmussen (1992) Boundary-layer receptivity: Freestream sound on an elliptical leading edge. *Bull. Am. Phys. Soc.*, vol 37, p. 1720.

Saric, W. S., H. L. Reed and E. J. Kerschen (1994a) Leading-edge receptivity to sound: Experiments, DNS, theory. AIAA Paper 94-2222.

Saric, W. S., W. Wei and B. K. Rasmussen (1994b) Effect of leading edge on sound receptivity. *Laminar-Turbulent Transition, Vol. IV.* Ed. R. Kobayashi. (Proc. IUTAM Symp., Sendai, Japan).

Schildt, H. (1995) *C: The Complete Reference*. Berkeley: Osborne McGraw-Hill, 3rd ed.

Schlichting, H. (1960) Some developments in boundary layer research in the past thirty years. *J. Roy. Aero. Soc.*, vol. 64, no. 590, pp. 64-79.

Schlichting, H. (1987) *Boundary-Layer Theory*. New York: McGraw-Hill, 7th ed.

Somers, D. M. and K. H. Horstmann (1985) Design of a medium-speed natural-laminar-flow airfoil for commuter aircraft applications. *DFLVR-IB/29-85/26*.

Sparrow, E. M. and J. L. Gregg (1960) Mass transfer, flow and heat transfer about a rotating disk. *Trans. ASME, J. Heat Transfer*, vol 82, pp. 294-302.

Stuart, J. T. (1953) The basic theory of the stability of three-dimensional boundary layers. ARC 15904.

Tadjfar, M. and D. C. Reda (1992) Experimental investigation of non-localized receptivity due to acoustic/2-D wavy wall interactions. *Bull. Am. Phys. Soc.*, vol. 37, p. 1720.

Tung, T. C. and R. J. Adrian (1980) Higher-order estimates of conditional eddies in isotropic turbulence. *Phys. Fluids*, vol. 23, no. 7, p. 1469.

Tutu, N. K. and R. Chevray (1975) Cross-wire anemometry in high intensity turbulence. *J. Fluid Mech.*, vol. 71, pp. 785-800.

Ukeiley, L. S. (1991) *An Examination of a Lobed Mixer Flow Field Using a One-Dimensional Scalar Proper Orthogonal Decomposition*. M.S. thesis, Clarkson University.

Ukeiley, L. S. (1995) *Dynamics of Large Scale Structures in a Plane Turbulent Mixing Layer*. Ph.D. diss., Clarkson University. Also Clarkson Report MAE-311.

Ukeiley, L. S., D. R. Cole and M. N. Glauser (1993a) An examination of the axisymmetric jet mixing layer using coherent structure detection techniques. In *Eddy Structure Identification in Free Turbulent Shear Flows*. (eds. J. P. Bonnet and M. N. Glauser). Kluwer Academic Press.

Ukeiley, L. S., M. N. Glauser and D. Wick (1993b) Downstream evolution of proper orthogonal decomposition eigenfunctions in a lobed mixer. *AIAA J.*, vol. 31, pp. 1392-1297.

von Kármán, T. (1946) On laminar and turbulent friction. NACA-TM 1092.

von Kármán, T. (1963) *Aerodynamics: Selected Topics in Light of Their Historical Development*, New York: McGraw-Hill.

Wei, W. (1994) *Boundary-Layer Receptivity: Freestream Sound on a 20:1 Elliptical Leading Edge*. M.S. thesis, Arizona State University.

Wlezien, R. W. (1994) Measurement of acoustic receptivity. AIAA Paper 94-2221.

Yang, J. M., J. Y. Yoo and H. Choi (1996) Correlation of the wall skin-friction and streamwise velocity fluctuations in a turbulent boundary layer. In *Advances in Turbulent Research*. Seoul, Korea. pp. 47-65.